



**HAL**  
open science

# Electronic properties of two-dimensional heterostructures based on graphene and transition metal dichalcogenides

Somepalli Venkateswarlu

► **To cite this version:**

Somepalli Venkateswarlu. Electronic properties of two-dimensional heterostructures based on graphene and transition metal dichalcogenides. Physics [physics]. CY Cergy Paris Université, 2021. English. NNT : 2021CYUN1018 . tel-03383066

**HAL Id: tel-03383066**

**<https://theses.hal.science/tel-03383066>**

Submitted on 18 Oct 2021

**HAL** is a multi-disciplinary open access archive for the deposit and dissemination of scientific research documents, whether they are published or not. The documents may come from teaching and research institutions in France or abroad, or from public or private research centers.

L'archive ouverte pluridisciplinaire **HAL**, est destinée au dépôt et à la diffusion de documents scientifiques de niveau recherche, publiés ou non, émanant des établissements d'enseignement et de recherche français ou étrangers, des laboratoires publics ou privés.



THÈSE DE DOCTORAT  
CY CERGY PARIS UNIVERSITÉ

Présentée par

**SOMEPELLI VENKATESWARLU**

POUR OBTENIR LE GRADE DE DOCTEUR

SPÉCIALITÉ : PHYSIQUE THÉORIQUE

---

**Electronic properties of two-dimensional  
heterostructures based on graphene and  
transition metal dichalcogenides.**

---

Date de la soutenance : 26 February 2021

Devant le jury de thèse :

Mme. Christine Richter	CY Cergy Paris Université	Présidente
M. Didier Mayou	Institut Néel	Rapporteur
M. Nicholas Hine	University of Warwick	Rapporteur
M. Guillaume Radtke	Sorbonne Université	Examineur
M. Andreas Honecker	CY Cergy Paris Université	Directeur de thèse
M. Guy Trambly de Lais-sardière	CY Cergy Paris Université	Co-encadrant de thèse

Unité de Recherche: [Laboratoire de Physique Théorique et Modélisation](#)

CY CERGY PARIS UNIVERSITÉ



DOCTORAL THESIS

---

**Electronic properties of two-dimensional  
heterostructures based on graphene and  
transition metal dichalcogenides.**

---

*Author:*

Somepalli  
Venkateswarlu

*Supervisors:*

Prof. Andreas Honecker  
Dr. Guy Trambly de Laissardière

*A thesis submitted in fulfillment of the requirements  
for the degree of Doctor of Philosophy*

*in the*

Laboratoire de Physique Théorique et Modélisation

**LPTM**  
Laboratoire de Physique  
Théorique et Modélisation

---

## *Abstract*

---

After the first demonstration of graphene, 2D materials have attracted tremendous attention in the electronic devices community. Graphene was regarded as a promising material for electronics due to its extremely high carrier mobility. However, graphene is a semi-metal that does not have a bandgap in its inherent form, which makes it inappropriate for switching devices in digital logic circuits. More recently new class of 2D semiconducting materials, such as Transition Metal Dichalcogenides (TMDs), have been found, and it has been shown that stacking layered materials to get heterostructures is a very powerful method to tailor their properties, mixing them, but also inducing new ones. In this context, this PhD thesis work focused on the electronic properties of monolayers of TMDs, graphene/TMDs bilayers, and twisted bilayers of TMDs. In order to study such a complex structures, we have combined the density functional theory (DFT) approaches and simplified tight-binding (TB) models.

The first part of this work is to study theoretically the imperfections in the crystal structure, such as point defects that can strongly modify the transport properties. We analyze the effect of vacant sites on the density of states, the conductivity, and the mobility of single layers of semiconducting TMDs with the form  $\text{MX}_2$  ( $\text{M} = \text{Mo}, \text{W}$  and  $\text{X} = \text{S}, \text{Se}, \text{Te}$ ). The electronic structure is considered within an eleven band-model, which accounts for the relevant combination of  $d$  orbitals of the metal  $\text{M}$  and  $p$  orbitals of the chalcogen  $\text{X}$ . We use a real-space recursion method (Lanczos method) and Kubo-Greenwood formula for the calculation of the conductivity in TMDs with different distributions of the disorder. Our result show that  $\text{M}$  or  $\text{X}$  vacant atoms create midgap states that localize charge carriers around the defects and which modify the transport properties.

The second part focuses on the electronic properties of van der Waals heterostructures of graphene/ $\text{MoS}_2$ , graphene/ $\text{WSe}_2$ , twisted bilayer  $\text{MoS}_2$  through

---

DFT and TB calculations. Plane-wave pseudopotential DFT calculations were carried out with the ABINIT software package using the generalized gradient approximations and local density approximations for the exchange- correlation potential. In order to obtain precise results, we have fully optimized atomic positions, as well as lattice parameters of all studied heterostructures. First-principles calculations show the effect of the interlayer spacing between the graphene monolayer and the  $\text{MX}_2$  monolayer on the location of the graphene Dirac cone in the band gap of  $\text{MX}_2$  semiconductor. We further examine the electronic properties with and without optimization of the atomic positions in different bilayer configurations. For that, we studied graphene/ $\text{MoS}_2$ :  $4\times 4/3\times 3$  [4:3],  $5\times 5/4\times 4$  [5:4], and  $9\times 9/7\times 7$  [9:7], and graphene/ $\text{WSe}_2$ :  $4\times 4/3\times 3$  [4:3] supercell geometries, having different magnitudes of lattice mismatch. It turns out that this mismatch is a key parameter, whereas it has been often forgotten in previous studies. Spin-orbit coupling interaction is also included to see how the strong spin-orbital coupling in  $\text{MX}_2$  may influence the one of graphene.

Finally, we investigate the electronic localization in twisted bilayer  $\text{MoS}_2$ . We propose a new DFT-based Slater-Koster TB model to find the band structure of twisted bilayer  $\text{MoS}_2$  with small rotation angles  $\theta$ , where the moiré unit cell becomes too large for DFT computations. This allows the first reliable and systematic studies of such states in twisted bilayer  $\text{MoS}_2$  for the whole range of rotation angles  $\theta$ . We show that isolated bands appear at low energy for  $\theta \lesssim 5 - 6^\circ$ . Moreover, these bands become “flat bands”, characterized by a vanishing average velocity, for the smallest angles  $\theta \lesssim 2^\circ$ , thus conforming the existence of moiré flat bands in twisted bilayer semiconductors, as they exist in twisted bilayer graphene.

---

## *Résumé*

---

Depuis la découverte du graphène, les matériaux 2D ont suscité une attention considérable dans la communauté des matériaux pour l'électronique. Le graphène est un matériau prometteur par la très grande mobilité de ses porteurs de charge. Cependant, pur, il est un semi-métal sans bande interdite, ce qui le rend inapproprié pour des dispositifs électroniques. Récemment, de nouvelles familles de semi-conducteurs 2D, tels que les dichalcogénures de métaux de transition (TMD), ont été découvertes. Et il a été démontré que l'empilement de matériaux en couches, formant des hétérostructures, est une méthode très performante pour modifier leurs propriétés, les mélanger et en induire de nouvelles. Dans ce contexte, cette thèse a porté sur les propriétés électroniques de monocouches de TMD, de bicouches de graphène/TMD et de bicouches tournées de TMD. Afin d'étudier ces structures complexes, nous avons combiné approches par théorie de fonctionnelle de la densité (DFT) et modèles simplifiés en liaisons fortes (TB).

La première partie consiste en une étude théorique des d'imperfections de la structure cristalline, telles que des défauts ponctuels pouvant modifier fortement les propriétés de transport. Nous analysons l'effet de lacunes atomiques sur la densité des états, la conductivité et la mobilité des monocouches de TMDs semi-conducteurs  $\text{MX}_2$  ( $\text{M} = \text{Mo}, \text{W}$  et  $\text{X} = \text{S}, \text{Se}, \text{Te}$ ). La structure électronique est décrite par onze bandes, combinaison des orbitales  $d$  du métal  $\text{M}$  et des orbitales  $p$  du chalcogène  $\text{X}$ . Par une méthode de récursion dans l'espace réel (méthode de Lanczos) et la formule de Kubo-Greenwood nous calculons la conductivité pour différentes distributions de désordre. Nos résultats montrent comment les lacunes créent des états d'impureté qui localisent les porteurs de charge autour des défauts et modifient les propriétés de transport.

La deuxième partie se concentre sur les propriétés d'hétérostructures de van der Waals bicouche graphène/ $\text{MoS}_2$ , graphène/ $\text{WSe}_2$  et de la bicouche tournée de

---

MoS<sub>2</sub> par des calculs DFT et TB. Les calculs de DFT, à partir d'ondes plane et de pseudo-potentiel, ont été effectués avec le logiciel ABINIT en utilisant l'approximation de gradient généralisées et de la densité locale pour le potentiel d'échange-corrélation. Afin d'obtenir des résultats précis, nous relaxons les positions atomiques ainsi que le paramètre de maille. Ces calculs montrent l'effet de l'espacement entre les monocouches de graphène et MX<sub>2</sub> sur la position du cône de Dirac du graphène dans la bande interdite du semi-conducteur MX<sub>2</sub>. Nous analysons aussi les propriétés électroniques avec et sans optimisation des positions atomiques dans différentes configurations de bicouches. Pour cela, nous avons étudié des super-mailles de graphène/MoS<sub>2</sub> (4×4/3×3 [4:3], 5×5/4×4 [5:4], and 9×9/7×7 [9:7]) et de graphène/WSe<sub>2</sub> (4×4/3×3 [4:3]) ayant des incompatibilités de paramètres de maille différentes. En effet cette incompatibilité est un paramètre clé, alors qu'il a souvent été négligé dans les études précédentes. Le couplage spin-orbite est également inclus pour étudier comment le fort spin-orbite du MX<sub>2</sub> peut influencer celui du graphène.

Enfin, nous étudions la localisation électronique dans les bicouches tournées de MoS<sub>2</sub>. Nous proposons un nouveau modèle TB, de type Slater-Koster basé sur la DFT, pour calculer la structure de bande de bicouches tournées aux petits angles de rotation  $\theta$ , qui formant un moiré de trop grande taille pour être traité en DFT. Cela permet l'une des premières études fiable et systématique pour une grande gamme des angles de rotation  $\theta$ . Nous montrons que des bandes isolées apparaissent à énergie faible pour  $\theta \lesssim 5 - 6^\circ$ . Ces bandes deviennent plates, caractérisées par une vitesse moyenne très faible, pour des angles plus petits  $\theta \lesssim 2^\circ$ , confirmant ainsi l'existence de bandes plates de moiré dans les bicouches tournées de semi-conducteurs, comme elles existent dans les bicouches de graphène.

---

## *Acknowledgements*

---

Undertaking this PhD has been a truly life-changing experience for me and it would not have been possible to do without the support and guidance that I received from many people.

I would like to thank my supervisors, Prof. Andreas Honecker and Dr. Guy Trambly de Laissardière for the constant support, patient guidance, encouragement and advice he has provided throughout my time as his student. I have been extremely lucky to have supervisors who cared so much about my work, and who responded to my questions and queries so promptly. On many occasions that I have been lost during this research, Prof. Guy Trambly de Laissardière and Prof. Andreas Honecker has always been there to point me in the right direction. I thank them especially for always being there to provide good advices personally and professionally.

I am profoundly grateful to Dr. Javad Vahedi who worked as a Postdoc in Laboratoire de Physique Théorique et Modélisation (LPTM) for help in python programming and Mean field theory. Many thanks to Cédric Gérard, Yann Costes and Baptiste Mary for their assistance, especially in relation to the computer, cluster and ABINIT. I also express my appreciation to Dr. Thi Thu Phúng, Dr. Ahmed Missaoui, Maheshwor Tiwari, and all members of the LPTM for supporting and helping me.

My sincere gratefulness to this work was supported by the ANR project J2D (ANR-15-CE24-0017) and the Paris//Seine excellence initiative (grant 2017-231-C01-A0) for financial support.

I must express my gratitude to my wife, Anuradha Somepalli and my family members for their continued support and encouragement.

I would like to dedicate this work to my late father Mr. Venkatarao Somepalli whose dreams for me have resulted in this achievement and without his loving upbringing and nurturing; I would not have been where I am today and what I am today. It is true that if god ever existed, he would be in the form of a father, because only a father can love and give without expecting anything in return.

---

# *Contents*

---

	<b>Page</b>
<b>Contents</b>	<b>v</b>
<b>List of Figures</b>	<b>ix</b>
<b>List of Tables</b>	<b>xxiii</b>
<b>1 Introduction</b>	<b>1</b>
<b>2 Theoretical and Methodological background</b>	<b>9</b>
2.1 The Born-Oppenheimer approximation . . . . .	10
2.1.1 Hartree-Fock approximation . . . . .	13
2.2 Density Functional Theory (DFT) . . . . .	14
2.2.1 The Hohenberg-Kohn theorems . . . . .	15
2.2.1.1 The Hohenberg-Kohn theorem-1 . . . . .	16
2.2.1.2 The Hohenberg-Kohn theorem-2 . . . . .	17
2.2.2 The Kohn-Sham (KS) equations . . . . .	19
2.3 Exchange-correlation functional . . . . .	22
2.3.1 The Local Density Approximation (LDA) . . . . .	22
2.3.2 The Generalized Gradient Approximation (GGA) . . . . .	24
2.3.3 Van der Waals interactions . . . . .	24
2.4 Tight-Binding Method . . . . .	24
2.4.1 Slater-Koster parameters . . . . .	26
2.4.2 Spin Orbit Coupling (SOC) . . . . .	31
2.4.3 Wannier functions . . . . .	34
2.5 Conclusion . . . . .	38
<b>3 Numerical methods of Quantum transport</b>	<b>39</b>
3.1 Recursion methods for computing the density of states and wave- packet dynamics . . . . .	41

---

3.1.1	Recursion method (Lanczos method) . . . . .	41
3.1.2	The density of states . . . . .	43
3.1.3	Termination of the continued fraction . . . . .	45
3.2	Recursion method for computing the wave packet dynamics . . . . .	48
3.2.1	Kubo-Greenwood method . . . . .	48
3.2.2	Relation between low frequency conductivity and quantum diffusion . . . . .	50
3.2.3	Relaxation time approximation (RTA) . . . . .	51
3.3	Chebyshev polynomials . . . . .	53
3.3.1	Spectral coefficient $C_n(T)$ . . . . .	54
3.3.2	Calculation of $ \phi'_{RP}(T)\rangle$ & $ \phi_{RP}(T)\rangle$ . . . . .	55
3.3.3	Numerical implementation of RTA . . . . .	57
3.4	Conclusion . . . . .	58
<b>4</b>	<b>Transport properties of different TMDs</b>	<b>59</b>
4.1	Atomic structure . . . . .	61
4.2	Electronic band calculation . . . . .	62
4.2.1	DFT-Electronic band structure . . . . .	63
4.2.1.1	Without spin orbit coupling (SOC) . . . . .	63
4.2.1.2	With spin orbit coupling (SOC) . . . . .	63
4.2.2	Tight-Binding model description for Transition Metal Dichalcogenides . . . . .	65
4.2.3	Electronic band structure of Wannier orbitals from DFT . . . . .	68
4.3	Local density of states (LDOS) . . . . .	69
4.4	Density of states with defects . . . . .	69
4.5	Transport properties . . . . .	73
4.5.1	Conductivity & Inelastic mean free path . . . . .	73
4.5.2	Microscopic conductivity . . . . .	76
4.5.3	Thermodynamic average conductivity at room temperature . . . . .	78
4.6	Conclusion . . . . .	83
<b>5</b>	<b>Structural and electronic properties of graphene/MoS<sub>2</sub> &amp; graphene/WSe<sub>2</sub></b>	<b>85</b>
5.1	Introduction & experimental motivation . . . . .	87
5.2	Computational details . . . . .	89
5.2.1	Density functional theory . . . . .	89
5.2.2	Choice of hexagonal supercell structure . . . . .	90
5.3	Graphene/MoS <sub>2</sub> heterostructure [4:3] . . . . .	90
5.3.1	Atomic structure . . . . .	90
5.3.1.1	Non relaxed structure . . . . .	90
5.3.1.2	Relaxed structure . . . . .	91

---

5.3.2	Electronic band structure . . . . .	92
5.3.2.1	Influence of pseudopotentials . . . . .	94
5.3.2.2	Interlayer distance effect . . . . .	95
5.3.2.3	Relaxation effect . . . . .	95
5.3.2.4	Spin orbit coupling effect . . . . .	98
5.4	Graphene/MoS <sub>2</sub> heterostructure [5:4] . . . . .	99
5.4.1	Atomic structure . . . . .	99
5.4.1.1	Non relaxed structure . . . . .	99
5.4.1.2	Relaxed structure . . . . .	100
5.4.2	Electronic band structure . . . . .	101
5.4.2.1	Relaxation effect . . . . .	101
5.4.2.2	Spin orbit coupling effect . . . . .	105
5.5	Graphene/MoS <sub>2</sub> heterostructure [9:7] . . . . .	106
5.5.1	Atomic structure . . . . .	106
5.5.1.1	Non relaxed structure . . . . .	106
5.5.1.2	Relaxed structure . . . . .	107
5.5.2	Electronic band structure . . . . .	108
5.5.2.1	Relaxation effect . . . . .	108
5.5.2.2	Spin orbit coupling effect . . . . .	113
5.6	Graphene/WSe <sub>2</sub> heterostructure [4:3] . . . . .	115
5.6.1	Atomic structure . . . . .	115
5.6.1.1	Non relaxed structure . . . . .	115
5.6.1.2	Relaxed structure . . . . .	116
5.6.2	Electronic band structure . . . . .	118
5.6.2.1	Relaxation effect . . . . .	118
5.6.2.2	Spin orbit coupling effect . . . . .	119
5.6.2.3	Structural imperfection effects . . . . .	120
5.7	Conclusion . . . . .	123
<b>6</b>	<b>Twisted bilayer of MoS<sub>2</sub></b> . . . . .	<b>125</b>
6.1	Atomic structure . . . . .	127
6.1.1	Non relaxed structure . . . . .	127
6.1.2	Structural relaxation . . . . .	127
6.2	DFT calculations (Large angles) . . . . .	130
6.2.1	Electronic band structure of different angles . . . . .	130
6.2.2	Electronic band structure of different angles with and without structural relaxation . . . . .	132
6.3	Tight-Binding (TB) calculations . . . . .	133
6.3.1	TB-model for MoS <sub>2</sub> monolayer . . . . .	133
6.3.2	TB model for twisted bilayer MoS <sub>2</sub> (tb-MoS <sub>2</sub> ) . . . . .	134

---

6.3.3	Moiré pattern of tb-MoS <sub>2</sub> . . . . .	137
6.3.4	Analysis of bands of tb-MoS <sub>2</sub> built from AA stacking . . .	139
6.3.5	Analysis of bands of tb-MoS <sub>2</sub> built from AB stacking . . .	141
6.3.6	Local density of states (LDOS) . . . . .	142
6.3.7	Confined state in the AA region of the moiré pattern . . .	145
6.3.7.1	Electronic band structure with SOC at $\theta = 3.15^\circ$ and $\theta = 1.61^\circ$ . . . . .	146
6.3.7.2	Eigenstates corresponding to flat bands ( $\theta = 1.61^\circ$ ) in tb-MoS <sub>2</sub> . . . . .	146
6.4	Conclusion . . . . .	149
<b>7</b>	<b>Summary</b> . . . . .	<b>151</b>
<b>Appendices</b> . . . . .		<b>155</b>
A	Spin Orbit Coupling (SOC) . . . . .	156
A.1	Spin Orbit Coupling (SOC) of d-orbitals . . . . .	156
A.2	Time Reversal Symmetry and Spatial Inversion Symmetry	156
B	Transport properties of MX <sub>2</sub> . . . . .	158
B.1	Conductivity and inelastic scattering length vs scattering time . . . . .	158
B.2	Elastic mean free path . . . . .	158
C	Graphene/MoS <sub>2</sub> bilayer heterostructures DFT+TB calculations .	162
C.1	Individual layers of graphene/MoS <sub>2</sub> heterostructures of different configurations 4:3 and 9:7 . . . . .	162
C.2	Electronic band structure of graphene/MoS <sub>2</sub> [4:3] heterostruc- ture with and without relaxation . . . . .	164
C.3	TB-model for graphene/MoS <sub>2</sub> (5:4 and 9:7) . . . . .	165
D	Electronic properties of tb-MoS <sub>2</sub> . . . . .	168
D.1	Electronic band structure of different pseudopotentials . .	168
D.2	Cut off distance of tb-MoS <sub>2</sub> . . . . .	169
D.3	TB-model (alternative) for twisted bilayer MoS <sub>2</sub> . . . . .	170
D.4	Eigenstates corresponding to flat bands ( $\theta = 3.15^\circ$ ) in tb- MoS <sub>2</sub> . . . . .	173
<b>Bibliography</b> . . . . .		<b>174</b>

---

---

## *List of Figures*

---

2.1	Flow chart for different type of codes for electronic structure calculations. . . . .	15
2.2	Flow chart: Computational approaches for Hohenberg-Kohn (HK) to calculate the energy. . . . .	18
2.3	Chart for connection between the many-body and independent particles through Kohn-Sham (KS) equations. . . . .	19
2.4	Flow chart for Kohn-Sham (KS) self-consistent approaches. . . . .	21
2.5	Representation of different type of matrix elements: (a) Represents one center, where the two orbitals and the potential are at the same atom, (b) represents two centers integrals, where each orbitals is sitting on a different atom and the potential on one of them, (c) represents two centers integrals, where the two orbitals are sitting on the same site but the potential is centered in another. The blue color circle indicates $S$ orbitals, Crimson color lobes indicates $P$ orbitals and Green circle indicates the potential $V(\mathbf{r})$ . . . . .	28
2.6	A two-center matrix element between $P_z$ orbitals on atoms $i$ and $j$ separated by the vector $R_{ij} = R_j - R_i$ . Each $P_z$ orbital may be expressed as a linear combination of $P_x$ , $P_y$ , and $P_z$ orbitals quantized relative to the $R_{ij}$ axis, so the matrix element is a linear combination of the Slater-Koster parameters $V_{pp\pi}$ and $V_{pp\sigma}$ . . . . .	29
2.7	Electronic band structure of graphene monolayer TB method [left] with $p_z$ -orbital only, and first neighbor coupling $V_{pp\pi} = -2.7$ eV. Comparison of DFT+TB [right], the DFT calculation includes all orbitals around the Dirac energy. . . . .	31
2.8	Electronic band structure of a graphene monolayer including spin orbit coupling (SOC). Spin splitting of bands at the Dirac point is $30\mu\text{eV}$ . Calculations are done by using the TB method including $s$ , $p_x$ , $p_y$ , $p_z$ orbitals. . . . .	34

---

2.9	Electronic band structure of a graphene monolayer. Estimated $p$ -orbital character of bands, computed by band projections using Wannier90 code. A color scheme is used to measure the $p$ -orbital character (red color) of the bands. . . . .	37
2.10	Electronic band structure of a graphene monolayer, Interpolation with Wannier90 on the $\Gamma - K - M - \Gamma$ path (red lines) and DFT (ABINIT) reference band structure (blue circles). . . . .	37
3.1	Schematic representation of the linear chain generated by the Lanczos procedure. . . . .	43
3.2	Effect of initial random phase states on the total density of states of a graphene monolayer: without vacancies, considered 3 different initial random phase state configurations are $\phi_{RP1}$ , $\phi_{RP2}$ , and $\phi_{RP3}$ . Number of recursion steps ( $N_r = 1000$ ) and resolution of energy $\epsilon = 5$ meV. TB model from [37]. . . . .	46
3.3	Recursion coefficients $a_n$ and $b_n$ of a graphene monolayer without vacancies. Number of recursion steps $N_r = 500$ . TB model from [37]. . . . .	47
3.4	Effect of number of recursion steps $N_r$ on the density of states of a graphene monolayer: without vacancies, number of steps of recursion $N_r = 50$ [Left], $N_r = 500$ [Right] and resolution of energy $\epsilon = 5$ meV. TB model from [37]. . . . .	48
3.5	Flow chart for Recursion method. This method has been developed by D. Mayou and his coworkers [106, 180–183, 216]. . . . .	58
4.1	Sketch of the atomic structure of $\text{MX}_2$ : (a) Top view of monolayer of $\text{MX}_2$ . <b>Blue (red)</b> circles indicates M (X) atoms. $\vec{\delta}_i$ (where $i = \pm 1, 2, 3$ ) indicates the nearest neighbor vectors and $\vec{a}_i$ ( $i = 1, 2$ ) indicates the next nearest neighbor vectors. (b) Brillouin zone for the $\text{MX}_2$ lattice, where $\vec{b}_1$ and $\vec{b}_2$ are the reciprocal lattice basis vectors, and $\Gamma$ , $M$ and $K$ are the highest symmetry points. . . . .	62
4.2	The electronic band structure of monolayer of a different TMDs of $\text{MX}_2$ ( $M = \text{Mo}, \text{W}$ and $X = \text{S}, \text{Se}, \text{Te}$ ) without SOC. The direct bandgap is obtained at highest symmetry point $K$ . (a) $\text{MoS}_2$ , (b) $\text{MoSe}_2$ , (c) $\text{MoTe}_2$ , (d) $\text{WSe}_2$ , and (e) $\text{WTe}_2$ . . . . .	64
4.3	The electronic band structure of a monolayer of different TMDs of $\text{MX}_2$ ( $M = \text{Mo}, \text{W}$ and $X = \text{S}, \text{Se}, \text{Te}$ ) with SOC. The direct bandgap is obtained at highest symmetry point $K$ . (a) $\text{MoS}_2$ , (b) $\text{MoSe}_2$ , (c) $\text{MoTe}_2$ , (d) $\text{WSe}_2$ , and (e) $\text{WTe}_2$ . . . . .	66
4.4	A comparison of electronic band structure of a monolayer of $\text{MoS}_2$ with Wannier-TB model and DFT [ABINIT]. . . . .	68

- 
- 4.5 The electronic band structure of monolayer of MoS<sub>2</sub> with the Wannier method showing the contribution of *d*-like MLWFs (proportion of *d*-character of the bands Mo) in red [top] and *p*-like MLWFs (proportion of *p*-character of the bands S) in red [bottom]. A color scheme is used to measure the proportion of orbital character of the bands. . . . . 70
- 4.6 TB-total density of states (DOS) and local DOS (LDOS),  $d_0 = d_{3z^2-r^2}$ ,  $d_1 = d_{xz}$ ,  $d_{yz}$  and  $d_2 = d_{xy}$ ,  $d_{x^2-y^2}$  monolayer of different TMDs without defects and without SOC. The LDOS and total DOS are calculated employing a broadening by a Lorentzian (see section 3.1.2) with  $\epsilon = 6$  meV. (a) MoS<sub>2</sub>, (b) MoSe<sub>2</sub>, (c) MoTe<sub>2</sub>, (d) WSe<sub>2</sub>, and (e) WTe<sub>2</sub>. . . . . 71
- 4.7 TB-Total density of states (DOS) with random distribution of vacancies (vacant M atoms or vacant X atoms) with different concentrations *c* of vacancies with respect to the total number of atoms (*c* = 0 %, 3 %, 2 %, 1 %, and 0.5 %) of monolayer of different TMDs. The DOS is calculated employing a broadening by a Lorentzian (see section 3.1.2) with  $\epsilon = 15$  meV. The peaks in the DOS associated to midgap bands is due to X or M defects. (a) MoS<sub>2</sub>, (b) MoSe<sub>2</sub>, (c) MoTe<sub>2</sub>, (d) WSe<sub>2</sub>, and (e) WTe<sub>2</sub>. . . . . 72
- 4.8 The variation of conductivity  $\sigma$  (solid line) and inelastic scattering length  $L_i$  (dashed line) in MX<sub>2</sub> versus inelastic scattering time  $\tau_i$  for the defect concentration *c* = 1 % of point defects (vacancies by random removal of atoms). For the three energy values: valence band (blue), inside the midgap states region (magenta) and conduction band (red). (a) MoS<sub>2</sub>, (b) MoSe<sub>2</sub>, (c) MoTe<sub>2</sub>, (d) WSe<sub>2</sub>, and (e) WTe<sub>2</sub>.  $G_0 = 2e^2/h$ . . . . . 75
- 4.9 The variation of microscopic conductivity  $\sigma_M$  versus energy *E* in MX<sub>2</sub> for different concentration (*c* = 0.5 %, 1 %, 2 %, 3 %, 5 %, and 10 %) of point defects (vacancies by random removal of atoms M = Mo, W or X = S, Se, Te). (a) MoS<sub>2</sub>, (b) MoSe<sub>2</sub>, (c) MoTe<sub>2</sub>, (d) WSe<sub>2</sub>, and (e) WTe<sub>2</sub>.  $G_0 = 2e^2/h$ . . . . . 77
- 4.10 The variation of the microscopic conductivity  $\sigma_M c$  (*c* in %) versus energy *E* in MX<sub>2</sub> for different concentration (*c* = 0.5 %, 1 %, 2 %, 3 %, 5 %, and 10 %) of point defects (vacancies by random removal of atoms M = Mo, W or X = S, Se, Te). (a) MoS<sub>2</sub>, (b) MoSe<sub>2</sub>, (c) MoTe<sub>2</sub>, (d) WSe<sub>2</sub>, and (e) WTe<sub>2</sub>.  $\sigma_M$  in  $G_0 = 2e^2/h$  and *c* in %. . . . . 78

4.11	Thermodynamic average conductivity at room temperature ( $\sigma_{300K}$ ) versus chemical potential ( $\mu_C$ ) in $\text{MX}_2$ for different concentration ( $c = 0.5\%$ , $1\%$ , $2\%$ , $3\%$ , $5\%$ , and $10\%$ ) of point defects (vacancies by random removal of atoms $M = \text{Mo}$ , $\text{W}$ or $X = \text{S}$ , $\text{Se}$ , $\text{Te}$ ). (a) $\text{MoS}_2$ , (b) $\text{MoSe}_2$ , (c) $\text{MoTe}_2$ , (d) $\text{WSe}_2$ , and (e) $\text{WTe}_2$ . $G_0 = 2e^2/h$ . . . . .	80
4.12	Thermodynamic average conductivity at room temperature ( $\sigma_{300K}$ ) versus number of charge carriers ( $N_e$ ) in $\text{MX}_2$ for different concentration ( $c = 0.5\%$ , $1\%$ , $2\%$ , $3\%$ , $5\%$ , and $10\%$ ) of point defects (vacancies by random removal of atoms $M = \text{Mo}$ , $\text{W}$ or $X = \text{S}$ , $\text{Se}$ , $\text{Te}$ ). (a) $\text{MoS}_2$ , (b) $\text{MoSe}_2$ , (c) $\text{MoTe}_2$ , (d) $\text{WSe}_2$ , and (e) $\text{WTe}_2$ . $G_0 = 2e^2/h$ . . . . .	81
4.13	Mobility ( $\mu$ ) at room temperature ( $T \approx 300K$ ) versus number of charge carriers ( $N_e$ ) in $\text{MX}_2$ for different concentration ( $c = 0.5\%$ , $1\%$ , and $2\%$ ) of point defects (vacancies by random removal of atoms $M = \text{Mo}$ , $\text{W}$ or $X = \text{S}$ , $\text{Se}$ , $\text{Te}$ ). (a) $\text{MoS}_2$ , (b) $\text{MoSe}_2$ , (c) $\text{MoTe}_2$ , (d) $\text{WSe}_2$ , and (e) $\text{WTe}_2$ . The numerical calculation of the mobility is no more valid when $N_e \rightarrow 0$ as the conductivity in equation 4.16 is overestimated because of the tail of the Lorentzian used in the recursion method, therefore the peak in $\mu$ at zero is a numerical artifact. . . . .	82
5.1	Non relaxed crystal structure of graphene/ $\text{MoS}_2$ [4:3] bilayer heterostructure. (a) Side view (blue lines indicate the distance between the carbon to molybdenum, and carbon to top sulfur). (b) Top view. (c) Unit cells of graphene and $\text{MoS}_2$ monolayers lattice mismatch. (d) Bilayer separation distance between the graphene ( $4 \times 4$ ) and $\text{MoS}_2$ ( $3 \times 3$ ) layers, with the lattice parameter of $\text{MoS}_2$ . All the calculations have been done by using LDA-PW-PAW pseudopotentials and basic reference was taken $\text{MoS}_2$ unit cell. . . . .	91
5.2	Simplified sketch of the lattice parameters of hexagonal superlattice of relaxed graphene/ $\text{MoS}_2$ [4:3] bilayer heterostructure, comparison to $\text{MoS}_2$ and graphene supercells alone. In our work the basic reference (without relaxation) has taken $\text{MoS}_2$ ( $3 \times 3$ ) unit cell. . . . .	92

---

5.3	Variation of atomic positions along the $z$ -direction in the unit cell of graphene/MoS <sub>2</sub> [4:3] bilayer heterostructure without (empty blue circles) and with (full red circles) relaxation: (a) Graphene layer, (b) MoS <sub>2</sub> layer-sulfur (top), (c) graphene/MoS <sub>2</sub> [4:3] bilayer heterostructure position of atoms in the unit cell, (d) MoS <sub>2</sub> layer-molybdenum, (e) MoS <sub>2</sub> layer-sulfur (bottom). . . . .	93
5.4	Electronic band structure of graphene/MoS <sub>2</sub> [4:3] bilayer heterostructure with optimized atomic positions and optimized lattice parameters, calculated with different pseudopotentials HGN-CPP, GGA-PBE-PAW+vdW and LDA-PW-PAW. Optimization with different pseudopotentials gives similar positions. . . . .	94
5.5	Electronic band structure of graphene/MoS <sub>2</sub> [4:3] bilayer heterostructure with different bilayer (interlayer) separation distance between carbon and molybdenum layers (C-Mo), all the calculations have done by using LDA-PW-PAW pseudopotentials. Calculations are done without relaxation and with the lattice parameter of MoS <sub>2</sub> . . . . .	95
5.6	Comparison of electronic band structure of graphene/MoS <sub>2</sub> [4:3] bilayer heterostructure with relaxation (red lines), without relaxation (blue lines), and the lattice parameters (acell) are relaxed and the atomic positions are not relaxed (black lines). Zoom of the bands around the Dirac point (inset). The points are calculated results and lines are guide for the eyes. All the calculations have been done by using GGA-PAW pseudopotentials (PBE) including vdW. For comparison of electronic bands, we shift the Dirac cone at zero energy. . . . .	96
5.7	Electronic band structure of relaxed graphene/MoS <sub>2</sub> [4:3] bilayer heterostructure. Comparison between the electronic bands of relaxed graphene/MoS <sub>2</sub> [4:3] bilayer heterostructure, electronic bands of graphene layer alone and with the carbon atomic positions of the relaxed graphene/MoS <sub>2</sub> [4:3] bilayer heterostructure, electronic bands of MoS <sub>2</sub> layer alone and with the atomic positions of the relaxed graphene/MoS <sub>2</sub> [4:3] bilayer heterostructure. Zoom of the bands around the Dirac point (inset). The points are calculated results and lines are guide for the eyes. All the calculations have been done by using GGA-PAW pseudopotentials (PBE) including vdW. For the comparison of electronic bands, we shift the Dirac cone to zero energy. The Fermi level is located in between the Dirac cone and the minimum of the conduction band. . . . .	98

5.8	Electronic band structure of graphene/MoS <sub>2</sub> [4:3] bilayer heterostructure with (blue lines) and without (red lines) spin orbit coupling along high symmetry lines. Zoom of the bands around the Dirac point (right). The points are calculated results and lines are guide for the eyes. After SOC the bandgap at the Dirac point is reduced by $\approx 1.86$ meV. All the calculations have been done by using GGA-PAW pseudopotentials (PBE) including vdW.	99
5.9	Non relaxed crystal structure of graphene/MoS <sub>2</sub> [5:4] bilayer heterostructure. (a) Side view (blue lines indicate the distance between the carbon to molybdenum, and carbon to top sulfur). (b) Top view. (c) Unit cells of graphene and MoS <sub>2</sub> monolayers lattice mismatch. (d) Bilayer separation distance between the graphene ( $5 \times 5$ ) and MoS <sub>2</sub> ( $4 \times 4$ ) layers, with the lattice parameter of MoS <sub>2</sub> . All the calculations have been done by using LDA-PW-PAW pseudopotentials and basic reference was taken MoS <sub>2</sub> ( $4 \times 4$ ) unit cell.	100
5.10	Simplified sketch of the lattice parameters of hexagonal super lattice of graphene/MoS <sub>2</sub> [5:4] bilayer heterostructure, comparison to MoS <sub>2</sub> and graphene supercells alone. In our work the basic reference (without relaxation) was taken to be MoS <sub>2</sub> ( $4 \times 4$ ) unit cell.	101
5.11	Variation of atomic positions along the $z$ -direction in the unit cell of graphene/MoS <sub>2</sub> [5:4] heterostructure without (empty blue circles) and with (full red circles) relaxation: (a) Graphene layer (b) MoS <sub>2</sub> layer-sulfur (top) (c) graphene/MoS <sub>2</sub> [5:4] heterostructure position of atoms in the unit cell, (d) MoS <sub>2</sub> layer-molybdenum, (e) MoS <sub>2</sub> layer-sulfur (bottom).	102
5.12	Comparison of electronic band structure of the graphene/MoS <sub>2</sub> [5:4] bilayer heterostructure with relaxation (red lines), without relaxation (blue lines). Zoom of the bands around the Dirac point (inset). The points are calculated results and lines are guide for the eyes. All the calculations have been done by using GGA-PAW pseudopotentials (PBE) including vdW. For the comparison of electronic bands, we shifted the Dirac cone to zero energy level and fermi level located near to the Dirac cone.	103

---

5.13	Electronic band structure of relaxed graphene/MoS <sub>2</sub> [5:4] bilayer heterostructure. Comparison between the electronic bands of relaxed graphene/MoS <sub>2</sub> [5:4] bilayer heterostructure, electronic bands of graphene layer alone and with the carbon atomic positions of the relaxed graphene/MoS <sub>2</sub> [5:4] bilayer heterostructure, electronic bands of MoS <sub>2</sub> layer alone and with the atomic positions of the relaxed graphene/MoS <sub>2</sub> [5:4] bilayer heterostructure. Zoom of the bands around the Dirac point (inset). The points are calculated results and lines are guide for the eyes. All the calculations have been done by using GGA-PAW pseudopotentials (PBE) including vdW. . . . .	105
5.14	Electronic band structure of the graphene/MoS <sub>2</sub> [5:4] bilayer heterostructure with (blue lines) and without (red lines) spin orbit coupling along high symmetry lines. Zoom of the bands around the Dirac point (right). The points are calculated results and lines are guide for the eyes. After SOC bandgap at the Dirac point is reduced by 2.02 meV. All the calculations have been done by using GGA-PAW pseudopotentials (PBE) including vdW. . . . .	106
5.15	Non relaxed crystal structure of graphene/MoS <sub>2</sub> [9:7] bilayer heterostructure different views (a) Side view (blue lines indicate the distance between the carbon to molybdenum, and carbon to top sulfur). (b) Top view. All the calculations have been done by using LDA-PW-PAW pseudopotentials and basic reference has taken MoS <sub>2</sub> (7×7) unit cell. . . . .	107
5.16	Simplified sketch of the lattice parameters of hexagonal super lattice of graphene/MoS <sub>2</sub> [9:7] bilayer heterostructure, comparison to MoS <sub>2</sub> and graphene supercells alone. In our work the basic reference (without relaxation) has been taken as the MoS <sub>2</sub> (7×7) unit cell. . . . .	108
5.17	Variation of atoms in the unit cell of graphene/MoS <sub>2</sub> [9:7] bilayer heterostructure along the $z$ -direction without (empty blue circles) and with (full red circles) relaxation: (a) Graphene layer (b) MoS <sub>2</sub> layer-sulfur (top) (c) graphene/MoS <sub>2</sub> [9:7] heterostructure position of atoms in the unit cell (d) MoS <sub>2</sub> layer-molybdenum (e) MoS <sub>2</sub> layer-sulfur (bottom). . . . .	109
5.18	Variation of atomic positions in the unit cell of the graphene/MoS <sub>2</sub> [9:7] bilayer heterostructure along the $xy$ -direction: The arrows show the displacement of atoms from non-relaxed positions to relaxed positions, with scaling factor of 400. . . . .	110

5.19 Comparison of electronic band structure of graphene/MoS <sub>2</sub> [9:7] bilayer heterostructure with relaxation (red lines), without relaxation (blue lines). Zoom of the bands around the Dirac point (right). The points are calculated results and lines are guide for the eyes. All the calculations have been done by using GGA-PAW pseudopotentials (PBE) including vdW. . . . .	111
5.20 Electronic band structure of a relaxed graphene/MoS <sub>2</sub> [9:7] bilayer heterostructure. Comparison between the electronic bands of relaxed graphene/MoS <sub>2</sub> [9:7] bilayer heterostructure, electronic bands of a graphene layer alone with the carbon atomic positions of the relaxed graphene/MoS <sub>2</sub> [9:7] bilayer heterostructure, electronic bands of MoS <sub>2</sub> layer alone with the atomic positions of the relaxed graphene/MoS <sub>2</sub> [9:7] bilayer heterostructure. Zoom of the bands around the Dirac point (right). The points are calculated results and lines are guide for the eyes. All the calculations have been done by using GGA-PAW pseudopotentials (PBE) including vdW. . . . .	112
5.21 Electronic band structure of graphene/MoS <sub>2</sub> [9:7] bilayer heterostructure with (blue lines) and without (red lines) spin orbit coupling along high symmetry lines. The fine structure of the low energy bands at the Fermi level, around the Dirac point ( $\Gamma$ -point)(right). The points are calculated results and lines are guide for the eyes. After SOC bandgap at the Dirac point is reduced by 0.77 meV. All the calculations have been done by using GGA-PAW pseudopotentials (PBE) including vdW. . . . .	113
5.22 Non relaxed crystal structure of the graphene/WSe <sub>2</sub> [4:3] bilayer heterostructure. (a) Side view (blue lines indicate the distance between the carbon to tungsten , and carbon to top selenium). (b) Top view. (c) Unit cells of graphene and WSe <sub>2</sub> monolayers lattice mismatching. (d) Bilayer separation distance between the graphene (4×4) and WSe <sub>2</sub> (3×3) layers, with the acell of MoS <sub>2</sub> . All the calculations have been done by using LDA-PAW pseudopotentials and basic reference was taken WSe <sub>2</sub> (3×3) unit cell. . . . .	115
5.23 Simplified sketch of the lattice parameters of a hexagonal super lattice of graphene/WSe <sub>2</sub> [4:3] bilayer heterostructure, comparison to WSe <sub>2</sub> and graphene supercells alone. In our work the basic reference was taken to be the WSe <sub>2</sub> (3×3) unit cell. . . . .	116

- 
- 5.24 Variation of atomic positions along the  $z$ -direction in the unit cell of graphene/WSe<sub>2</sub> [4:3] bilayer heterostructure without (empty blue circles) and with (full red circles) relaxation: (a) Graphene layer (b) WSe<sub>2</sub> layer-selenium (top) (c) graphene/WSe<sub>2</sub> [4:3] heterostructure positions in the unit cell (d) WSe<sub>2</sub> layer-tungsten (e) WSe<sub>2</sub> layer-selenium (bottom). Basic reference was taken to be the WSe<sub>2</sub>(3×3) unit cell. . . . . 117
- 5.25 Electronic band structure of relaxed graphene/WSe<sub>2</sub> [4:3] bilayer heterostructure. Comparison between the electronic bands of relaxed graphene/WSe<sub>2</sub> [4:3] bilayer heterostructure, electronic bands of graphene layer alone with the carbon atomic positions of the relaxed graphene/WSe<sub>2</sub> [4:3] bilayer heterostructure, electronic bands of WSe<sub>2</sub> layer alone with the atomic positions of the relaxed graphene/WSe<sub>2</sub> [4:3] bilayer heterostructure. Zoom of the bands around the Dirac point (inset). The points are calculated results and lines are guide for the eyes. All the calculations have been done by using GGA-PAW pseudopotentials (PBE) including vdW. . . . . 119
- 5.26 Electronic band structure of graphene/WSe<sub>2</sub> [4:3] bilayer heterostructure with (blue lines) and without (red lines) spin orbit coupling along high symmetry lines. The fine structure of the low energy bands at the Fermi level, around the Dirac point (right). The points are calculated results and lines are guide for the eyes. After SOC bandgap at Dirac point reduced by 0.07 meV. All the calculations have been done by using GGA-PAW pseudopotentials (PBE) including vdW. . . . . 120
- 5.27 Atomic structure (left) and electronic band structure (right) of graphene/WSe<sub>2</sub> [4:3] bilayer heterostructure with point and substitutional defects (a) graphene/WSe<sub>2</sub>-V<sub>C</sub> (removal of one carbon atom in the graphene layer), (b) graphene/WSe<sub>2</sub>-V<sub>W</sub> (removal of one tungsten atom in the WSe<sub>2</sub> layer), (c) graphene/WSe<sub>2</sub>-V<sub>di-Se</sub> (removal of two selenium atoms (top and bottom) in WSe<sub>2</sub> layer), (d) graphene/WSe<sub>2</sub>-SV<sub>Fe</sub> (substituting iron (in place of tungsten) atom in the WSe<sub>2</sub> layer). All the calculations have been done by using GGA-PAW pseudopotentials (PBE) including vdW. All the calculations have been done with optimization and Without SOC. 122
- 6.1 Atomic structure of bilayer MoS<sub>2</sub> at a twist angle  $\theta = 13.17^\circ$  ( $n = 2$  and  $m = 3$ ). (a) side view. (b) top view. . . . . 128

---

6.2	Variation of atomic positions along the $xz$ -direction of tb-MoS <sub>2</sub> with (full blue circles) and without (empty red circles) relaxation of tb-MoS <sub>2</sub> different angles: (a) (1, 2) $\theta = 21.79^\circ$ , (b) (2, 3) $\theta = 13.17^\circ$ , (c) (3, 4) $\theta = 9.43^\circ$ , and (d) (4, 5) $\theta = 7.34^\circ$ . . . . .	128
6.3	Variation of atomic positions along the $xz$ -direction of tb-MoS <sub>2</sub> with relaxation of tb-MoS <sub>2</sub> different angles: (a) (1, 2) $\theta = 21.79^\circ$ , (b) (2, 3) $\theta = 13.17^\circ$ , (c) (3, 4) $\theta = 9.43^\circ$ , and (d) (4, 5) $\theta = 7.34^\circ$ . . . . .	129
6.4	DFT conduction band (top) and valence band (bottom) in tb-MoS <sub>2</sub> : (1, 2) $\theta = 21.79^\circ$ , (2, 3) $\theta = 13.17^\circ$ , (3, 4) $\theta = 9.43^\circ$ and (4, 5) $\theta = 7.34^\circ$ . For every rotation angle, the origin of energy is fixed at the energy of the state $S_0$ (see bottom). The first Brillouin zone is sketched in the insert, all the calculations have done by using LDA-PAW pseudopotentials. . . . .	131
6.5	DFT bands around the gap in (1, 2) $\theta = 21.79^\circ$ tb-MoS <sub>2</sub> (built from AA stacking): Comparison between computation with and without structural relaxation. All the calculations have done by using LDA-PAW pseudopotentials. . . . .	132
6.6	DFT bands around the gap in (2, 3) $\theta = 13.17^\circ$ tb-MoS <sub>2</sub> (built from AA stacking): Comparison between computation with and without structural relaxation. . . . .	133
6.7	DFT and TB bands in monolayer MoS <sub>2</sub> . The origin of the energy is chosen at the maximum energy of the valence band, <i>i.e.</i> , at the energy of the states labeled $S_0$ , $E(S_0) = 0$ . Since $E(S_1) < E(S_0)$ the gap is direct at K. The first Brillouin zone is sketched in the insert. . . . .	134
6.8	TB and DFT bands around the gap in tb-MoS <sub>2</sub> : (left) (1, 2) $\theta = 21.79^\circ$ and (right) (3, 4) $\theta = 9.43^\circ$ . . . . .	135
6.9	Atomic structure of (6,7) tb-MoS <sub>2</sub> built from AA stacked bilayers. Black lines show the unit cell. AA stacking regions are at the corners of this cell, BA' and AB' stacking regions are at 1/3 and 2/3 of its longest diagonal, respectively. . . . .	138
6.10	Atomic structure of (6,7) tb-MoS <sub>2</sub> built from AB stacked bilayers. Black lines show the unit cell. AB stacking regions are at the corners of this cell, AA' and BA stacking regions are at 1/3 and 2/3 of the longest diagonal, respectively. . . . .	139

- 
- 6.11 Dependence of valence bands on rotation angle  $\theta$ : (a) Valence band dispersion of (4, 5) tb-MoS<sub>2</sub>,  $\theta = 7.34^\circ$ . (b) Energy  $E(S_2)$  of the state  $S_2$  (see panel (a)) versus  $\theta^2$ . (c) Energy difference between the states  $S_4$  and  $S_2$ ,  $\Delta E_{24} = E(S_4) - E(S_2)$ , versus  $\theta$ . A negative value of  $\Delta E_{24}$  means that a gap  $|\Delta E_{24}|$  exists between the band below the gap and the other valence bands. (d) Average slope of  $E(\vec{k})$  of the band between states  $S_2$  and  $S_3$ . For every rotation angle, the origin of energy is fixed at the energy  $E(S_0)$  of the state  $S_0$  (see Figs. 6.4). . . . . 140
- 6.12 Dependence of valence bands on rotation angle  $\theta$ : Comparison between tb-MoS<sub>2</sub> built from AA stacking and tb-MoS<sub>2</sub> built from AB stacking. The TB-AA curves coincide with those of Fig. 6.11. (a) valence-band dispersion of (4, 5) tb-MoS<sub>2</sub>,  $\theta = 7.34^\circ$ . (b) Energy  $E(S_2)$  of state  $S_2$  (see panel (a)) versus  $\theta^2$ . (c) Energy difference between states  $S_4$  and  $S_2$ ,  $\Delta E_{24} = E(S_4) - E(S_2)$ , versus  $\theta$ . A negative  $\Delta E_{24}$  value means that a gap  $|\Delta E_{24}|$  exists between the band below the gap and the other valence bands. (d) Average slope of  $E(\vec{k})$  of the band between states  $S_2$  and  $S_3$ . For every rotation angle, the origin of energy is fixed at the energy  $E(S_0)$  of the state  $S_0$  (see Fig. 6.4). . . . . 142
- 6.13 TB local density of states (LDOS) of the  $4d_{z^2}$  Mo orbital at the center of the AA stacking region for different rotation angles of tb-MoS<sub>2</sub>. The LDOS is calculated employing a Gaussian broadening with a standard deviation  $\sigma = 2$  meV. . . . . 143
- 6.14 TB local density of states (LDOS) of the Mo orbital around the main gap in (6,7)  $\theta = 5.09^\circ$  tb-MoS<sub>2</sub> (built from AA stacking, see Fig. 6.9): (Top panel) LDOS of the  $d_0 = d_{z^2}$  Mo orbital at the center of AA, BA', and AB' stacking regions. (Bottom panel) LDOS of  $d_0$ ,  $d_1 = 4d_{xz}$ ,  $4d_{yz}$  and  $d_2 = 4d_{x^2-y^2}$ ,  $4d_{xy}$  Mo orbitals at the center of the AA stacking region. The LDOS is calculated employing a Gaussian broadening with the standard deviation  $\sigma = 2$  meV. . . . . 144

6.15	TB band dispersion and local density of states (LDOS) of $d_0 = d_{z^2}$ Mo atoms at the center of the AA stacking region and the center of the AB region: (a) for (10, 11) tb-MoS <sub>2</sub> $\theta = 3.15^\circ$ , and (b) for (20, 21) tb-MoS <sub>2</sub> $\theta = 1.61^\circ$ . In a moiré cell, two symmetrically equivalent AB stacking regions are located at 1/3 and 2/3 of the longest diagonal of the cell (see Fig. 6.9)). Each AB stacking region contains two types of Mo atoms: (AB-A) Mo atom of a layer lying above an S atom of the other layer, (AB-B) Mo atom of a layer not lying above an atom of the other layer. . . . .	145
6.16	TB electronic band structure with and without SOC: (Top) for (10, 11) tb-MoS <sub>2</sub> $\theta = 3.15^\circ$ , and (Bottom) for (20, 21) tb-MoS <sub>2</sub> $\theta = 1.61^\circ$ . . . . .	147
6.17	Average weight of the eigenstates at $\Gamma$ , K, and M, of the flat band around the gap in real space in (20, 21) tb-MoS <sub>2</sub> (built from AA stacking, see Fig. 6.9)) with a rotation angle $\theta = 1.61^\circ$ , Conduction band: (a) Average of the four-fold quasi-degenerate band at energy $E \simeq 1.686 \pm 0.002$ eV and (b) average of the two-fold quasi-degenerate band at energy $E \simeq 1.6626 \pm 0.0002$ eV. Valence band: (c) non-degenerate bands at energy $E \simeq 0.26249 \pm 0.00001$ eV, and (d) average of the two-fold quasi-degenerate band at energy $E \simeq 0.2518 \pm 0.0003$ eV. The corresponding bands are shown in Fig. 6.15(b). The color scale shows the weight of the eigenstate on each $d_0 = 4d_{z^2}$ orbital of the Mo atoms. The sum of these weights is more than 98% and 95% of each state for the valence and conduction band, respectively. Black lines show the unit cell containing 2522 Mo atoms. AA stacking regions are at the corners of this cell. . . . .	148
1	Conductivity $\sigma$ (solid line) and inelastic scattering length $L_i$ (dashed line) in MX <sub>2</sub> versus inelastic scattering time $\tau_i$ for defect concentration $c = 3\%$ of point defects (creating a vacancy by removal of atoms M = Mo, W or X = S, Se, Te randomly). For three energy values: Valence band (blue), inside midgap states region (magenta) and conduction band (red). (a) MoS <sub>2</sub> , (b) MoSe <sub>2</sub> , (c) MoTe <sub>2</sub> , (d) WSe <sub>2</sub> , and (e) WTe <sub>2</sub> . Where, $G_0 = 2e^2/h$ . . . . .	159

---

2	Conductivity $\sigma$ (solid line) and inelastic scattering length $L_i$ (dashed line) in $\text{MX}_2$ versus inelastic scattering time $\tau_i$ for defect concentration $c = 10\%$ of point defects (creating a vacancy by removal of atoms $\text{M} = \text{Mo}, \text{W}$ or $\text{X} = \text{S}, \text{Se}, \text{Te}$ randomly). For three energy values: Valence band (blue), inside midgap states region (magenta) and conduction band (red). (a) $\text{MoS}_2$ , (b) $\text{MoSe}_2$ , (c) $\text{MoTe}_2$ , (d) $\text{WSe}_2$ , and (e) $\text{WTe}_2$ . Where, $G_0 = 2e^2/h$ . . . . .	160
3	Elastic mean free path $L_e(E)$ versus energy $E$ in $\text{MX}_2$ for different concentration ( $c = 0.5\%, 1\%, 2\%, 3\%, 5\%$ , and $10\%$ ) of point defects (creating a vacancy by removal of atoms $\text{M} = \text{Mo}, \text{W}$ or $\text{X} = \text{S}, \text{Se}, \text{Te}$ randomly). (a) $\text{MoS}_2$ , (b) $\text{MoSe}_2$ , (c) $\text{MoTe}_2$ , (d) $\text{WSe}_2$ , and (e) $\text{WTe}_2$ . . . . .	161
4	Electronic band structure of supercells of graphene ( $4 \times 4$ ) [Left] and $\text{MoS}_2$ ( $3 \times 3$ ) [Right] with optimized atomic positions and lattice parameters of graphene/ $\text{MoS}_2$ [4:3] bilayer heterostructures. All the calculations have been done using LDA-PW-PAW pseudopotentials. . . . .	162
5	Electronic band structure of supercells of graphene ( $9 \times 9$ ) [Left] and $\text{MoS}_2$ ( $7 \times 7$ ) [Right] with optimized atomic positions and lattice parameters of graphene/ $\text{MoS}_2$ [9:7] bilayer heterostructures. All the calculations have been done using LDA-PW-PAW pseudopotentials. . . . .	163
6	Comparison of electronic band structure of graphene/ $\text{MoS}_2$ [4:3] bilayer heterostructure with relaxation (red lines), without relaxation (cyan lines). Atomic positions are not relaxed and lattice parameters are relaxed (blue lines), and atomic positions are relaxed and lattice parameters are not relaxed (green lines). All the calculations have been done by using GGA-PAW pseudopotentials (PBE) including vdW. . . . .	164
7	DFT and TB electronic band structure of graphene/ $\text{MoS}_2$ [5:4] bilayer heterostructure without relaxation. . . . .	167
8	DFT and TB electronic band structure of graphene/ $\text{MoS}_2$ [9:7] bilayer heterostructure without relaxation. . . . .	167
9	DFT bands around the gap in (1,2) $\theta = 21.79^\circ$ tb- $\text{MoS}_2$ (built from AA stacking): Comparison between LDA-PAW and the GGA-PAW + Van der Waals exchange-correlation functional. . . . .	168
10	DFT bands around the gap in tb- $\text{MoS}_2$ (built from AA stacking): (a) (1,2) $\theta = 21.79^\circ$ , (b) (2,3) $\theta = 13.17^\circ$ . (red color) bilayer, (black color) monolayer represented in the bilayer unit cell. . . . .	169

- 11 Dependence of valence bands on rotation angle  $\theta$ : (a) Valence band dispersion of (4, 5) tb-MoS<sub>2</sub>,  $\theta = 7.34^\circ$ . (b) Energy  $E(S_2)$  of the state  $S_2$  (see panel (a)) versus  $\theta^2$ . (c) Energy difference between the states  $S_4$  and  $S_2$ ,  $\Delta E_{24} = E(S_4) - E(S_2)$ , versus  $\theta$ . A negative value of  $\Delta E_{24}$  means that a gap  $|\Delta E_{24}|$  exists between the band below the gap and the other valence bands. (d) Average slope of  $E(\vec{k})$  of the band between states  $S_2$  and  $S_3$ . . . . . 172
- 12 Weight of the eigenstates at  $\Gamma$ , K, and M, of the non-degenerate flat band below the gap (valence band), in real space, in (10, 11) tb-MoS<sub>2</sub> (built from AA) with a rotation angle  $\theta = 3.15^\circ$ . The color palette is the weight of the eigenstate on each orbital  $d_0 = 4d_{z^2}$  Mo. The sum of these weights is more than 98% of each state. 173

---

## *List of Tables*

---

2.1	Energy integrals for a crystal in terms of two-center integrals where $n, l, m$ are direction of cosines shown in Fig. 2.6. . . . .	30
2.2	Spin orbit Hamiltonian in the basis set of atomic orbitals ( $s$ and $p$ ). . . . .	33
4.1	The DFT optimized lattice parameters, first neighbor distance and bandgap for monolayer $\text{MX}_2$ , where the metal M is Mo or W and chalcogen X is S or Se or Te. . . . .	65
4.2	Tight-binding parameters and SOC ( $\lambda$ ) for monolayer $\text{MX}_2$ , where the metal M is Mo or W and chalcogen X is S or Se or Te. * indicates values from the reference [194]. . . . .	67
5.1	Simplified comparison of the DFT optimized lattice parameters and atomic positions of different supercell geometries of graphene/ $\text{MoS}_2$ bilayer. WP (with optimization) and WOP (without optimization). . . . .	114
6.1	Calculated interlayer distance and supercell size of twisted bilayer $\text{MoS}_2$ with and without relaxation in different configurations. . . . .	130
6.2	Tight-binding (TB) Slater-Koster parameters for monolayer $\text{MoS}_2$ , and pair of neighbors for which the hopping term is non zero. Lattice parameter of monolayer $\text{MoS}_2$ $a = 0.318$ nm. . . . .	135
6.3	TB Slater-Koster parameters for interlayer hopping terms in tb- $\text{MoS}_2$ . $d^0$ is the interlayer distance; for the definition of $d_{\text{Mo-Mo}}$ , $d_{\text{Mo-Mo}}$ , and $d_{\text{Mo-S}}$ , see Fig. 6.1. . . . .	136
6.4	$(n, m)$ twisted bilayer $\text{MoS}_2$ (tb- $\text{MoS}_2$ ) structures that have been used in the present work. $\theta$ is the rotation angle between the two layers and $N$ the number of atoms in a cell. . . . .	136
1	Spin orbit coupling Hamiltonian parameters in the basis set of atomic orbital ( $d$ ). . . . .	156

---

2	Tight-binding (TB) Slater-Koster parameters for the graphene/MoS <sub>2</sub> bilayer heterostructure, and pair of neighbors for which the hopping term is non zero. The lattice parameter of the graphene/MoS <sub>2</sub> [5:4] are $a = 1.276$ nm and graphene/MoS <sub>2</sub> [9:7] $a = 2.214$ nm. . . . .	166
3	TB Slater-Koster parameters for interlayer hopping terms in graphene/MoS <sub>2</sub> . $d^0$ is the interlayer distance; for the definition of $d_{C-S}$ . The $q$ and $d^0$ are parameters for the exponential decay (see appendix D.2) . . . . .	166
4	Alternative Tight-binding (TB) Slater-Koster parameters for monolayer MoS <sub>2</sub> , and pairs of neighbors for which the hopping term is non zero. The lattice parameter of monolayer MoS <sub>2</sub> is $a = 0.318$ nm. . . . .	171
5	TB Slater-Koster parameters for interlayer hopping terms in tb-MoS <sub>2</sub> . $d^0$ is the interlayer distance; for the definition of $d_{Mo-Mo}$ , $d_{S-S}$ , and $d_{Mo-S}$ . . . . .	171

---

## *List of Abbreviations*

---

<b>BO</b> .....	Born Oppenheimer
<b>DFT</b> .....	Density Functional Theory
<b>DOS</b> .....	Density Of States
<b>GGA</b> .....	Generalized Gradient Approximation
<b>HF</b> .....	Hartree Fock
<b>HK</b> .....	Hohenberg Kohn
<b>KS</b> .....	Kohn Sham
<b>LCAO</b> .....	Linear Combination of Atomic Orbitals
<b>LDA</b> .....	Local Density Approximation
<b>LDOS</b> .....	Local Density Of States
<b>MLWF</b> .....	Maximally Localized Wannier Functions
<b>NCPP</b> .....	Norm Conserving Pseudo Potentials
<b>PAW</b> .....	Projector Augmented Wave
<b>PBE</b> .....	Perdew Burke Ernzerhof
<b>RTA</b> .....	Relaxation Time Approximation
<b>SK</b> .....	Slater Koster
<b>SOC</b> .....	Spin Orbit Coupling
<b>TB</b> .....	Tight Binding
<b>TMDs</b> .....	Transition Metal Dichalcogenides
<b>XC</b> .....	Exchange Correlation

## *Chapter No. 1*

---

### *Introduction*

---

The characterization of materials deals with many parameters and properties, being the dimensionality of the system one of the determining points taken for such a procedure. The arrival of new technologies enhances the possibility of discovery and later production of new kind of materials, this is what happened with graphene, the first 2D material synthesized in the laboratory [8,67,155,248]. For a long time it was believed that the realization of 2D materials was not possible. Theoreticians working in that aspect like Landau and Peierls [100,167] argued that any 2D crystal was thermodynamically unstable. After 2004, Andre Geim and Kostya Novoselov from Manchester University were able to isolate a graphene sheet containing a single layer of carbon atom using “Scotch tape” method [155,156]. This result was awarded the Nobel prize in Physics 2010.

The family of 2D layered materials has gained appreciable attention over the last few years, starting with graphene [157]. The disclosure of every new material leads to enthusiasm and mystery because of the contrasting properties of these 2D materials from their bulk materials. The 2D library is increasing in size every year and contains more than 150 exotic materials that can easily be cleaved into sub-nanometer 2D monolayers [19,245]. These 2D materials [246] include transition metal dichalcogenides (TMDs), e.g. MoS<sub>2</sub>, MoSe<sub>2</sub>, MoTe<sub>2</sub>, WS<sub>2</sub>, WSe<sub>2</sub>, WTe<sub>2</sub>, hexagonal boron nitride (h-BN), 2D silicene, 2D-germanium and MXenes (2D carbides/nitrides) [206].

### *Electronic properties of 2D materials.*

Graphene, hexagonal boron nitride monolayers [107] and TMDs with a 2H symmetry (2H-TMDs) [127] are all well-established 2D materials. Graphene displays a sixfold rotational symmetry and also has three mirror planes, while hBN and hexagonal 2H-TMDs have a sixfold rotational-inversion symmetry with two mirror planes. The physical properties of these materials have been studied by many groups (for reviews see for instance [5,151]). But two-dimensional structural anisotropy implies that a given material displays different physical properties when probed along different spatial directions, and lowering the symmetry of graphene and of other two-dimensional materials by the application of strain leads to remarkable effects, not available in the highly symmetric phase. A striking effect from a lowered local symmetry is the superconductivity observed in twisted bilayer graphene [22].

The discovery of graphene, however, was just the beginning of the story related to these 2 dimensional materials. Graphene is a prominent material from the other 2D materials because of its peculiar properties like exclusive electronic

band structure, high transparency with 0 eV bandgap, and thermal conductivity ( $3000\text{-}5000\text{ Wm}^{-1}\text{K}^{-1}$ ) [251]. These unique properties enabled graphene to be a significant actor in liquid crystal displays and LEDs, etc. However graphene is a semimetal with zero bandgap, and in this scenario, one can say that other 2D materials, particularly TMDs, have what graphene does not: a bandgap range of 1.2 to 1.9 eV [64], which admirably corresponds to the solar spectrum and analogs to ongoing industrial needs in photovoltaics. The upcoming generations of nanoelectronics require a discourse of the enhancing desire of reducing the size of elements in the circuit but not the quality. Due to the usage of monoatomic thin layers of 2D materials and their fine quality, it is possible to control electrostatic conductivity more efficiently. Moreover, the charge carrier scattering is reduced in 2D materials as compared to their bulk materials, owing to the reduced number of dangling bonds [221].

The 2D materials have a layered structure with strong covalent interlayer bonding and relatively weak interlayer van der Waals forces [19]. The layered structure of 2D materials permits efficient electronic properties and conductivity much higher within the layers than between the layers, normally three or four orders of magnitude [51, 153]. Some of the noticeable properties that make 2D materials interesting are: high carrier mobility, superconductivity, mechanical flexibility, exceptional thermal conductivity, large photoluminescence, high optical and UV absorption, quantum spin Hall effect, strong light-matter interactions, and observation of highly confined plasmon polaritons [114, 119, 126, 151, 237]. Interestingly, these properties can be efficiently harnessed in 2D materials by means of strain engineering, number of atomic layers, adsorption, and interlayer twist [54, 140, 225, 237].

### *Transition Metal Dichalcogenides.*

The layered 2D transition metal dichalcogenides contain a large number of crystals and are represented by the general formula of  $\text{MX}_2$  where M is a transition metal from groups IV B (Ti, Zr, Hf), V B (V, Nb, Ta), VI B (Mo, W), VII B (Tc, Re) and X is a chalcogen element from group VI A (S, Se, Te) [83, 173]. Depending upon the layer number, elemental conjunction, and presence or absence of dopant, TMDs exhibit a bandgap ranging from 0 to 2 eV, unlike pure graphene which is a semimetal with zero bandgap [226].

The TMDs are classified into metals, semimetals, insulators and superconductors based upon the elemental composition and structural layout. Layered TMDs are leading successors of graphene and they are transparent, flexible and as thin

as graphene [244]. Apart from sharing comparability of bandgap, on/off ratio, and charge carrier mobility to that of ever-present in silicon, TMDs can also be stacked on to the flexible substrate and can bear stress and strain consents of flexible support [26].

The crystalline structure of TMDs ( $\text{MX}_2$ ) has a atomic layer of transition metal (M) that is sandwiched between two atomic layers of chalcogens (X). In an  $\text{MX}_2$  monolayer, a covalent bond is formed by coordination of  $d$  orbitals of M and  $p$  orbitals of X atoms. Every individual layer has weak van der Waals forces (vdW). Because of weak vdW interaction between each layer, bulk TMDs can be exfoliated into monolayers by chemical, mechanical or electrochemical exfoliation methods. On account of the quantum confinement effect and surface properties, there are various properties observed in monolayer TMDs which are not observed in their bulk materials. The bandgap of TMDs convert from direct to indirect: a monolayer of TMDs, like  $\text{MoS}_2$  (1.8 eV),  $\text{MoSe}_2$  (1.5 eV),  $\text{MoTe}_2$  (1.1 eV),  $\text{WSe}_2$  (1.6 eV) shows a direct bandgap, though their bulk materials show indirect bandgap with smaller energies [97].

The  $\text{MX}_2$  have three types of crystal structures based upon the atomic stacking: trigonal prismatic (2H) phase, an octahedral (1T) phase, and a rhombohedral (3R) phase [76, 210]. In the 2H- $\text{MX}_2$  phase, every M atom prismatically collaborates to six neighboring X atoms and in the 1T- $\text{MX}_2$  phase, the nearby six X atoms exhibit a distorted octahedron, circling one M atom. The 2H phase is thermodynamically stable and the 1T phase is metastable. The 1T phase is thermodynamically unstable and it shows metallic behavior, whereas the 2H phase is thermodynamically stable and it shows semiconducting behavior which is important for optoelectrical properties [150]. In my thesis, we used the most stable and semiconducting natural phase (2H- $\text{MX}_2$ ).

#### *Van der Waals Heterostructures.*

The 2D layered materials have covered an amazing range of electrical, chemical, optical and mechanical properties, perhaps the most surprising discovery is that these crystals can be combined freely to create altogether new materials [54]. Strong covalent bonds provide in-plane stability of 2D layered materials of the crystals; these materials are called van der Waals heterostructures because the atomically thin layers are not mixed through a chemical reaction but rather attached to each other via a weak van der Waals interaction [157]. More recently, considerable efforts have been devoted to the van der Waals integration of different 2D layered materials by vertically stacking distinct 2D layered materials

---

to form 2D–2D heterostructures and superlattices. 2D–2D heterostructures of distinct 2D layered materials (graphene, MoS<sub>2</sub>, WSe<sub>2</sub>, etc.) give rise to intriguing possibilities for controlling and manipulating the generation, confinement and transport of charge carriers [115]. An important consideration when stacking 2D layered materials is the crystal orientation; the relative alignment of the lattice can have a significant impact on the structural outcome of certain systems (such as the resulting moiré and other periodic patterns), which might result in a commensurate to incommensurate transition [230]. Generally, a moiré pattern appears only when the regular patterns are rotated by a small twist angle relative to each other, but similar pitches. In my thesis, we study two different types of vdW heterostructures: graphene/MoS<sub>2</sub>, graphene/WSe<sub>2</sub> and twisted bilayer MoS<sub>2</sub>.

### *Electronic property calculations.*

Since the 1990s, electronic structure calculations based on density functional theory become more and more popular in condensed matter physics, quantum chemistry, and materials science. Density functional theory is by far the most widely used approach for electronic structure calculations nowadays. It is usually called first-principle method or *ab initio* method, because it allows people to determine many properties of a condensed matter system by just giving some basic structural information without any adjustable parameter. It provides an alternative way to investigate condensed matter systems, other than the traditional experimental method and pure theoretical method based on quantum field theory [218]. It is becoming a useful tool used by both experimentalists and theorists to understand characteristic properties of materials and to make specific predictions of experimentally observable phenomena for real materials and to design new materials.

The most widely used programs today are based on the Kohn-Sham ansatz to original density functional theory [34, 128]. The Kohn-Sham ansatz is to replace the original many-body problem by an auxiliary independent-particle system, specifically, it maps the original interacting system with a real potential onto a fictitious non-interacting system whereby the electrons move within an effective Kohn-Sham single-particle potential. The many-body effects are approximated by a exchange-correlation functional in the effective Kohn-Sham single-particle potential. The most widely used exchange-correlation functionals are the local density approximation (LDA) [128, 160] and the generalized gradient approximation (GGA) [65, 128].

When the number of atoms and electrons is very small we can use an exact method like configuration interaction to calculate the true many-electron wave function. However, beyond about 10 electrons we hit the exponential wall and such calculations become impossible. For larger systems containing up to a few hundred or a few thousand atoms we can use DFT techniques to find the ground state density and ground state energy of the interacting system without explicitly calculating the many-electron wave function. In a DFT calculation we can calculate an approximation to the actual band structure of the crystal.

In even larger systems with around thousands or more atoms, we can no longer use self-consistent DFT calculations to take into account the full interaction. To calculate the band structure and set of approximate single-particle states we instead try to include the effects of the interaction in a semiempirical way, using a tight-binding model, based on Slater-Koster (SK) parameters. The SK parameters are extracted from the DFT on smaller systems. The starting point for all semiempirical approaches is the physics. In metals, for example, the electrons are almost free and so we can treat the single-particle states in terms of plane waves. We could also take a very different approach and assume that the states in a crystal look like combinations of the wave functions of isolated atoms. We might imagine this is more likely to be the case in insulators or semiconductors.

### *Outline of the Thesis.*

The structure of the thesis is summarized in the following: The first two chapters (chapter-2 and 3) are a review of methods developed by other groups, briefly explain about the first principle calculations, tight-binding method, spin-orbit coupling, and numerical methods for quantum transport properties. The physics starts only in chapter-4, first with a bit more details on 2D materials (lattice, Brillouin zone, etc), then with our new results (chapter-4, 5, and 6).

## **Chapter-2**

In this chapter, we briefly describe the methods used along the thesis to perform the theoretical calculations of the electronic properties of the studied materials. This includes density functional theory (DFT) and the tight-binding method (TB).

## **Chapter-3**

This chapter focuses on the implementation of numerical methods of quantum transport. Particularly, we focus on the implementation of the recursion method

(Lanczos) to calculate the density of states (DOS) and transport properties based on the Chebyshev polynomials and the Kubo-Greenwood formula.

## Chapter-4

We studied imperfections in the crystal structure, such as point defects, that can strongly modify the transport properties of materials. Here, we study the effect of point defects on the quantum conductivity of single layers of semiconducting transition metal dichalcogenides with the form  $\text{MX}_2$ , where  $\text{M} = \text{Mo}, \text{W}$  and  $\text{X} = \text{S}, \text{Se}, \text{Te}$ . The electronic structure is considered within an eleven band tight-binding model, which accounts for the relevant combination of  $d$  orbitals of the transition metal  $\text{M}$  (5-orbitals) and  $p$  orbitals of the chalcogen  $\text{X}$  [(top-X) 3 + (bottom-X) 3 = 6-orbitals]. We use the Kubo-Greenwood formula for the calculation of the conductivity in samples with different distributions of disorder.

## Chapter-5

In this chapter, we discuss the structural and electronic properties of different heterostructures like graphene/ $\text{MoS}_2$  and graphene/ $\text{WSe}_2$ . Vertically stacked graphene and  $\text{MoS}_2$  monolayers have a huge lattice mismatch between the layers. To reduce the lattice mismatch between the layers we consider different supercell geometries of graphene and  $\text{MoS}_2$ : graphene/ $\text{MoS}_2$  [ $4 \times 4$  (graphene)/ $3 \times 3$  ( $\text{MoS}_2$ ) 4:3, similarly 5:4 and 9:7]. Some research groups [174, 192, 196] have tried and succeeded to reduce the lattice mismatch between the layers up to 2.9 %. Finally, we reduced the lattice mismatch between the layers (graphene/ $\text{MoS}_2$ ) from 3.5 % to 0.5 %, and for graphene/ $\text{WSe}_2$  to 0.6%. After that, we studied the electrical properties of the above configurations with and without relaxations.

## Chapter-6

We report moiré patterns that are known to confine electronic states in TMDs bilayers, thus generalizing the notion of magic angles discovered in twisted bilayer graphene to semiconductors. Here, we present a new Slater-Koster tight-binding model that allows the first reliable and systematic studies of such states in twisted bilayer  $\text{MoS}_2$  for the whole range of rotation angles  $\theta$ . We show that isolated bands appear at low energy for  $\theta \leq 5 - 6^\circ$ . Moreover, these bands become “flat bands”, characterized by a vanishing average velocity, for the smallest angles  $\theta \leq 2^\circ$ .



## *Chapter No. 2*

---

### *Theoretical and Methodological background*

---

	<b>Page</b>
2.1 The Born-Oppenheimer approximation . . . . .	10
2.1.1 Hartree-Fock approximation . . . . .	13
2.2 Density Functional Theory (DFT) . . . . .	14
2.2.1 The Hohenberg-Kohn theorems . . . . .	15
2.2.1.1 The Hohenberg-Kohn theorem-1 . . . . .	16
2.2.1.2 The Hohenberg-Kohn theorem-2 . . . . .	17
2.2.2 The Kohn-Sham (KS) equations . . . . .	19
2.3 Exchange-correlation functional . . . . .	22
2.3.1 The Local Density Approximation (LDA) . . . . .	22
2.3.2 The Generalized Gradient Approximation (GGA) . . . . .	24
2.3.3 Van der Waals interactions . . . . .	24
2.4 Tight-Binding Method . . . . .	24
2.4.1 Slater-Koster parameters . . . . .	26
2.4.2 Spin Orbit Coupling (SOC) . . . . .	31
2.4.3 Wannier functions . . . . .	34
2.5 Conclusion . . . . .	38

---

In the twentieth century, one of the most important advances in physics was the development of quantum mechanics and the many experimental observations which confirmed this theory [36,236]. The translation of quantum mechanics and statistical mechanics of molecular and solid-state systems into efficient numerical algorithms has allowed us to accurately study many systems computationally. This was used to obtain a deeper understanding of physics beyond experimental observations.

In the last three decades onwards, Density functional theory (DFT) has become one of the most popular and widely used methods to solve the many-body problems in physics and chemistry. The main reason is that DFT can treat many problems with high accuracy.

In this chapter, we introduce some concepts related to quantum physics to set the basis to explain briefly the standard time-independent DFT. Several approximations such as Born-Oppenheimer (BO), exchange correlations (LDA, GGA ...) are described. We only try to give a brief explanation without attempting to discuss the underlying mathematics. For solving the many-body problem, we made two approximations. One is the Born-Oppenheimer (BO) approximation and the second one is the Hartree-Fock (HF) approximation.

## 2.1 The Born-Oppenheimer approximation

The forces on both electrons and nuclei due to their electric charge are of the same order of magnitude, and so the changes which occur in their momenta as a result of these forces must also be the same. Therefore, assume that the actual momenta of the electrons and nuclei were of similar magnitude. In this case, since the nuclei are so much more massive than the electrons, they must have much smaller velocities. Thus it is possible that on the typical time scale of the nuclear motion, the electrons will rapidly relax to the instantaneous ground state configuration, so that in solving the time-independent Schrödinger equation resulting from the Hamiltonian.

$$\hat{H} = -\frac{1}{2} \sum_i \nabla_i^2 - \sum_\alpha \frac{1}{2m_\alpha} \nabla_\alpha^2 - \sum_i \sum_\alpha \frac{Z_\alpha}{|r_i - r_\alpha|} + \frac{1}{2} \sum_i \sum_{i \neq j} \frac{1}{|r_i - r_j|} + \sum_\alpha \sum_{\beta \neq \alpha} \frac{Z_\alpha Z_\beta}{|r_\alpha - r_\beta|} \quad (2.1)$$

where  $m_\alpha$  is nuclear mass and  $Z_\alpha$  atomic numbers. In equation 2.1 the first term represents the kinetic energy of the electrons, the second term represents the kinetic energy of the nucleus, the third term represents electron and nuclei interaction, the fourth term represents electron-electron interaction, and the final term represents inter-nuclear Coulomb interaction energies. We can assume

that the nuclei are stationary and solve for the electronic ground state first, and then calculate the energy of the system in that configuration and solve for the nuclear motion. This separation of electronic and nuclear motion is known as the **Born-Oppenheimer (BO) approximation** [15]. According to Ziman principles [252], eigen-function for the above Hamiltonian equation 2.1 can be written as

$$\tilde{\psi}(\{r_i\}, \{r_\alpha\}) = \psi(\{r_i\}, \{r_\alpha\})\phi(\{r_\alpha\}). \quad (2.2)$$

Where  $\psi(\{r_i\}, \{r_\alpha\})$  is a wave function only for the  $\{r_i\}$  with the  $\{r_\alpha\}$  as parameters satisfy the time independent Schrödinger equation

$$\begin{aligned} \left[ -\frac{1}{2} \sum_i \nabla_i^2 - \sum_i \sum_\alpha \frac{Z_\alpha}{|r_i - r_\alpha|} + \frac{1}{2} \sum_i \sum_{i \neq j} \frac{1}{|r_i - r_j|} \right] \psi(\{r_i\}, \{r_\alpha\}) \\ = \mathcal{E}_e\{r_\alpha\} \psi(\{r_i\}, \{r_\alpha\}) \end{aligned} \quad (2.3)$$

in which the dependence of the eigenvalues  $\mathcal{E}_e$  on the nuclear positions  $\{r_\alpha\}$  are acknowledged. We apply the full Hamiltonian of equation (2.1)

$$\hat{H}\tilde{\psi}(\{r_i\}, \{r_\alpha\}) = \left[ -\frac{1}{2} \sum_\beta \frac{1}{m_\beta} \nabla_\beta^2 + \mathcal{E}_e\{r_\alpha\} + \frac{1}{2} \sum_\beta \sum_{\gamma \neq \beta} \frac{Z_\beta Z_\gamma}{|r_\beta - r_\gamma|} \right] \tilde{\psi}(\{r_i\}, \{r_\beta\}) \quad (2.4)$$

and substitute equation 2.2 in equation 2.4. Then we can get,

$$\begin{aligned} = \psi(\{r_i\}, \{r_\beta\}) \left[ -\frac{1}{2} \sum_\beta \frac{1}{m_\beta} \nabla_\beta^2 + \mathcal{E}_e\{r_\alpha\} + \frac{1}{2} \sum_\beta \sum_{\gamma \neq \beta} \frac{Z_\beta Z_\gamma}{|r_\beta - r_\gamma|} \right] \phi(\{r_\alpha\}) \\ - \sum_\beta \frac{1}{2m_\beta} \left[ 2\nabla_\beta \phi(\{r_\alpha\}) \cdot \nabla_\beta \psi(\{r_i\}, \{r_\beta\}) + \phi(\{r_\alpha\}) \nabla_\beta^2 \psi(\{r_i\}, \{r_\beta\}) \right] \end{aligned} \quad (2.5)$$

The energy  $\mathcal{E}_e\{r_\alpha\}$  is called the adiabatic contribution of the electrons to the energy of the system. The remaining non-adiabatic terms contribute very little to the energy, which can be demonstrated using time-independent perturbation theory [201]. The first-order correction arising from the first non-adiabatic term on the last line of equation 2.5 reads

$$- \int \prod_j dr_j \prod_\beta dr_\beta \psi^*(\{r_i\}, \{r_\alpha\}) \phi^*(\{r_\alpha\}) \sum_r \frac{1}{m_r} \left[ \nabla_r \phi(\{r_\alpha\}) \cdot \nabla_r \psi(\{r_i\}, \{r_\alpha\}) \right] \quad (2.6)$$

$$= - \sum_r \int \prod_\beta dr_\beta \phi^*(\{r_\alpha\}) \nabla_r \phi(\{r_\alpha\}) \cdot \left[ \int \prod_j dr_j \psi^*(\{r_i\}, \{r_\alpha\}) \nabla_r \psi(\{r_i\}, \{r_\alpha\}) \right] \quad (2.7)$$

The part of the above equation inside the big bracket term reads

$$\left[ \int \prod_j dr_j \psi^* \left( \{r_i\}, \{r_\alpha\} \right) \nabla_r \psi \left( \{r_i\}, \{r_\alpha\} \right) \right]. \quad (2.8)$$

Rearranging the terms of above equation leads to

$$\frac{1}{2} \nabla_r \left[ \int \prod_j dr_j \left| \psi \left( \{r_i\}, \{r_\alpha\} \right) \right|^2 \right], \quad (2.9)$$

From equation 2.9 the term inside the bracket (normalization) goes to zero  $\frac{1}{2} \nabla_r [1] = 0$ .

Therefore, the normalization of the electronic wave-function does not change when the nuclei move so that the first-order contribution vanishes. The second-order shift due to this term does not vanish and gives rise to transitions between electronic states as the ions move, otherwise known as electron-phonon interaction, which will modify the energy. The second non-adiabatic term in the final term of equation 2.5 will be the largest when the electrons labeled 'i' are tightly bound to the nuclei labeled  $\alpha$ .

The wave function can be written as  $\psi \left( \{r_i\}, \{r_\alpha\} \right) = \psi \left( \{u_{(i,\alpha)}\} \right)$ ,

where  $u_{(i,\alpha)} = r_i - r_\alpha$  and the second term of the last line of equation 2.5 is

$$- \int \prod_j dr_j \prod_\beta dr_\beta \psi^* \left( \{u_{(i,\alpha)}\} \right) \phi^* \left( \{r_\alpha\} \right) \sum_r \frac{1}{2m_\alpha} \left[ \phi \left( \{r_\alpha\} \right) \nabla_r^2 \psi \left( \{u_{(i,\alpha)}\} \right) \right] \quad (2.10)$$

$$\begin{aligned} &= - \sum_r \frac{1}{2m_r} \left[ \int \prod_\beta dr_\beta \left| \phi \left( \{r_\alpha\} \right) \right|^2 \right] \left[ \int \prod_{(j,\beta)} du_{(j,\beta)} \psi^* \left( \{u_{(i,\alpha)}\} \right) \nabla_r^2 \psi \left( \{u_{(i,\alpha)}\} \right) \right] \\ &= - \sum_{(k,r)} \frac{1}{m_r} \int \prod_{(j,\beta)} \psi^* \left( \{u_{(i,\alpha)}\} \right) \frac{1}{2} \nabla_{(k,r)}^2 \psi \left( \{u_{(i,\alpha)}\} \right). \end{aligned} \quad (2.11)$$

The order of the electronic kinetic energy multiplied by the ratio of the electron and nuclear masses is much smaller, so the contribution of this term is neglected. Therefore neglecting the non-adiabatic terms in equation 2.4 is justified if  $\phi \{r_\alpha\}$  obeys the Schrödinger equation of the form

$$\left[ - \frac{1}{2} \sum_\beta \frac{1}{m_\beta} \nabla_\beta^2 + \mathcal{E}_e \{r_\alpha\} + \frac{1}{2} \sum_\beta \sum_{\gamma \neq \beta} \frac{Z_\beta Z_\gamma}{|r_\beta - r_\gamma|} \right] \phi \{r_\alpha\} = \mathcal{E} \phi \{r_\alpha\}. \quad (2.12)$$

The adiabatic principle is crucial because it allows us to separate the nuclear and electron motion, leaving a residual electron-phonon interaction.

From this point, it is assumed that the electrons respond instantaneously to the nuclear motion and always occupy the ground state of that nuclear configuration.

### 2.1.1 Hartree-Fock approximation

In the Hartree-Fock (HF) approximation the electronic wave function  $\psi$  [50,124], introduced in the BO approximation, is rewritten as an anti-symmetric product of one-particle wave functions  $\phi_i(r_i, \sigma_i)$ ,

$$\psi(r_1, \sigma_1, r_2, \sigma_2 \dots) = \frac{1}{\sqrt{N!}} \sum_p^{N!} (-1)^p \hat{P}[\phi_1(r_1, \sigma_1) \times \phi_2(r_2, \sigma_2) \dots \times \phi_N(r_N, \sigma_N)] \quad (2.13)$$

where  $N$  is the number of electrons and  $\hat{P}$  is the permutation operator yielding  $N!$  permutations. Each of these is characterized by a number of elementary permutations of the two electrons,  $p$ . As such, the wave function can be rewritten as a determinant, the so called Slater determinant

$$\psi(r_1, \sigma_1, r_2, \sigma_2 \dots) = \frac{1}{\sqrt{N!}} \begin{vmatrix} \phi_1(r_1, \sigma_1) & \phi_2(r_1, \sigma_1) & \dots & \phi_N(r_1, \sigma_1) \\ \phi_1(r_2, \sigma_2) & \phi_2(r_2, \sigma_2) & \dots & \phi_N(r_2, \sigma_2) \\ \vdots & \vdots & \ddots & \vdots \\ \phi_1(r_N, \sigma_N) & \phi_2(r_N, \sigma_N) & \dots & \phi_N(r_N, \sigma_N) \end{vmatrix}. \quad (2.14)$$

An equation for the one-particle orbitals  $\phi_i$  can be derived by making use of the variational principle of quantum mechanics. It states that the energy corresponding to a variational wave function  $\tilde{\psi}$  always exceeds the ground state energy  $E_0$ ,

$$E_0 \leq \frac{\langle \tilde{\psi} | H | \tilde{\psi} \rangle}{\langle \tilde{\psi} | \tilde{\psi} \rangle}. \quad (2.15)$$

Ortho-normalization of the one-electron orbitals,  $\langle \phi | \phi \rangle = \delta_{ij}$ , is imposed by using Lagrange multipliers. The derivation is too long to present it here [92]. The result of the HF approximation is the Hartree-Fock equation for the one electron orbitals  $\phi_i(r_1)$ . The Hamiltonian consists of a one electron operator  $\hat{h}_1$  and two electron operators  $\hat{J}$  and  $\hat{K}$ . The electron operators are:

$$[\hat{h}_1 + \hat{J} - \hat{K}] \phi_i(r_1) = \epsilon_i \phi_i(r_1) \quad (2.16)$$

The one electron operator is:

$$\hat{h}_1 = -\frac{1}{2} \nabla_1^2 - \sum_I \frac{Z_I}{r_{1I}} \quad (2.17)$$

where  $r_{1I} = |r_1 - R_I|$ . The first term represents the kinetic energy of the electron and the second term is the operator of the Coulomb interaction between the electron and the nuclei. The first two electron operator,  $\hat{J}$ , is the direct operator. It is given by

$$\hat{J} \phi_i(r_1) = \sum_j \int \frac{\phi_j^*(r_2) \phi_j(r_2) \phi_i(r_1)}{r_{12}} dr_2 \quad (2.18)$$

with  $r_{12} = |r_1 - r_2|$ . The second two electron operator,  $\hat{K}$ , is the exchange operator given by

$$\hat{K}\phi_i(r_1) = \sum_{j||i} \int \frac{\phi_j^*(r_2)\phi_j(r_1)\phi_i(r_2)}{r_{12}} dr_2 \quad (2.19)$$

The summation over  $j||i$  runs over all electrons with spin parallel to the spin of particle  $i$ .

### HF approximation summary:

- The exchange density is subtracted and based on electrons with spin parallel to that of electron  $i$  are located outside the region around  $i$ . The region is called the Fermi exchange hole.
- The self interaction between the electrons are canceled in the HF approximation, because of the presence of the exchange operator.
- In the Hartree approximation, the antisymmetrization of the wave function is not carried out. Therefore, it suffered from self-interaction. The corresponding energy  $H_{HF}$  is always higher than that of the ground state energy  $E_0$ . The energy difference is called as the correlation energy,  $E_C = E_{HF} - E_0$ .
- By using post-HF methods, one can systematically increase the accuracy of the HF approximation.

The flow chart Fig. 2.1 indicates the possibilities of electronic structure calculation with different codes, mainly two types of codes. A first one is wave function based and the second one is electronic density based as shown in Fig. 2.1. In my thesis, I worked with electronic density based codes and the explanation of parameters can be found in the next sections.

## 2.2 Density Functional Theory (DFT)

The quantum mechanical wave function contains, in principle, all the information about a given system. For the case of a simple 2-D square potential or even a hydrogen atom we can solve the Schrödinger equation exactly [33] in order to get the wave function of the system. We can then determine the allowed energy states of the system. Unfortunately it is impossible to solve the Schrödinger equation for a  $N$ -body system. Evidently, we must involve some approximations to render the problem soluble albeit tricky. Here we have our simplest definition of DFT: A method of obtaining an approximate solution to the Schrödinger equation of a many-body system.

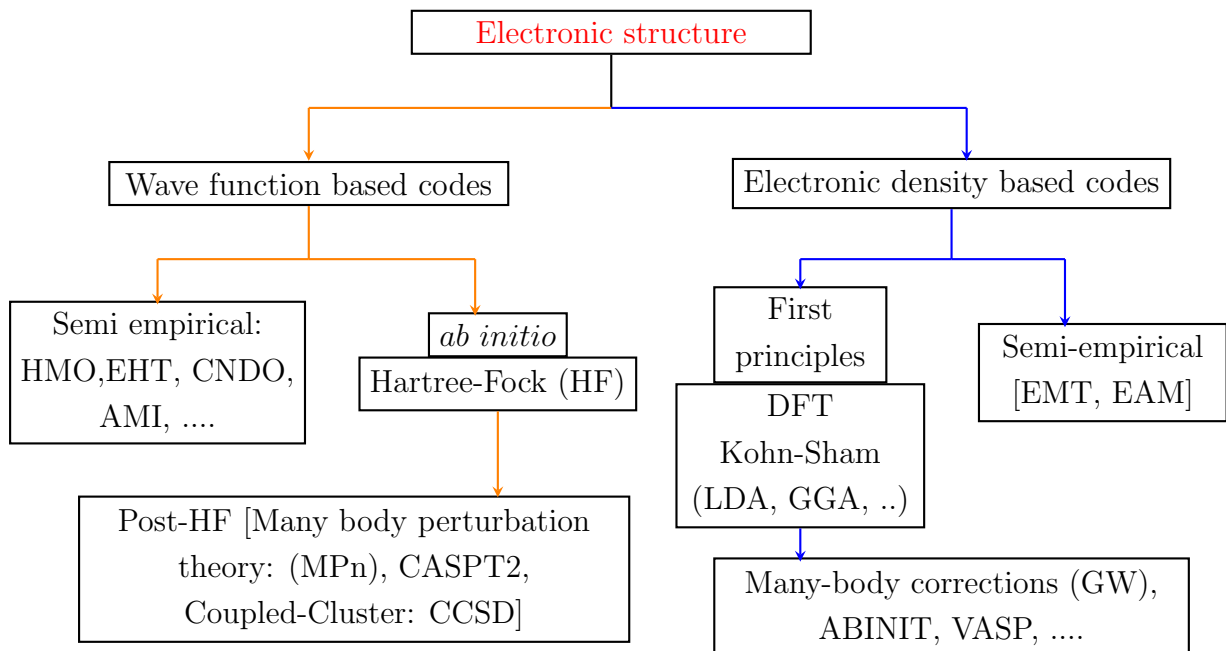


Figure 2.1: Flow chart for different type of codes for electronic structure calculations.

In DFT the electron density  $n(r)$  is the principal quantity. The aim of general DFT [34, 73, 93, 128] is to reformulate the quantum mechanical theory in terms of the density instead of the wave function. DFT computational codes are used in practiced to investigate the structural, magnetic and electronic properties of molecules, materials with or without defects.

### 2.2.1 The Hohenberg-Kohn theorems

As a result of the Born-Oppenheimer approximation, the Coulomb potential arising from the nuclei is treated as a static potential  $V_{ext}(r)$

$$\hat{H} = \hat{F} + \hat{V}_{ext}, \quad (2.20)$$

such that

$$\hat{F} = -\frac{1}{2} \sum_i \nabla_i^2 + -\frac{1}{2} \sum_i \sum_{j \neq i} \frac{1}{|r_i - r_j|}, \quad (2.21)$$

and

$$\hat{V}_{ext} = \sum_i V_{ext}(r_i) = - \sum_{\alpha} \frac{Z_{\alpha}}{|r - r_{\alpha}|}, \quad (2.22)$$

$\hat{F}$  is the same for all  $N$ -electron systems, so that the Hamiltonian, and hence the ground state  $|\psi_0\rangle$ , are completely determined by  $\hat{F}$  and  $V_{ext}$ . The ground state

$|\psi_0\rangle$  for this Hamiltonian gives rise to a ground state electronic density  $n_0(r)$ ,

$$n_0(r) = \langle \psi_0 | \hat{n} | \psi_0 \rangle = \int \prod_{i=2}^N dr_i |\psi_0(r_1, r_2, r_3 \cdots r_N)|^2. \quad (2.23)$$

Thus the ground states  $|\psi_0\rangle$  and density  $n_0(r)$  are both functionals of their number of electrons  $N$  and the external potential  $V_{ext}(r)$ . DFT was introduced in 1964 by Hohenberg and Kohn [73, 74, 93, 105].

### 2.2.1.1 The Hohenberg-Kohn theorem-1

#### Statement-1:

For any system of interacting particles the external potential  $V_{ext}(r)$  is uniquely determined by the corresponding ground state density, to within an additive content.

“The external potential  $V(r)$  is determined, within a trivial additive constant by the ground-state electron density  $\rho$ ”.

#### Proof:

The first external potential  $V_{ext}(r)$  and ground state  $|\psi_0\rangle$ , 2<sup>nd</sup> external potential  $V'_{ext}(r)$  and ground state  $|\psi'_0\rangle$ .

Both give the same ground state density  $n_0(r)$ .

The corresponding ground state energies are  $E_0 = \langle \psi_0 | \hat{H} | \psi_0 \rangle$  and  $E'_0 = \langle \psi'_0 | \hat{H}' | \psi'_0 \rangle$ . where  $\hat{H} = \hat{F} + \hat{V}_{ext}$  and  $\hat{H}' = \hat{F} + \hat{V}'_{ext}$

Taking  $|\psi'_0\rangle$  as a trial wave function for the Hamiltonian  $\hat{H}$ , we obtain the strict inequality.

$$E_0 < \langle \psi'_0 | \hat{H} | \psi'_0 \rangle = \langle \psi'_0 | \hat{H}' | \psi'_0 \rangle + \langle \psi'_0 | \hat{H} - \hat{H}' | \psi'_0 \rangle \quad (2.24)$$

$$E_0 < \langle \psi'_0 | \hat{H} | \psi'_0 \rangle = E'_0 + \int dr n_0(r) [V_{ext}(r) - V'_{ext}(r)] \quad (2.25)$$

where taking  $|\psi_0\rangle$  as a trial wave function for  $\hat{H}'$  gives

$$E'_0 < \langle \psi_0 | \hat{H}' | \psi_0 \rangle = \langle \psi_0 | \hat{H} | \psi_0 \rangle + \langle \psi_0 | \hat{H}' - \hat{H} | \psi_0 \rangle \quad (2.26)$$

$$E'_0 < \langle \psi_0 | \hat{H}' | \psi_0 \rangle = E_0 - \int dr n_0(r) [V_{ext}(r) - V'_{ext}(r)] \quad (2.27)$$

adding equations 2.25 and 2.27 leads to

$$E_0 + E'_0 < E'_0 + E_0. \quad (E_0 = \langle \psi_0 | \hat{H} | \psi_0 \rangle < \langle \psi'_0 | \hat{H} | \psi'_0 \rangle) \quad (2.28)$$

Which is clearly a contradiction [73, 74].

Thus, at least in principle, the ground state density determines (up to a constant), the external potential of the Schrödinger equation of which it is a solution,

the external potential and the number of electrons  $N = \int dr n_0(r)$  determine all the ground state properties of the system since the Hamiltonian and the ground state wave function is determined by them.

So far, the functional  $F(n) = \langle \psi | \hat{F} | \psi \rangle$  is special and well defined for all densities  $n(r)$  that are ground state densities for some external potential (V-representable). Therefore  $n(r)$  determines the external potential and  $N$  (and therefore  $\hat{F}$ ) and hence  $|\psi\rangle$ . Now a functional for an arbitrary external potential  $V(r)$  unrelated to the potential  $V_{ext}(r)$  determined by  $n(r)$  can be defined:

$$E_v[n] = F[n] + \int dr V(r)n(r). \quad (2.29)$$

### 2.2.1.2 The Hohenberg-Kohn theorem-2

#### Statement-2:

For all V-representable densities  $n(r)$ ,  $E_v[n] \geq E_0$  where  $E_0$  is now the ground state energy for  $N$  electrons in the external potential  $V(r)$ .

The first Hohenberg-Kohn theorem proves a one to one mapping between the external potential and ground-state densities in a many-electron system.

**It does not say anything about neither the analytic form of the universal functional  $F[n]$  nor the practical ways to obtain the ground-state electron densities.**

The second theorem concerns the latter issue.

By the first theorem, a given  $n(r)$  determines its own external potential  $V_{ext}(r)$  and ground state  $|\psi\rangle$ . If this state is used as a trial state for the Hamiltonian with external potential  $V(r)$ , we have

$$\langle \psi | \hat{H} | \psi \rangle = \langle \psi | \hat{F} | \psi \rangle + \langle \psi | \hat{V} | \psi \rangle = F[n] + \int dr V(r)n(r) = E_v[n] \geq E_0 \quad (2.30)$$

by the variational principle. For non-degenerate ground states, equality only holds if  $|\psi\rangle$  is the ground state for the potential  $V(r)$  [73, 74].

### The constrained search formulation

A functional of density  $n(r)$  for the operator  $\hat{F}$  is:

$$F[n] = \min_{|\psi\rangle \rightarrow n} \langle \psi | \hat{F} | \psi \rangle. \quad (2.31)$$

That is the functional takes the minimum value of the expectation value with respect to all states  $|\psi\rangle$  which gives the density  $n(r)$ . For a system with external potential  $V(r)$  and ground state  $|\psi\rangle$  with energy  $E_0$  consider a state  $|\psi_{[n]}\rangle$  an  $N$ -electron state which yields density  $n(r)$  and minimizes  $F[n]$

$$E_v[n] = F[n] + \int dr V(r)n(r) = \langle \psi_{[n]} | (\hat{F} + \hat{V}) | \psi_{[n]} \rangle \quad (2.32)$$

Since  $\hat{H} = \hat{F} + \hat{V}$ , by the variational principle

$$E_v[n] \geq E_0 \quad (2.33)$$

with equality only if  $|\psi_{[n]}\rangle = |\psi_0\rangle$ .

This holds for all densities which can be obtained from an  $N$ -electron wave function. But from the equation 2.24, we can get

$$F[n_0] \leq \langle \psi_0 | \hat{F} | \psi_0 \rangle. \quad (2.34)$$

Therefore  $|\psi_0\rangle$  must be one of the states which yields  $n_0(r)$ . Adding  $\int dr V(r)n(r)$  gives

$$E_v[n] \leq E_0 \quad (2.35)$$

which combined with the result of equation 2.26 is

$$E_v[n] \geq E_v[n_0] = E_0 \quad (2.36)$$

Thus the ground state density  $n_0(r)$  minimizes the functional  $E_v[n]$  and the minimal value is the ground state energy.

**NOTE:**

The requirement for non-degeneracy of the ground state has disappeared, and further that instead of considering only V-representable densities, we can now consider N-representable densities. The requirements of N-representability are much weaker and satisfied by any well-behaved density, such as the quantity  $\int dr \left| \nabla n^{\frac{1}{2}}(r) \right|^2$ .

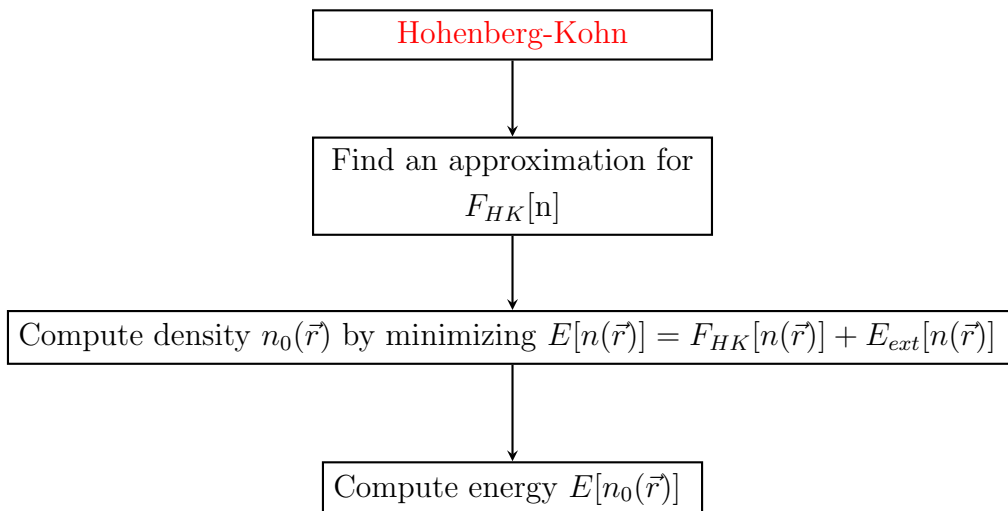


Figure 2.2: Flow chart: Computational approaches for Hohenberg-Kohn (HK) to calculate the energy.

The flow chart Fig. 2.2 indicates that to calculate the energy by using HK approximation, for that choose suitable approximation for functional density and then compute density using Hohenberg-Kohn constrained search formulation.

### 2.2.2 The Kohn-Sham (KS) equations

In order to take advantage of the power of DFT without sacrificing accuracy (that is including exchange and correlation effects), I follow the method of Kohn and Sham [93] to map the problem of the system of interacting electrons onto a fictitious system of non-interacting “electrons”. Fig. 2.3 indicates the con-

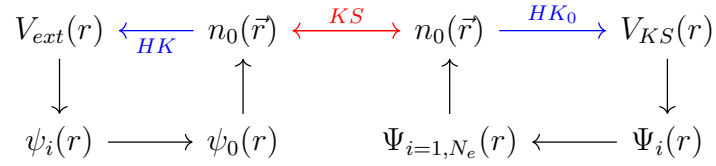


Figure 2.3: Chart for connection between the many-body and independent particles through Kohn-Sham (KS) equations.

nection between the many-body and independent particles through Kohn-Sham equations [93]. Here  $HK_0$  denotes the Hohenberg-Kohn theorem applied to the non-interacting problems. Kohn-Sham (KS) provides the connection in both directions between the many-body particles and independent particle systems so that the arrows connect any point to any other point. Therefore, in principle a solution of the independent particle Kohn-Sham [93] determines all properties of the full many-body system shown in Fig. 2.3.

The variational problem of the Hohenberg-Kohn density functional, with a Lagrange multiplier  $\mu$  to limit the number of electrons to  $N$ : leads to

$$\delta \left[ F[n] + \int dr V_{ext}(r)n(r) - \mu \left( \int dr n(r) - N \right) \right] = 0 \quad (2.37)$$

Kohn and Sham [93] separated  $F[n]$  into three parts

$$F[n] = T_s[n] + \frac{1}{2} \int dr dr' \frac{n(r)n(r')}{|r-r'|} + E_{xc}[n] \quad (2.38)$$

where  $T_s[n]$  is the kinetic energy of a non-interacting gas with density  $n(r)$  (**not the same as that of the interacting system, although we might hope that the two quantities are of the same order of magnitude**). Here  $\frac{1}{2} \int dr dr' \frac{n(r)n(r')}{|r-r'|}$  is classical electrostatic (Hartree) energy,  $E_{xc}[n]$  is the exchange-correlation energy which contains the non-classical electrostatic interaction energy and the difference between the kinetic energy of the interacting and non-interacting systems.

The first and second terms can be dealt with simply, and the last term, which contains the effect of the complex behavior is a small fraction of the total energy and can be approximated surprisingly well.

Using this separation equation 2.37 can be written as

$$\frac{\delta T_s[n]}{\delta n(r)} + V_{ks}(r) = \mu \quad (2.39)$$

in which the Kohn-Sham potential  $V_{ks}(r)$  is given by

$$V_{ks}(r) = \int dr' \frac{n(r')}{|r - r'|} + V_{xc}(r) + V_{ext}(r) \quad (2.40)$$

and the exchange-correlation potential  $V_{xc}(r)$  is

$$V_{xc}(r) = \frac{\delta E_{xc}[n]}{\delta n(r)} \quad (2.41)$$

Here, the equation 2.39 is precisely the same equation which would be obtained for a non-interacting system of particles moving in an external potential  $V_{ks}(r)$ . To find the ground state density  $n_0(r)$  for this non-interacting system we simply solve the one-electron Schrödinger equations:

$$\left[ -\frac{1}{2}\nabla^2 + V_{ks}(r) \right] \psi_i(r) = \mathcal{E}_i \psi_i(r) \quad (2.42)$$

for  $\frac{1}{2}N$  single-particle state  $V_{ext}(r)$ ,  $|\psi\rangle_i$  with energies  $\mathcal{E}_i$ . The density form

$$n(r) = 2 \sum_{i=1}^{\frac{N}{2}} |\psi_i(r)|^2. \quad (2.43)$$

Here the factor 2 is for spin degeneracy.

Assume that orbitals are single-occupied and the non-interacting kinetic-energy  $T_s[n]$  from equations 2.38 and 2.43 is given by

$$T_s[n] = - \sum_{i=1}^{\frac{N}{2}} \int dr \psi_i^*(r) \nabla^2 \psi_i(r) \quad (2.44)$$

Since the Kohn-Sham potential  $V_{ks}$  depends upon the density  $n(r)$  it is necessary to solve these equations self-consistently that is having made a guess for the form of the density, the Schrödinger equation is solved to obtain a set of orbitals  $\psi_i(r)$  from which a new density is constructed and the process repeated until the input and output densities are the same.

The energy of the non-interacting system, the sum of a one-electron eigenvalue is

$$2 \sum_{i=1}^{\frac{N}{2}} \mathcal{E}_i = T_s[n] + \int dr n(r) V_{ks}(r), \quad (2.45)$$

after rearrangement of the equation 2.45

$$2 \sum_{i=1}^{\frac{N}{2}} \mathcal{E}_i = T_s[n] + \int dr dr' \frac{n(r)n(r')}{|r-r'|} + \int dr n(r)V_{xc}(r) + \int dr n(r)V_{ext}(r) \quad (2.46)$$

If we compare this to the interacting system, one double-counts the Hartree energy and over-counts the exchange-correlation energy so that the interaction energy is

$$E = 2 \sum_{i=1}^{\frac{N}{2}} \mathcal{E}_i - \frac{1}{2} \int dr dr' \frac{n(r)n(r')}{|r-r'|} - \int dr n(r)V_{xc}(r) + E_{xc}[n]. \quad (2.47)$$

A direct solution of the Schrödinger equation for the extended non-interacting orbitals  $\psi_i(r)$  requires a computational effort **which scales as the cube of the system-size**  $N$ , due to the cost of diagonalizing the Hamiltonian or orthogonalising the orbitals, whereas the original complexity of finding a minimum of the Hohenberg-Kohn functional only required an effort which scaled linearly with  $N$ . Thus a linear scaling method must modify this Kohn-Sham scheme.

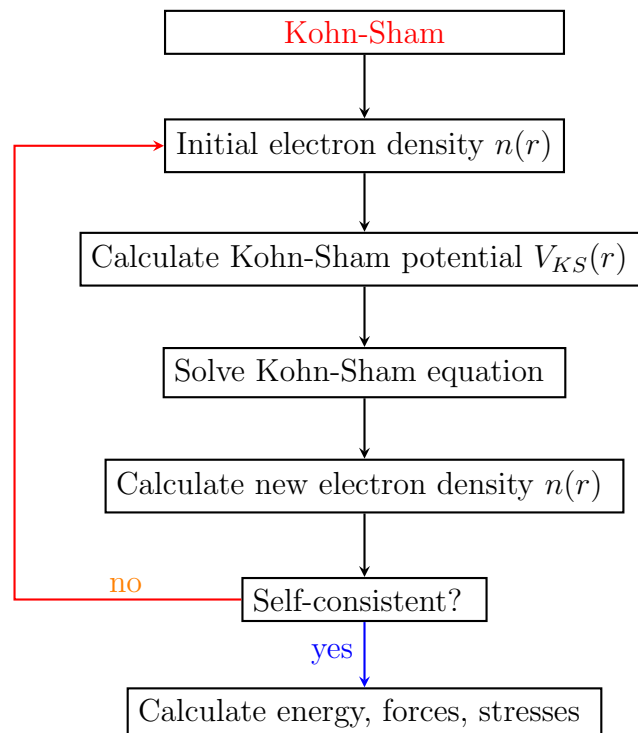


Figure 2.4: Flow chart for Kohn-Sham (KS) self-consistent approaches.

A flow chart of the iteration scheme is shown in Fig. 2.4. At first, an initial guess for the electron density is assumed, which is required for the calculation of  $V_{KS}(r)$ , the diagonalization of the Kohn-Sham equations, and the subsequent

evaluation of  $n(r)$  along with  $E_{tot}$ . As long as the convergence criterion (self-consistent) is not fulfilled, the numerical procedure is continued with the last  $n(r)$  instead of the initial guess. When the criterion (self-consistent) is satisfied, various output quantities are computed.

## 2.3 Exchange-correlation functional

The most widely used exchange-correlation (XC) approximations [73,93] are the local density approximation (LDA) exchange-correlation functional [88] and the Perdew-Burke-Ernzerhof (PBE) parameterized generalized gradient approximation (GGA) exchange-correlation functional [168].

### 2.3.1 The Local Density Approximation (LDA)

The results so far are exact, provided that the functional form of  $E_{xc}[n]$  is known. The problem of determining the functional form of **the universal Hohenberg-Kohn density functional has now been transferred to this one term, but this term is not known exactly.**

To make a simple exchange-correlation energy approximation that works extremely well, and the simplest of these is the local density approximation (LDA), which is the approximation used in this work [88].

In the LDA, the contribution to the exchange-correlation energy from each infinitesimal volume in space,  $dr$ , is taken to be the value it would have if the whole of space was filled with a homogeneous electron gas with the same density as found in  $dr$  that is.

$$E_{xc}^{LDA}[n] = \int \mathcal{E}_{xc}(n(r))n(r)dr \quad (2.48)$$

where  $\mathcal{E}_{xc}(n(r))$  is the exchange-correlation energy per electron in a homogeneous electron gas of density  $n(r)$ .

The exchange-correlation potential  $V_{xc}(r)$  is

$$V_{xc} = \frac{\delta E_{xc}[n]}{\delta n(r)} = \mathcal{E}_{xc}(n(r)) + n(r) \frac{d\mathcal{E}_{xc}n(r)}{dn}. \quad (2.49)$$

The exchange-correlation energy for the homogeneous electron gas has been calculated by Cerperely and Alder [25] using Monte Carlo methods and parameterize by Perdew and Zonger [169].

The LDA is exact in the limit of slowly-varying densities, however the density in systems of interest varies rapidly, and the LDA would appear to be a crude approximation. It is used as justified a posterior by its surprising success at predicting physical properties in real systems. This success may be due in part

to the fact that the sum rule for the exchange-correlation hole, which must be obeyed by the real functional, is reproduced by the LDA.

Now we can connect the interacting and non-interacting systems using a variable coupling constant  $\lambda$  which varies between 0 and 1. We replace the Coulomb interaction by  $\frac{\lambda}{|r-r'|}$ , and but  $\lambda$  vary in the presence of an external potential  $V_\lambda(r)$  so that the ground-state density for all values of  $\lambda$  is the same [66].

The Hamiltonian is

$$\hat{H}_\lambda = -\frac{1}{2} \sum_i \nabla_i^2 + \frac{1}{2} \sum_i \sum_{i \neq j} \frac{\lambda}{|r_i - r_j|} + \hat{V}_{ext} + \hat{V}_\lambda. \quad (2.50)$$

The exchange-correlation hole  $n_{xc}(r, r')$  is then defined in terms of a coupling constant integration of the pair correlation function  $g(r, r' : \lambda)$  of the system with density  $n(r)$  and scaled Coulomb interaction

$$n_{xc}(r, r') = n(r') \int_0^1 d\lambda [g(r, r' : \lambda) - 1]. \quad (2.51)$$

The exchange-correlation energy can be expressed in the form of a classical interaction between the density  $n(r)$  and the hole density  $n_{xc}(r, r')$

$$E_{xc}[n] = \frac{1}{2} \int dr dr' \frac{n(r) n_{xc}(r, r')}{|r - r'|}. \quad (2.52)$$

A sum rule follows from the definition of the pair correlation function

$$\int dr' n_{xc}(r, r') = -1. \quad (2.53)$$

The main factors of success of LDA are:

- The exchange-correlation hole excludes electrons as expected.
- The exchange-correlation energy depends only weakly on the detailed shape of the exchange correlation hole.

**PROS and CONS of LDA:** [58–60]

1. Structural, elastic, and vibrational properties are often imprecise
  - The bond length is 4 % and atomization energy is 2 % of the experimental data.
  - Crystal bulk lattice constants are accurate to within 3 %, usually underestimated.
  - Bulk modulation is somewhat too large, >10 % error is common for d-orbitals.
  - Phonons are somewhat stiff.

2. Overestimation of binding energies (up to several eV), and underestimation of the bonding distances between atoms.
3. Activation energies in chemical reactions are unreliable and relative stability of crystal bulk phases can be uncertain.
4. Electronic structure can be usefully interpreted (Density of states and band structures), except for bandgaps.

### 2.3.2 The Generalized Gradient Approximation (GGA)

The LDA approximation can be improved on, taking into account the spatial change in the local density by including the gradient in the XC functional. This approach is called as the generalized gradient approximation (GGA). It is important to note that the GGA is a semi-local approximation since only the gradient at the same coordinate is taken into account. Thus XC functional is in the form of

$$E_{xc}^{GGA}[n] = \int \mathcal{E}_{xc}(n(r), |\nabla n(r)|) n(r) dr. \quad (2.54)$$

A widely used GGA functional is the Perdew-Burke-Ernzerhof (PBE) functional [168].

### 2.3.3 Van der Waals interactions

Long-range correlations are considered to be the source of van der Waals interactions, but both the LDA and GGA approximations to the exchange-correlations energy in DFT struggle to catch them. To include van der Waals interactions, DFT-D methods have been implemented inside ABINIT, namely DFT-D2 [62] and DFT-D3 [63]. The implementation includes the contribution of these methods to forces and stresses, in view of geometry optimization, as well as to first-order response functions like dynamical matrices.

## 2.4 Tight-Binding Method

The tight-binding (TB) method based on Bloch's formalism and Linear Combination of Atomic Orbital (LCAO) [145] is used in chemistry to study electronic wave functions in a molecule. The TB method is built with atomic orbitals of isolated atoms [61]. The TB method was successfully implemented by Slater and Koster in 1954 [198] and applied to that periodic structures, as we make a general theory that considers all orbitals. We know the electrons in a crystal

obey the Schrödinger equation. The Hamiltonian for the electron in the solid is

$$\hat{H} |\psi\rangle = E |\psi\rangle \quad (2.55)$$

where  $\hat{H}$  is the Hamiltonian operator,  $|\psi\rangle$  is the electronic wave function of the system and  $E$  is the total energy ( $E = \frac{p^2}{2m} + V$ ) of the electrons. The wave function  $|\psi\rangle$  has the periodicity of the lattice. Suppose that there are  $M$  atoms in each unit cell and  $\Gamma_M$  orbitals per atom are considered to play a role in the electrical properties of the studied material.

The LCAO theory, the starting point of the TB model is to consider that an electronic wave function in a crystal is given by the superposition of the wave functions of the isolated atoms. The first step is to decompose the total wave function  $\psi$  as a linear combination of the periodic wave functions  $\psi_{i\alpha}$ . Here,  $i$  stands for the label of an atom in the unit cell ( $1 \leq i \leq M$ ) and  $\alpha$  stands for one orbital of this atom ( $1 \leq \alpha \leq \Gamma_M$ ). The linear combination is obtained by multiplying each  $E$  by a proportionality factor  $a_i$ .

$$\psi = \sum_{i,\alpha} a_{i\alpha} \psi_{i\alpha}. \quad (2.56)$$

The wave function of the orbital  $\alpha$  of an isolated atom  $i$  is called  $\phi_{i\alpha}(r - R_i)$ , where  $R_i$  stands for the Bravais lattice vector corresponding to the cell where orbital  $i$  is.  $R_i$  is the position of the orbital only if there is 1 atom per cell. The positions of the atom  $i$  in one of the lattice unit cells is obtained by applying Bloch's theorem [12],  $\psi_{i\alpha}$  can be built with the functions  $\phi_{i\alpha}(r - R_i)$  as [198]

$$\psi_{i\alpha} = \frac{1}{\sqrt{N}} \sum_{R_i} e^{(ik \cdot R_i)} \phi_{i\alpha}(r - R_i) \quad (2.57)$$

where  $N$  is the number of unit cells in the crystal. By applying  $\langle \psi_{j\beta} |$  and  $\psi = \sum_{i\alpha} a_{i\alpha} \psi_{i\alpha}$  to the Schrödinger equation

$$\langle \psi_{j\beta} | \hat{H} \left( \sum_{i,\alpha} a_{i\alpha} |\psi_{i\alpha}\rangle \right) = E \langle \psi_{j\beta} | \sum_{i,\alpha} a_{i\alpha} |\psi_{i\alpha}\rangle \quad (2.58)$$

after rearranging the above equation 2.58

$$\sum_{i,\alpha} a_{i\alpha} \langle \psi_{j\beta} | \hat{H} | \psi_{i\alpha} \rangle = E \sum_{i,\alpha} a_{i\alpha} \langle \psi_{j\beta} | \psi_{i\alpha} \rangle \quad (2.59)$$

To make the problem easier, let us consider a new notation

$$H_{j\beta i\alpha} = \langle \psi_{j\beta} | \hat{H} | \psi_{i\alpha} \rangle \quad \text{and} \quad S_{j\beta i\alpha} = \langle \psi_{j\beta} | \psi_{i\alpha} \rangle \quad (2.60)$$

The Hamiltonian matrix of the system can be written as

$$H_{nm} a_m = E S_{nm} a_m \quad (2.61)$$

where the  $m \rightarrow i\alpha$  and  $n \rightarrow j\beta$ .

Rearranging the above equation 2.61 leads to  $(H_{nm} - ES_{nm})a_m = 0$ . A non trivial solution is formed when the determinant of the matrix  $(H - ES)$  should be zero.

$$|H - ES| = 0 \quad (2.62)$$

The determinant gives an equation  $\lambda(E) = 0$ . The solution of this equation yields the eigenvalues  $\epsilon_i$  of the Schrödinger equation. Each eigenvalue corresponds to an energy dispersion, also called an energy band of the system. Indeed, the components of  $H$  and  $S$  depend on the wave vector  $k$ , and also the set of eigenvalues then depends on  $k$ .

### 2.4.1 Slater-Koster parameters

To study the matrix elements from the TB method and extract the Slater-Koster [198] parameters. In real space  $H_{j\beta i\alpha}$  and  $S_{j\beta i\alpha}$  can be written as [165]:

$$H_{j\beta i\alpha} = \frac{1}{N} \sum_{R_j} \sum_{R_i} e^{(ik \cdot (R_i - R_j))} \int \phi_{j\beta}^*(r - R_j) \hat{H} \phi_{i\alpha}(r - R_i) dr \quad (2.63)$$

$$S_{j\beta i\alpha} = \frac{1}{N} \sum_{R_j} \sum_{R_i} e^{(ik \cdot (R_i - R_j))} \int \phi_{j\beta}^*(r - R_j) \phi_{i\alpha}(r - R_i) dr. \quad (2.64)$$

Due to the periodicity of the lattice, one only considers the difference of the positions of the atoms  $R = R_j - R_i$ . For the reference position of the atom,  $i$  can be taken as zero position ( $R_i = 0$ ). From the position of the atom  $i$ , the sum can be influenced by the other atoms, at position of the atom  $j$ . If the crystal contains  $N$  unit cells each distance  $R = R_j - R_i$  is to be taken to  $N$  times. A simplified version of the above equations is

$$H_{j\beta i\alpha} = \sum_R e^{(-ik \cdot R)} \int \phi_{j\beta}^*(r - R) \hat{H} \phi_{i\alpha}(r) dr \quad (2.65)$$

$$S_{j\beta i\alpha} = \sum_R e^{(-ik \cdot R)} \int \phi_{j\beta}^*(r - R) \phi_{i\alpha}(r) dr \quad (2.66)$$

where  $\int \phi_{j\beta}^*(r - R) \hat{H} \phi_{i\alpha}(r) dr$  is called the bond energy or the hopping parameter or on-site energy of Slater-Koster parameter, and is denoted by  $\gamma_{j\beta i\alpha}$ ,  $t_{j\beta i\alpha}$  or  $E_{j\beta i\alpha}$  (energy difference of  $i$  and  $j$  while bonding). The high value of this parameter indicates that the electron could be easily moved from atom  $i$  to  $j$ , by tunneling one orbital to another.  $\int \phi_{j\beta}^*(r - R) \phi_{i\alpha}(r) dr$  is called the overlap integral.

The Slater-Koster parameters are mainly composed of the angle between the two atoms or orbitals (direction of cosines  $l$ ,  $m$ , and  $n$ ), bond integral between

two orbitals, and also the distance between the two atoms.

To get rid of the electron-electron interaction, we can write the independent electron Hamiltonian:

$$\hat{H}_e = \hat{T}_e + \hat{V}_{eff} \quad (2.67)$$

where  $\hat{V}_{eff}$  is an effective potential that contains all the possible interactions in the solid. Assume that the effective potential ( $\hat{V}_{eff}$ ) is just the sum of the atomic potential generated by all the atoms in the solid:

$$\hat{V}_{eff} = \sum_j v(r - R_j) \quad (2.68)$$

Substituting this equation in  $H_{j\beta i\alpha}$ , we can get the different type of matrix elements, see Fig. 2.5.

- One center, where the two orbitals and the potential are at the same atom.

$$\int \phi_{j\beta}^*(r - R_j) v(r - R_j) \phi_{j\beta}(r - R_j) dr. \quad (2.69)$$

- Two center, where each orbitals is sitting on a different atom and the potential on one of them

$$\int \phi_{i\alpha}^*(r - R_i) v(r - R_j) \phi_{j\beta}(r - R_j) dr. \quad (2.70)$$

- Two centers, where the two orbitals are sitting on the same site but the potential is centered in another

$$\int \phi_{j\beta}^*(r - R_j) v(r - R_i) \phi_{j\beta}(r - R_j) dr. \quad (2.71)$$

- Three center, where all the three ( the two orbitals and the potential) are centered on different atoms

$$\int \phi_{i\alpha}^*(r - R_i) v(r - R_j) \phi_{k\gamma}(r - R_k) dr. \quad (2.72)$$

Since calculating all the matrix elements of the Hamiltonian that involves even multi-center integrals is computationally expensive, so an approximation be made. J. C. Slater and G. F. Koster [198] proposed that all the matrix elements could be treated in an effective way as two center integrals and then fit them into experimental or first principal's calculations data.

We have also three-center integrals, and also compute the transition amplitude of jump from one site to another site but mediated by the atomic potentials located in different sites of the lattice. Actually, these integrals are small compared with the two-center integrals.

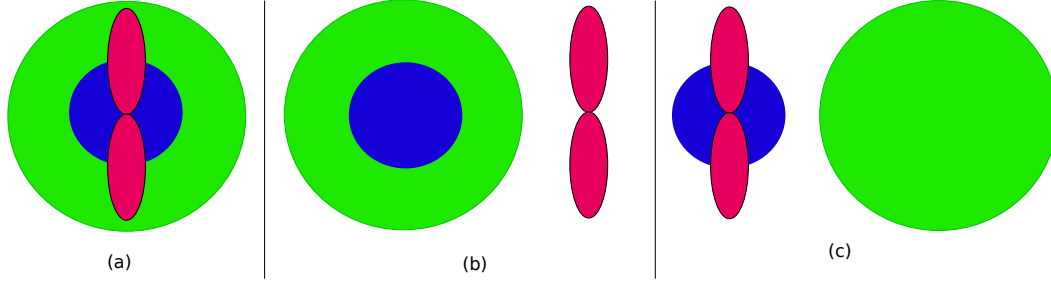


Figure 2.5: Representation of different type of matrix elements: (a) Represents one center, where the two orbitals and the potential are at the same atom, (b) represents two centers integrals, where each orbitals is sitting on a different atom and the potential on one of them, (c) represents two centers integrals, where the two orbitals are sitting on the same site but the potential is centered in another. The blue color circle indicates  $S$  orbitals, Crimson color lobes indicates  $P$  orbitals and Green circle indicates the potential  $V(r)$ .

In the Slater-Koster approximation, three-center integrals are neglected. Thus, in this approximation, when we evaluate each matrix element between two different atoms, we are considering that the rest of the atoms do not interact, therefore, the problem is equivalent to consider an electron in a diatomic molecule. Most of the Hamiltonian matrix elements are zero due to the symmetry if you consider the  $z$ -axis as the quantization axis of the orbitals. The Slater-Koster parameters are those matrix elements in the real atomic basis set. In this way, if the ordering of the basis set is:  $s, p_x, p_y, p_z, d_{xy}, d_{yz}, d_{zx}, d_{x^2-y^2}, d_{z^2}$  the parameters are defined in the independent two-center hopping integrals between two atoms on the  $z$ -axis in the form of a matrix shown as below [48].

$$H = \begin{bmatrix} V_{ss\sigma} & 0 & 0 & V_{sp\sigma} & 0 & 0 & 0 & 0 & V_{sd\sigma} \\ 0 & V_{pp\pi} & 0 & 0 & 0 & 0 & V_{pd\pi} & 0 & 0 \\ 0 & 0 & V_{pp\pi} & 0 & 0 & V_{pd\pi} & 0 & 0 & 0 \\ -V_{sp\sigma} & 0 & 0 & V_{pp\sigma} & 0 & 0 & 0 & 0 & V_{pd\sigma} \\ 0 & 0 & 0 & 0 & V_{dd\sigma} & 0 & 0 & 0 & 0 \\ 0 & 0 & -V_{pd\pi} & 0 & 0 & V_{dd\pi} & 0 & 0 & 0 \\ 0 & -V_{pd\pi} & 0 & 0 & 0 & 0 & V_{dd\pi} & 0 & 0 \\ 0 & 0 & 0 & 0 & 0 & 0 & 0 & V_{dd\sigma} & 0 \\ V_{sp\sigma} & 0 & 0 & -V_{pd\sigma} & 0 & 0 & 0 & 0 & V_{dd\delta} \end{bmatrix}$$

The matrix indicates that hopping between the different orbitals. The determination of Slater-Koster parameters in two-center integrals for the different orbitals ( $s$ ,  $p$ , and  $d$ ) [52, 198] is a straightforward matter of rotating axes and transforming spherical harmonics in terms of one set of axes into spherical harmonics with respect to another set, to find the nature of these integrals. Thus,

atomic orbitals can be set up with respect to a set of rectangular axes. From equation 2.64, let the direction of cosines of the direction of the vector  $R_j - R_i$  point from one atom to the other, be  $l$ ,  $m$ , and  $n$  as shown in Fig. 2.6.

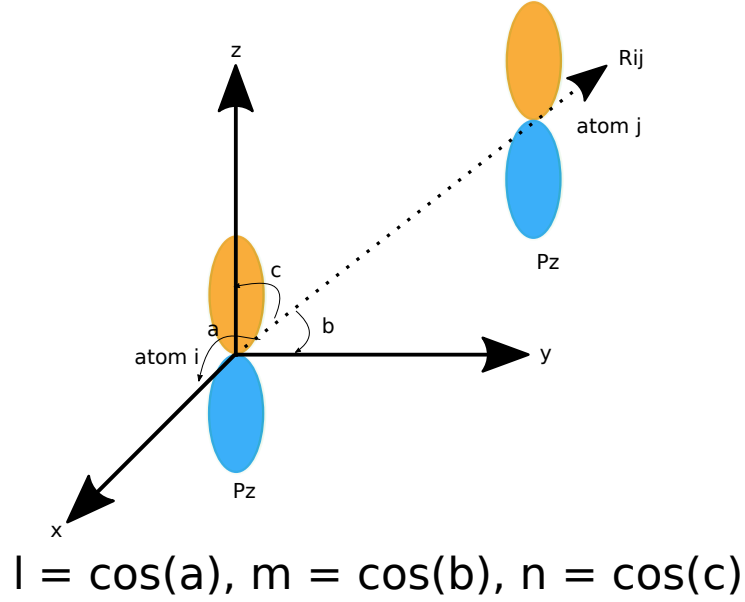


Figure 2.6: A two-center matrix element between  $P_z$  orbitals on atoms  $i$  and  $j$  separated by the vector  $R_{ij} = R_j - R_i$ . Each  $P_z$  orbital may be expressed as a linear combination of  $P_x$ ,  $P_y$ , and  $P_z$  orbitals quantized relative to the  $R_{ij}$  axis, so the matrix element is a linear combination of the Slater-Koster parameters  $V_{pp\pi}$  and  $V_{pp\sigma}$ .

For example writing a Slater-Koster energy integral of  $E_{x,xy}$  [52, 198], meaning an integral in which the function  $\psi_n$  is a  $P_x$  like wave function;  $\psi_m$  is function worth symmetry properties like  $xy$ . This particular function can be written approximately in terms of two integrals: that between a  $p\sigma$  orbital on the first atom and a  $d\sigma$  orbital on the second; and that between a  $p\pi$  on the first and a  $d\pi$  on the second. Let the first of these be symbolized by  $(pd\sigma)$  and the second by  $(pd\pi)$ ; we shall assume that the first index, such as  $p$ , refers to the first orbital, the second, as  $d$ , to the second, **interchanging the order has no effect if the sum of the parities of the orbital is even, but changes the sign if the sum of the parities is odd.**

$$E_{x,xy} = \sqrt{3}l^2m(V_{pd\sigma}) + m(1 - 2l^2)(V_{pd\pi}) \quad (2.73)$$

Similarly, different combinations work as listed in Table. 2.1 [198].

Using the above TB calculations, we made a test on a simple graphene monolayer considering only  $P_z$ -orbitals, got good agreement with DFT [ABINIT] shown in Fig. 2.7. Left-hand side represents the electronic band structure of a

$E_{x,x}$	$l^2(V_{pp\sigma} + (1 - l^2)(V_{pp\pi}))$
$E_{x,y}$	$lm(V_{pp\sigma} - lm(V_{pp\pi}))$
$E_{x,z}$	$ln(V_{pp\sigma} - ln(V_{pp\pi}))$
$E_{x,xy}$	$\sqrt{3}l^2m(V_{pd\sigma}) + m(1 - 2l^2)(V_{pd\pi})$
$E_{x,yz}$	$\sqrt{3}lmn(V_{pd\sigma}) - 2lmn(V_{pd\pi})$
$E_{x,zx}$	$\sqrt{3}l^2n(V_{pd\sigma}) + n(1 - 2l^2)(V_{pd\pi})$
$E_{x,x^2-y^2}$	$\frac{1}{2}\sqrt{3}l(l^2 - m^2)(V_{pd\sigma}) + l(1 - l^2 + m^2)(V_{pd\pi})$
$E_{y,x^2-y^2}$	$\frac{1}{2}\sqrt{3}m(l^2 - m^2)(V_{pd\sigma}) - m(1 + l^2 - m^2)(V_{pd\pi})$
$E_{z,x^2-y^2}$	$\frac{1}{2}\sqrt{3}n(l^2 - m^2)(V_{pd\sigma}) - n(l^2 - m^2)(V_{pd\pi})$
$E_{x,3z^2-r^2}$	$l[n^2 - \frac{1}{2}(l^2 + m^2)](V_{pd\sigma}) - \sqrt{3}ln^2(V_{pd\pi})$
$E_{y,3z^2-r^2}$	$m[n^2 - \frac{1}{2}(l^2 + m^2)](V_{pd\sigma}) - \sqrt{3}mn^2(V_{pd\pi})$
$E_{z,3z^2-r^2}$	$n[n^2 - \frac{1}{2}(l^2 + m^2)](V_{pd\sigma}) + \sqrt{3}n(l^2 + m^2)(V_{pd\pi})$
$E_{xy,xy}$	$3l^2m^2(V_{dd\sigma}) + (l^2 + m^2 - 4l^2m^2)(V_{dd\pi}) + (n^2 + l^2m^2)(V_{dd\delta})$
$E_{xy,yz}$	$3lm^2n(V_{dd\sigma}) + ln(1 - 4m^2)(V_{dd\pi}) + ln(m^2 - 1)(V_{dd\delta})$
$E_{xy,zx}$	$3l^2mn(V_{dd\sigma}) + mn(1 - 4l^2)(V_{dd\pi}) + mn(l^2 - 1)(V_{dd\delta})$
$E_{xy,x^2-y^2}$	$\frac{3}{2}lm(l^2 - m^2)(V_{dd\sigma}) + 2lm(m^2 - l^2)(V_{dd\pi}) + \frac{1}{2}lm(l^2 - m^2)(V_{dd\delta})$
$E_{yz,x^2-y^2}$	$\frac{3}{2}mn(l^2 - m^2)(V_{dd\sigma}) - mn[1 + 2(l^2 - m^2)](V_{dd\pi}) + mn[1 + \frac{1}{2}(l^2 - m^2)](V_{dd\delta})$
$E_{zx,x^2-y^2}$	$\frac{3}{2}nl(l^2 - m^2)(V_{dd\sigma}) + nl[1 - 2(l^2 - m^2)](V_{dd\pi}) - nl[1 - \frac{1}{2}(l^2 - m^2)](V_{dd\delta})$
$E_{xy,3z^2-r^2}$	$\sqrt{3}lm[n^2 - \frac{1}{2}(l^2 + m^2)](V_{dd\sigma}) - 2\sqrt{3}lmn^2(V_{dd\pi}) + \frac{1}{2}\sqrt{3}lm(1 + n^2)(V_{dd\delta})$
$E_{yz,3z^2-r^2}$	$\sqrt{3}nm[n^2 - \frac{1}{2}(l^2 + m^2)](V_{dd\sigma}) + \sqrt{3}mn(l^2 + m^2 - n^2)(V_{dd\pi}) - \frac{1}{2}\sqrt{3}nm(l^2 + m^2)(V_{dd\delta})$
$E_{zx,3z^2-r^2}$	$\sqrt{3}nl[n^2 - \frac{1}{2}(l^2 + m^2)](V_{dd\sigma}) + \sqrt{3}ln(l^2 + m^2 - n^2)(V_{dd\pi}) - \frac{1}{2}\sqrt{3}nl(l^2 + m^2)(V_{dd\delta})$
$E_{x^2-y^2,x^2-y^2}$	$\frac{3}{4}(l^2 - m^2)^2(V_{dd\sigma}) + [l^2 + m^2 - (l^2 + m^2)^2](V_{dd\pi}) + [n^2 + \frac{1}{4}(l^2 - m^2)^2](V_{dd\delta})$
$E_{x^2-y^2,3z^2-r^2}$	$\frac{1}{2}\sqrt{3}(l^2 - m^2)[n^2 - \frac{1}{2}(l^2 + m^2)](V_{dd\sigma}) + \sqrt{3}n^2(m^2 - l^2)(V_{dd\pi}) + \frac{1}{4}\sqrt{3}(1 + n^2)(l^2 - m^2)(V_{dd\delta})$
$E_{3z^2-r^2,3z^2-r^2}$	$[n^2 - \frac{1}{2}(l^2 + m^2)]^2(V_{dd\sigma}) + 3n^2(m^2 + l^2)(V_{dd\pi}) + \frac{3}{4}(1 + n^2)(l^2 + m^2)^2(V_{dd\delta})$

Table 2.1: Energy integrals for a crystal in terms of two-center integrals where  $n, l, m$  are direction of cosines shown in Fig. 2.6.

graphene monolayer (TB method) including Slater-Koster parameters and right-hand side represents the electronic band structure of a graphene monolayer *ab initio* ABINIT (first principle calculations) + TB method.

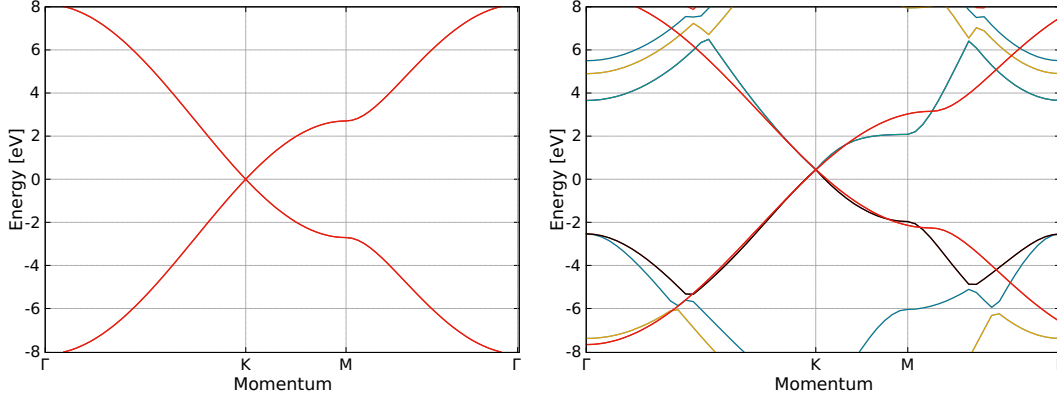


Figure 2.7: Electronic band structure of graphene monolayer TB method [left] with  $p_z$ -orbital only, and first neighbor coupling  $V_{pp\pi} = -2.7$  eV. Comparison of DFT+TB [right], the DFT calculation includes all orbitals around the Dirac energy.

## 2.4.2 Spin Orbit Coupling (SOC)

The Spin-Orbit Coupling (SOC) is a relativistic effect that has to be considered in the Schrödinger equation. This interaction relates the spin degree of freedom  $\vec{S}$  with the angular momentum of the electron  $\vec{L}$ . We have included the spin degree of freedom ( $s = \uparrow, \downarrow$ ) in the tight-binding formalism duplicating the size of the basis set. Now the spin-orbital states are denoted by  $|i, \alpha, s\rangle = |i, \alpha\rangle \otimes |s\rangle$  [where  $i$  indicates the atomic sites and  $\alpha$  indicates the orbital]. We derived the expressions to include this interaction in the tight-binding method.

Considering an electron moving with velocity,  $\vec{v}$ , in an electric field,  $\vec{E}$ , this electric field is created by the effective potential of the atoms,  $-e\vec{E} = -\Delta V_{eff}$ . In the reference system where the electron is at rest, it will lead to an induced magnetic field,  $\vec{B} = -\frac{\vec{v}}{c} \times \vec{E}$  [81]. The induced field interacts with the spin magnetic moment,  $\vec{\mu} = \frac{eg}{m^2c^2}\vec{S}$ , resulting in a new term in the Hamiltonian

$$\begin{aligned} \hat{H}_{SOC} &= -\frac{1}{2}\vec{\mu} \cdot \vec{B} = \frac{1}{2} \left[ \vec{\mu} \cdot \left( \frac{\vec{v}}{c} \times \vec{E} \right) \right] = \frac{1}{2} \frac{1}{m^2c^2} \left[ \vec{S} \cdot (\vec{p} \times (-\Delta V_{eff})) \right] \\ &= \frac{1}{2} \frac{1}{m^2c^2} \left[ \vec{S} \cdot (\Delta V_{eff} \times \vec{p}) \right] \end{aligned} \quad (2.74)$$

where the  $\frac{1}{2}$  factor in the definition is originated by the Thomas precession [81]. Classically, this is due to the fact that the electron trajectory is not straight and uniform. We have to consider that  $g \approx 2$ , to obtain the final result in equation

## 2.74.

In the Slater-Koster approximation, we assume that the potential created by a solid is the sum of effective atomic potentials located at each atom in equation 2.69. This way, for each of these effective potentials  $V_{eff}^i(\vec{r})$  (we assumed that they are referred to the atomic site in  $\vec{R}_i$ ). We can approximate these potentials with spherical symmetry,  $V_{eff}^i(\vec{r}) = V_{eff}^i(r)$ , at least in the closer region to the nucleus. Therefore, we can evaluate  $\Delta V_{eff}^i$ ,

$$\Delta V_{eff}^i(r) = \frac{\vec{r} dV_{eff}^i(r)}{r dr}. \quad (2.75)$$

Including this expression into equation 2.74 we get

$$\hat{H}_{SOC} = \frac{1}{2} \frac{1}{m^2 c^2} \frac{1}{r} \frac{dV_{eff}^i}{dr} \left[ \vec{S} \cdot (\vec{r} \times \vec{p}) \right] = \lambda^i(r) \vec{L} \cdot \vec{S} \quad (2.76)$$

where  $\lambda^i(r) = \frac{1}{2} \frac{1}{m^2 c^2} \frac{1}{r} \frac{dV_{eff}^i}{dr}$  is a radial function which is different for each atomic species. The scalar product of the spin and angular momentum can be written as

$$\vec{L} \cdot \vec{S} = \frac{1}{2} (\hat{L}_+ \hat{S}_- + \hat{L}_- \hat{S}_+) + \hat{L}_z \hat{S}_z \quad (2.77)$$

with  $\hat{L}_\pm$  and  $\hat{S}_\pm$  the ladder operators defined as

$$\hat{L}_\pm = \hat{L}_x \pm i \hat{L}_y = \hat{S}_x \pm i \hat{S}_y. \quad (2.78)$$

Representing this Hamiltonian in the basis set of complex atomic orbitals,  $|l, m\rangle$ , eigenstates of  $\hat{L}^2$  and  $\hat{L}_z$ , is straightforwardly using the eigenvalue relations

$$\hat{L}_z |l, m\rangle = \hbar m |l, m\rangle \quad (2.79)$$

$$\hat{L}_\pm |l, m\rangle = \hbar \sqrt{l(l+1) - m(m \pm 1)} |l, m \pm 1\rangle \quad (2.80)$$

The matrix elements of equation 2.76 expressed in the real space representation of the atomic orbitals,  $\langle \vec{r} | i, l, m \rangle = R_l^{(i)}(r) Y_{l,m}^{(i)}(\theta, \phi)$  are

$$\begin{aligned} \langle i, l, m, s | \hat{H} | i', l', m', s' \rangle &= \int_0^\infty dr r^2 \xi(r) (R_l^{(i)})^*(r) R_{l'}^{(i')}(r) \\ &\times \int_0^{2\pi} \int_0^\pi d\theta d\phi \sin(\theta) (Y_{l,m}^{(i)}(\theta, \phi))^* \langle s | \vec{L} \cdot \vec{S} | s' \rangle Y_{l',m'}^{(i')}(\theta, \phi). \end{aligned} \quad (2.81)$$

We divided this expression in two parts:  $\lambda_{l,l'}^{i,i'}(r)$  which encodes the radial dependence and  $\langle l, m, s | \vec{L} \cdot \vec{S} | l', m', s' \rangle$  containing the angular dependence

$$\lambda_{l,l'}^{i,i'}(r) = \int_0^\infty dr r^2 \xi(r) (R_l^{(i)})^*(r) R_{l'}^{(i')}(r) \quad (2.82)$$

$$\langle l, m, s | \vec{L} \cdot \vec{S} | l', m', s' \rangle = \int_0^{2\pi} \int_0^{\pi} d\theta d\phi \sin(\theta) (Y_{l,m}^{(i)}(\theta, \phi))^* \langle s | \vec{L} \cdot \vec{S} | s' \rangle Y_{l',m'}^{(i')}(\theta, \phi) \quad (2.83)$$

Thus, we rewrite the SOC Hamiltonian in a much more compact form

$$\langle i, l, m, s | \hat{H} | i', l', m', s' \rangle = \lambda_{l,l'}^{i,i'}(r) \langle l, m, s | \vec{L} \cdot \vec{S} | l', m', s' \rangle \quad (2.84)$$

$\vec{L} \cdot \vec{S}$  does not mix states with different orbital quantum number  $l$ . Therefore, the only elements different from zero are those with  $l = l'$ . On the other hand, due to the local character of the wave functions and the effective potential, we can consider that the integrals  $\lambda_{l,l'}^{i,i'}(r)$  are local, that is the only terms different from zero are intra-atomic ( $a = a'$ ). These two features reduce the number of  $\lambda_i^a$  integrals for each atomic species, only one per type of orbital ( $\lambda_p^i, \lambda_d^i, \lambda_f^i$ ). In the tight-binding method, these integrals are considered also as parameters obtained from experiments or fitted from DFT calculations.

Thus, the matrix representation of the SOC in the basis of atomic orbital eigenstates of  $\vec{L}^2$  and  $L_z$ ,  $|i, l, m, s\rangle$ , are

$$\langle i, l, m, s | \hat{H} | i', l', m', s' \rangle = \lambda_l^i(r) \langle l, m, s | \vec{L} \cdot \vec{S} | l', m', s' \rangle \delta_{l,l'}. \quad (2.85)$$

Similarly, we can express the Hamiltonian in the basis set of real atomic orbitals  $|i, \alpha, s\rangle$

$$\langle i, \alpha, s | \hat{H} | i', \alpha', s' \rangle = \lambda_l^i(r) \langle \alpha, s | \vec{L} \cdot \vec{S} | \alpha', s' \rangle. \quad (2.86)$$

The radial part is independent of the orbital representation, thus the parameters  $\lambda_l^i$  are the same in both basis sets. We show the specific matrix representation of  $\langle \alpha, s | \vec{L} \cdot \vec{S} | \alpha', s' \rangle$  for  $s$  and  $p$  orbitals in the table below [for the d-orbitals see appendix 1].

	$ s^\uparrow\rangle$	$ p_x^\uparrow\rangle$	$ p_y^\uparrow\rangle$	$ p_z^\uparrow\rangle$	$ s^\downarrow\rangle$	$ p_x^\downarrow\rangle$	$ p_y^\downarrow\rangle$	$ p_z^\downarrow\rangle$
$ s^\uparrow\rangle$	0	0	0	0	0	0	0	0
$ p_x^\uparrow\rangle$	0	$-i\frac{\lambda}{2}$	0	0	0	0	0	$\frac{\lambda}{2}$
$ p_y^\uparrow\rangle$	0	$i\frac{\lambda}{2}$	0	0	0	0	0	$-i\frac{\lambda}{2}$
$ p_z^\uparrow\rangle$	0	0	0	0	0	$-\frac{\lambda}{2}$	$-i\frac{\lambda}{2}$	0
$ s^\downarrow\rangle$	0	0	0	0	0	0	0	0
$ p_x^\downarrow\rangle$	0	0	0	$-\frac{\lambda}{2}$	0	0	$i\frac{\lambda}{2}$	0
$ p_y^\downarrow\rangle$	0	0	0	$-i\frac{\lambda}{2}$	0	$-i\frac{\lambda}{2}$	0	0
$ p_z^\downarrow\rangle$	0	$\frac{\lambda}{2}$	$i\frac{\lambda}{2}$	0	0	0	0	0

Table 2.2: Spin orbit Hamiltonian in the basis set of atomic orbitals ( $s$  and  $p$ ).

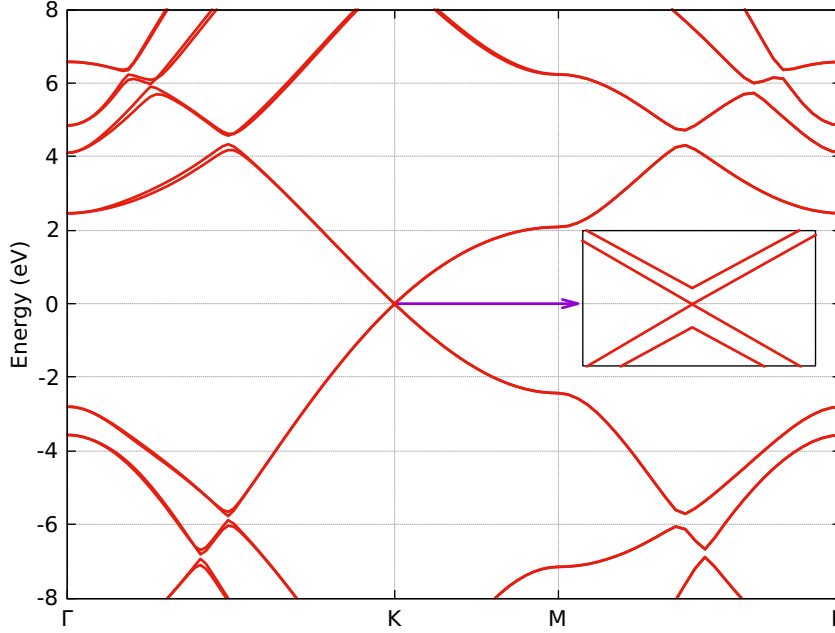


Figure 2.8: Electronic band structure of a graphene monolayer including spin orbit coupling (SOC). Spin splitting of bands at the Dirac point is  $30\mu\text{eV}$ . Calculations are done by using the TB method including  $s, p_x, p_y, p_z$  orbitals.

We made a calculation on a graphene monolayer by the TB method including SOC. Fig. 2.8 represents the electronic band structure of a graphene monolayer including spin-orbit coupling, we observe very small splitting at the Dirac point is  $30\mu\text{eV}$  in good agreement with first principle calculations  $24\mu\text{eV}$  [55],  $\lambda_{SOC} = 0.35\text{ eV}$  and hopping parameters are  $V_{ss\sigma} = -0.55\text{ eV}$ ,  $V_{sp\sigma} = -8.25\text{ eV}$ ,  $V_{pp\pi} = -1.7\text{ eV}$  and  $V_{pp\sigma} = -2.7\text{ eV}$ .

### 2.4.3 Wannier functions

As we mentioned, in the tight-binding method, the Bloch wave functions can also be expanded using other local orbitals instead of atomic orbitals, these are called Wannier functions because they were introduced by G. Wannier [229]. Wannier functions of such local orbitals, though they are not localized in some cases where the bandwidths are wide, are not like the atomic wave functions. Wannier functions behave like a Fourier transformation of Bloch wave functions  $\psi_{n\mathbf{k}}(\mathbf{r})$ . Since  $\psi_{n\mathbf{k}}(\mathbf{r})$  is periodic in the reciprocal lattice, i.e,  $\psi_{n\mathbf{k}+\mathbf{G}}(\mathbf{r}) = \psi_{n\mathbf{k}}(\mathbf{r})$ , where  $\mathbf{G}$  is a reciprocal lattice vector,  $\psi_{n\mathbf{k}}(\mathbf{r})$  can be expanded in plane waves as

$$\psi_{n\mathbf{k}}(\mathbf{r}) = \sum_{\mathbf{R}} w_n(\mathbf{r} - \mathbf{R}) e^{i\mathbf{R}\cdot\mathbf{k}} \quad (2.87)$$

where the coefficients  $w_n(\mathbf{r} - \mathbf{R})$  are Wannier functions, which depend only on  $\mathbf{r} - \mathbf{R}$  instead of  $\mathbf{r}$  and  $\mathbf{R}$  independently due to the Bloch theorem.

The Wannier functions  $w_n(\mathbf{r} - \mathbf{R})$  can be obtained by inverse transformations

$$w_n(\mathbf{r} - \mathbf{R}) = \frac{\Omega_{cell}}{(2\pi)^3} \int_{BZ} e^{i\mathbf{R}\cdot\mathbf{k}} \psi_{n\mathbf{k}}(\mathbf{r}) d\mathbf{k} \quad (2.88)$$

where  $\Omega_{cell}$  is the volume of the real-space primitive cell of the crystal.

The Wannier functions so obtained are not unique because of any Bloch function  $\psi_{n\mathbf{k}}(\mathbf{r})$  does not change any physically meaningful quantity under a ‘‘gauge transformation’’

$$\psi_{n\mathbf{k}}(\mathbf{r}) \rightarrow \tilde{\psi}_{n\mathbf{k}}(\mathbf{r}) = e^{i\phi_n(\mathbf{k})} \psi_{n\mathbf{k}}(\mathbf{r}) \quad (2.89)$$

A more general form of the Wannier functions is given by

$$w_n(\mathbf{r} - \mathbf{R}) = \frac{\Omega_{cell}}{(2\pi)^3} \int_{BZ} e^{i\phi_n(\mathbf{k})} e^{-i\mathbf{R}\cdot\mathbf{k}} \psi_{n\mathbf{k}}(\mathbf{r}) d\mathbf{k} \quad (2.90)$$

The non-uniqueness of the Wannier functions is totally due to the presence of the phase factor  $\phi_n(\mathbf{k})$ . In addition to the freedom in the choice of phase factor  $\phi_n(\mathbf{k})$ , there is also a degree of freedom associated with the choice of a full unitary matrix  $U_{nm}^{\mathbf{k}}$ , which transforms the  $N$  Bloch wave functions  $\psi_{n\mathbf{k}}(\mathbf{r})$  between themselves at every wave vector  $k$ , but leaves the electronic energy functional invariant. This leads to the most general construction of Wannier functions from Bloch wave functions  $\psi_{n\mathbf{k}}(\mathbf{r})$  in the form

$$w_n(\mathbf{r} - \mathbf{R}) = \frac{\Omega_{cell}}{(2\pi)^3} \int_{BZ} \sum_{m=1}^N U_{nm}^{\mathbf{k}} e^{-i\mathbf{R}\cdot\mathbf{k}} \psi_{m\mathbf{k}}(\mathbf{r}) d\mathbf{k} \quad (2.91)$$

where  $U^{\mathbf{k}}$  is an  $M \times N$  unitary matrix with  $M \leq N$ . Remark that  $U^{\mathbf{k}}$  is not necessarily a square matrix as one can use this procedure to construct  $M$  Wannier functions out of  $N$  bands. Again, in the procedure, the choice of  $U^{\mathbf{k}}$  is not unique. Actually, one can use this freedom to construct Wannier functions with properties of ones own interest, such as the most symmetric, or maximally projected, or maximally localized. A widely used one is the maximally localized Wannier function proposed by Vanderbilt and coworkers [129, 200], in which the quantity

$$\Omega = \sum_{n=1}^N (\langle \mathbf{r}^2 \rangle_n - \langle \mathbf{r} \rangle_n^2) \quad (2.92)$$

equation 2.92 represents the total spread of the Wannier functions in real space [129]. This is minimized by choosing appropriate  $U^{\mathbf{k}}$ , where  $\langle \dots \rangle_n$  is the expectation value over the  $n^{th}$  Wannier function in the unit cell. There are also other Wannier functions in use which are constructed by using projections onto local orbitals to emphasize symmetries [96, 235].

The Wannier functions  $w_n(\mathbf{r} - \mathbf{R})$  for all the bands  $\mathbf{n}$  and  $\mathbf{R}$  form a complete

orthogonal set. This is to say that the Wannier functions are orthogonal at different sites or different bands,

$$\int w_n(\mathbf{r} - \mathbf{R}_j)w_m(\mathbf{r} - \mathbf{R}_j) = \delta_{n,m}\delta_{i,j} \quad (2.93)$$

In the tight binding approach, if Wannier functions are used as the local orbitals, the overlap matrix  $s_{n,m}(\mathbf{R})$  is greatly simplified to

$$s_{n,m}(\mathbf{R}) = \delta_{n,m}\delta_{\mathbf{0},\mathbf{R}} \quad (2.94)$$

The result for the overlap Hamiltonian matrix is

$$S_{n,m}(\mathbf{k}) = \sum_{\mathbf{R}} e^{i\mathbf{R}\cdot\mathbf{k}} s_{n,m}(\mathbf{R}) = \sum_{\mathbf{R}} e^{i\mathbf{R}\cdot\mathbf{k}} \delta_{n,m}\delta_{\mathbf{0},\mathbf{R}} = \delta_{n,m} \quad (2.95)$$

Now, we can change the Hamiltonian of the matrix, so this is the main advantage to use Wannier functions in the tight-binding method.

In practice, Wannier functions are constructed from the result of DFT calculations and used as the local orbitals in the tight-binding method. The hopping parameters and onsite energies are obtained by fitting the eigenvalues (obtained from the tight-binding method) to the band structures of DFT calculations. The hopping parameters are then used to construct a model Hamiltonian to study many-body effects (Note that the overlap matrix is the identity matrix due to the use of Wannier functions as local orbitals). The Wannier functions are not localized if the bands have large bandwidths. This procedure is better for systems with an isolated set of narrow bands. Using the Wannier90 code [144, 172] we measured the projections of the orbital character in the band structure of the systems energy example of a graphene monolayer [Fig. 2.9].

We examine the graphene monolayer band structure, interpolated with Wannier90 [144, 172] on the  $\Gamma - K - M - \Gamma$  path. Using  $s$ ,  $p$ , and  $d$  orbitals as initial guesses for the MLWFs of the graphene monolayer shown in Fig. 2.9 shows that the bands of interest have very high  $p$  character in the graphene monolayer electronic band structure.

In the same spirit, We use the Wannier90 code [144, 172] to calculate a Wannier Hamiltonian from DFT results, extract the bands and compare the electronic band structure of a graphene monolayer, interpolated with Wannier90 on the  $\Gamma - K - M - \Gamma$  path and DFT (ABINIT) reference as shown in Fig. 2.10.

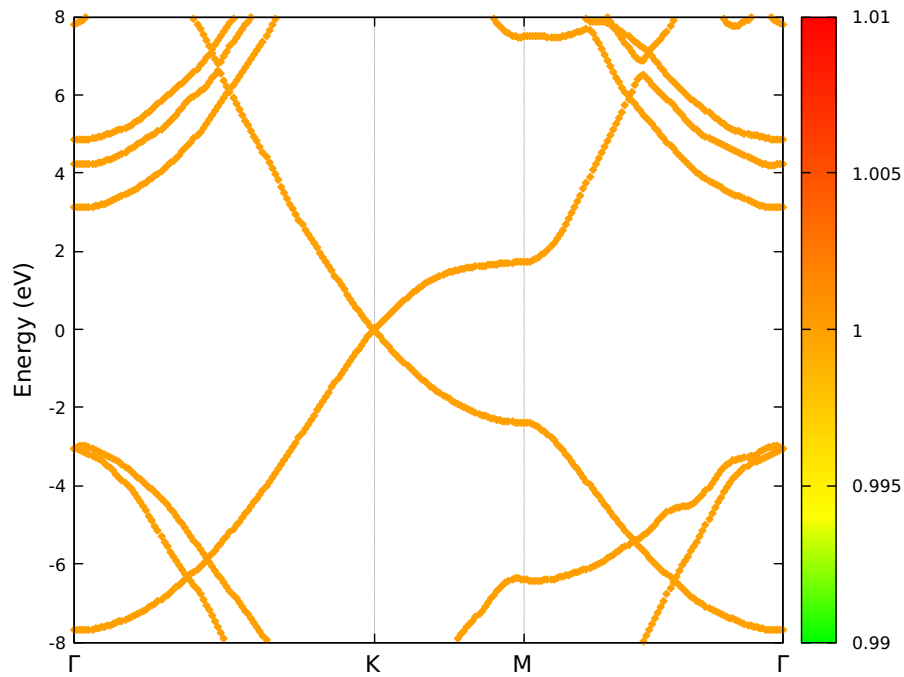


Figure 2.9: Electronic band structure of a graphene monolayer. Estimated  $p$ -orbital character of bands, computed by band projections using Wannier90 code. A color scheme is used to measure the  $p$ -orbital character (red color) of the bands.

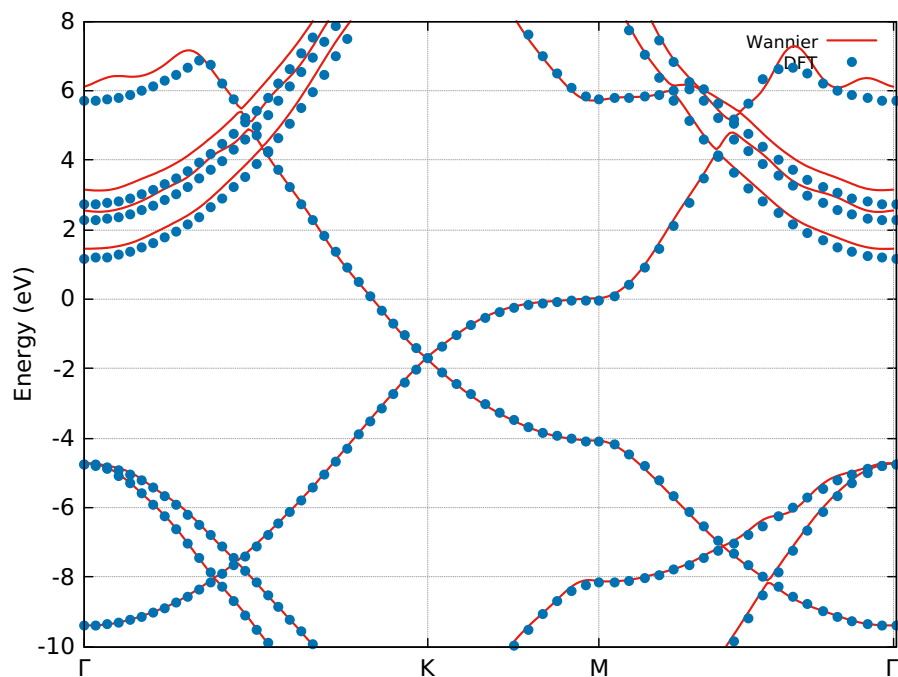


Figure 2.10: Electronic band structure of a graphene monolayer, Interpolation with Wannier90 on the  $\Gamma - K - M - \Gamma$  path (red lines) and DFT (ABINIT) reference band structure (blue circles).

## 2.5 Conclusion

In this chapter, we discussed some concepts related to the quantum physics to set the basis to explain briefly the standard time-independent DFT. We explained several approximations such as Born-Oppenheimer (BO), exchange correlation functionals (LDA and GGA). We gave a brief explanation without attempting to discuss the underlying mathematics. For solving the many-body problem, we made two approximations: One is the Born-Oppenheimer (BO) approximation and the second one is the Hartree-Fock (HF) approximation. We constructed a tight-binding method on Bloch's formalism and linear combination of atomic orbitals. We included a spin-orbit coupling in the tight-binding method to study the electronic structure of graphene and transition metal dichalcogenides. We introduced Wannier functions of local orbitals to study the orbital contribution in the electronic band structure.

## Chapter No. 3

---

### *Numerical methods of Quantum transport*

---

	Page
3.1 Recursion methods for computing the density of states and wave-packet dynamics . . . . .	41
3.1.1 Recursion method (Lanczos method) . . . . .	41
3.1.2 The density of states . . . . .	43
3.1.3 Termination of the continued fraction . . . . .	45
3.2 Recursion method for computing the wave packet dynamics . . . . .	48
3.2.1 Kubo-Greenwood method . . . . .	48
3.2.2 Relation between low frequency conductivity and quantum diffusion . . . . .	50
3.2.3 Relaxation time approximation (RTA) . . . . .	51
3.3 Chebyshev polynomials . . . . .	53
3.3.1 Spectral coefficient $C_n(T)$ . . . . .	54
3.3.2 Calculation of $ \phi'_{RP}(T)\rangle$ & $ \phi_{RP}(T)\rangle$ . . . . .	55
3.3.3 Numerical implementation of RTA . . . . .	57
3.4 Conclusion . . . . .	58

---

The Lanczos iteration [99] was proposed as a method for tridiagonalizing Hermitian matrices. Like the related Arnoldi method [4] for non Hermitian matrices, this method initially received a great attention because of Lanczos basically replaces matrix diagonalization by matrix-vector products are relatively inexpensive to perform. The Lanczos method is particularly efficient for the determination of extreme eigenvalues and eigenvectors. Therefore, it was rediscovered in the 1970s [159], when the computers had become sufficiently powerful to treat large enough matrices for the Lanczos algorithm to perform general methods, nicely illustrating the Fundamental Law of Computer Science: the faster the computer, the greater the importance of the speed of algorithms [215].

The Lanczos method is mainly suitable for dealing with large scattered Hamiltonian's, it is the method of choice for systems with short range interactions. For density of states and electronic band structure calculations in a linear combination of atomic orbitals (LCAO) or tight-binding (TB) basis, it is known as the recursion method [70]. The basic idea here is to switch from the Bloch picture of a perfectly periodic solid to a local picture, replacing the solution of the Schrödinger equation in terms of Bloch waves by the calculation of the local density of states. The crucial technical point is to calculate the density of states not via a spectral representation (in terms of Bloch waves), but by repeated application of the Hamiltonian  $H$  to a localized single electron state. With each application of  $H$  the electron explores more and more sites. Thus, if the hopping matrix elements beyond a certain distance are zero, such calculations can be performed without having to restrict the system to a finite size.

It has to be defined on a finite cluster, giving rise to a finite dimensional Hamiltonian matrix. Since the size of the Hilbert space grows exponentially with system size, actual calculations are stopped by the available computer memory. In a typical simulation, first the ground state is calculated by a Lanczos iteration. Building on this, spectral functions are calculated in a similar way as in the recursion method. The great advantage of this approach is that it gives the dynamical properties of the ground state ( $T=0$  K) directly in real space.

In this chapter, we introduce some concepts related to the recursion methods for computing the density of states (DOS). Several approximations such as the Lanczos method, density of states, termination of the continued fraction, wave-packet propagation method. We only try to give a brief explanation (mathematical description) of the methods, most of the things in this chapter follow from Didier Mayou, Triozon, Khanna, Roche research works [130, 131, 183, 184, 217].

In the Kubo-Greenwood approach for transport properties, the quantum diffusion  $D$  is computed by using the polynomial expansion of the average square spreading,  $\Delta X^2$ , for charge carriers. This method, developed by Didier Mayou, Khanna, Roche and Triozon [130, 131, 183, 184, 217], allows for very efficient numerical calculations by recursion in real space that takes into account all quantum effects. Static defects are included directly in the structural modelling of the system and they are randomly distributed on a supercell containing up to  $\approx 10^7$  orbitals. Inelastic scattering is computed [37] within the relaxation time approximation (RTA), including an inelastic scattering time  $\tau_i$  beyond which the propagation becomes diffusive due to the destruction of coherence by inelastic processes.

### 3.1 Recursion methods for computing the density of states and wave-packet dynamics

The Lanczos tridiagonalization method transforms real symmetric matrix into a symmetric tridiagonal form. Basically, this very simple algorithm is suitable for calculations of lower eigenvalues and the corresponding eigenvectors of very large Hermitian matrices, for the full diagonalization is impossible. In this chapter, we explain the basics of the recursion method based on the Lanczos tridiagonalization and explain how to calculate the DOS as well as the wave-packets dynamics (Diffusivity and related conductivity) [211].

#### 3.1.1 Recursion method (Lanczos method)

The Lanczos method is a highly effective and efficient recursive approach for calculation of the electronic structure as well as the DOS [99]. This method was developed based on Lanczos eigenvalue approach [68, 69] and they were included Green's function matrix elements by continued fraction expansion. It can be implemented in real or reciprocal space. This method is suitable for treating disorder and defect related problems, using a tight-binding approximation [116] to calculate the density of states and electronic structure for amorphous semiconductors, transition metals [16].

Since the computational cost is proportional to the total number of atoms defining the disordered structure, the recursion method should be of order  $N$  [32], a basis transformation that has proven to be very useful for dealing with tight-binding Hamiltonians for which diagonalization methods are ineffective. The Lanczos method allows simulation of the electronic behavior of disordered systems up to the scale of 100 millions of orbitals using high performance computing

resources. A very efficient computational trick [183, 184] is to compute the trace of any operator related to electronic and transport properties on a reduced number of random phase states ( $N_{RP}$ ) instead of a complete and orthogonal basis:

$$Tr[\delta(E - \hat{H})] = \sum_{j=1}^N \langle \phi_j | \delta(E - \hat{H}) | \phi_j \rangle = \frac{N}{N_{RP}} \times \sum_{i=1}^{N_{RP}} \langle \phi_{RP}^i | \delta(E - \hat{H}) | \phi_{RP}^i \rangle \quad (3.1)$$

where  $N$  is the dimension of the Hamiltonian  $\hat{H}$  in the TB basis,  $\phi_j$  is an atomic orbital state of the system and  $|\phi_{RP}\rangle$  is defined by

$$|\phi_{RP}\rangle = \frac{1}{\sqrt{N}} \sum_{j=1}^N e^{i2\pi\theta_j} |\phi_j\rangle \quad (3.2)$$

with  $\theta_j$  a random number between 0 and 1. This state  $|\phi_{RP}\rangle$  has a random phase on each orbital of the TB basis.

To evaluate numerically equation 3.1, we compute the local density of states (LDOS) on an orbital  $\psi_0$  by the recursion method, as follows.

We can construct an orthonormal basis  $|\psi_n\rangle$  of the  $N$  space. We start with the normalized vector  $|\psi_0\rangle$ . The second basis vector  $|\psi_1\rangle$  is constructed by using the Lanczos method.

$$b_1 |\psi_1\rangle = |\tilde{\psi}_1\rangle = H |\psi_0\rangle - a_0 |\psi_0\rangle \quad (3.3)$$

where  $a_0 = \langle \psi_0 | H | \psi_0 \rangle$  and  $b_1^2 = \langle \tilde{\psi}_1 | \tilde{\psi}_1 \rangle$ . The next basis vector is likewise constructed as  $H |\psi_n\rangle$  orthogonalized to all previous vectors and normalized

$$b_2 |\psi_2\rangle = |\tilde{\psi}_2\rangle = H |\psi_1\rangle - \sum_{i=0}^1 |\psi_i\rangle \langle \psi_i | H | \psi_1 \rangle = H |\psi_1\rangle - a_1 |\psi_1\rangle - b_1 |\psi_0\rangle \quad (3.4)$$

where  $a_1 = \langle \psi_1 | H | \psi_1 \rangle$  and  $b_2^2 = \langle \tilde{\psi}_2 | \tilde{\psi}_2 \rangle$ . The fourth basis vector is

$$b_3 |\psi_3\rangle = |\tilde{\psi}_3\rangle = H |\psi_2\rangle - \sum_{i=0}^2 |\psi_i\rangle \langle \psi_i | H | \psi_2 \rangle = H |\psi_2\rangle - a_2 |\psi_2\rangle - b_2 |\psi_1\rangle. \quad (3.5)$$

Here,  $a_n$  and  $b_n$  are vanishing (when  $n >$  dimension of Hilbert space) in the orthogonalization, when  $H$  is Hermitian: equation 3.3 together with the orthogonality of the basis vectors for  $n = 0 \dots 2$  implies  $\langle \psi_2 | H | \psi_0 \rangle = 0$ . When  $H$  is Hermitian it follows that  $\langle \psi_1 | H | \psi_2 \rangle = 0$ . The construction of the further basis vectors follows the same scheme

$$b_{n+1} |\psi_{n+1}\rangle = |\tilde{\psi}_{n+1}\rangle = H |\psi_n\rangle - \sum_{i=0}^n |\psi_i\rangle \langle \psi_i | H |\psi_n\rangle = H |\psi_n\rangle - a_n |\psi_n\rangle - b_n |\psi_{n-1}\rangle \quad (3.6)$$

with  $a_n = \langle \psi_n | H | \psi_n \rangle$  and  $b_{n+1}^2 = \langle \tilde{\psi}_{n+1} | \tilde{\psi}_{n+1} \rangle$ . Rearranging the above equation 3.6 shows that  $H$  is tridiagonalized

$$H |\psi_n\rangle = b_n |\psi_{n-1}\rangle + a_n |\psi_n\rangle + b_{n+1} |\psi_{n+1}\rangle. \quad (3.7)$$

Equation 3.7 shows that the Hamiltonian is similar to that of a linear chain with interaction between nearest neighbors where the coefficients  $a_n$  and  $b_n$  represent the site energies of each atom and the jump integrals between the nearest neighbor atoms see Fig. 3.1.

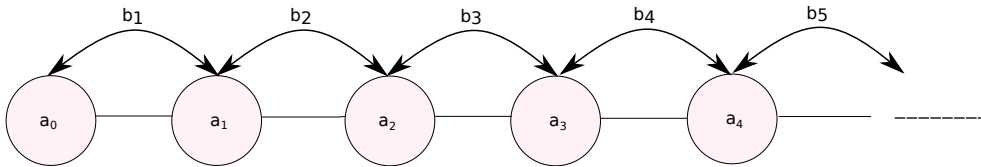


Figure 3.1: Schematic representation of the linear chain generated by the Lanczos procedure.

$a_n$  and  $b_n$  are called the recursion coefficients, they are respectively the diagonal and off-diagonal elements of the matrix representation of  $\hat{H}$  in the Lanczos basis (that we write  $\hat{H}$ ). In equation 3.6, we see that  $\hat{H} |\psi_i\rangle$  is orthogonal to all basis states except  $|\psi_i\rangle$  and  $|\psi_{i\pm 1}\rangle$  [99]

$$\hat{H} = \begin{pmatrix} a_0 & b_1 & 0 & 0 & 0 & 0 & 0 \\ b_1 & a_1 & b_2 & 0 & 0 & 0 & 0 \\ 0 & b_2 & a_2 & b_3 & 0 & 0 & 0 \\ 0 & 0 & b_3 & a_3 & b_4 & 0 & 0 \\ 0 & 0 & 0 & \ddots & \ddots & \ddots & 0 \\ 0 & 0 & 0 & 0 & \ddots & \ddots & b_N \\ 0 & 0 & 0 & 0 & 0 & b_N & a_N \end{pmatrix}. \quad (3.8)$$

### 3.1.2 The density of states

The total density of states  $n(E)$  of the system energy  $E$  is defined by  $n(E)dE$ , the number of energy states between  $E$  and  $E + dE$ . The density of states can

be represented as

$$n(E) = \frac{2}{N_{orbital}} \sum_n \delta(E - E_n) \quad (3.9)$$

where  $N_{orbital}$  is the total number of orbitals, the factor 2 is the spin degeneracy factor and  $E_n$  is the  $n^{th}$  energy state. In equation 3.9  $E_n$  is calculated by using the Schrödinger time independent equation

$$\hat{H} |\psi_n\rangle = E_n |\psi_n\rangle. \quad (3.10)$$

The total density of states can be expressed in terms of the Hamiltonian of the Schrödinger time independent equation [recursion method to avoid calculating the eigenstates]

$$n(E) = \frac{2}{N_{orbital}} Tr[\delta(E - \hat{H})] \quad (3.11)$$

Here, the trace is invariant, now we are able to determine the matrix  $\delta(E - \hat{H})$  in any basis.

The local density of states (LDOS)  $n_i$  on the site  $i$  is the projection of the density of states and can be written as:

$$n_i(E) = \langle i | \delta(E - \hat{H}) | i \rangle \quad (3.12)$$

if the system contains one orbital per site. The total density per site will be the normalized sum of all the local densities:

$$n(E) = \frac{1}{N_{orbital}} \sum_i^{N_{orbital}} n_i(E). \quad (3.13)$$

In our calculations, I projected on the states of random phase to reduce the computing time, see the previous section 3.1.1. The total average density of states of the system can be expressed in terms of the total density of states of the random phase  $\phi_{RP}$ :

$$n(E) = \langle \phi_{RP} | \delta(E - \hat{H}) | \phi_{RP} \rangle. \quad (3.14)$$

The Dirac function can be represented as:

$$\delta(x) = \lim_{\epsilon \rightarrow 0^+} \left( -\frac{Im}{\pi} \frac{1}{x + i\epsilon} \right) \quad (3.15)$$

where  $Im$  is the imaginary part, the density of states  $n_{RP}(E)$  is the local DOS on state  $\psi_0 = \psi_{RP}$ :

$$\begin{aligned} n_{RP}(E) &= \langle \phi_{RP} | \delta(E - \hat{H}) | \phi_{RP} \rangle = \langle \psi_0 | \delta(E - \hat{H}) | \psi_0 \rangle \\ &= -\frac{1}{\pi} \lim_{\epsilon \rightarrow 0^+} Im \left[ \langle \psi_0 | \frac{1}{(E + i\epsilon - \hat{H})} | \psi_0 \rangle \right] \end{aligned} \quad (3.16)$$

For the calculation of LDOS, we have chosen the fractional method. The eigenstates of the system are not determined with this approach. The density of states will be the imaginary part of the Green's function (G) of the system in terms of recursion coefficients  $a_n$  and  $b_n$ , which can be determined by a fractional method [35].  $\langle \psi_0 | \frac{1}{(E+i\epsilon-\hat{H})} | \psi_0 \rangle$  can be written in the form of a fraction:

$$\langle \psi_0 | \frac{1}{(E+i\epsilon-\hat{H})} | \psi_0 \rangle = \frac{1}{(E+i\epsilon-a_1) + \frac{b_1^2}{(E+i\epsilon-a_2) + \frac{b_2^2}{(E+i\epsilon-a_3) + \frac{b_3^2}{(E+i\epsilon-a_4) + \frac{b_4^2}{(E+i\epsilon-a_5) + \dots}}}}} \quad (3.17)$$

which is called the continued fraction. In the density of states calculation, the density is convoluted by the Lorentzian  $\frac{1}{\pi} \frac{\epsilon}{\epsilon^2 + E^2}$  for large  $\epsilon$ , which means that it is independent of the chain being truncated or extended after site  $N_r$ , when  $N_r$  is sufficiently large. We need to define the number of stages of the continuous fraction to which, we must stop the precision of energy computation. In practice we must introduce a termination, typically after  $N_r \approx 1000$  recursion steps.

I changed the configuration of random numbers in the state  $\phi_{RP}$  (equation 3.1) to verify the dependency of the calculation on the construction of  $\phi_{RP}$ . We calculated the total density of states of a graphene monolayer without vacancies considered 3 different initial random phase state configurations:  $\phi_{RP1}$ ,  $\phi_{RP2}$ , and  $\phi_{RP3}$  see Fig. 3.2. The Tight-Binding Hamiltonian adopted from [37]. I observed, the density of states of different initial random phase states have a similar behavior, so single random phase state is sufficient to calculate the density of states.

### 3.1.3 Termination of the continued fraction

The termination (named TERM) of the fraction determined based on the system (with and without bandgap). In case the system is a conductor, we can observe that after certain number of steps the recursion coefficients  $a_n$  and  $b_n$  are almost constant.

$$\langle \psi_0 | \frac{1}{(E+i\epsilon-\hat{H})} | \psi_0 \rangle = \frac{1}{(E+i\epsilon-a_1) + \frac{b_1^2}{(E+i\epsilon-a_2) + \frac{b_2^2}{(E+i\epsilon-a_3) + \frac{b_3^2}{(E+i\epsilon-a_4) + \frac{b_4^2}{(E+i\epsilon-a_5) + \dots \times TERM}}}}} \quad (3.18)$$

For simplification, let  $G_0(z) = \langle \psi_0 | \frac{1}{(z-\hat{H})} | \psi_0 \rangle$  with  $z = E + i\epsilon$ . To define  $G_1(z)$  until  $G_n(z)$

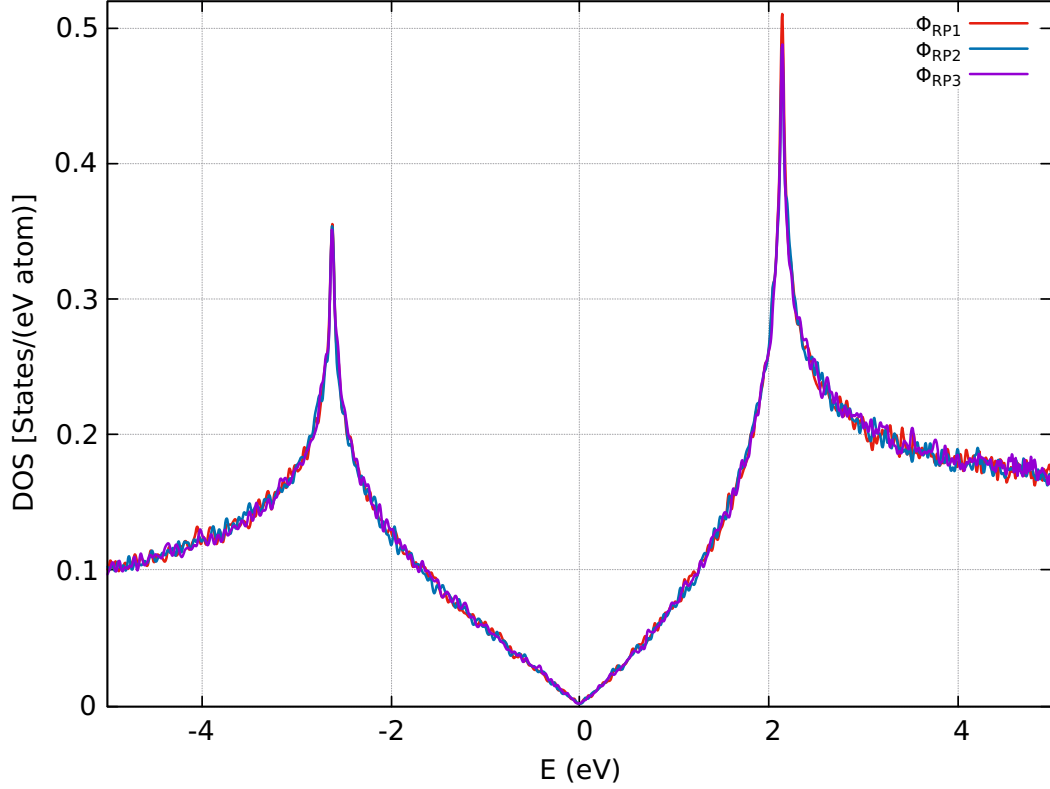


Figure 3.2: Effect of initial random phase states on the total density of states of a graphene monolayer: without vacancies, considered 3 different initial random phase state configurations are  $\phi_{RP1}$ ,  $\phi_{RP2}$ , and  $\phi_{RP3}$ . Number of recursion steps ( $N_r = 1000$ ) and resolution of energy  $\epsilon = 5$  meV. TB model from [37].

$$G_1(z) = \frac{1}{z - a_1 - b_1^2 G_2} \quad (3.19)$$

⋮

$$G_n(z) = \frac{1}{z - a_n - b_n^2 G_{n+1}} \quad (3.20)$$

In practice, we can use  $n$  is a fraction, and  $N_r$  is the number of steps of the recursion ( $a_{n=N_r}$ ,  $b_{n=N_r}$ ,  $G_0(z)$ ) can be written as:

$$G_0(z) = \frac{1}{z - a_1 + \frac{b_1^2}{z - a_2 + \frac{b_2^2}{z - a_3 + \frac{b_3^2}{z - a_4 + \frac{b_4^2}{\dots G_{N+1}(z)}}}}} \quad (3.21)$$

where  $G_{N+1}(z)$  denotes such a termination. As we said the recursion coefficients are constant after the number of recursion steps. We set asymptotic limits [72]  $a_n = a_{n+1} = a_\infty$  and  $b_n = b_{n+1} = b_\infty$ , these limits are related to the bandwidth of spectrum. The bandwidth  $[a_\infty - 2b_\infty, a_\infty + 2b_\infty]$  indicates the spectrum of  $\hat{H}$ . The termination then satisfies

$$G_{N+1}(z) = \frac{1}{z - a_\infty - b_\infty^2 G_{N+2}} = \frac{1}{z - a_\infty - b_\infty^2 G_{N+1}} \quad (3.22)$$

above equation 3.22 is a second degree polynomial,

$$-b_\infty^2 G_{N+1}^2(z) + (z - a_\infty)G_{N+1}(z) - 1 = 0 \quad (3.23)$$

and straightforwardly solved

$$\Delta = (z - a_\infty)^2 - (2b_\infty)^2 \quad (3.24)$$

$$G_{N+1}(z) = \frac{z - a_\infty - i\sqrt{((2b_\infty)^2 - (z - a_\infty)^2)}}{(2b_\infty)^2}. \quad (3.25)$$

The periodic termination of the continuous fraction is good for single band energy systems. For other systems, G. Allan [2] has identified more appropriate terminations that make it possible to evaluate the recursion coefficients  $a_n$  and  $b_n$  of the continuum  $[a_\infty - 2b_\infty, a_\infty + 2b_\infty]$  has prohibited the band. From equation 3.25 the periodic termination of continuous fraction make it possible to determine the recursion coefficients  $a_n$  and  $b_n$  of a graphene monolayer see Fig. 3.3.

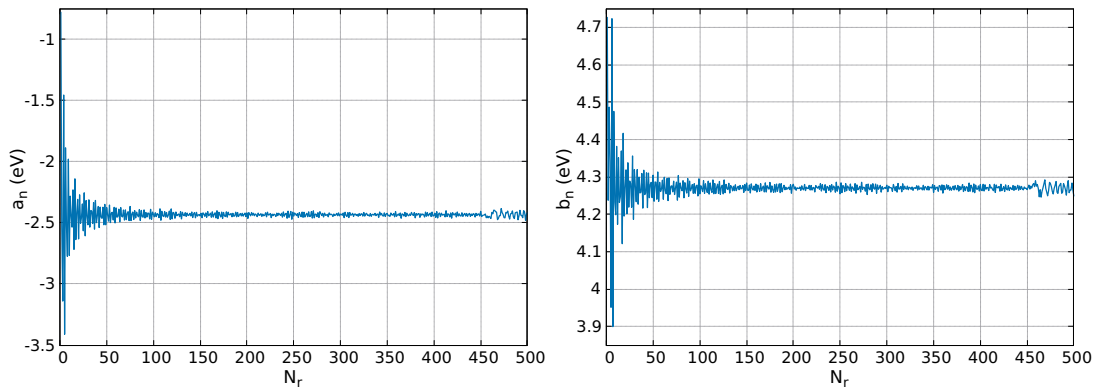


Figure 3.3: Recursion coefficients  $a_n$  and  $b_n$  of a graphene monolayer without vacancies. Number of recursion steps  $N_r = 500$ . TB model from [37].

Figure. 3.3 shows recursion coefficients  $a_n$  and  $b_n$  for the monolayer of a graphene. A closed form of the termination can be introduced after a few hundreds of recursion steps ( $N_r = 100-500$ ), these recursion steps depends on cell size.

I have calculated the total density of states of a graphene monolayer with different number of recursion steps  $N_r = 50$  and  $N_r = 500$  see Fig. 3.4. I observed oscillations which are digital artifacts, the resolution is too ambitious compared

to the size of the system. On the other hand number of recursion steps and energy resolution are very important parameters to calculate the density of states of a graphene monolayer without vacancies results are shown in Fig. 3.4.

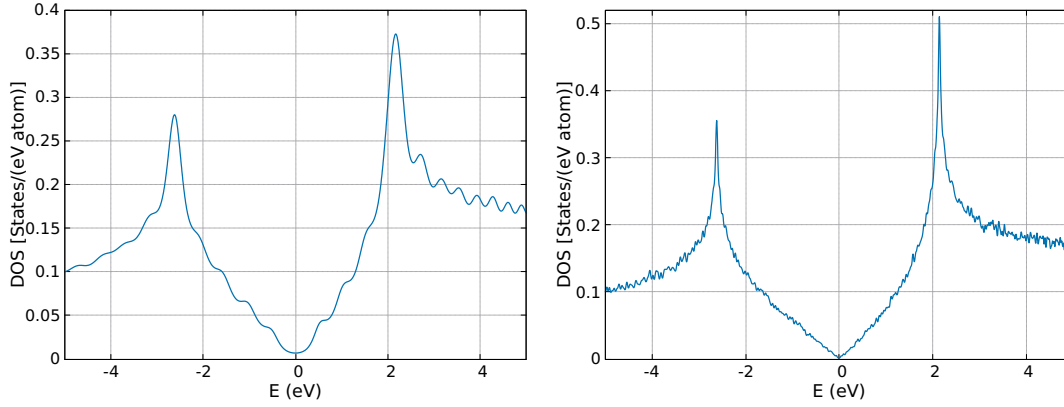


Figure 3.4: Effect of number of recursion steps  $N_r$  on the density of states of a graphene monolayer: without vacancies, number of steps of recursion  $N_r = 50$  [Left],  $N_r = 500$  [Right] and resolution of energy  $\epsilon = 5$  meV. TB model from [37].

## 3.2 Recursion method for computing the wave packet dynamics

This method has been developed 20 years ago by D. Mayou and his coworkers [106, 180–183, 216]. This method has also been used by other groups [106, 181, 182].

### 3.2.1 Kubo-Greenwood method

The wave packet spreading in an arbitrary complex disordered material is computed by the Lanczos method. D. Mayou and his colleagues computationally implemented the Kubo-Greenwood approach (real space and order  $N$ ) [106, 180–183, 216]. The Kubo-Greenwood conductivity written in terms of the diffusivity

$$\sigma(E_F) = e^2 n(E_F) D(E_F) \quad (3.26)$$

where,  $e$  is charge,  $n(E_F)$  is density of states and  $D(E_F)$  is diffusivity at the energy  $E_F$  (it corresponds to the static and  $0K$  conducting). The diffusivity can be calculated by using mean square spread,  $\Delta X^2$ .

$$D(E_F) = \frac{1}{2} \lim_{t \rightarrow \infty} \frac{d}{dt} \Delta X^2(E_F, t). \quad (3.27)$$

One thus has to compute  $\Delta X^2(E, t)$  at every significant energy  $E$  and the time  $t$  is

$$\Delta X^2(E, t) = \langle |\hat{X}(t) - \hat{X}(0)|^2 \rangle_E \quad (3.28)$$

where  $\hat{X}(t)$  the position operator in the Heisenberg representation. In general the average operator of an energy state  $E$  is given by:

$$\langle \hat{A} \rangle_E = \frac{\text{Tr}[\delta(E - \hat{H})\hat{A}]}{\text{Tr}[\delta(E - \hat{H})]}. \quad (3.29)$$

From the definition of average operator equation 3.29, the average square spread  $\Delta X^2(E, t)$  becomes

$$\Delta X^2(E, t) = \frac{\text{Tr}[\delta(E - \hat{H})|\hat{X}(t) - \hat{X}(0)|^2]}{\text{Tr}[\delta(E - \hat{H})]}. \quad (3.30)$$

We rearrange the term  $|\hat{X}(t) - \hat{X}(0)|^2$  in equation 3.30

$$\Delta X^2(E, t) = \frac{\text{Tr}[(\hat{X}(t) - \hat{X}(0))^\dagger \delta(E - \hat{H}) (\hat{X}(t) - \hat{X}(0))]}{\text{Tr}[\delta(E - \hat{H})]} \quad (3.31)$$

and then use several identities and definitions to rewrite  $(\hat{X}(t) - \hat{X}(0))$ :

$$\hat{X}(t) = e^{i\frac{\hat{H}t}{\hbar}} \hat{X}(0) e^{-i\frac{\hat{H}t}{\hbar}} \quad (3.32)$$

$$\hat{U}(t) = e^{-i\frac{\hat{H}t}{\hbar}} \quad (3.33)$$

where,  $\hat{U}(t)$  is the evolution operator,

$$\hat{X}(t) - \hat{X}(0) = \hat{U}^\dagger(t) \hat{X}(0) \hat{U}(t) - \hat{X}(0), \quad (3.34)$$

$$\hat{X}(t) - \hat{X}(0) = \hat{U}^\dagger(t) \hat{X}(0) \hat{U}(t) - \hat{U}^\dagger(t) \hat{U}(t) \hat{X}(0), \quad (3.35)$$

$$\hat{X}(t) - \hat{X}(0) = \hat{U}^\dagger(t) [\hat{X}(0), \hat{U}(t)] \quad (3.36)$$

using  $\hat{U}^\dagger(t) \hat{U}(t) = 1$ , and  $[\hat{X}(0), \hat{U}(t)]$  the commutator, equation 3.36 substituted in equation 3.31 one gets,

$$\Delta X^2(E, t) = \frac{\text{Tr} [[\hat{X}(0), \hat{U}(t)]^\dagger \hat{U}(t) \delta(E - \hat{H}) \hat{U}^\dagger(t) [\hat{X}(0), \hat{U}(t)]]}{\text{Tr}[\delta(E - \hat{H})]}. \quad (3.37)$$

Using the random phase states as initial states, we find

$$\Delta X^2(E, t) = \frac{\langle \phi_{RP} | [\hat{X}(0), \hat{U}(t)]^\dagger \delta(E - \hat{H}) [\hat{X}(0), \hat{U}(t)] | \phi_{RP} \rangle}{\langle \phi_{RP} | \delta(E - \hat{H}) | \phi_{RP} \rangle}. \quad (3.38)$$

For the equation 3.36, we define the states  $|\phi'_{RP}\rangle = [\hat{X}(0), \hat{U}(t)] |\phi_{RP}\rangle$ , and then

$$\Delta X^2(E, t) = \frac{\langle \phi'_{RP} | \delta(E - \hat{H}) | \phi'_{RP} \rangle}{\langle \phi_{RP} | \delta(E - \hat{H}) | \phi_{RP} \rangle}. \quad (3.39)$$

The technique used for the computation of the density of states can thus also be employed for the computation of  $\Delta X^2(E, t)$ , provided that one first evaluates  $|\phi'_{RP}\rangle$ . The evaluation of  $|\phi'_{RP}\rangle$  needs  $\hat{U}(t) |\phi_{RP}\rangle$  together with  $[\hat{X}, \hat{H}]$ .

### 3.2.2 Relation between low frequency conductivity and quantum diffusion

The velocity operator is defined as  $V_x(t) = \frac{dX(t)}{dt}$ , its correlation function  $C(E, t)$  is defined as

$$C(E, t) = \langle V_x(t)V_x(0) + V_x(0)V_x(t) \rangle_E = 2\text{Re}\langle V_x(t)V_x(0) \rangle_E \quad (3.40)$$

where  $\text{Re}A$  is the real part of  $A$  and it is related to quantum diffusion [132] through

$$\frac{d}{dt}\Delta X^2(E, t) = \int_0^t C(E, t') dt'. \quad (3.41)$$

The real part of the low frequency conductivity is then related to quantum diffusion. Indeed from the Kubo-Greenwood formula the real part of the conductivity is given by

$$\text{Re}\sigma(\omega) = \int_{\mu-\hbar\omega}^{\mu} \frac{dE}{\hbar\omega} F(E, \omega) \quad (3.42)$$

where  $\mu$  is the chemical potential. In equation 3.42 the Fermi-Dirac distribution function is taken equal to its zero temperature value. This is valid provided that the electronic properties vary smoothly on the thermal energy scale  $kT$ . For finite temperature, it has been shown [37] that the conductivity of a graphene depends mainly on the temperature through the diffusivity but not through the Fermi-Dirac distribution function. Therefore in the following, the Fermi-Dirac distribution function is taken equal to its zero temperature value<sup>1</sup>. But the effect of defects and temperature (scattering by phonons) on the diffusivity is taken into account via the relaxation time approximation. The central quantity  $F(E, \omega)$  is given by

$$F(E, \omega) = \frac{2\pi\hbar e^2}{\Omega} \text{Tr} \langle \delta(E - H) V_x \delta(E + \hbar\omega - H) V_x \rangle \quad (3.43)$$

where  $\Omega$  is the volume of the system. Expressing the operator  $\delta(E - H)$  as the Fourier transform of the evolution operator  $e^{-iHt}$  shows that

<sup>1</sup>A non-zero  $T$  Fermi-Dirac distribution function will be introduced to calculate the thermodynamic average conductivity and the mobility in semiconductor TMDs (chapter-4)

$$\frac{2F(E, \omega)}{e^2 n(E)} = \int_{-\infty}^{\infty} dt e^{i\omega t} \langle V_x(t) V_x(0) \rangle_E \quad (3.44)$$

and

$$\frac{2F(E - \hbar\omega, \omega)}{e^2 n(E)} = \int_{-\infty}^{\infty} dt e^{i\omega t} \langle V_x(0) V_x(t) \rangle_E \quad (3.45)$$

where  $n(E)$  is the density of states per unit volume (summed over up and down spins which are assumed to have the same transport properties here). Then one finds

$$2\text{Re}\tilde{\sigma}(E, \omega) = F(E, \omega) + F(E - \hbar\omega, \omega) \quad (3.46)$$

where

$$\tilde{\sigma}(E, \omega) = e^2 \frac{n(E)}{2} \int_0^{\infty} e^{i\omega t} C(E, t) dt \quad (3.47)$$

Let us note that the function  $\tilde{\sigma}(E, \omega)$  is analytical in the upper half of the complex plane. For large  $\omega \Rightarrow \tilde{\sigma}(E, \omega) \propto \frac{1}{\omega}$  and the Kramers-Kronig relations are valid. Finally, the usual sum rule is valid

$$\int_0^{\infty} \tilde{\sigma}(E, \omega) d\omega = \frac{\pi e^2 n(E)}{2} C(E, t=0) = \frac{\pi e^2 n}{2m^*} \quad (3.48)$$

where  $m^*$  is the effective mass.

If the variation of  $F(E, \omega)$  with energy is small in the interval  $[E_F - \hbar\omega, E_F + \hbar\omega]$ , one deduces from the previous equations that

$$\text{Re}\sigma(\omega) \approx e^2 \frac{n(E_F)}{2} \text{Re} \int_0^{\infty} e^{i\omega t} C(E_F, t) dt \quad (3.49)$$

equation 3.49 is valid at sufficiently small values of  $\omega$ . In particular at zero frequency the conductivity is given by the Einstein relation

$$\sigma(0) = e^2 n(E_F) D(E_F) \quad (3.50)$$

with

$$D(E_F) = \lim_{t \rightarrow \infty} \frac{1}{2} \frac{d}{dt} \Delta X^2(E_F, t). \quad (3.51)$$

### 3.2.3 Relaxation time approximation (RTA)

Within the relaxation time approximation one assumes that the response currents respectively with disorder  $j(t)$  and without impurities  $j_0(t)$  are related through [133]

$$j(t) = j_0(t) e^{-\frac{|t|}{\tau}} \quad (3.52)$$

where  $\tau$  is the relaxation time. So the relaxation time approximation (RTA) allows to treat the effect of disorder on quantum diffusion and conductivity. We give the relations satisfied by conductivity and quantum diffusion in this approximation. The complex conductivity is  $\sigma(\omega) = \int_0^\infty e^{i\omega t} j(t) dt$  [since:  $j(t) = \frac{J(t)}{E}$ ], and within the RTA, the conductivity with disorder  $\sigma(\omega, t)$  and without disorder  $\sigma_0(z)$  are related by

$$\sigma(\omega, t) = \sigma_0\left(\omega + \frac{i}{\tau}\right) \quad (3.53)$$

The real part of conductivity with defects  $Re\sigma(\omega, \tau)$  and without defects  $Re\sigma_0(\omega)$  are related simply. Using complex conductivity to get [133]

$$Re\sigma(\omega, t) = \frac{1}{\pi\tau} \int_{-\infty}^{+\infty} \frac{Re\sigma_0(\omega')}{(\omega - \omega')^2 + \frac{1}{\tau^2}} d\omega' \quad (3.54)$$

which allows to compute the real part of the conductivity with defects.

The RTA defined from the point of view of quantum diffusion. In all cases, consider that the influence of disorder is much stronger on the quantum diffusion than on the density of states. Now neglect the variation of  $n(E)$  with disorder. From  $j(t) \approx e^{2\frac{n(E_F)}{2}} C(E_F, t)$  one deduces that, for not too large disorder that is for sufficiently large relaxation time  $\tau$  the RTA is equivalent to

$$C(E, t) = C_0(E, t) e^{-\frac{|t|}{\tau}} \quad (3.55)$$

where  $C(E, t)$  and  $C_0(E, t)$  are respectively the velocity correlation functions with and without disorder. After equation 3.41 one deduces that the long time propagation is diffusive with a diffusion coefficient defined as

$$D(E) = \frac{1}{2} \int_0^{+\infty} C_0(E, t) e^{-\frac{|t|}{\tau}} dt \quad (3.56)$$

which is equivalent to

$$D(E) = \frac{1}{2} \frac{d}{dt} \Delta X^2(E, t) \quad \{\text{if } t \gg \tau\}. \quad (3.57)$$

At zero frequency the diffusivity can be written in the useful form [37]

$$D(E_F, \tau) = \frac{L^2(E_F, \tau)}{2\tau}. \quad (3.58)$$

Using the  $t = 0$  conditions  $\Delta X^2(E, t = 0) = 0$  and  $\frac{d}{dt} \Delta X^2(E, t = 0) = 0$  and performing integration by parts and we get

$$L^2(E_F, \tau) = \frac{\int_0^{+\infty} \Delta X_0^2(E_F, t) e^{-\frac{t}{\tau}} dt}{\int_0^{+\infty} e^{-\frac{t}{\tau}} dt} \simeq \langle \Delta X^2(E_F, t) \rangle_\tau \quad (3.59)$$

where  $L$  is scattering length,  $\langle \dots \rangle_\tau$  is a time average on a time scale  $\tau$ .  $\Delta X(E_F, t)$  is the spreading of states of energy  $E$ , in the perfect system i.e. without disorder.

More generally at low frequency, using equation 3.50 one can define a frequency dependent diffusivity  $D(E_F, \omega)$  such that

$$Re\sigma(\omega) \approx e^2 n(E_F) D(E_F, \omega) \quad (3.60)$$

and

$$D(E_F, \omega) = \frac{1}{2} \int_0^\infty e^{i\omega t} C(E_F, t) dt. \quad (3.61)$$

Within the RTA the above equation 3.61 becomes

$$D(E_F, \omega) = \frac{1}{2} Re \int_0^{+\infty} e^{(i\omega - \frac{1}{\tau})t} C_0(E, t) dt \quad (3.62)$$

It can be convenient to use the equivalent from which expresses the frequency dependent diffusivity  $D(E_F, \omega)$  in terms of the quantum diffusion without disorder  $\Delta X_0^2(E, t)$  [37]:

$$D(E_F, \omega) = \frac{1}{2} Re \left[ \left( \frac{1}{2} - i\omega \right)^2 \int_0^{+\infty} e^{(i\omega - \frac{1}{\tau})t} \Delta X_0^2(E, t) dt \right] \quad (3.63)$$

### 3.3 Chebyshev polynomials

Now, we focus on the calculation of  $\hat{U}(t) |\phi_{RP}\rangle = |\phi_{RP}(t)\rangle$ . The time evolution of the random phase wave packet is followed through use of the evolution operator  $\hat{U}(t)$ , which can be efficiently approximated using a basis of orthogonal polynomials, with the Chebyshev polynomials as the most computationally efficient [130]. For a given time step ( $T$ ) we can write such a decomposition as

$$\hat{U}(T) = e^{-i\frac{\hat{H}T}{\hbar}} = \sum_{n=0}^{\infty} c_n(T) Q_n(\hat{H}) \quad (3.64)$$

where  $Q_n$  is a Chebyshev polynomial of order  $n$ . The Chebyshev polynomials ( $T_n$ ) usually act on the interval  $[-1:1]$ , whereas the Hamiltonians considered here have larger bandwidths  $[-1:1]$  so some rescaling to the all spectrum of the polynomials needs to be performed to use their recurrent properties. While for the rescaled Chebyshev polynomials ( $\forall E \in [a - 2b : a + 2b]$ ) we get

$$Q_0(E) = 1 \quad \{\text{if } n = 0\} \quad (3.65)$$

$$Q_1(E) = \sqrt{2} \frac{\hat{H} - a}{2b} \quad \{\text{if } n = 1\} \quad (3.66)$$

$$Q_2(E) = 2\sqrt{2} \left( \frac{\hat{H} - a}{2b} \right)^2 - \sqrt{2} \quad \{\text{if } n = 2\} \quad (3.67)$$

$$Q_n(E) = \sqrt{2}T_n\left(\frac{\hat{H} - a}{2b}\right) \quad (\forall n \geq 1) \quad (3.68)$$

with the recurrence relation  $n \geq 2$ ,

$$Q_{n+1}(E) = 2\left(\frac{\hat{H} - a}{2b}\right)Q_n(E) - Q_{n-1}(E) \quad (3.69)$$

Equation 3.69 represents the recurrence relation of Chebyshev polynomials  $Q_n(E)$ , once the  $Q_n(E)$  polynomials are well defined, one needs to compute the related  $c_n(T)$  coefficients.

### 3.3.1 Spectral coefficient $C_n(\mathbf{T})$

Let us consider a normalized state  $|\psi_0\rangle$ , and then construct a generalized (different) states [141]:

$$|\psi_i\rangle = Q_i(E) |\psi_0\rangle \quad (3.70)$$

ortho-normalized basis states is  $\langle\psi_i|\psi_j\rangle = \delta_{ij}$ , since the polynomials  $Q_i$  are orthogonal. Multiply  $|\psi_0\rangle$  both sides of the equation 3.64 we get

$$\hat{U}(T) |\psi_0\rangle = \sum_i c_i(T) Q_i(E) |\psi_0\rangle = \sum_i c_i(T) \cdot |\psi_i\rangle \quad (3.71)$$

The coefficients  $c_i$  are determined as follows

$$c_i(T) = \langle\psi_i|\hat{U}(T)|\psi_0\rangle \quad (3.72)$$

To calculate  $\hat{U}(T) |\psi_0\rangle$  in the basis of  $|\psi_i\rangle$  write  $\hat{H}$  in the basis of  $|\psi_i\rangle$ : for  $i \geq 1$

$$Q_{i+1}(E) |\psi_0\rangle = \left(\frac{\hat{H} - a}{b}\right) Q_i(E) |\psi_0\rangle - Q_{i-1}(E) |\psi_0\rangle \quad (3.73)$$

$$|\psi_{i+1}\rangle = \left(\frac{\hat{H} - a}{b}\right) |\psi_i\rangle - |\psi_{i-1}\rangle \quad (3.74)$$

Multiply  $\langle\psi_i|$  ( $\forall i$ ) and  $\langle\psi_{i+1}|$  ( $\forall i + 1$ ) in equation 3.74

$$\begin{aligned} 0 &= \langle\psi_i|\hat{H}|\psi_i\rangle - a \langle\psi_i|\psi_i\rangle \\ a &= \langle\psi_i|\hat{H}|\psi_i\rangle \end{aligned} \quad (3.75)$$

and

$$\begin{aligned} 0 &= \langle\psi_{i+1}|\hat{H}|\psi_i\rangle - b \langle\psi_{i+1}|\psi_{i+1}\rangle \\ b &= \langle\psi_{i+1}|\hat{H}|\psi_i\rangle \end{aligned} \quad (3.76)$$

For  $i = 0$ ,



$$[\hat{X}, Q_{n+1}(\hat{H})] = \left( \frac{\hat{H} - a}{b} \right) [\hat{X}, Q_n(\hat{H})] + \left[ \hat{X}, \frac{\hat{H} - a}{b} \right] Q_n(\hat{H}) - [\hat{X}, Q_{n-1}(\hat{H})] \quad (3.83)$$

The evolution of the random phase state as a function of time is also determined by the evolution operator

$$|\phi_{RP}(T)\rangle = \hat{U}(T) |\phi_{RP}\rangle \quad (3.84)$$

A similar development of the Chebyshev polynomial yields

$$|\phi_{RP}(T)\rangle = \sum_{n=0}^N c_n(T) Q_n(E) |\phi_{RP}\rangle = \sum_{n=0}^N c_n(T) |\alpha_n\rangle \quad (3.85)$$

with  $|\alpha_n\rangle = Q_n(E) |\phi_{RP}\rangle$ . The state  $|\alpha_n\rangle$  satisfies to the recurrence relations;

$$|\alpha_0\rangle = |\phi_{RP}\rangle \quad (3.86)$$

$$|\alpha_1\rangle = \left( \frac{\hat{H} - a}{\sqrt{2}b} \right) |\alpha_0\rangle \quad (3.87)$$

$$|\alpha_2\rangle = \left( \frac{\hat{H} - a}{b} \right) |\alpha_1\rangle - \sqrt{2} |\alpha_0\rangle \quad (3.88)$$

For  $n \geq 2$  in the recurrence relation

$$|\alpha_{n+1}\rangle = \left( \frac{\hat{H} - a}{b} \right) |\alpha_n\rangle - |\alpha_{n-1}\rangle \quad (3.89)$$

The definition of  $|\alpha_n\rangle$  in equation 3.85 and  $|\beta_n\rangle$  in equation 3.81 multiply  $|\phi_{RP}\rangle$  then;

$$|\beta_{n+1}\rangle = \left( \frac{\hat{H} - a}{b} \right) |\beta_n\rangle - |\beta_{n-1}\rangle + \left[ \hat{X}, \frac{\hat{H} - a}{b} \right] |\alpha_n\rangle \quad (3.90)$$

Simplify the commutator in equation 3.90

$$\left[ \hat{X}, \frac{\hat{H} - a}{b} \right] = \frac{1}{b} [\hat{X}, (\hat{H} - a)] = \frac{1}{b} \left[ [\hat{X}, \hat{H}] - [\hat{X}, -a] \right] = \frac{1}{b} \left[ [\hat{X}, \hat{H}] - 0 \right] = \frac{1}{b} [\hat{X}, \hat{H}] \quad (3.91)$$

Substitute equation 3.91 in equation 3.90

$$|\beta_{n+1}\rangle = \left( \frac{\hat{H} - a}{b} \right) |\beta_n\rangle - |\beta_{n-1}\rangle + \frac{1}{b} [\hat{X}, \hat{H}] |\alpha_n\rangle \quad (3.92)$$

Equation 3.92 states that the calculation of  $|\beta_{n+1}\rangle$  requires a  $|\alpha_n\rangle$  and the commutator  $[\hat{X}, \hat{H}]$ . In the algorithm recurrence coefficients  $|\alpha_n\rangle$  and  $|\beta_n\rangle$  are parallel calculations

$$\hat{U}(T) |\phi_{RP}\rangle = \sum_{n=0}^{N_{Tc}} c_n(T) |\alpha_n\rangle \quad (3.93)$$

$$[\hat{X}, \hat{U}(T)] |\phi_{RP}\rangle = \sum_{n=0}^{N_{Tc}} c_n(T) |\beta_n\rangle \quad (3.94)$$

where  $N_{Tc}$  is the maximum order of the Chebyshev polynomial. For the calculations of conductivity, and microscopic conductivity, we follow different time steps ( $\phi(0), \phi(1T), \phi(2T), \dots, \phi(mT)$ ) to reach the maximum conductivity.

### 3.3.3 Numerical implementation of RTA

The relaxation time approximation (RTA) is a way to introduce the effects of inelastic collisions. The advantage of this approximation is simplicity in numerical implementation. It allows to study in a simple way the inelastic phenomenon (Integral calculation). Inelastic mean free path which defined by (from equation 3.59)

$$L_i^2(E_F, \tau_i) = \frac{\int_0^{+\infty} \Delta X_0^2(E_F, t) e^{-\frac{t}{\tau_i}} dt}{\int_0^{+\infty} e^{-\frac{t}{\tau_i}} dt} \quad (3.95)$$

where  $\Delta X_0^2(E_F, t)$  is the quadratic spread of the perfect system (without defects) in the energy eigenstate  $E$ . Equation 3.95 is a well known auto correlation function of the speed  $C(E, t)$  and that includes two integrals. The first integral is  $\int_0^{+\infty} e^{-\frac{t}{\tau_i}} dt$  only  $\tau_i$ . The second integral upper limit infinity. For the great values of time  $t$ , now we interpolate the quantity  $\Delta X_0^2(E_F, t)$  from  $at + b$ .

$$\int_0^{+\infty} \Delta X_0^2(E_F, t) e^{-\frac{t}{\tau_i}} dt = \int_0^{t_{max}} \Delta X_0^2(E_F, t) e^{-\frac{t}{\tau_i}} dt + \int_{t_{max}}^{+\infty} (at + b) e^{-\frac{t}{\tau_i}} dt \quad (3.96)$$

with  $t_{max}$  the last calculated time.

This method has been developed by D. Mayou and his coworkers [106, 180–183, 216]. We adapted this code to 2D material systems, for work flow see in Fig. 3.5.

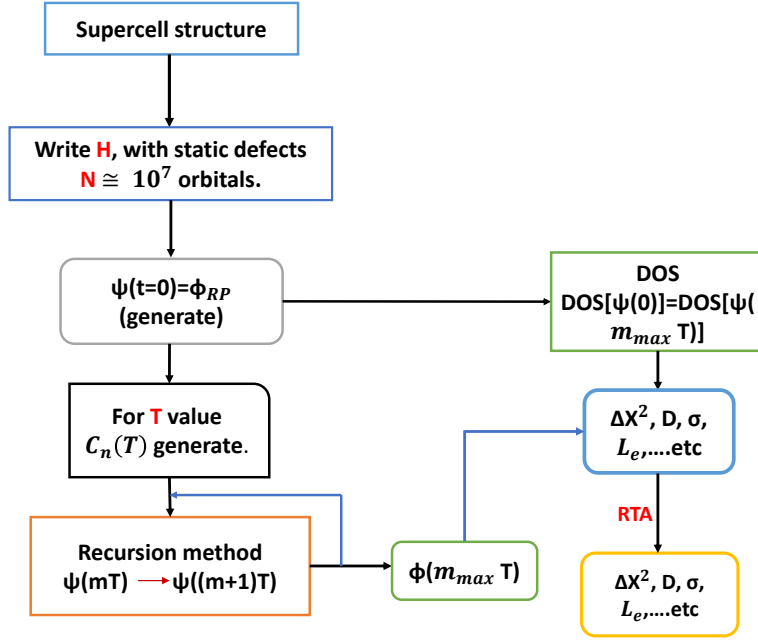


Figure 3.5: Flow chart for Recursion method. This method has been developed by D. Mayou and his coworkers [106, 180–183, 216].

### 3.4 Conclusion

In this chapter we have presented a numerical method to study the electronic transport properties based on the Kubo-Greenwood formalism. We explained the relation between the Kubo-Greenwood conductivity and the mean square spread  $\Delta X^2$  (quantum diffusion); this analytical development allows us to simplify the expression of  $\Delta X^2$ . The recurrence relations deduced from a development on the Chebyshev polynomials of the evolution operator. The recursion method used to calculate the density of states. We have determined the diffusion quantity  $\Delta X^2$  as a function of time and energy, these quantities that allow us the phenomenon of electronic transport. This numerical method allows an efficient processing of the quantum transport due to defects. The defects that act as a static disorder (elastic scattering) are directly introduced into the Hamiltonian, while inelastic scattering (electron-phonon collision, and an external magnetic field) can be treated by introducing an inelastic scattering with relaxation time approximation.

## Chapter No. 4

---

### *Transport properties of different TMDs*

---

	<b>Page</b>
4.1 Atomic structure . . . . .	61
4.2 Electronic band calculation . . . . .	62
4.2.1 DFT-Electronic band structure . . . . .	63
4.2.1.1 Without spin orbit coupling (SOC) . . . . .	63
4.2.1.2 With spin orbit coupling (SOC) . . . . .	63
4.2.2 Tight-Binding model description for Transition Metal Dichalco- genides . . . . .	65
4.2.3 Electronic band structure of Wannier orbitals from DFT . . . . .	68
4.3 Local density of states (LDOS) . . . . .	69
4.4 Density of states with defects . . . . .	69
4.5 Transport properties . . . . .	73
4.5.1 Conductivity & Inelastic mean free path . . . . .	73
4.5.2 Microscopic conductivity . . . . .	76
4.5.3 Thermodynamic average conductivity at room temperature . . . . .	78
4.6 Conclusion . . . . .	83

---

2D materials are attracting a lot of interest as possible candidates for replacing traditional semiconductors (Si, Ge, etc.) in the next generation of nano-electronic devices. These materials may provide a variety of benefits, including excellent electronic properties such as very high mobility [14, 80]. The most known and widely studied 2D material, graphene, has no bandgap in its electronic structure. This characteristic electron property limits its application in integrated circuits. But 2D TMD materials (group-VIB Transition Metal Dichalcogenides  $\text{MX}_2$  ( $M = \text{Mo}, \text{W}$ ;  $X = \text{S}, \text{Se}, \text{Te}$ )) have an intrinsic bandgap, and thus an attractive possibility for the electronic, optoelectronic applications and use as conductive channel in field effect transistors [112, 175]. An important limitation of transport properties are static defects that are often found in the structure [41, 108, 121]. It is thus essential to understand more correctly the effect of those types of defects on transport properties.

Atomically thin  $\text{MX}_2$  semiconductors ( $M = \text{Mo}, \text{W}$  and  $X = \text{S}, \text{Se}, \text{Te}$ ) form a sandwich structure with a honeycomb lattice [233], where one atomic layer of transition metal atoms ( $M$ ) is sandwiched between two atomic layers of chalcogens ( $X$ ) is shown in Fig. 4.1-(a). These semiconductors exhibit a strong SOC in their valence bands, which increases with increasing mass of the  $M$  atoms.  $\text{MoS}_2$  and  $\text{WSe}_2$  are widely studied TMDs with a tunable bandgap in the visible and infrared (IR) regions of the electromagnetic spectrum as the number of atomic layers in the crystal changes. Bulk  $\text{MoS}_2$  exhibits an indirect bandgap  $\approx 1.2$  eV and bulk  $\text{WSe}_2$  exhibits an indirect bandgap  $\approx 0.7$  eV which increases with decreasing number of layers [10, 57, 84, 226]. A monolayer of  $\text{MoS}_2$  and  $\text{WSe}_2$  shows a direct bandgap with an energy gap  $\approx 1.7$  to 1.9 eV and  $\approx 1.5$  to 1.7 eV, respectively, at the highest symmetry point  $K$  of the hexagonal Brillouin zone shown in Fig. 4.1-(b). Because of broken inversion symmetry, SOC effects lifts the spin degeneracy of bands and substantially split the highest valence bands at the  $K$  symmetry point [40].

On the theoretical level, one of the reasons for the strong popularity of graphene is the availability of a paradigmatic Hamiltonian model for the single layer in terms of a few tight-binding (TB) parameters [177, 224] (actually only one, the nearest neighbors carbon-carbon hopping  $\gamma_0$ , in the simplest case [151]). The well known Dirac equation can thus be derived from that as a low-energy expansion. Crucial to the development of the theoretical analysis in graphene is also the fact that model Hamiltonians for multi-layer graphene can be built using the single layer TB description as a fundamental block and just adding additional interlayer hopping terms [134, 158, 166, 219]. Different stacking orders can also be easily investigated. Tight-binding approaches can be also more con-

venient than first-principles methods such as density functional theory (DFT) for investigating systems involving a very large number of atoms [199], and have been thoroughly applied to large scale graphene related problems, but they are still computationally challenging and demanding. Therefore, TB has been the method of choice for the study of disordered and inhomogeneous systems [24, 161, 170, 178, 239], materials nanostructured in large scales or in twisted multi-layer materials [11, 117, 137, 143, 202, 205, 213].

In this chapter, after obtaining our own DFT-based TB model, we study the effect of point defects (see discussion) on electronic structure and quantum transport properties of several transition metal dichalcogenides ( $\text{MX}_2$ ). Imperfections can strongly modify the optical and transport properties of these materials. We analyzed the effect of point defects on the inelastic mean free path scattering length and microscopic conductivity of single layers of TMDs ( $\text{MX}_2$ , where  $\text{M} = \text{Mo}$  or  $\text{W}$  and  $\text{X} = \text{S}$ ,  $\text{Se}$ ,  $\text{Te}$ ). We use the Kubo-Greenwood formula for the calculation of conductivity with different distributions of disorder as explained in chapter-3.

## 4.1 Atomic structure

The crystal structure of  $\text{MX}_2$  is shown in Fig. 4.1(a). A single layer is composed by an inner layer of metal  $\text{M}$  atoms ordered on a triangular lattice, which is sandwiched between two layers of chalcogen  $\text{X}$  atoms placed on the triangular lattice of alternating empty sites. The lattice constant  $a$  represents the distance between nearest neighbor in-plane  $\text{M}$ - $\text{M}$  and  $\text{X}$ - $\text{X}$  atoms. The in-plane Brillouin zone is a hexagon is shown in Fig. 4.1(b). It contains the high-symmetry points  $\Gamma$ ,  $K$  and  $M$ .

The two Bravais primitive lattice vectors are:

$$\vec{\mathbf{a}}_1 = (a, 0, 0), \quad \vec{\mathbf{a}}_2 = \left( \frac{a}{2}, \frac{\sqrt{3}}{2}a, 0 \right). \quad (4.1)$$

The reciprocal lattice vectors are

$$\vec{\mathbf{b}}_1 = \frac{4\pi}{\sqrt{3}a} \left( \frac{\sqrt{3}}{2}, -\frac{1}{2}, 0 \right), \quad \vec{\mathbf{b}}_2 = \frac{4\pi}{\sqrt{3}a} (0, 1, 0). \quad (4.2)$$

The distance between the two  $\text{X}$  layers is  $d \cos \theta_b = \frac{a}{\sqrt{3}}$ , where  $\theta_b \approx 40.6^\circ$  is the angle between the  $\text{M}_o$ - $\text{S}$  bond and the  $\text{M}_o$  plane and  $d$  is the distance between neighboring  $\text{Mo}$  and  $\text{S}$  atoms for  $\text{MoS}_2$  see [179]. The nearest-neighbor vectors, connecting  $\text{M}$  and  $\text{X}$  atoms are given by

$$\vec{\delta}_{\pm 1} = d(0, \cos \theta_b, \pm \sin \theta_b) \quad (4.3)$$

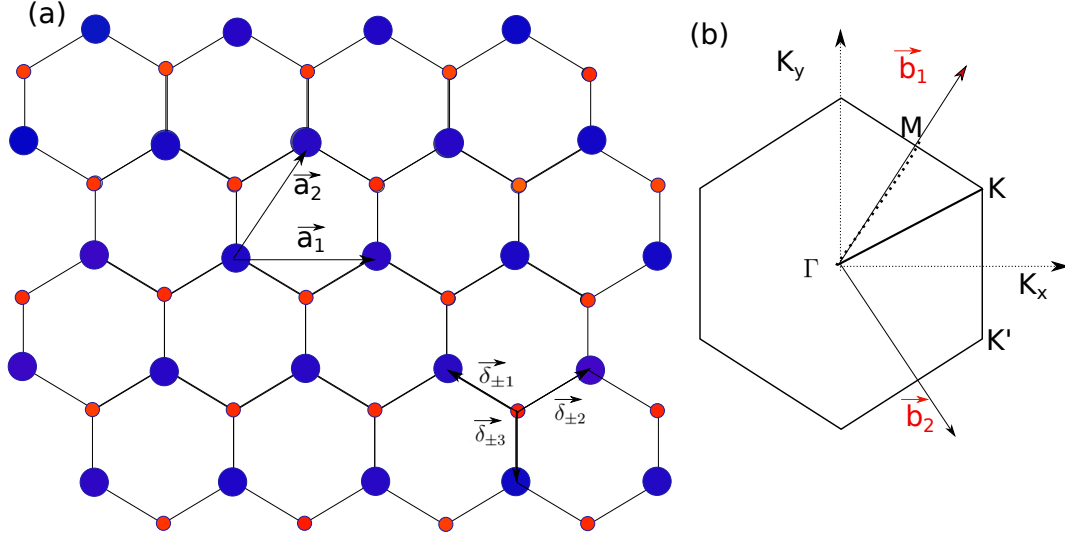


Figure 4.1: Sketch of the atomic structure of  $\text{MX}_2$ : (a) Top view of monolayer of  $\text{MX}_2$ . **Blue (red)** circles indicates M (X) atoms.  $\vec{\delta}_i$  (where  $i=\pm 1, 2, 3$ ) indicates the nearest neighbor vectors and  $\vec{a}_i$  ( $i=1, 2$ ) indicates the next nearest neighbor vectors. (b) Brillouin zone for the  $\text{MX}_2$  lattice, where  $\vec{b}_1$  and  $\vec{b}_2$  are the reciprocal lattice basis vectors, and  $\Gamma$ ,  $M$  and  $K$  are the highest symmetry points.

$$\vec{\delta}_{\pm 2} = d \left( -\frac{\sqrt{3}}{2} \cos \theta_b, -\frac{1}{2} \cos \theta_b, \pm \sin \theta_b \right) \quad (4.4)$$

$$\vec{\delta}_{\pm 3} = d \left( \frac{\sqrt{3}}{2} \cos \theta_b, -\frac{1}{2} \cos \theta_b, \pm \sin \theta_b \right) \quad (4.5)$$

The  $\text{MX}_2$  Brillouin zone is hexagonal. The highest symmetry points and symmetry lines are indicated see Fig. 4.1(b), namely  $\Gamma$ ,  $M$  and  $K$  [ $M = \frac{1}{3}(2\vec{b}_1 - \vec{b}_2)$ ,  $K = \frac{1}{2}(\vec{b}_1)$ ].

$$\Gamma = (0, 0, 0), M = \frac{2\pi}{3a} \left( \frac{3}{2}, -\frac{\sqrt{3}}{2}, 0 \right), K = \frac{2\pi}{3a} \left( 1, -\sqrt{3}, 0 \right). \quad (4.6)$$

## 4.2 Electronic band calculation

It is well known that first principle computations may not give the correct bandgap when compared to the experimental outcome. Since we do not have sufficient experimental data to match the Slater-Koster parameters in the tight-binding model, we used a DFT electronic band structure as a reference.

### 4.2.1 DFT-Electronic band structure

In the construction of a reliable TB model for semiconducting dichalcogenides, we are guided by first-principles DFT calculations that will provide the reference on which to calibrate the TB model. The first principle calculations of  $\text{MX}_2$  ( $\text{M} = \text{Mo}, \text{W}$  and  $\text{X} = \text{S}, \text{Se}, \text{Te}$ ) monolayer are carried out using density functional theory as implemented in the ABINIT software package [60]. A plane wave cutoff of 544 eV (20 Hartree) and the generalized gradient approximation of Perdew, Burke, and Ernzerhof (PBE) [168] to the exchange correlation functional are used. Integrals in reciprocal space are calculated using a Gamma-centered  $18 \times 18 \times 1$  k-mesh. Along the  $c$ -axis, a vacuum region greater than  $12.72 \text{ \AA}$  ( $\approx 20 \text{ \AA}$ ) has been maintained to avoid spurious interactions between the images [109]. All structures are relaxed until the forces on the atoms have decreased to  $0.01 \text{ eV/\AA}$ . For the hexagonal unit cell, the lattice constants of optimized  $\text{MoS}_2$ ,  $\text{MoSe}_2$ ,  $\text{MoTe}_2$ ,  $\text{WSe}_2$ , and  $\text{WTe}_2$  are  $3.18 \text{ \AA}$ ,  $3.30 \text{ \AA}$ ,  $3.52 \text{ \AA}$ ,  $3.30 \text{ \AA}$ , and  $3.60 \text{ \AA}$  respectively. The bond lengths and bandgaps are summarized in Table 4.1, cell values which are consistent with the measured value as reported in experimental results [13].

#### 4.2.1.1 Without spin orbit coupling (SOC)

Single layer TMDs are direct bandgap semiconductors, with the gap located at  $K$  point of the Brillouin zone. The main orbital character at near the bandgap region of the valence band is due to a combination of the  $d_{x^2-y^2}$  and  $d_{xy}$  orbitals of the metal M, which hybridize with  $p_x$  and  $p_y$  orbitals of the chalcogen X. On the other hand, near the bandgap region of the conduction band is formed by the  $d_{3z^2-r^2}$  orbital of M, plus some contribution of  $p_x$  and  $p_y$  orbitals of the chalcogen X. The  $\Gamma$ -point lies close to the top of the valence band (VB), the energy difference between  $\Gamma$  and  $K$  is very small at VB ( $\approx 46.4 \text{ meV}$ ,  $106 \text{ meV}$ ,  $410 \text{ meV}$ ,  $268 \text{ meV}$ , and  $423 \text{ meV}$  for  $\text{MoS}_2$ ,  $\text{MoSe}_2$ ,  $\text{MoTe}_2$ ,  $\text{WSe}_2$ , and  $\text{WTe}_2$ , respectively) as shown in Fig. 4.2. Our DFT band structures are in good agreement with previous works [110, 186]. Hence, hole-doped samples of  $\Gamma$  and  $K$  symmetry points will contribute to the electronic transport [95]. The direct bandgap is located at  $K$ -point. The  $M$ -point signaling a local minimum in the conduction band (CB) along the circuit  $\Gamma$  and  $K$ , received a lot of attention due to relevance for transport properties [138, 147], since energy minimum at  $M$  close to the bottom of the CB is shown in Fig. 4.2.

#### 4.2.1.2 With spin orbit coupling (SOC)

Another important feature of TMDs is the SOC; the atoms are heavy and the outermost electronic states are from  $d$ -orbitals that have a strong spin orbit

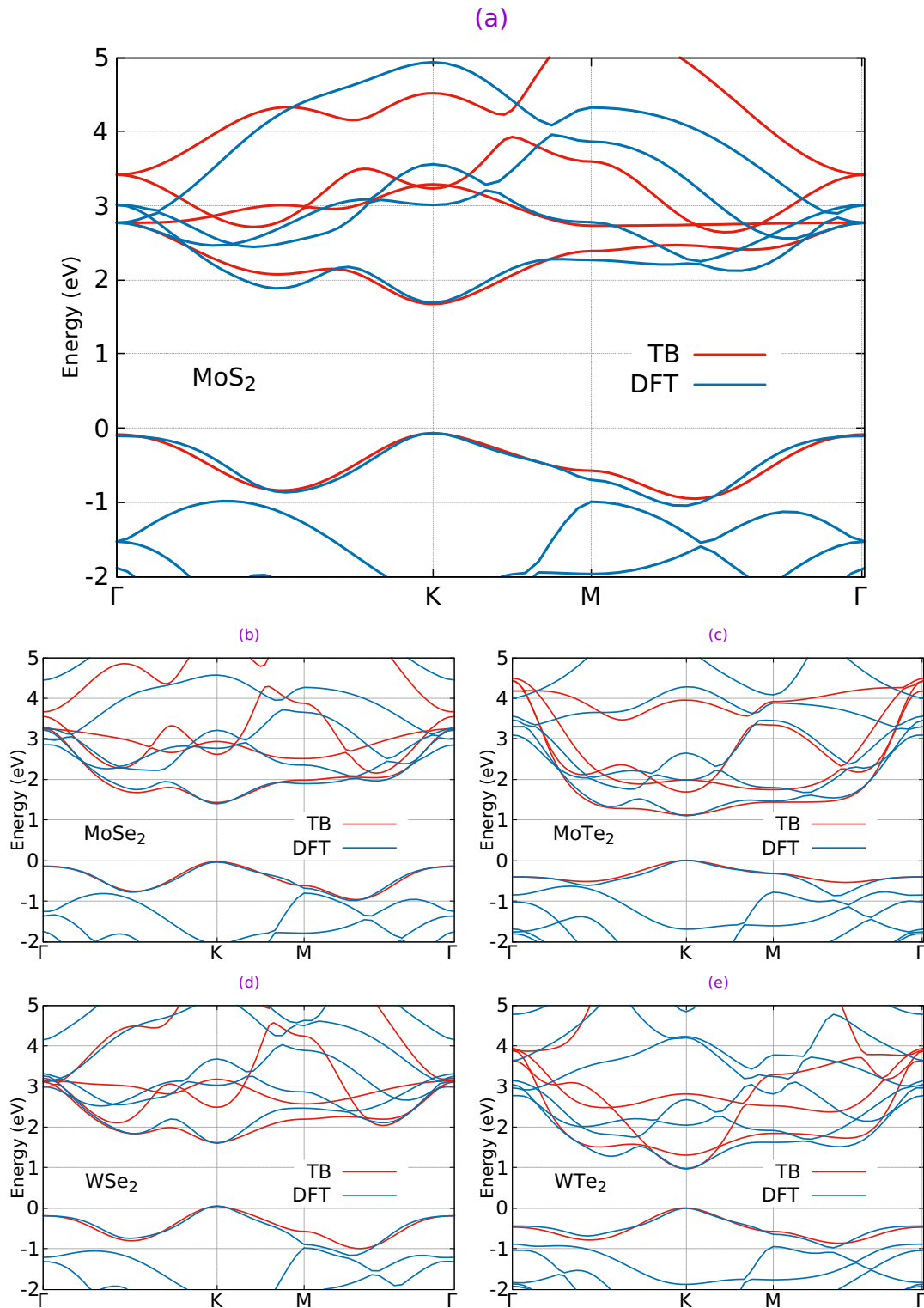


Figure 4.2: The electronic band structure of monolayer of a different TMDs of  $MX_2$  ( $M = \text{Mo}, \text{W}$  and  $X = \text{S}, \text{Se}, \text{Te}$ ) without SOC. The direct bandgap is obtained at highest symmetry point  $K$ . (a) MoS<sub>2</sub>, (b) MoSe<sub>2</sub>, (c) MoTe<sub>2</sub>, (d) WSe<sub>2</sub>, and (e) WTe<sub>2</sub>.

Lattice parameters and bandgap of single layer MX <sub>2</sub>				
MX <sub>2</sub>	a (Å)	M-X (Å)	X-X (Å)	Bandgap (eV)
MoS <sub>2</sub>	3.18	2.4017	3.1237	1.765
MoSe <sub>2</sub>	3.30	2.4900	3.2409	1.444
MoTe <sub>2</sub>	3.52	2.7160	3.5350	1.108
WSe <sub>2</sub>	3.30	2.5260	3.2877	1.556
WTe <sub>2</sub>	3.60	2.7410	3.6342	0.983

Table 4.1: The DFT optimized lattice parameters, first neighbor distance and bandgap for monolayer MX<sub>2</sub>, where the metal M is Mo or W and chalcogen X is S or Se or Te.

coupling (SOC) as shown in Fig. 4.3. Our DFT band structures are in good agreement with previous literatures [110,185,186]. This SOC removes the spin degeneracy in both conduction and valence band which leads to a large energy splitting between spin up and down states of the valence band at the highest symmetry point of the Brillouin zone of  $K$  is shown in Fig. 4.3. The splitting is high for W based TMDs than that of Mo based TMDs, because of the heavier mass of W based TMDs. SOC also leads to a splitting of the conduction band at the  $K$  point as well as the minimum in between  $K$  and  $\Gamma$  is shown in Fig. 4.3.  $K$ : the direct bandgap located at  $K$ -point and the spin splitting at VB ( $K$ -point) is larger  $\approx$  145 meV, 188 meV, 218 meV, 475 meV, and 506 meV for MoS<sub>2</sub>, MoSe<sub>2</sub>, MoTe<sub>2</sub>, WSe<sub>2</sub>, and WTe<sub>2</sub>, respectively. We observed that mass or atomic number ( $Z$ ) of transition metal (M) or chalcogen (X) increases the spin splitting at VB ( $K$ ) increases.

When the atomic number and weight of the chalcogenides increases along with transition metal the bandgap is decreasing, and also spin splitting (SOC) increasing at valence band ( $K$ ), the SOC effect will be more and more important for the calculation of transport properties of single layer TMDs.

### 4.2.2 Tight-Binding model description for Transition Metal Dichalcogenides

We describe the monolayer of MX<sub>2</sub>, the states around the gap at the Fermi energy  $E_F$  are mainly  $d$  states of M. However, to describe valence and conduction bands correctly, it is not sufficient to restrict an effective Hamiltonian to  $d$  M orbitals. Indeed, the ligand field (X atoms) splits the  $d$  levels of the transition metal (M) atoms, and thus creates a direct gap at the  $K$  point [79]. Therefore, all TB models proposed in the literature include at least  $p$  X orbitals [23,179,194]. The valence band has mainly  $d_0 = 4d_{z^2}$  M character, whereas the conduction band has  $d_0$  character mixed with  $d_2 = d_{x^2-y^2}, d_{xy}$  M character near the gap,

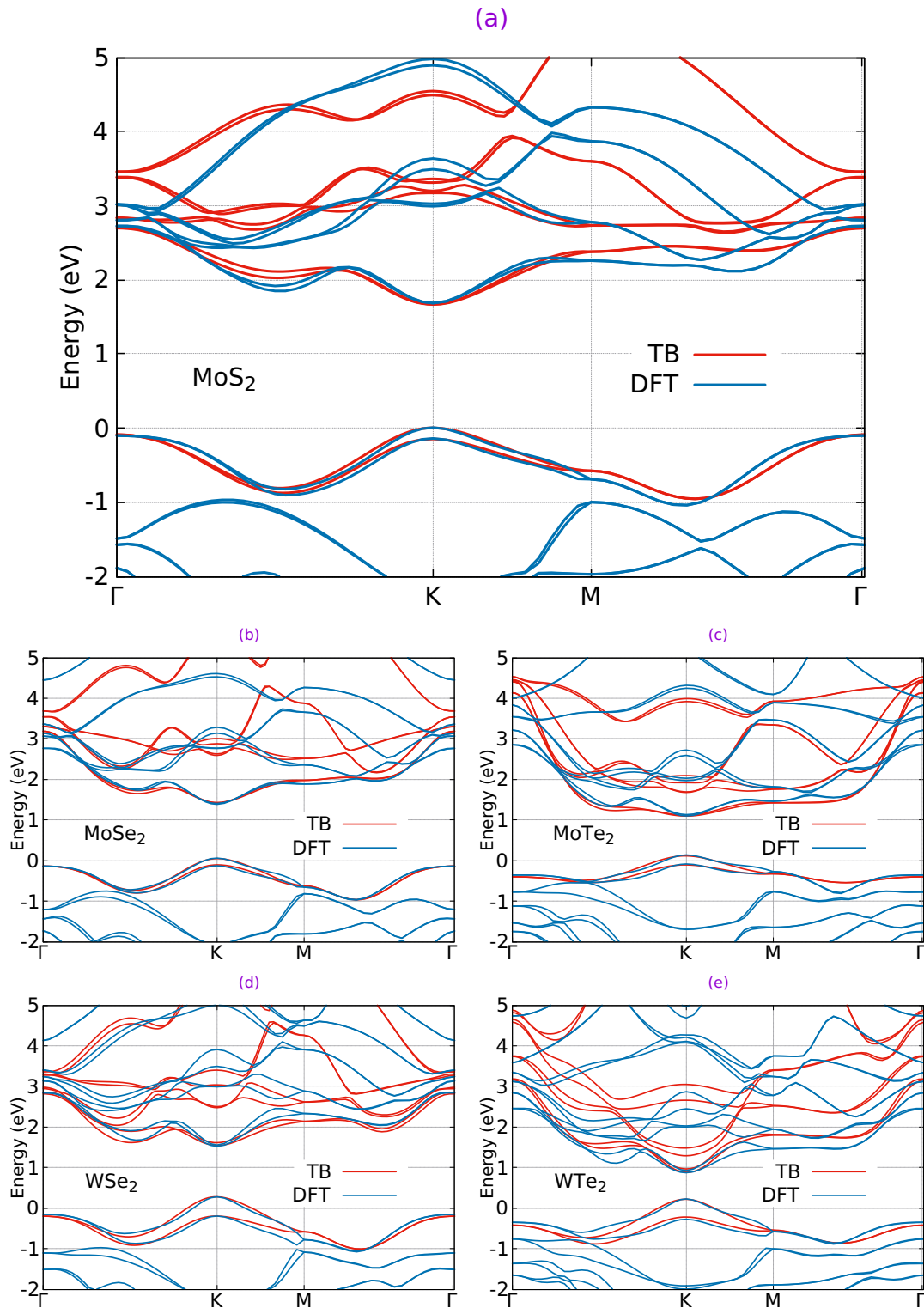


Figure 4.3: The electronic band structure of a monolayer of different TMDs of  $\text{MX}_2$  ( $M = \text{Mo}, \text{W}$  and  $X = \text{S}, \text{Se}, \text{Te}$ ) with SOC. The direct bandgap is obtained at highest symmetry point  $K$ . (a) MoS<sub>2</sub>, (b) MoSe<sub>2</sub>, (c) MoTe<sub>2</sub>, (d) WSe<sub>2</sub>, and (e) WTe<sub>2</sub>.

<b>Tight-Binding parameters</b>					
	MoS <sub>2</sub>	MoSe <sub>2</sub>	MoTe <sub>2</sub>	WSe <sub>2</sub>	WTe <sub>2</sub>
<b>On-site energies of d-orbital of M (Mo, W)</b>					
$\Delta_2 = d_{xy} = d_{x^2-y^2}$ (eV)	-0.0563	-0.0009	-0.0425	-0.010	-0.0576
$\Delta_1 = d_{zy} = d_{zx}$ (eV)	-0.4916	-0.440	-0.6948	-0.80	-0.6727
$\Delta_0 = d_{3z^2-r^2}$ (eV)	0.0644	0.0349	0.0168	0.0149	0.0568
<b>On-site energies of p-orbital of X (S, Se, Te)</b>					
$\Delta_p = p_x = p_y$ (eV)	-38.7786	-35.3295	-22.0570	-36.3295	-43.5846
$\Delta_z = p_z$ (eV)	-29.5254	-27.9754	-17.5945	-27.9754	-15.2913
<b>Slater-Koster parameters of MX<sub>2</sub></b>					
$V_{dd\sigma}$ (M-M) (eV)	-0.9035	-0.8124	-0.5509	-0.8524	-0.8442
$V_{dd\pi}$ (M-M) (eV)	0.7027	0.6611	0.3842	0.6611	0.6039
$V_{dd\delta}$ (M-M) (eV)	0.0897	0.0836	0.0089	0.0836	0.0162
$V_{pp\sigma}$ (X-X) (eV)	8.0790	10.5297	7.5192	10.5297	12.9422
$V_{pp\pi}$ (X-X) (eV)	-2.6784	-3.5751	-0.7837	-3.5751	-1.0655
$V_{dp\sigma}$ (M-X) (eV)	-7.1933	-6.3099	-4.9915	-6.5099	-6.1066
$V_{dp\pi}$ (M-X) (eV)	3.2674	3.1085	1.9374	3.3085	2.6339
<b>Spin-Orbit-Coupling (SOC) of MX<sub>2</sub></b>					
$\lambda_M$ (eV)	0.075, 0.086*	0.077, 0.089*	0.109	0.235, 0.251*	0.215
$\lambda_X$ (eV)	0.042, 0.052*	0.175, 0.256*	0.375	0.475, 0.439*	7.052

Table 4.2: Tight-binding parameters and SOC ( $\lambda$ ) for monolayer MX<sub>2</sub>, where the metal M is Mo or W and chalcogen X is S or Se or Te. \* indicates values from the reference [194].

and  $d_1 = d_{xz}, d_{yz}$  M character for higher energies [23]. It seems that  $p$  X orbitals, which have lower on-site energies, act as a perturbation of the  $d$  M bands. For this reason, several TB models [23, 179, 194] fit rather well to the DFT band structure, while they propose very different parameters (on-site energies and Slater-Koster parameters).

We constructed new tight-binding models for TMDs based on Slater-Koster parameters. This TB approximation contains 11 orbitals per layer and per unit cell: the five  $d$  orbitals of the transition metal M atom and the six  $p$  orbitals of the two chalcogen X atoms in the unit cell [23, 179]. The Slater-Koster parameters that account for the relevant hopping processes of the model are  $V_{pd\sigma}$  and  $V_{pd\pi}$  for M-X bonds,  $V_{dd\sigma}$ ,  $V_{dd\pi}$  and  $V_{dd\delta}$  for M-M bonds, and  $V_{pp\sigma}$  and  $V_{pp\pi}$  for X-X bonds. Additional parameters of the theory are on-site energies which depend

on the crystal fields for  $d$  orbitals:  $\Delta_0, \Delta_1, \Delta_2$ , and for  $p$  orbitals:  $\Delta_p, \Delta_z$ . The Slater-Koster parameters and the on-site energies that we choose to simulate the DFT bands for the five compounds are given in table 4.2. We notice that the main restriction of the TB model considered here is that it only includes up to next-nearest neighbor hopping terms, and this is why the fit to the DFT bands cannot be perfect. Moreover our TB-model does not include  $p$  orbital of M which seems not necessary to simulate bands around the gap [222].

### 4.2.3 Electronic band structure of Wannier orbitals from DFT

More sophisticated methods such as DFT based tight-binding Hamiltonian represented in the basis of maximally localized Wannier functions (MLWFs) (see section 2.4.3) can lead to better agreement, at the cost of inclusion of longer range hopping terms [98, 144, 172]. The band structure of the Wannier Hamiltonian calculated with Wannier90 code [144, 172], is in good agreement with DFT calculations is shown in Fig. 4.4. The Wannier-semiempirical-TB [144, 172] model has broad range of hopping terms and on-site energies that are structure dependent. Therefore these terms are no more valid when static defects are introduced in the atomic structure. It is thus not possible to use the Wannier orbitals for our transport calculations. So, we are using our tight-binding model parameters for the calculation of transport properties. Nevertheless, the Wannier approach allows us to check the character of states, as follows.

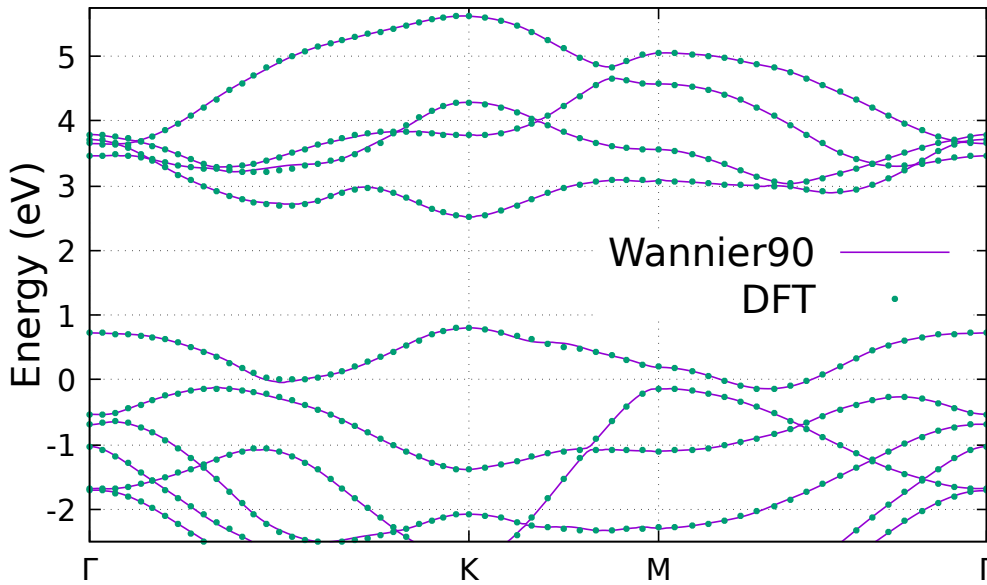


Figure 4.4: A comparison of electronic band structure of a monolayer of MoS<sub>2</sub> with Wannier-TB model and DFT [ABINIT].

The electronic band structure of transition metal dichalcogenides (TMDs) obtained a bandgap, main contribution  $d$ -orbitals of the transition metals ( $M = \text{Mo}, \text{W}$ ). Now, we are justified (ex:  $\text{MoS}_2$ )  $d$ -orbitals have a major contribution in the band structure around the gap region is shown in Fig. 4.5. The orbital contributions, calculated using the orbital projections (Wannier) in the electronic band structure are shown in Fig. 4.5. The bands of interest around the gap region of the conduction and valence bands have very little contribution of  $p$ -orbital (chalcogenides) character is shown in Fig. 4.5 [bottom] and major contribution of  $d$ -orbital (transition metal) character is shown in Fig. 4.5 [top].

### 4.3 Local density of states (LDOS)

The TB total and local density of states (LDOS) are calculated by the recursion method (see section 3.1.1) employed uniform broadening by Lorentzian with  $\epsilon = 6$  meV. We use a large number of recursion steps, with  $Nr = 3000$  in the real space unit cell. The total DOS and LDOS are shown in Fig. 4.6 for different monolayer TMDs. It shows also the contributions of  $d_0 = d_{3z^2-r^2}$ ,  $d_1 = d_{xz}$ ,  $d_{yz}$  and  $d_2 = d_{xy}$ ,  $d_{x^2-y^2}$ . For all TMDs, the density of states around the energy gap have a  $d_0 = d_{3z^2-r^2}$  major contributions in the valence and conduction bands, the other  $d$  orbitals of  $M$  have a small contribution.

### 4.4 Density of states with defects

In this section, we study the TB-total density of states of TMDs with a random distribution of vacant atoms (vacancies) in a large supercell containing 2799468 atoms, which corresponds to an  $L_1 = L_2 = 1000$  cell of  $\text{MX}_2$ . The effect of point defects in the DOS of different TMDS ( $\text{MX}_2$ ) with the defect concentration ( $c = 0\%$ ,  $3\%$ ,  $2\%$ ,  $1\%$ , and  $0.5\%$ ) with respect to the total number of atoms without defects is shown in Fig. 4.7. The defects lead to the appearance of a series of peaks in the gaped region of the DOS, which are associated to the creation of midgap states localized around the defects, whose energy and strength depends on the specific missing atoms, their concentration as well as the specific arrangement of the point defects [53, 240]. In order to identify the energy of  $M$ -vacancy midgap states and  $X$ -vacancy midgap states (Fig. 4.7), we have compare the total DOS calculated with only one of the two types of vacancies. The energies of midgap states seems to be a little different from the previous works [240], this may come from the different TB model.

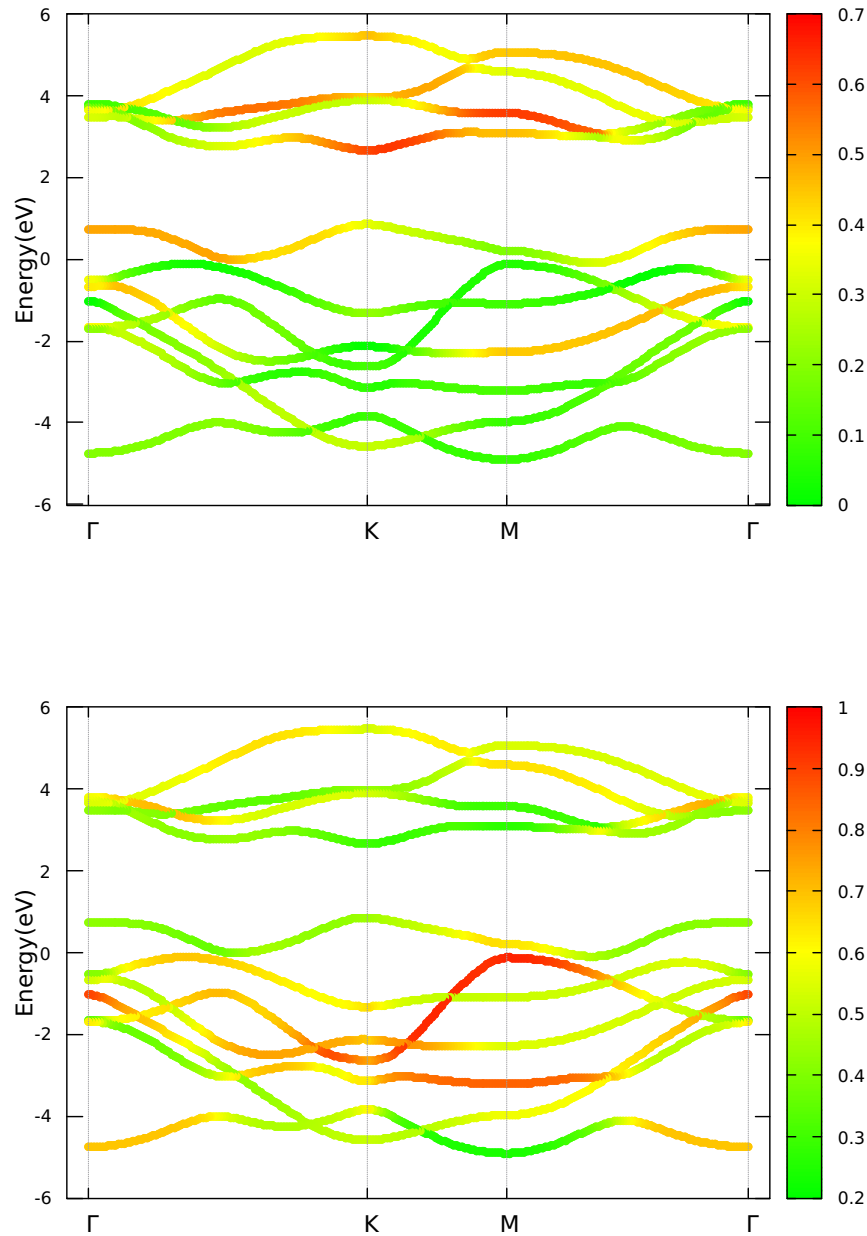


Figure 4.5: The electronic band structure of monolayer of MoS<sub>2</sub> with the Wannier method showing the contribution of *d*-like MLWFs (proportion of *d*-character of the bands Mo) in red [top] and *p*-like MLWFs (proportion of *p*-character of the bands S) in red [bottom]. A color scheme is used to measure the proportion of orbital character of the bands.

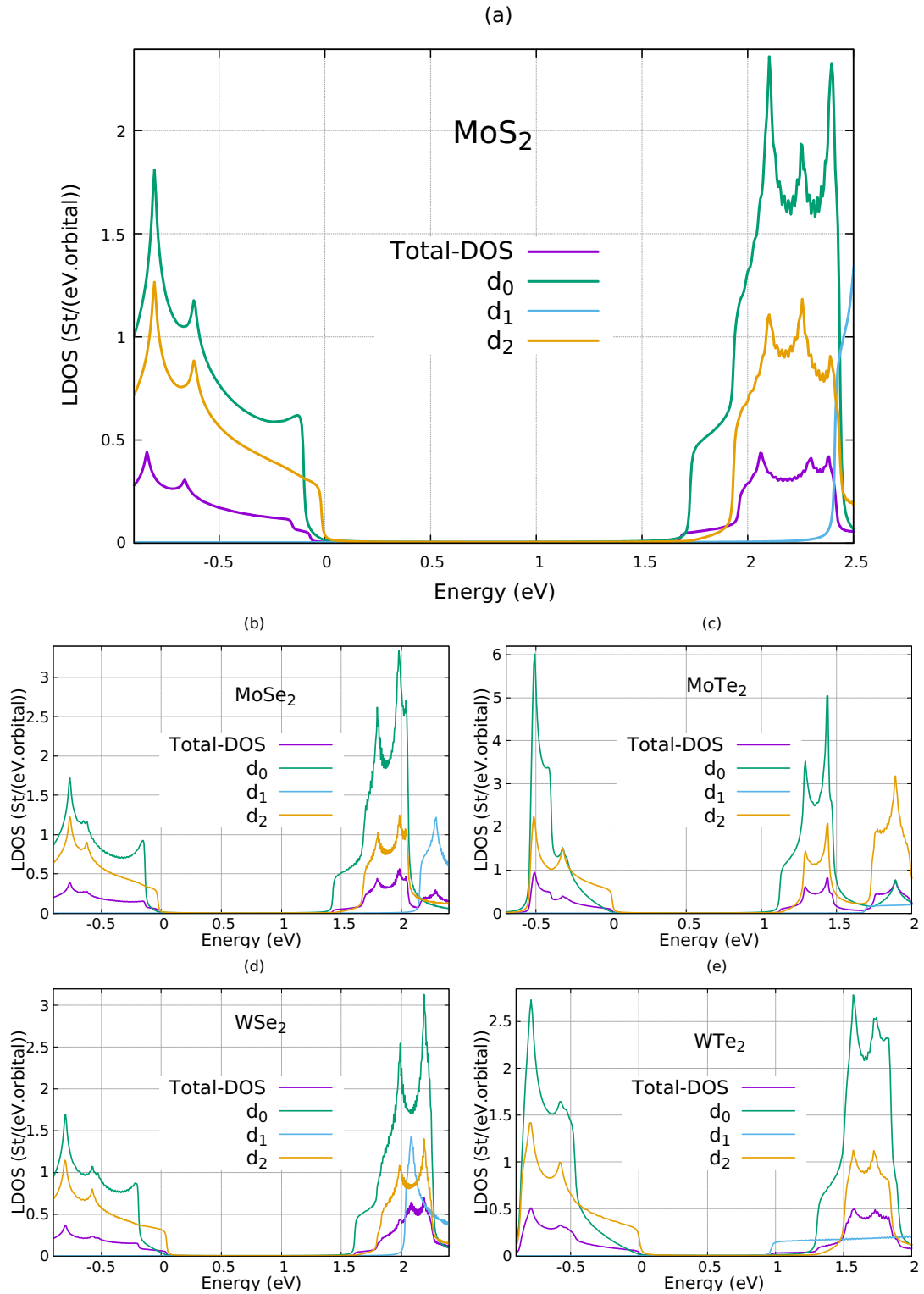


Figure 4.6: TB-total density of states (DOS) and local DOS (LDOS),  $d_0 = d_{3z^2-r^2}$ ,  $d_1 = d_{xz}, d_{yz}$  and  $d_2 = d_{xy}, d_{x^2-y^2}$  monolayer of different TMDS without defects and without SOC. The LDOS and total DOS are calculated employing a broadening by a Lorentzian (see section 3.1.2) with  $\epsilon = 6$  meV. (a) MoS<sub>2</sub>, (b) MoSe<sub>2</sub>, (c) MoTe<sub>2</sub>, (d) WSe<sub>2</sub>, and (e) WTe<sub>2</sub>.

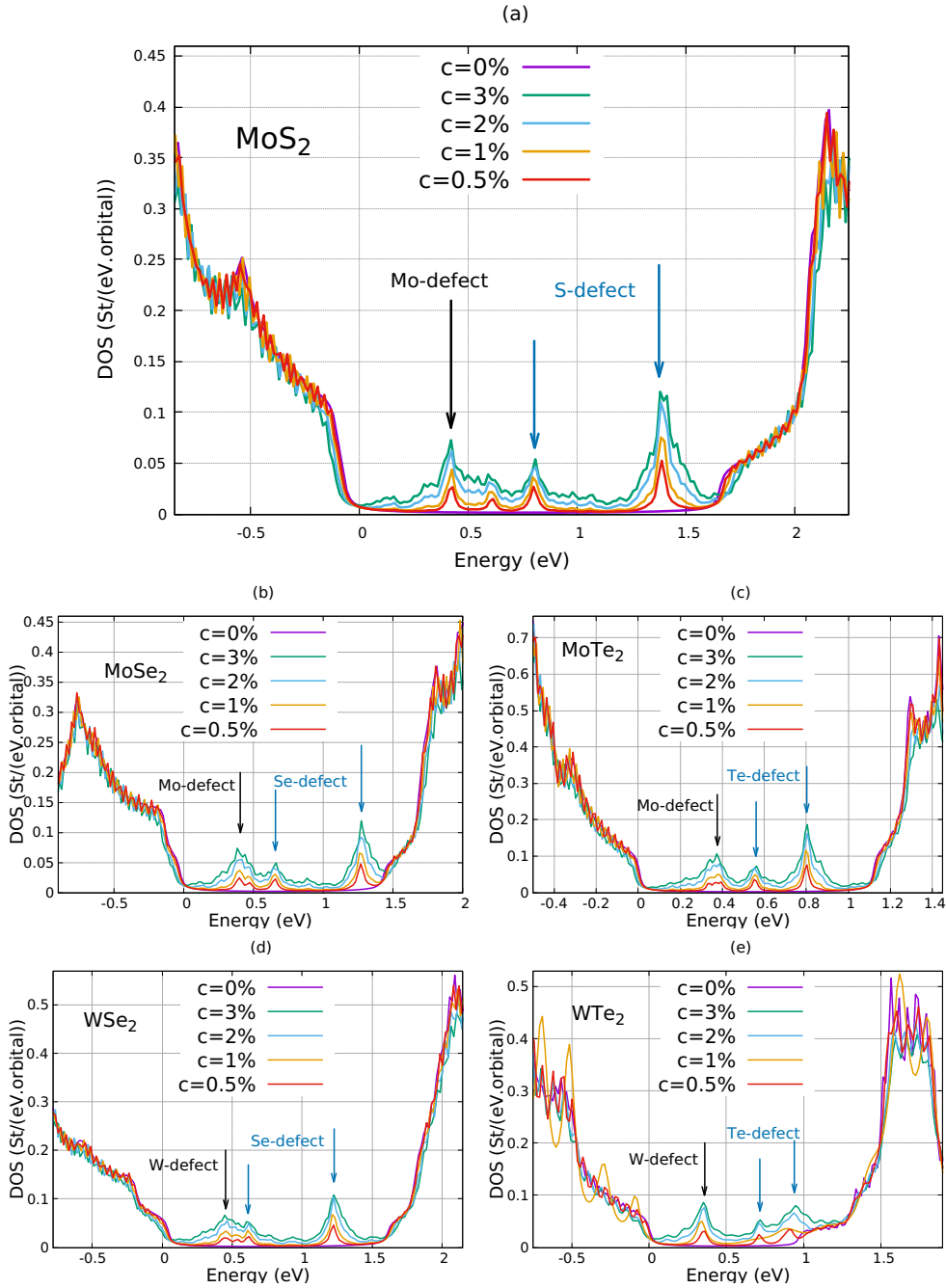


Figure 4.7: TB-Total density of states (DOS) with random distribution of vacancies (vacant M atoms or vacant X atoms) with different concentrations  $c$  of vacancies with respect to the total number of atoms ( $c = 0\%$ ,  $3\%$ ,  $2\%$ ,  $1\%$ , and  $0.5\%$ ) of monolayer of different TMDS. The DOS is calculated employing a broadening by a Lorentzian (see section 3.1.2) with  $\epsilon = 15$  meV. The peaks in the DOS associated to midgap bands is due to X or M defects. (a)  $\text{MoS}_2$ , (b)  $\text{MoSe}_2$ , (c)  $\text{MoTe}_2$ , (d)  $\text{WSe}_2$ , and (e)  $\text{WTe}_2$ .

## 4.5 Transport properties

In the framework of the Kubo-Greenwood formula for the electronic transport properties, the quantum diffusion coefficient  $D$  (diffusivity) and conductivity ( $\sigma$ ) are computed by using the polynomial expansion method, developed by Didier Mayou and his co-workers [130, 131, 183, 184, 217] described in chapter 3. This numerical approach allows very efficient calculations by recursion (Lanczos algorithm) in real space which take into account all quantum effects. Now we are using this recursion method to study quantum transport in disordered TMDs. Our calculations are performed on samples containing up to  $28 \times 10^5$  M (transition metal) and X (chalcogenides) atoms, which corresponds to typical sizes of about one micrometer square and allows to study systems with elastic mean free path length of the order of a few hundred nanometers.

### 4.5.1 Conductivity & Inelastic mean free path

The elastic scattering events are taken into account in the Hamiltonian, but effects of inelastic scattering by phonons at temperature  $T$  are not included in the Hamiltonian. To consider the inelastic processes, we introduce an inelastic scattering time  $\tau_i(T)$  beyond which the propagation becomes diffusive due to the destruction of coherence by these inelastic processes see section 3.2.3. The effect of a magnetic field on the electron propagation is not included directly in the TB model, but a magnetic field  $B$  can have also a similar incoherent dephasing effect. This dephasing effect occurs on a length  $L_i(B)$  such that the flux of the magnetic field enclosed in the disk of radius  $L_i(B)$  is equal to the flux quantum  $\frac{h}{e}$ , that is  $\frac{h}{e} \approx \sqrt{\frac{h}{eB}}$ . We treat these two dephasing effects in a phenomenological way through a Relaxation Time Approximation (RTA) [133] as described here after. In the RTA, the conductivity along the x-axis is given by [37] (see section 3.3.3)

$$\sigma(E_F, \tau_i) = e^2 n(E_F) D(E_F, \tau_i), \quad (4.7)$$

$$D(E_F, \tau_i) = \frac{L_i^2(E_F, \tau_i)}{2\tau_i} \quad (4.8)$$

where  $E_F$  is the Fermi energy,  $n(E_F)$  is the density of states (DOS) and  $L_i$  is the inelastic mean free path along the x-axis.  $L_i(E_F, \tau_i)$  is the typical distance of propagation during the time interval  $\tau_i$  for electrons at energy  $E$ .

We compute the distance  $L_i$  from equation 3.95, and then from 4.7 and 4.8, the diffusivity  $D$  and the conductivity  $\sigma$  at all inelastic scattering times  $\tau_i$  and

all energies  $E$  for a model Hamiltonian that includes elastic scatterers (vacancies) distributed randomly in the supercell. At short times  $\tau_i$ , i.e.  $\tau_i$  lower than elastic scattering time  $\tau_e$ , the propagation is ballistic and the conductivity  $\sigma$  increases when  $\tau_i$  increases in the ballistic region is shown in Fig. 4.8.

The three main transport regimes which can be generically followed through the time evaluation of the wave packet dynamics are [104,211]:

- **Ballistic regime.** For small  $\tau_i$ , electrons travel through the system without suffering any scattering, so the  $D(E, \tau_i)$  and  $L_i(\tau_i)$  remains linear functions in  $\tau_i$ , with slopes respectively equal to  $v_F^2$  and  $v_F$ .
- **Diffusive regime.** For intermediate  $\tau_i$ , behavior in weakly disordered and its characterized by a saturation of  $D(E, \tau_i)$ . The saturation value identifies the elastic relaxation time  $\tau_e$ , above which diffusive regime is reached.
- **Localized regime.** For large  $\tau_i$ , behavior in a strongly disordered system is manifested by an increasing contribution of quantum interference which reduces the diffusion coefficient, not always it depends on the system: thus  $D$  decreases when  $t$  increases [104]. The spreading  $L_i(\tau_i)$  reaches an asymptotic value that is related to the localization length  $\xi(E)$ .

The variation of the conductivity  $\sigma$  and inelastic mean free path  $L_i$  versus  $\tau_i$  for different energies corresponding to the valence band region to conduction band region is shown in Fig. 4.8. The first case (i) conduction band region: MoS<sub>2</sub> ( $E = 1.90$  eV), MoSe<sub>2</sub> ( $E = 1.88$  eV), MoTe<sub>2</sub> ( $E = 1.36$  eV), WSe<sub>2</sub> ( $E = 2.10$  eV), and WTe<sub>2</sub> ( $E = 1.62$  eV). The large values of  $\tau_i$ , the conductivity  $\sigma$  is almost constant as expected in a diffusive regime. This regime corresponds to energies for which the DOS is weakly affected by scatterers. We have checked that  $\sigma$  with different concentration of vacancies ( $c$ ),  $\sigma$  is almost independent on  $c$  which is expected by the Boltzmann theory of transport. Second case (ii) bandgap region: MoS<sub>2</sub> ( $E = 0.80$  eV), MoSe<sub>2</sub> ( $E = 0.66$  eV), MoTe<sub>2</sub> ( $E = 0.56$  eV), WSe<sub>2</sub> ( $E = 0.60$  eV), and WTe<sub>2</sub> ( $E = 0.72$  eV), the transport is determined by diffusion of midgap states which are localized states. Therefore, the localization regime is reached at small  $\tau_i$ . Third case (iii) valence band region: MoS<sub>2</sub> ( $E = -0.60$  eV), MoSe<sub>2</sub> ( $E = -0.64$  eV), MoTe<sub>2</sub> ( $E = -0.32$  eV), WSe<sub>2</sub> ( $E = -0.56$  eV), and WTe<sub>2</sub> ( $E = -0.58$  eV) the behavior is similar to the first case. The first and third cases, for  $\tau_i$  closed to the elastic scattering time  $\tau_e$ , there is a diffusive behavior where  $\sigma(\tau_i)$  reaches a maximum,  $\sigma_M$ ; for larger values of  $\tau_i$ ,  $\tau_i \gg \tau_e$ ,  $\sigma(\tau_i)$  decreases progressively as expected in the localization regime due to Anderson localization in 2D [104]. Variation of conductivity and inelastic scattering length versus inelastic scattering time for a large concentration of vacancies 3 % and 10

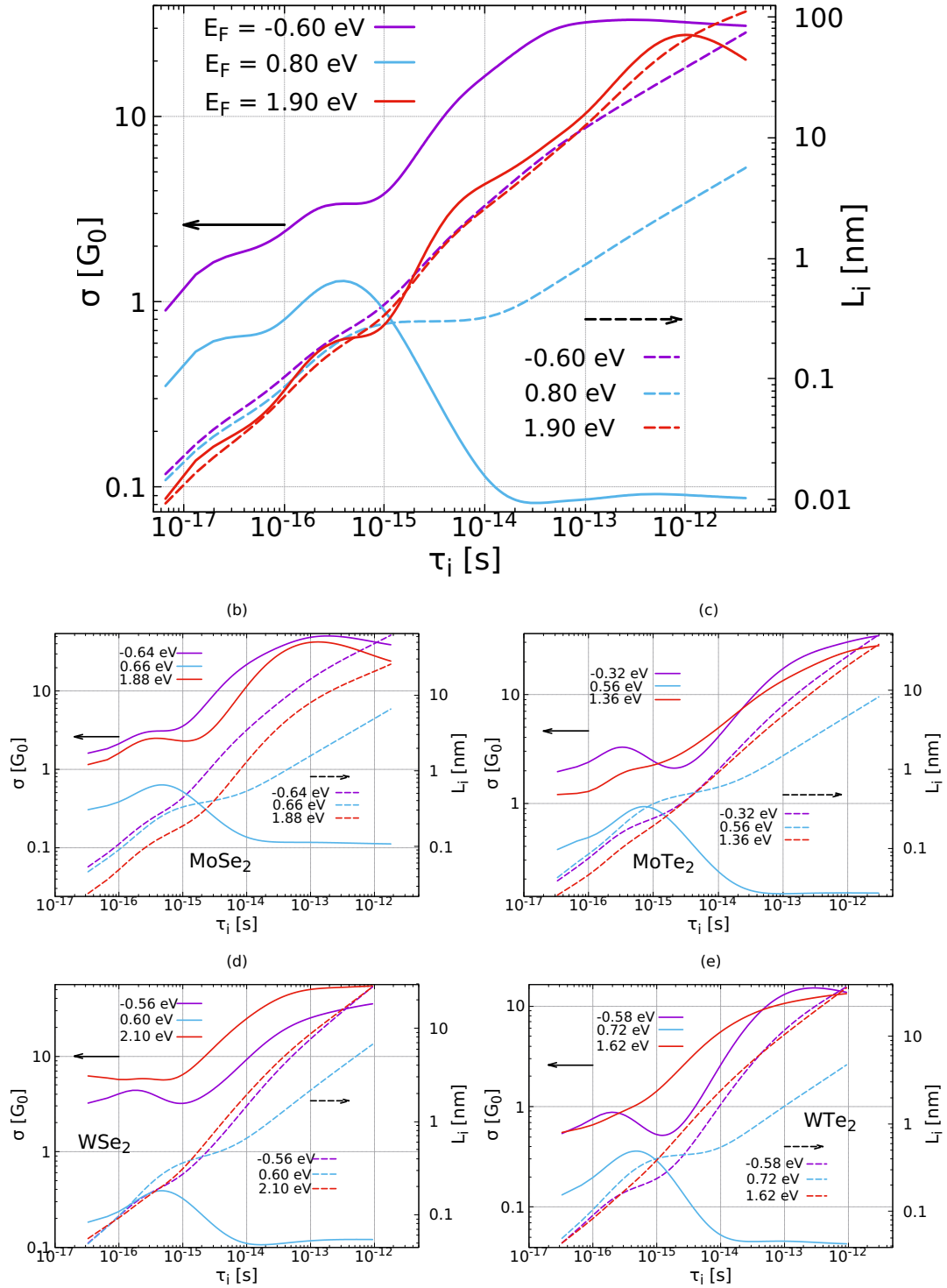


Figure 4.8: The variation of conductivity  $\sigma$  (solid line) and inelastic scattering length  $L_i$  (dashed line) in MX<sub>2</sub> versus inelastic scattering time  $\tau_i$  for the defect concentration  $c = 1\%$  of point defects (vacancies by random removal of atoms). For the three energy values: valence band (blue), inside the midgap states region (magenta) and conduction band (red). (a) MoS<sub>2</sub>, (b) MoSe<sub>2</sub>, (c) MoTe<sub>2</sub>, (d) WSe<sub>2</sub>, and (e) WTe<sub>2</sub>.  $G_0 = 2e^2/h$ .

% in a large supercell are shown in appendix B.1. We observed that when the concentration of defects increases the diffusive regime is reached at very small  $\tau_i$ , therefore, the localization length is also smaller.

### 4.5.2 Microscopic conductivity

As shown in the previous paragraph,

$$L_i(E, \tau_i) \simeq V_0(E)\tau_i \quad \text{when} \quad \tau_i \ll \tau_e, \quad (4.9)$$

where  $V_0$  is a velocity at the energy  $E$  and short time  $t$ . In crystals, when inter-band terms are negligible  $V_0 = V_B$ , where  $V_B$  is the Boltzmann velocity (intra-band velocity) [38]. According to the renormalization theory [104] in 2D systems with static defects, diffusivity  $D$  always goes to zero at very large  $\tau_i$ . Thus, at each energy, the microscopic diffusivity  $D_M$  (microscopic conductivity  $\sigma_M$ ) is defined as the maximum value of  $D(\tau_i)$  ( $\sigma(\tau_i)$ ).

The microscopic conductivity is

$$\sigma_M(E) = e^2 n(E) D_M(E). \quad (4.10)$$

We compute also the elastic mean free path  $L_e$  along the  $x$ -axis, from the relation [37],

$$L_e(E) = \frac{1}{V_0(E)} \text{Max}_{\tau_i} \left\{ \frac{L_i^2(E, \tau_i)}{\tau_i} \right\} = \frac{2D_M(E)}{V_0(E)}. \quad (4.11)$$

$L_e$  is the average distance between two elastic scattering events. At each energy, the elastic scattering times  $\tau_e$  is deduced from  $L_e$  by  $L_e = V_0(E)\tau_e(E)$ . The variation of the elastic mean free path  $L_e$  along the  $x$ -axis as a function of the energy  $E$  is shown of appendix B Fig. 3 for different values of point defect concentrations in  $\text{MX}_2$ .

The microscopic conductivity  $\sigma_M$  versus energy  $E$  as a function of the energy ( $E$ ) see Fig. 4.9 for different values of point defect concentrations in  $\text{MX}_2$ . According to the renormalization theory [104], this value is obtained when the inelastic mean free path  $L_i$  and the elastic mean free path  $L_e$  are comparable,  $L_e \simeq L_i$ , which corresponds to  $\tau_e \simeq \tau_i$ . As  $L_i$  and  $\tau_i$  decrease when the temperature  $T$  increases, the microscopic conductivity is a good estimation of the high-temperature conductivity (room temperature and higher temperature conductivity).

We analyze the microscopic conductivity with concentration  $\sigma_{Mc}$  ( $c$  in %) versus energy  $E$  for different values of point defect concentrations in  $\text{MX}_2$  see Fig. 4.10.  $\sigma_M = \frac{\text{constant}}{c}$  ( $c$  in %) implies  $\sigma_{Mc} = \text{constant}$  for every energy. Therefore,  $\sigma_{Mc}$

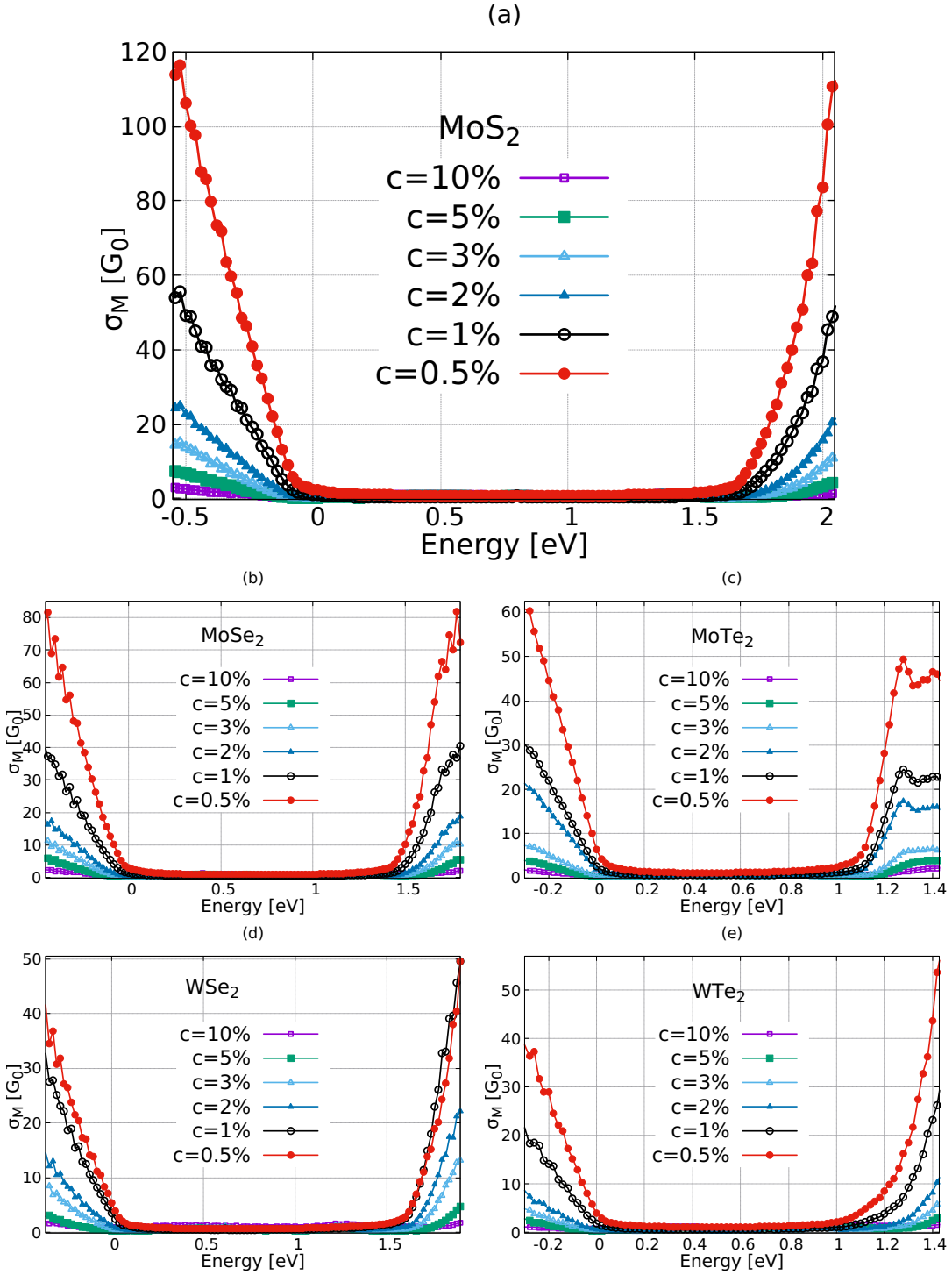


Figure 4.9: The variation of microscopic conductivity  $\sigma_M$  versus energy  $E$  in  $\text{MX}_2$  for different concentration ( $c = 0.5\%$ ,  $1\%$ ,  $2\%$ ,  $3\%$ ,  $5\%$ , and  $10\%$ ) of point defects (vacancies by random removal of atoms  $M = \text{Mo}$ ,  $\text{W}$  or  $X = \text{S}$ ,  $\text{Se}$ ,  $\text{Te}$ ). (a)  $\text{MoS}_2$ , (b)  $\text{MoSe}_2$ , (c)  $\text{MoTe}_2$ , (d)  $\text{WSe}_2$ , and (e)  $\text{WTe}_2$ .  $G_0 = 2e^2/h$ .

$\approx$  constant as expected in Boltzmann theory of transport around the valence and conduction band region, but this is not true in the midgap states.

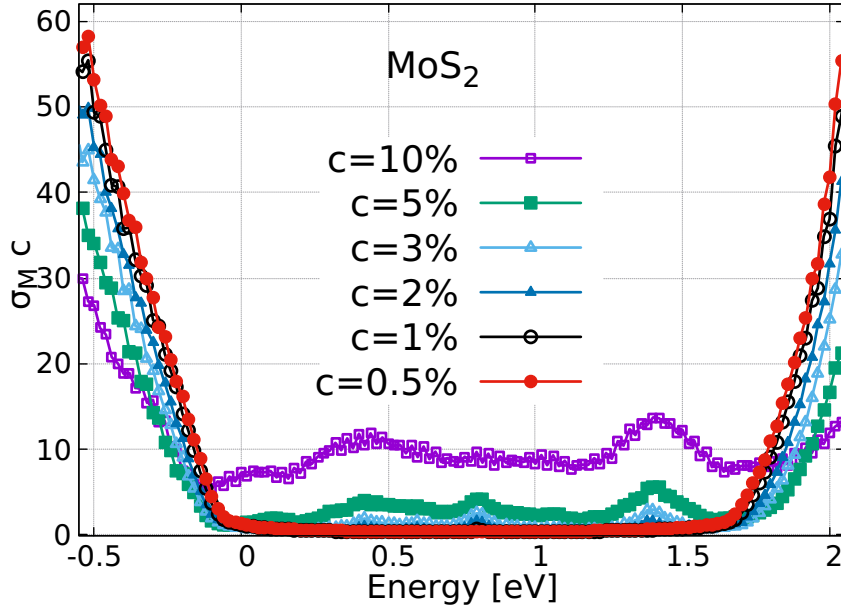


Figure 4.10: The variation of the microscopic conductivity  $\sigma_{MC}$  ( $c$  in %) versus energy  $E$  in  $\text{MX}_2$  for different concentration ( $c = 0.5\%$ ,  $1\%$ ,  $2\%$ ,  $3\%$ ,  $5\%$ , and  $10\%$ ) of point defects (vacancies by random removal of atoms  $M = \text{Mo}, \text{W}$  or  $X = \text{S}, \text{Se}, \text{Te}$ ). (a)  $\text{MoS}_2$ , (b)  $\text{MoSe}_2$ , (c)  $\text{MoTe}_2$ , (d)  $\text{WSe}_2$ , and (e)  $\text{WTe}_2$ .  $\sigma_M$  in  $G_0 = 2e^2/h$  and  $c$  in %.

### 4.5.3 Thermodynamic average conductivity at room temperature

We define the thermodynamic average conductivity at room temperature ( $T \approx 300$  K) as

$$\sigma(\mu_C, T \approx 300\text{K}) = \int_{-\infty}^{+\infty} dE \sigma_M(E) \left( -\frac{\partial f}{\partial E} \right), \quad (4.12)$$

where  $\mu_C$  is the chemical potential, and  $\sigma_M$  is the microscopic conductivity. The Fermi-Dirac distribution function  $f$  is defined as

$$f(E, \mu_C, T) = \frac{1}{e^{\left(\frac{E-\mu_C}{k_B T}\right)} + 1} \quad (4.13)$$

and  $N_e$  is the number of charge carriers with respect to the neutral system

$$N_e(\mu_C, T) = \int_{-\infty}^{+\infty} dE n(E) f(E, \mu_C, T) - \int_{-\infty}^{+\infty} dE n(E) f(E, \mu_C = E_{F0}, T = 0), \quad (4.14)$$

where  $E_{F0}$  is the Fermi energy at  $T = 0$  K of the undoped system. We choose  $E_{F0}$  to be at the middle of the gap of the  $\text{MX}_2$  without static defects.

At temperature  $T$ , the mobility  $\mu$  is related with conductivity  $\sigma$  by [53, 240]:

$$\sigma(\mu_C, T) = e |N_e(\mu_C, T)| \mu(\mu_c, T). \quad (4.15)$$

Therefore, at room temperature ( $T \approx 300\text{K}$ ), mobility is

$$\mu(\mu_C, T = 300\text{K}) = \frac{1}{e |N_e|} \int_{-\infty}^{+\infty} dE \sigma_M(E) \left(-\frac{\partial f}{\partial E}\right). \quad (4.16)$$

The thermodynamic average conductivity ( $\sigma_{300\text{K}}$ ) versus chemical potential ( $\mu_C$ ) is shown in Fig. 4.11 for different concentrations of vacancies of  $\text{MX}_2$ .

The thermodynamic average conductivity ( $\sigma_{300\text{K}}$ ) and the corresponding mobility versus number of charge carriers ( $N_e$ ) at room temperature (300K) for different concentration of vacancies of  $\text{MX}_2$  is shown in Fig. 4.12 and Fig. 4.13. When the defect concentration is too large, there is too large midgap states in the gap region and thus mobility also, which is a semiconductor quantity, is not significant so we do not plot it see Fig. 4.13. When  $N_e \approx 0$  shows a numerical error in the calculation of mobility because of conductivity does not go correctly to zero (tail of Lorentzian expansion).  $\sigma_{300\text{K}}$  with respect to the charge carriers, we found that for  $n$ -doped samples,  $\text{MoTe}_2$ ,  $\text{MoSe}_2$ ,  $\text{MoS}_2$  show similar behavior, where as for  $p$ -doped samples.  $\sigma_{300\text{K}}$  for  $n$ -doped samples,  $\text{MoTe}_2$ ,  $\text{MoSe}_2$ ,  $\text{MoS}_2$  smaller than that of  $p$ -doped samples of  $\text{MoTe}_2$ ,  $\text{MoSe}_2$ ,  $\text{MoS}_2$ .  $\sigma_{300\text{K}}$  with respect to the charge carriers, we observed that for  $n$ -doped samples,  $\text{WTe}_2$ ,  $\text{WSe}_2$  show similar behavior, where as for  $p$ -doped samples  $\text{WTe}_2$ ,  $\text{WSe}_2$ . The thermodynamic average conductivity ( $\sigma_{300\text{K}}$ ) for  $n$ -doped samples,  $\text{MoTe}_2$ ,  $\text{MoSe}_2$ ,  $\text{MoS}_2$  is larger than that of  $p$ -doped samples of  $\text{MoTe}_2$ ,  $\text{MoSe}_2$ ,  $\text{MoS}_2$ .

We observed that  $n$  doping corresponds to M (Mo, W) point defects, whereas  $p$  doping corresponds to X (S, Se, Te) point defects with different concentration of vacancies is shown in Fig. 4.13. We found that for  $n$ -doped samples,  $\text{MX}_2$  show similar mobilities, where as for  $p$ -doped samples, the mobility of  $\text{WTe}_2$  is larger than for  $\text{WSe}_2$ ,  $\text{MoTe}_2$ ,  $\text{MoSe}_2$ ,  $\text{MoS}_2$ . Our results show that in general, the mobilities of TMDs are low, but they are larger for holes than for electrons, in agreement with experimental results [250]. The results for the mobility suggest that it is independent of carrier concentration, except at the edge of the valence band. If the concentration of the vacancies increases mobility decreases.

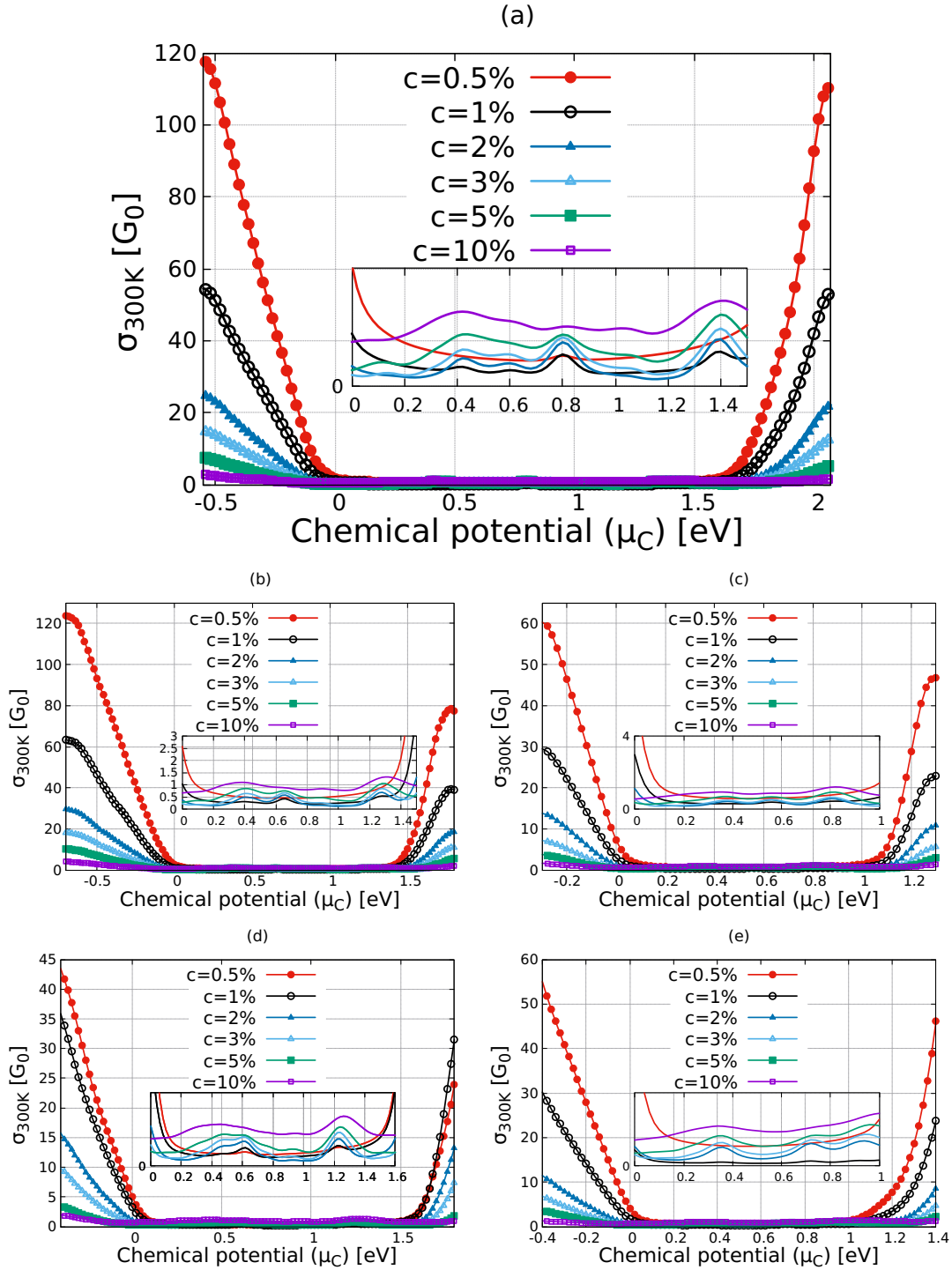


Figure 4.11: Thermodynamic average conductivity at room temperature ( $\sigma_{300K}$ ) versus chemical potential ( $\mu_C$ ) in MX<sub>2</sub> for different concentration ( $c = 0.5\%$ ,  $1\%$ ,  $2\%$ ,  $3\%$ ,  $5\%$ , and  $10\%$ ) of point defects (vacancies by random removal of atoms  $M = Mo, W$  or  $X = S, Se, Te$ ). (a) MoS<sub>2</sub>, (b) MoSe<sub>2</sub>, (c) MoTe<sub>2</sub>, (d) WSe<sub>2</sub>, and (e) WTe<sub>2</sub>.  $G_0 = 2e^2/h$ .

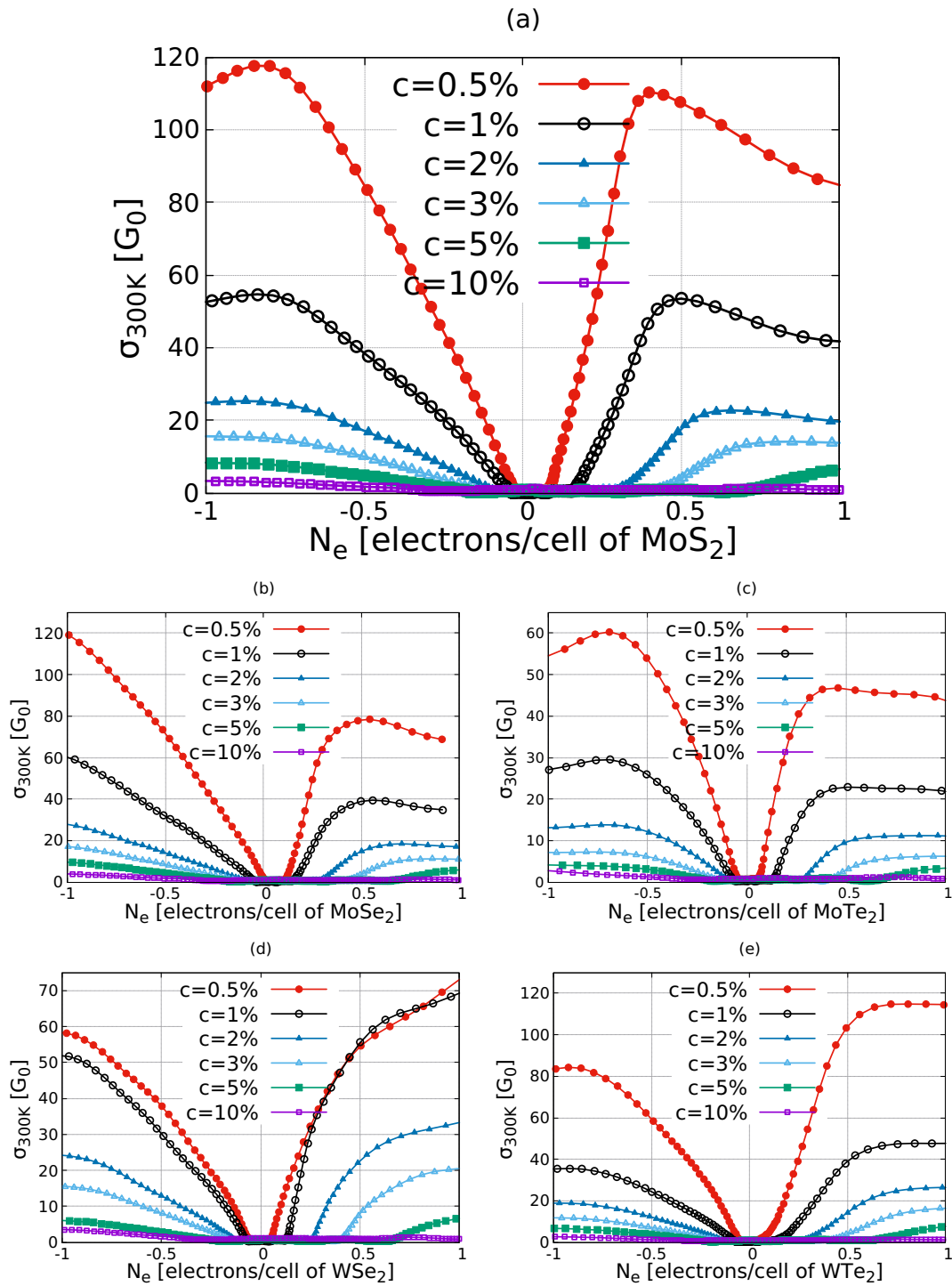


Figure 4.12: Thermodynamic average conductivity at room temperature ( $\sigma_{300K}$ ) versus number of charge carriers ( $N_e$ ) in  $MX_2$  for different concentration ( $c = 0.5\%$ ,  $1\%$ ,  $2\%$ ,  $3\%$ ,  $5\%$ , and  $10\%$ ) of point defects (vacancies by random removal of atoms  $M = Mo, W$  or  $X = S, Se, Te$ ). (a)  $MoS_2$ , (b)  $MoSe_2$ , (c)  $MoTe_2$ , (d)  $WSe_2$ , and (e)  $WTe_2$ .  $G_0 = 2e^2/h$ .

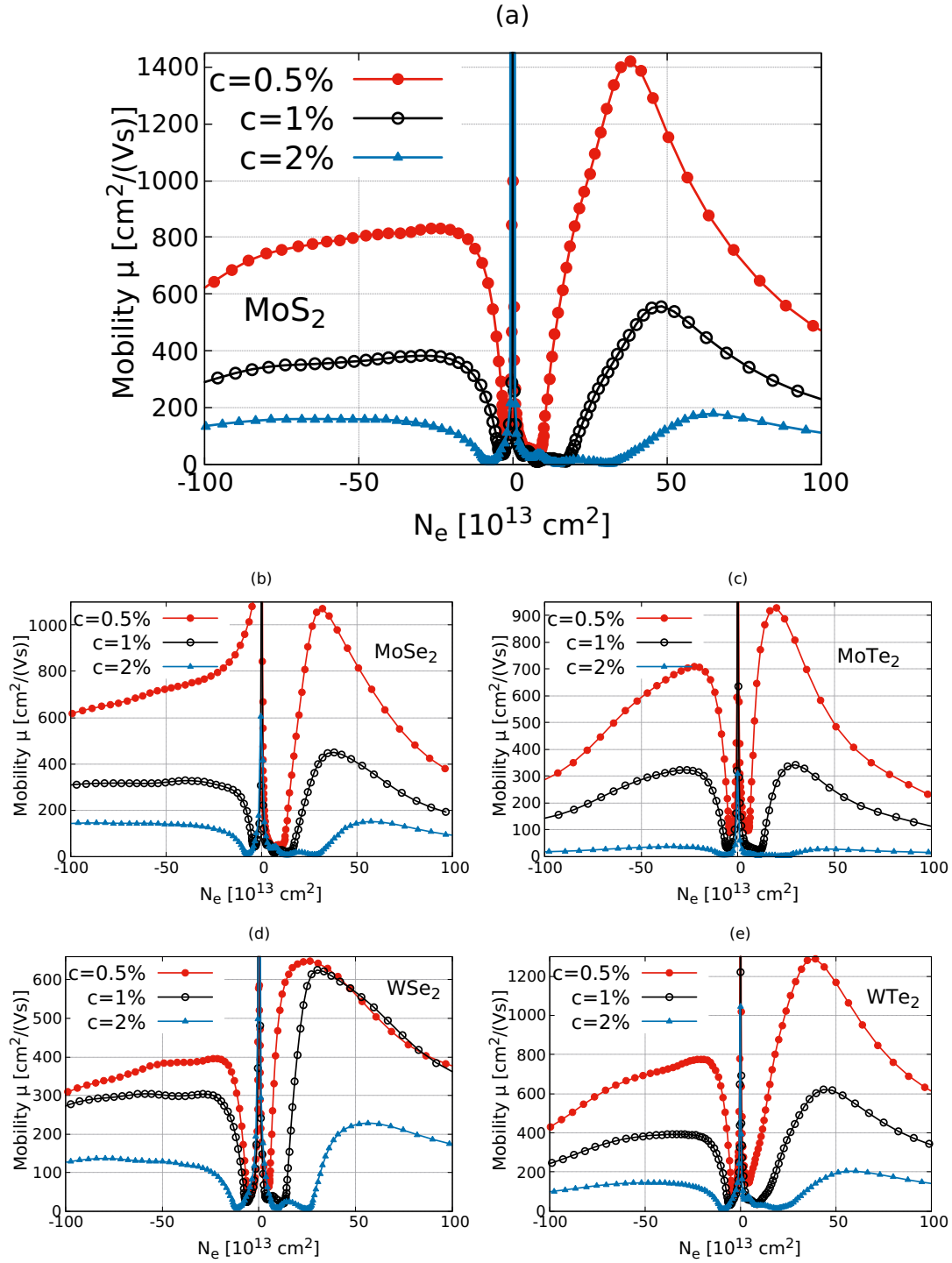


Figure 4.13: Mobility ( $\mu$ ) at room temperature ( $T \approx 300\text{K}$ ) versus number of charge carriers ( $N_e$ ) in  $\text{MX}_2$  for different concentration ( $c = 0.5\%$ ,  $1\%$ , and  $2\%$ ) of point defects (vacancies by random removal of atoms  $\text{M} = \text{Mo}, \text{W}$  or  $\text{X} = \text{S}, \text{Se}, \text{Te}$ ). (a)  $\text{MoS}_2$ , (b)  $\text{MoSe}_2$ , (c)  $\text{MoTe}_2$ , (d)  $\text{WSe}_2$ , and (e)  $\text{WTe}_2$ . The numerical calculation of the mobility is no more valid when  $N_e \rightarrow 0$  as the conductivity in equation 4.16 is overestimated because of the tail of the Lorentzian used in the recursion method, therefore the peak in  $\mu$  at zero is a numerical artifact.

## 4.6 Conclusion

In this chapter, we proposed an eleven band tight-binding model for different TMDS, and investigate the electronic band structure with and without spin orbit coupling compared to the first-principle calculations done with the ABINIT program. We have studied the density of states without and with point defects using recursion method. The point defects in the TMDS create midgap states. We have studied numerically the quantum diffusion of charge carriers in monolayers of different types of TMDS in the presence of local defects. For the transport properties, we used Kubo-Greenwood formulas to calculate Diffusivity, conductivity, inelastic mean free path, elastic mean free path and microscopic conductivity. We analyze conductivity versus scattering time obtained the three different types of regimes as expected: ballistic regime, Diffusive regime and localized regime. In the ballistic regime, electrons are traveling through the system without suffering any scattering that means conductivity remains a linear function (not exactly linear function in time because of many orbitals in the TMDS) in time. In the diffusive regime, weak disorder is characterized by a saturation of diffusivity, this saturation identifies the transport or relaxation time. In the localized regime, strong disorder by an increasing contribution of quantum interference reduces the diffusion coefficient. Once the system reached the diffusive regime, which corresponds to an inelastic relaxation time close to the elastic relaxation time, we can calculate the microscopic conductivity at every energy  $E$ , the thermodynamic average conductivity, and the mobility.

The presented results are preliminary results that show qualitatively good agreement with the experiments [121] and the previous theoretical works [53,240]. For small concentration of defects, the microscopic conductivity has a behavior close to that expected in the Boltzmann theory. For large concentration of defects, situation is different as defects change a lot, the density of states and multiple scattering effect may be more important. A perspective for future works is to study the spin orbit coupling effect on transport [223] (calculations are now in progress but computation time is very long), and the analysis in more details of the effects of specific static defects such as atomic substitutional S atoms by Ni, that have been found from STM measurements [41].



## Chapter No. 5

---

### *Structural and electronic properties of graphene/MoS<sub>2</sub> & graphene/WSe<sub>2</sub>*

---

	Page
5.1 Introduction & experimental motivation . . . . .	87
5.2 Computational details . . . . .	89
5.2.1 Density functional theory . . . . .	89
5.2.2 Choice of hexagonal supercell structure . . . . .	90
5.3 Graphene/MoS <sub>2</sub> heterostructure [4:3] . . . . .	90
5.3.1 Atomic structure . . . . .	90
5.3.1.1 Non relaxed structure . . . . .	90
5.3.1.2 Relaxed structure . . . . .	91
5.3.2 Electronic band structure . . . . .	92
5.3.2.1 Influence of pseudopotentials . . . . .	94
5.3.2.2 Interlayer distance effect . . . . .	95
5.3.2.3 Relaxation effect . . . . .	95
5.3.2.4 Spin orbit coupling effect . . . . .	98
5.4 Graphene/MoS <sub>2</sub> heterostructure [5:4] . . . . .	99
5.4.1 Atomic structure . . . . .	99
5.4.1.1 Non relaxed structure . . . . .	99
5.4.1.2 Relaxed structure . . . . .	100
5.4.2 Electronic band structure . . . . .	101
5.4.2.1 Relaxation effect . . . . .	101
5.4.2.2 Spin orbit coupling effect . . . . .	105
5.5 Graphene/MoS <sub>2</sub> heterostructure [9:7] . . . . .	106
5.5.1 Atomic structure . . . . .	106
5.5.1.1 Non relaxed structure . . . . .	106
5.5.1.2 Relaxed structure . . . . .	107

---

5.5.2	Electronic band structure . . . . .	108
5.5.2.1	Relaxation effect . . . . .	108
5.5.2.2	Spin orbit coupling effect . . . . .	113
5.6	Graphene/WSe <sub>2</sub> heterostructure [4:3] . . . . .	115
5.6.1	Atomic structure . . . . .	115
5.6.1.1	Non relaxed structure . . . . .	115
5.6.1.2	Relaxed structure . . . . .	116
5.6.2	Electronic band structure . . . . .	118
5.6.2.1	Relaxation effect . . . . .	118
5.6.2.2	Spin orbit coupling effect . . . . .	119
5.6.2.3	Structural imperfection effects . . . . .	120
5.7	Conclusion . . . . .	123

---

## 5.1 Introduction & experimental motivation

The last decade onwards, several 2D materials namely graphene, BN, MoS<sub>2</sub>, MoSe<sub>2</sub>, WS<sub>2</sub>, WSe<sub>2</sub>, MoTe<sub>2</sub>, Xene sheets (X = Si, Ge, Sn), phosphorene, bismuthene, and many more, have been fabricated and extensively investigated due to their promising applications in the electronic, valleytronic, spintronics, catalysis, energy and bi-sensing areas [7, 49, 91, 139, 152, 154, 190, 191, 197, 226]. Several types of 2D materials can be vertically stacked to design van der Waals (vdW) heterostructures which often enhance the desirable properties of the constituent atomic layers [54, 82, 140, 237]. These heterostructures offer unique ways to tailor their remarkable properties, hence they have promising applications in modern technology. However, control of the doping type, carrier concentration and stoichiometry remains challenging in most of the known 2D materials and vdW heterostructures [82].

A single layer of a graphene exhibits numerous novel features such as ultra high intrinsic mobility ( $200000 \text{ cm}^2\text{V}^{-1}\text{s}^{-1}$ ), large electrical conductivity, excellent thermal conductivity ( $5000 \text{ Wm}^{-1}\text{K}^{-1}$ ), bio-sensing, and exceptional elastic and mechanical properties with a large Young's modulus ( $\approx 1.0 \text{ TPa}$ ) [3, 90, 151]. However, the negligible intrinsic spin orbit coupling (SOC) and correspondingly small energy bandgap limit many practical applications of pristine graphene in spintronics. In recent years, researchers have succeeded in enhancing the bandgap of graphene by several orders using unconventional methods and substrate proximity effects. The availability of many other 2D materials allow us to design new graphene based vdW heterostructures having strong proximity effects. A particular family of such 2D crystals is given by the semiconducting Transition Metal Dichalcogenides (TMDs) MX<sub>2</sub> (M = Mo, W and X = S, Se, Te) that shows interesting optoelectronic and valleytronic features, and offer strong proximity effects on graphene's electronic band structure [1, 56, 57, 84, 227].

In pursuit of combining the novel features of graphene and MoS<sub>2</sub> monolayers, and mitigate their undesirable properties, researchers have recently made outstanding efforts to combine graphene and MoS<sub>2</sub> monolayers, and built graphene/MoS<sub>2</sub> vdW bilayer heterostructures [9, 28, 54, 140, 188]. Lattice incommensurate graphene/MoS<sub>2</sub> bilayer heterostructures show intriguing properties that can be controlled by tuning several factors such as strain, relative sliding between the layers, interlayer twist, doping, bending, stacking order, and interrelation [27, 44, 164, 189, 228]. Due to the lattice mismatch between the graphene and MoS<sub>2</sub> monolayer, moiré patterns are expected to appear in graphene/MoS<sub>2</sub> vdW heterostructures, which

has been observed in the recent experiments [6, 56, 120, 238].

The proximity of MoS<sub>2</sub> induces relatively strong SOC effects in graphene opening an energy bandgap in the scale of meV at the Dirac point [56]. This bandgap can be further enhanced by means of gating and strain. Interestingly, the substrate induced SOC effects compete with the intrinsic SOC of graphene causing anti crossing of spin-split bands near the Dirac point [1]. One can also realize distinct topological quantum phases in graphene/MoS<sub>2</sub> heterostructures by exploiting interlink between the proximity effects, SOC and staggered potential [1]. Gmitra et al. [56] have demonstrated that a SOC induced band inversion occurs near the Dirac point in graphene/WSe<sub>2</sub> heterostructure, thanks to the large SOC of W, which yields a quantum spin Hall phase with chiral edge states in the graphene/WSe<sub>2</sub> heterostructure. A similar topological phase transition can be realized in graphene/MoS<sub>2</sub> heterostructures by applying a gate voltage [56]. In addition, recent works report the observation of exceptional optical response with large quantum efficiency, gate tunable persistent photoconductivity, excellent mechanical response, high power conversion efficiency, photo current generation, and negative compressibility in the graphene/MoS<sub>2</sub> heterostructures [9, 18, 28, 101, 188]. In practical applications, researchers have constructed electronic logic gates, transistors, memory devices, optical switches and biosensors using graphene/MoS<sub>2</sub> heterostructures [9, 18, 27, 28, 101, 188].

In this chapter, we report DFT results for the structural and electronic properties of graphene/MoS<sub>2</sub> and graphene/WSe<sub>2</sub> bilayer heterostructures, with and without structural relaxation and also with and without spin orbit coupling.

- **Without relaxation:** We take the reference of MoS<sub>2</sub> simple monolayer (acell (lattice parameters), position of atoms, ...etc), constructing super cells to avoid lattice mismatch between the graphene and MoS<sub>2</sub> layers. Thus, the lattice parameters of the graphene is adapted according to the choice of the supercell.
- **With relaxation:** We start from the case without relaxation (above case) and the lattice parameters of the hexagonal supercell and the atomic positions are optimized.

An important task is to analyze the behavior (stretching or compressing) of graphene layer and TMD layer in the graphene/MoS<sub>2</sub> and graphene/WSe<sub>2</sub> vdW bilayer heterostructure, for different choice of the supercell. Graphene/MoS<sub>2</sub>[4:3] and graphene/MoS<sub>2</sub>[5:4] structures have significant lattice mismatches, whereas there is no experimental evidence of such a lattice mismatch. This mismatch introduce important modifications of the band structures (for instance a charge

transfer from one layer to the other in graphene/MoS<sub>2</sub>[4:3]) that are not conform by experimental result. This is why we investigated the graphene/MoS<sub>2</sub>[9:7] configuration, which seems more realistic since it has a small lattice mismatch. Indeed, we will find that this modifies the result for the band structure and in particular no charge transfer occurs in the graphene/MoS<sub>2</sub>[9:7] system.

## 5.2 Computational details

### 5.2.1 Density functional theory

Density functional theory (DFT) [73, 93] based first principle calculations were carried out by the ABINIT code [60], using the Perdew-Burke-Ernzerhof (PBE) parameterized generalized gradient approximation (GGA) exchange-correlation functional [168] and the local density approximation (LDA) exchange-correlation functional [88]. Fourteen valence electrons of W ( $5s^2, 5p^6, 5d^4, 6s^2$ ), Mo ( $4s^2, 4p^6, 4d^5, 5s^1$ ), six valence electrons of Se ( $4s^2, 4p^4$ ), S ( $3s^2, 3p^4$ ) and four valence electrons of C ( $2s^2, 2p^2$ ) are taken into account in the PAW-PBE pseudopotential. In order to minimize the lattice mismatch between the graphene and MoS<sub>2</sub> layers, we considered three different types of supercell geometries like  $4 \times 4$  (graphene)/ $3 \times 3$  (MoS<sub>2</sub>) [hereafter 4:3],  $5 \times 5$  (graphene)/ $4 \times 4$  (MoS<sub>2</sub>) [hereafter 5:4] and  $9 \times 9$  (graphene)/ $7 \times 7$  (MoS<sub>2</sub>) [hereafter 9:7] to reduce the lattice mismatch of the graphene and MoS<sub>2</sub> layers.

The total number of atoms in each heterostructures unit cell. There are 309 atoms in graphene/MoS<sub>2</sub> [9:7], 98 atoms in graphene/MoS<sub>2</sub> [5:4], and 59 atoms in graphene/MoS<sub>2</sub> [4:3]. Another very similar heterostructure was built from 4 unit cells of graphene and 3 unit cells of different material WSe<sub>2</sub> (graphene/WSe<sub>2</sub> [4:3]). A vacuum thickness larger than 20 Å was added along the c-axis to avoid the periodic interactions. The lattice parameters and inner coordinates of atoms were optimized until the Hellmann-Feynman forces (Tolerance on the Difference of Forces) was less than  $10^{-4}$  eV/Å per atom, and  $10^{-10}$  eV was defined as the total energy difference criterion for convergence of the electronic self consistent calculations. We used 20 Hartree (544 eV) as the kinetic energy cutoff of plane wave basis set and a  $\Gamma$ -type  $3 \times 3 \times 1$  [9:7],  $\Gamma$ -type  $6 \times 6 \times 1$  [5:4] and  $\Gamma$ -type  $12 \times 12 \times 1$  [4:3] k-point mesh was employed to sample the irreducible Brillouin zone of heterostructures and also van der Waals (vdW) corrections were included in the structural optimization. We have checked different pseudopotentials and xc functionals (LDA-PW-PAW and GGA-PBE-PAW <sup>1</sup>) for 4:3 and 5:4 heterostructures, but for 9:7 heterostructure we have checked only LDA-PW-

<sup>1</sup>I used a pseudopotentials produced by Jollet et al using PAW atomic datasets [86] in ABINIT. Note: LDA-PW and GGA-PBE are exchange-correlation functional.

PAW, because of the band structure calculations with both LDA-PW-PAW and GGA-PBE-PAW give a very similar results. The crystal structure figures are made by XCRYSDEN visualization [94].

### 5.2.2 Choice of hexagonal supercell structure

The large lattice mismatch between the graphene and MoS<sub>2</sub> monolayers ( $\approx 22.67\%$ ) makes the *ab initio* modeling of graphene/MoS<sub>2</sub> bilayer heterostructures computationally demanding. In order to minimize the lattice mismatch, one can vertically stack two commensurate supercells of graphene and MoS<sub>2</sub> monolayers. The most commonly used graphene/MoS<sub>2</sub> heterostructures are [45,176,195,196]: (i) graphene/MoS<sub>2</sub> [4:3], and (ii) graphene/MoS<sub>2</sub> [5:4], where the latter has relatively smaller lattice mismatch like 4:3 ( $\approx 3.33\%$ , number of atoms in the unit cell 59) and 5:4 ( $\approx 2.52\%$ , number of atoms in the unit cell 98) but larger number of atoms/cell. In my work, I tried to reduce the lattice mismatch between the graphene and MoS<sub>2</sub> layers, for that we create a larger supercell, nine unit cells of graphene and seven unit cells of MoS<sub>2</sub> monolayers, vertically stacked graphene/MoS<sub>2</sub> [9:7] heterostructure has very small lattice mismatch ( $\approx 0.53\%$ , and number of atoms in the unit cell 309).

## 5.3 Graphene/MoS<sub>2</sub> heterostructure [4:3]

### 5.3.1 Atomic structure

#### 5.3.1.1 Non relaxed structure

The crystal structure of the graphene/MoS<sub>2</sub> bilayer heterostructure is shown in Fig. 5.1(a) side view, Fig. 5.1(b) top view. Unit cells and lattice parameters of graphene and MoS<sub>2</sub> monolayers are shown in Fig. 5.1(c) and also bilayer (interlayer) separation distance the between graphene (4×4) and MoS<sub>2</sub> (3×3) layers see Fig. 5.1(d). The crystal structure of graphene/MoS<sub>2</sub> [4:3] bilayer heterostructure was constructed with the reference of MoS<sub>2</sub> cell. We have done bilayer separation distance calculations by using LDA-PAW pseudopotentials obtained a bilayer (interlayer) separation distance between the two layers C-Mo distance 4.9 Å and C-S distance 3.33 Å.

In graphene/MoS<sub>2</sub> [4:3] bilayer heterostructures, graphene and MoS<sub>2</sub> monolayers weakly interact through long range vdW interactions. The experimentally reported interlayer distance between the graphene and MoS<sub>2</sub> nano sheets is  $3.4\pm 0.1\text{Å}$  [171]. However, many first principles studies inconsistently predicted interlayer gap (C-S distance) values ranging from 3.1 Å to 4.3 Å [43, 56, 75, 85, 102, 189, 193]. This is mainly because of the inadequate evaluation of weak

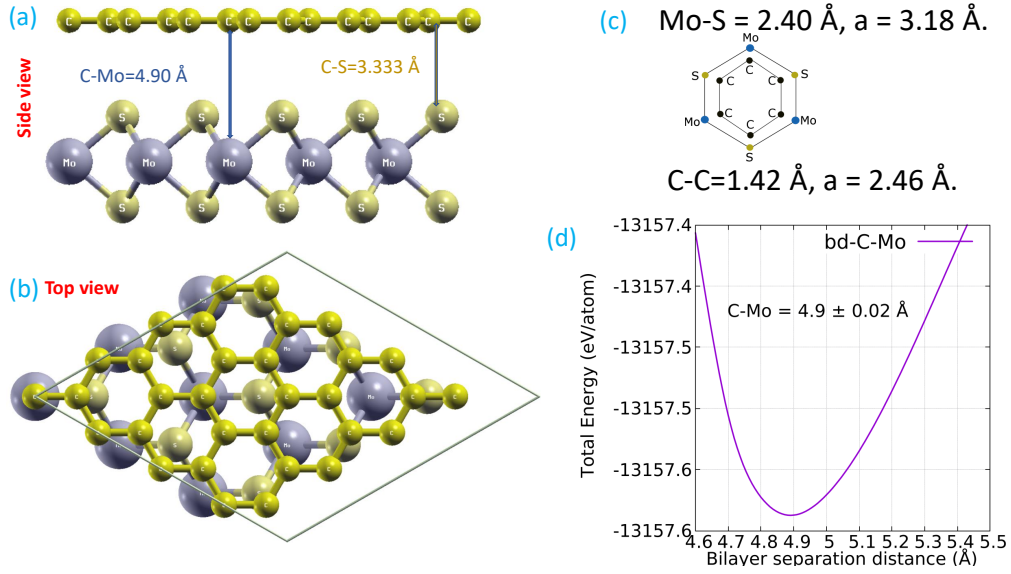


Figure 5.1: Non relaxed crystal structure of graphene/MoS<sub>2</sub> [4:3] bilayer heterostructure. (a) Side view (blue lines indicate the distance between the carbon to molybdenum, and carbon to top sulfur). (b) Top view. (c) Unit cells of graphene and MoS<sub>2</sub> monolayers lattice mismatch. (d) Bilayer separation distance between the graphene (4×4) and MoS<sub>2</sub> (3×3) layers, with the lattice parameter of MoS<sub>2</sub>. All the calculations have been done by using LDA-PW-PAW pseudopotentials and basic reference was taken MoS<sub>2</sub> unit cell.

nonlocal vdW interactions with the DFT framework. Various DFT-vdW methods [62, 103] have been used to describe this system to be insufficient, for vdW corrections efficiently evaluates the long range vdW interactions in this system, and accurately predicts the interlayer spacing between graphene and MoS<sub>2</sub> sheets, which is in remarkable agreement with the experimental data [171].

### 5.3.1.2 Relaxed structure

To find out the most stable configuration of the graphene/MoS<sub>2</sub> bilayer heterostructure, we relaxed the heterostructure using several starting positions of the graphene layer relative to the MoS<sub>2</sub> layer. The optimized lattice parameters of the 4:3 bilayer with the least lattice mismatch are  $a = b = 9.784$  Å as shown in Fig. 5.2. For the structural optimization, the atomic positions and unit cell lattice parameters are changed; in the case of MoS<sub>2</sub> unit cell is extended by 2.45 % and the graphene unit cell is compressed by 0.61 %. Optimized average interlayer distances are: C-Mo distance 4.902 Å, C-S distance 3.367 Å and S-S distance 3.073 Å. The bond lengths of Mo-S and C-C are changed which is in good agreement with the experimentally reported [171].

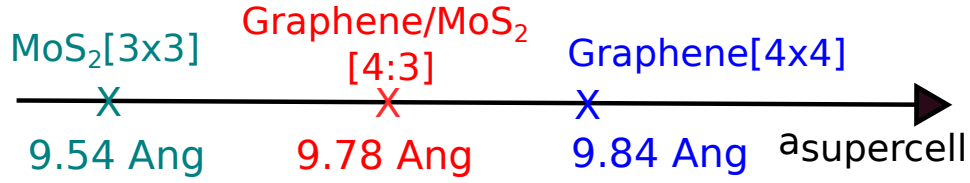


Figure 5.2: Simplified sketch of the lattice parameters of hexagonal superlattice of relaxed graphene/MoS<sub>2</sub> [4:3] bilayer heterostructure, comparison to MoS<sub>2</sub> and graphene supercells alone. In our work the basic reference (without relaxation) has taken MoS<sub>2</sub> (3×3) unit cell.

We analyzed structural optimization of graphene/MoS<sub>2</sub> [4:3] bilayer heterostructure along the  $z$ -direction see Fig. 5.3. Without optimization of carbon layer, atomic positions occupied along the  $c$ -axis at 4.9 Å, after optimization the atoms are moving up and down it seems to look like a cosine wave see Fig. 5.3-(a). The carbon layer atoms are moving along the  $c$ -axis the maximum is 4.914 Å and the minimum is 4.8874 Å. This same phenomenon happened to the MoS<sub>2</sub> layer, without optimization the Mo atoms are at rest position at 0.0 Å along the  $c$ -axis, after optimization the Mo atoms are moving along the  $c$ -axis the maximum is 0.0012 Å and the minimum is -0.0026 Å see Fig. 5.3-(d). Without optimization the top S atoms are at rest position at 1.5667 Å along the  $c$ -axis, after optimization the top S atoms are moving along the  $c$ -axis the maximum is 1.5352 Å and the minimum is 1.5335 Å see Fig. 5.3-(b). Without optimization the bottom S atoms stay at -1.5667 Å along the  $c$ -axis, after optimization the bottom S atoms are moving along the  $c$ -axis the maximum is -1.5381 Å and the minimum is -1.5387 Å see Fig. 5.3-(e). We took the reference of MoS<sub>2</sub> (3×3) unit cell value then constructed a 4:3 structure without optimization. After atomic positions and lattice parameter optimization, the graphene layer was compressed and the MoS<sub>2</sub> layer has stretched as shown in Fig. 5.2. We checked displacement of atoms along the  $xy$ -direction, it is very small  $\approx 10^{-4} a$  ( $a = 9.54$  Å). This much of small atomic displacement in the  $xy$  plane have not effect on the electronic properties of the vdW heterostructures.

### 5.3.2 Electronic band structure

The electronic band structures of bilayer heterostructure of graphene/MoS<sub>2</sub> [4:3] are calculated, including vdW, with and without SOC along with high symmetry directions of the hexagonal Brillouin zone. The electronic properties of graphene and MoS<sub>2</sub> monolayers are well preserved due to the weak vdW interactions between the monolayers. The linear dispersion of the Dirac cone lies above the bandgap of the MoS<sub>2</sub> monolayer in the graphene/MoS<sub>2</sub> [4:3] bilayer heterostruc-

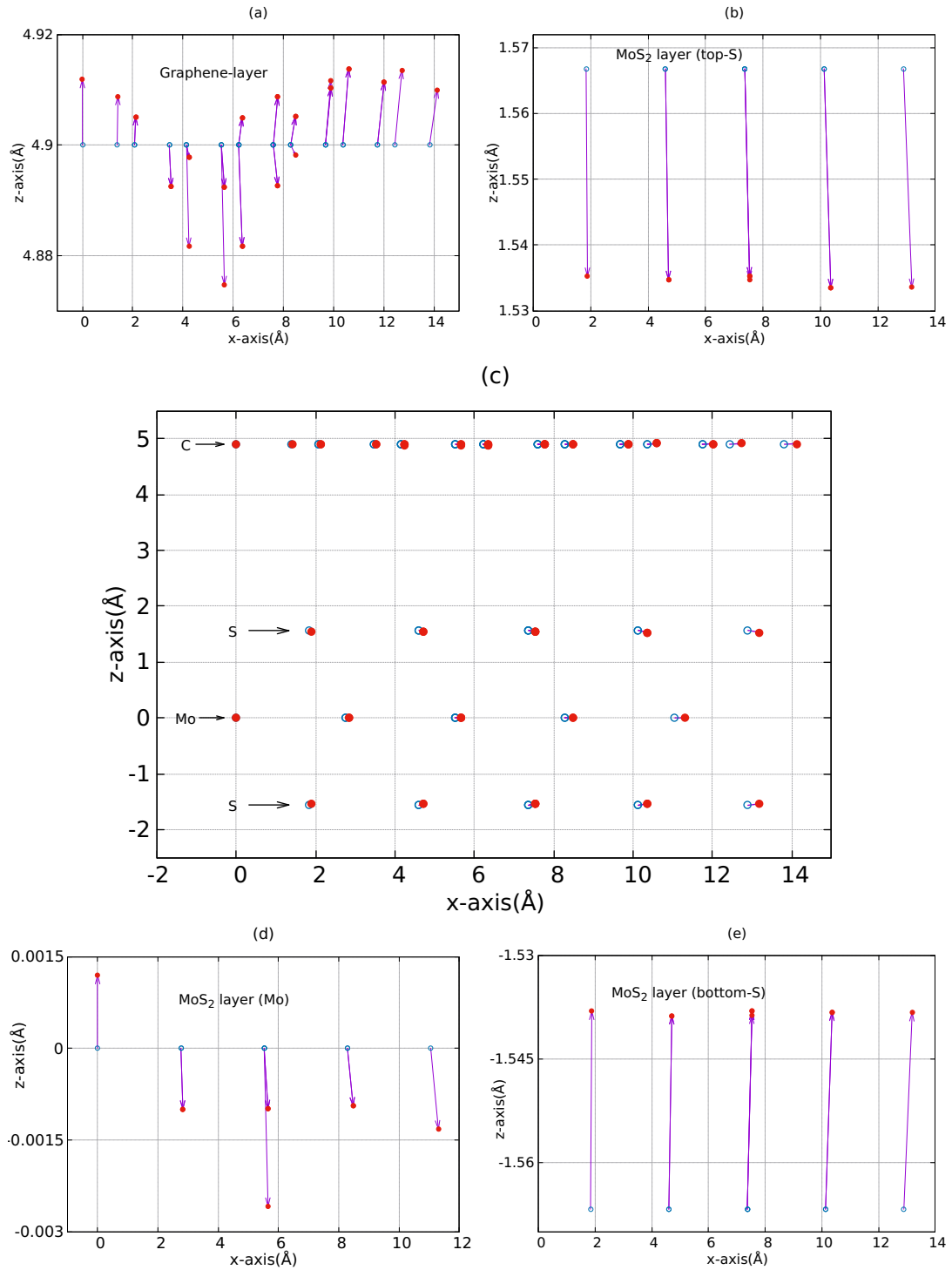


Figure 5.3: Variation of atomic positions along the  $z$ -direction in the unit cell of graphene/MoS<sub>2</sub> [4:3] bilayer heterostructure without (empty blue circles) and with (full red circles) relaxation: (a) Graphene layer, (b) MoS<sub>2</sub> layer-sulfur (top), (c) graphene/MoS<sub>2</sub> [4:3] bilayer heterostructure position of atoms in the unit cell, (d) MoS<sub>2</sub> layer-molybdenum, (e) MoS<sub>2</sub> layer-sulfur (bottom).

ture.

### 5.3.2.1 Influence of pseudopotentials

We have calculated the electronic band structure of graphene/MoS<sub>2</sub> bilayer heterostructures using different pseudopotentials and xc functionals [LDA-PW-PAW, GGA-PBE-PAW+vdW and Hartwigsen-Goedecker-Hutter (HGH) (norm conserving pseudopotentials (NCPP))] see Fig. 5.4. For the comparison of electronic bands of three different pseudopotentials, we shift the Dirac point at zero energy level, the LDA-PW-PAW pseudopotential gives a large bandgap at the highest symmetry point of Brillouin zone  $\Gamma$  because of choosing the electrons in the core and valence shells. HGH and GGA-PBE-PAW gives almost similar result on energy scale around the gap. Further calculations in this thesis will be performed by HGH and GGA-PAW+vdW<sup>2</sup>. Optimization with different pseudopotentials gives similar atomic positions. Electronic bands of individual layers of graphene/MoS<sub>2</sub>[4:3] as shown in Appendix C.1, in MoS<sub>2</sub> layer direct bandgap shifted  $K$  to  $\Gamma$ <sup>3</sup>.

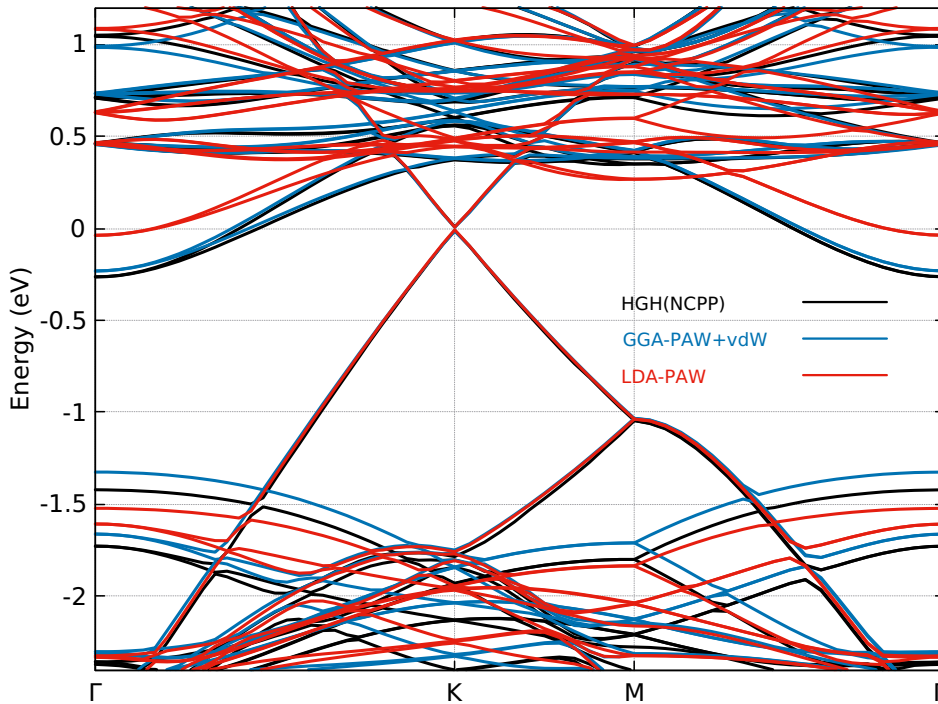


Figure 5.4: Electronic band structure of graphene/MoS<sub>2</sub> [4:3] bilayer heterostructure with optimized atomic positions and optimized lattice parameters, calculated with different pseudopotentials HGH-NCPP, GGA-PBE-PAW+vdW and LDA-PW-PAW. Optimization with different pseudopotentials gives similar positions.

<sup>2</sup>HGH( $E_{cut} \approx 20$  Hartree), GGA-PBE-PAW ( $E_{cut} \approx 22$  Hartree) and LDA-PW-PAW( $E_{cut} \approx 21$  Hartree).

<sup>3</sup>In the Brillouin zone of a  $n \times n$  supercell, the K point is shift to  $\Gamma$  when  $n$  is a multiple of 3 (see Appendix A.2).

### 5.3.2.2 Interlayer distance effect

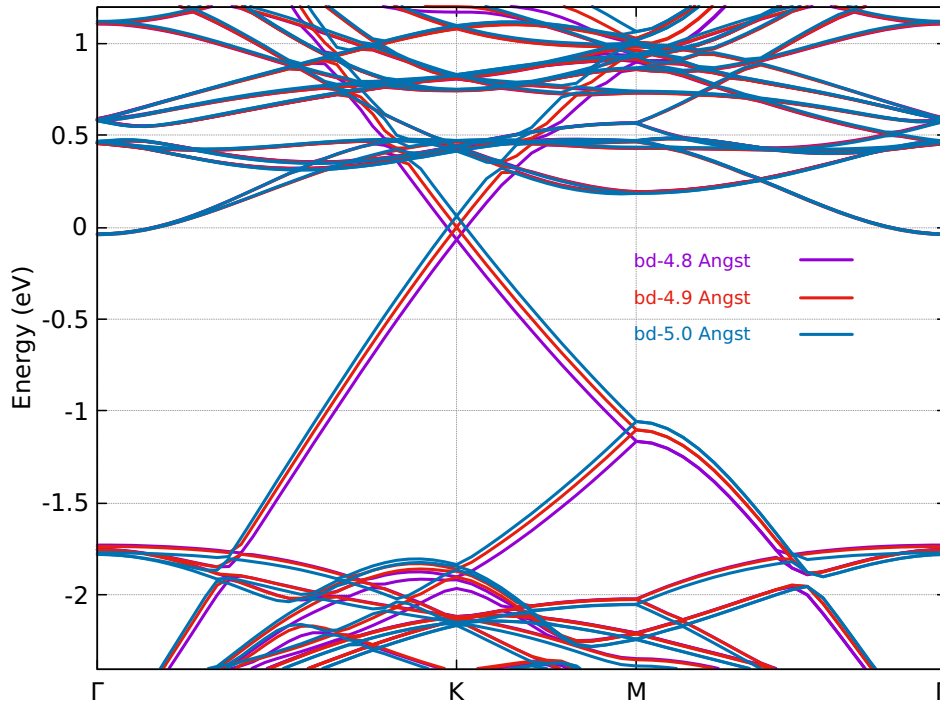


Figure 5.5: Electronic band structure of graphene/MoS<sub>2</sub> [4:3] bilayer heterostructure with different bilayer (interlayer) separation distance between carbon and molybdenum layers (C-Mo), all the calculations have done by using LDA-PW-PAW pseudopotentials. Calculations are done without relaxation and with the lattice parameter of MoS<sub>2</sub>.

After structural relaxation of the graphene/MoS<sub>2</sub> [4:3] bilayer heterostructure, we obtained a bilayer separation (interlayer) distance is 4.9 Å. Fig. 5.5 show that the effect of a different bilayer separation (interlayer) distance. The bilayer separation (interlayer) distance between the layers increases, the Dirac point moves up in the energy ( $y$ -axis) level corresponding to the highest symmetry points of the Brillouin zone  $\Gamma$  and  $K$  points at the conduction band. The bilayer (interlayer) separation distance between the layers decreases, the Dirac point moves down in the energy ( $y$ -axis) level corresponding to the highest symmetry points of Brillouin zone  $\Gamma$  and  $K$  points at the conduction band.

### 5.3.2.3 Relaxation effect

A comparison of electronic band structure of graphene/MoS<sub>2</sub> [4:3] bilayer heterostructures with relaxation, without relaxation and also atomic positions are not relaxed and lattice parameters are relaxed is shown in Fig. 5.6. After relaxation, the position of atoms and unit cell parameters are changed either compressed or stretched graphene and MoS<sub>2</sub> layers is shown in Fig. 5.3 and Fig. 5.2.

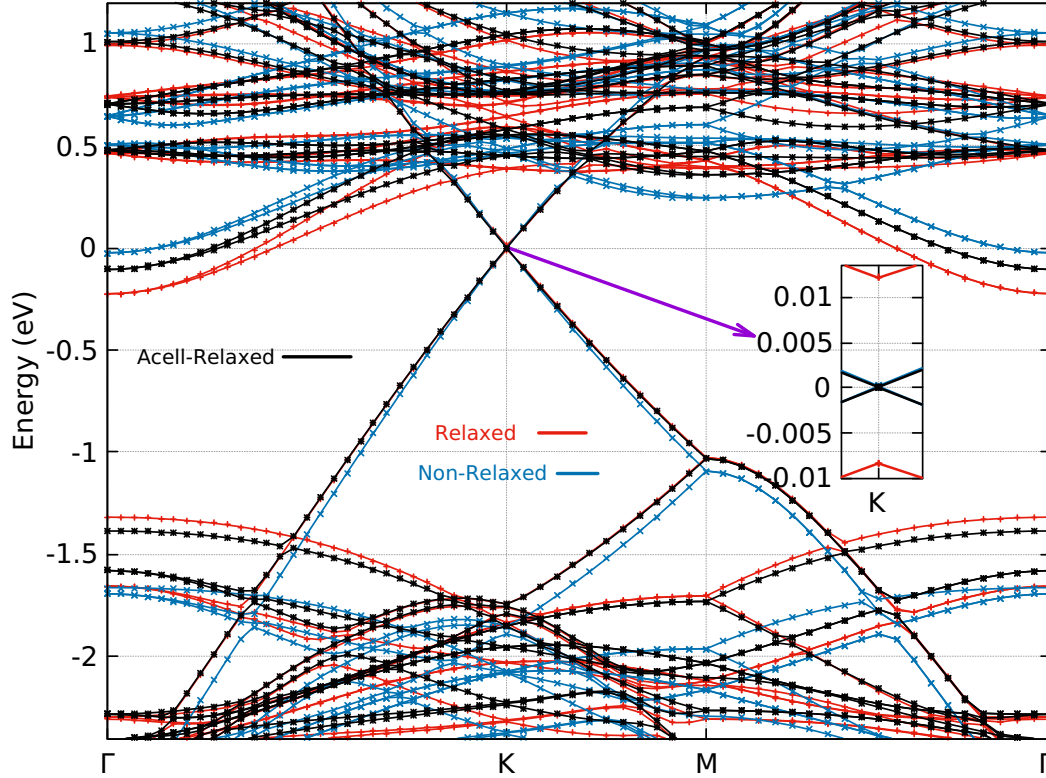


Figure 5.6: Comparison of electronic band structure of graphene/MoS<sub>2</sub> [4:3] bilayer heterostructure with relaxation (red lines), without relaxation (blue lines), and the lattice parameters (acell) are relaxed and the atomic positions are not relaxed (black lines). Zoom of the bands around the Dirac point (inset). The points are calculated results and lines are guide for the eyes. All the calculations have been done by using GGA-PAW pseudopotentials (PBE) including vdW. For comparison of electronic bands, we shift the Dirac cone at zero energy.

4:3 band structure has a bandgap at Dirac point ( $K$ -point in the Brillouin zone) due to the optimized atomic positions, at  $\Gamma$ -point in the Brillouin zone minimum of the conduction band bands and maximum of the valence band bands close together because of optimized lattice parameters (major contribution) and also optimized atomic positions is shown in Fig. 5.6. After the relaxation of atomic positions and lattice parameters of graphene/MoS<sub>2</sub> [4:3] bilayer heterostructure has an internal stress and strain because of that we got a small bandgap ( $\approx 20.5$  meV) at the Dirac point ( $K$ -point), this bandgap mainly comes from relaxed atomic positions of graphene/MoS<sub>2</sub> [4:3] bilayer heterostructure is shown in Fig. 5.6. For the calculation of electronic and optical properties of the system, structural and lattice optimization play a crucial role. The effect of relaxed atomic positions and non-relaxed lattice parameters on electronic band structure of graphene/MoS<sub>2</sub> [4:3] bilayer heterostructure is shown in Fig. 6 of appendix C.2.

The weak vdW interaction between graphene and MoS<sub>2</sub> monolayers yields a small, but it significant, bandgap at the Dirac point. Fig. 5.6 shows that the bandgap in 4:3 bilayer is  $\approx 20.5$  meV. Another interesting result of the 4:3 bilayer heterostructure is a shift of the optical (direct) bandgap of MoS<sub>2</sub> monolayer from  $K$  to the  $\Gamma$  point of Brillouin zone (the bandgap of MoS<sub>2</sub> monolayer changes from 1.8 to 1.13 eV). Near the bandgap region valence and conduction bands have  $Mo-d_{z^2}$  character at  $\Gamma$  point. Consequently, the direct energy bandgap of the MoS<sub>2</sub> monolayer decreases in magnitude and shifts from the  $K$ -point to the  $\Gamma$  point of Brillouin zone and for the individual layers of graphene and MoS<sub>2</sub> see appendix C.1.

The charge transfer between the graphene and MoS<sub>2</sub> layers is found in Fig. 5.6. The Dirac point in the 4:3 bilayer is shifted above the Fermi-level and resides above the lowest conduction band with MoS<sub>2</sub> character. This indicates transfer of electrons from the graphene to the MoS<sub>2</sub> monolayer. The net shift of the Dirac point above the Fermi-level is  $\approx 0.265$  eV. Since the Dirac point has shifted above the Fermi-level, the bottom of the conduction band of MoS<sub>2</sub> is expected to dip below the Fermi-level to catch the electrons transferred from graphene. The lowest conduction band of MoS<sub>2</sub> near the Fermi level shows that the Fermi-level is almost 0.009 eV above the bottom of the conduction band at the  $\Gamma$  point, thus showing the presence of electrons around the  $\Gamma$  point.

In order to study the effect of direct interlayer coupling between the two layers, we compare the bands of relaxed graphene/MoS<sub>2</sub> [4:3] bilayer heterostructures with bands of graphene alone with relaxed positions of a relaxed graphene/MoS<sub>2</sub> [4:3] bilayer heterostructure and MoS<sub>2</sub> layer alone with the positions of relaxed graphene/MoS<sub>2</sub> [4:3] bilayer heterostructures see Fig. 5.7. A direct effect of interlayer coupling is would have found that at Dirac point ( $K$ -point) and at the  $\Gamma$ -point it is very small. Indeed the electronic bands of graphene/MoS<sub>2</sub> [4:3] bilayer heterostructure are similar to a sum of the electronic bands of graphene alone and the electronic bands of MoS<sub>2</sub> alone [energy shift of Dirac cone due to interlayer distance is discussed in section 5.3.2.2, atomic positions and lattice parameter values are discussed in section 5.3.1.2]. Therefore our calculations show that hopping terms of the Hamiltonian have no direct effect near the Dirac point on the electronic band structure, but the relaxation of atomic positions and lattice parameters of the heterostructure modify significantly the electronic band structure. The relaxation effect on graphene/MoS<sub>2</sub> bilayer heterostructure has not been discussed in previous literature [43, 56, 75, 85, 102, 189, 193].

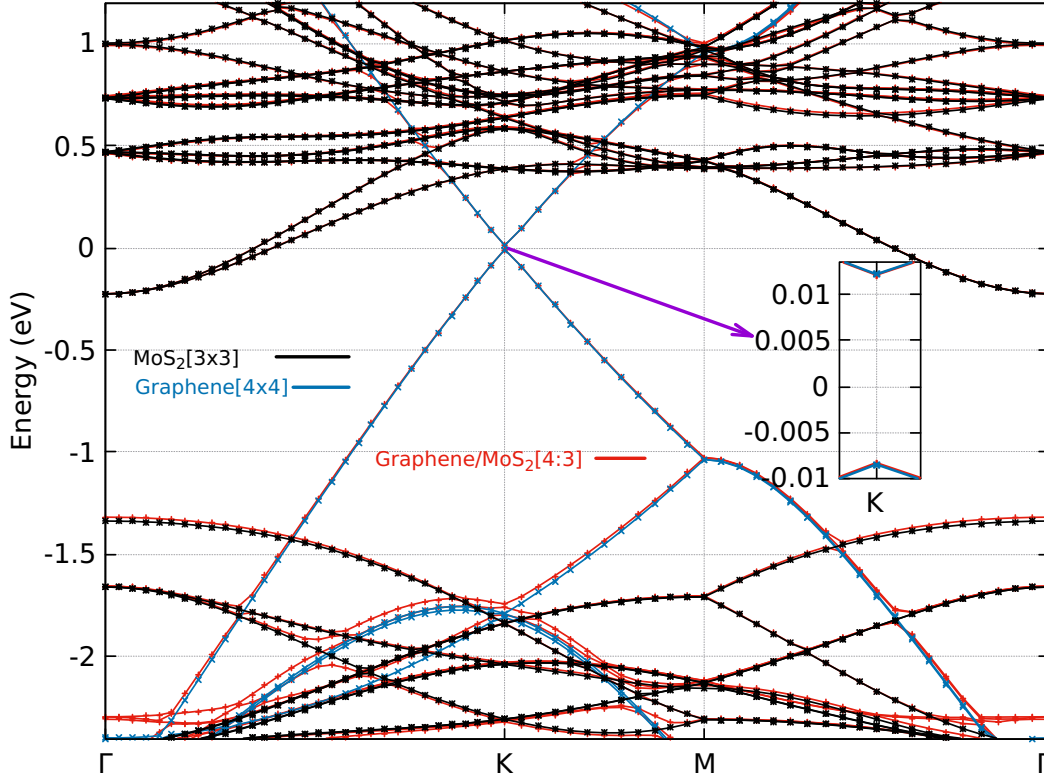


Figure 5.7: Electronic band structure of relaxed graphene/MoS<sub>2</sub> [4:3] bilayer heterostructure. Comparison between the electronic bands of relaxed graphene/MoS<sub>2</sub> [4:3] bilayer heterostructure, electronic bands of graphene layer alone and with the carbon atomic positions of the relaxed graphene/MoS<sub>2</sub> [4:3] bilayer heterostructure, electronic bands of MoS<sub>2</sub> layer alone and with the atomic positions of the relaxed graphene/MoS<sub>2</sub> [4:3] bilayer heterostructure. Zoom of the bands around the Dirac point (inset). The points are calculated results and lines are guide for the eyes. All the calculations have been done by using GGA-PAW pseudopotentials (PBE) including vdW. For the comparison of electronic bands, we shift the Dirac cone to zero energy. The Fermi level is located in between the Dirac cone and the minimum of the conduction band.

#### 5.3.2.4 Spin orbit coupling effect

The effect of the spin orbit coupling (SOC) of graphene/MoS<sub>2</sub> [4:3] bilayer heterostructure is not strong around the Dirac point see Fig. 5.8. The MoS<sub>2</sub> monolayer have a strong SOC effect at valence band (K-point) and band splitting is  $\approx 148$  meV which is in good agreement with the first principle calculations [47, 95, 186] and the band splitting of conduction band at the Dirac point is very small. The energy bandgap difference of graphene/MoS<sub>2</sub> [4:3] bilayer

heterostructure with and without SOC at the Dirac point is 1.86 meV.

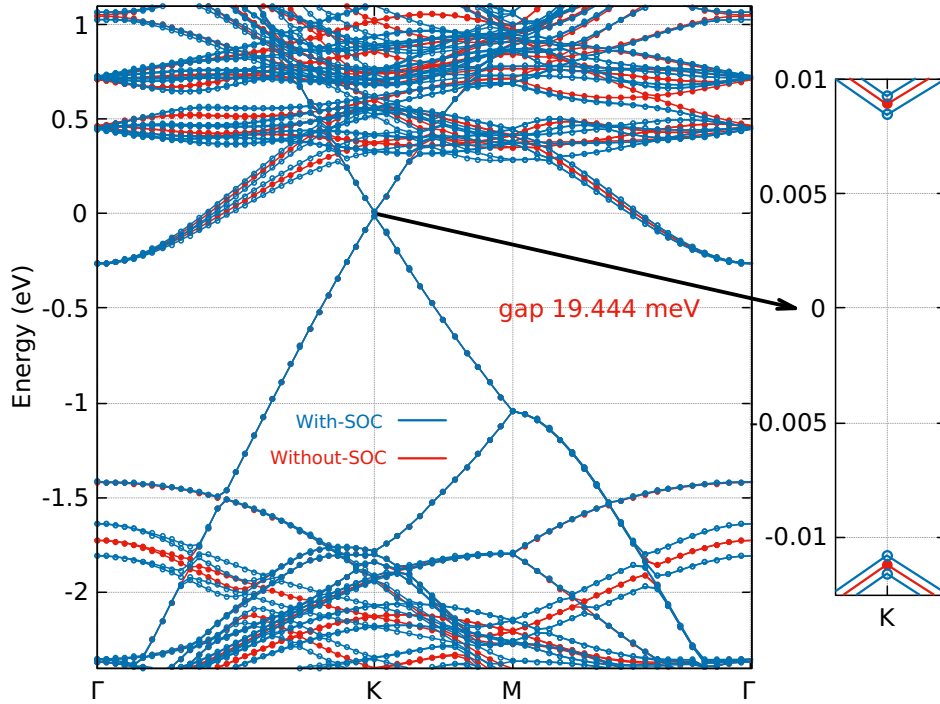


Figure 5.8: Electronic band structure of graphene/MoS<sub>2</sub> [4:3] bilayer heterostructure with (blue lines) and without (red lines) spin orbit coupling along high symmetry lines. Zoom of the bands around the Dirac point (right). The points are calculated results and lines are guide for the eyes. After SOC the bandgap at the Dirac point is reduced by  $\approx 1.86$  meV. All the calculations have been done by using GGA-PAW pseudopotentials (PBE) including vdW.

## 5.4 Graphene/MoS<sub>2</sub> heterostructure [5:4]

### 5.4.1 Atomic structure

#### 5.4.1.1 Non relaxed structure

The crystal structure of graphene/MoS<sub>2</sub> [5:4] bilayer heterostructure is shown in Fig. 5.9(a) side view, Fig. 5.9(b) top view. Unit cells and lattice parameters of graphene and MoS<sub>2</sub> monolayers are displayed Fig. 5.9(c) and bilayer (interlayer) separation distance between the graphene and MoS<sub>2</sub> layers see Fig. 5.9(d). The crystal structure of graphene/MoS<sub>2</sub> [5:4] bilayer heterostructure was constructed with the reference of MoS<sub>2</sub> cell. We have done bilayer (interlayer) separation distance calculations by using LDA-PAW pseudopotentials obtained a bilayer (interlayer) separation distance C-Mo between the two layers 4.9 Å and

C-S distance 3.33 Å.

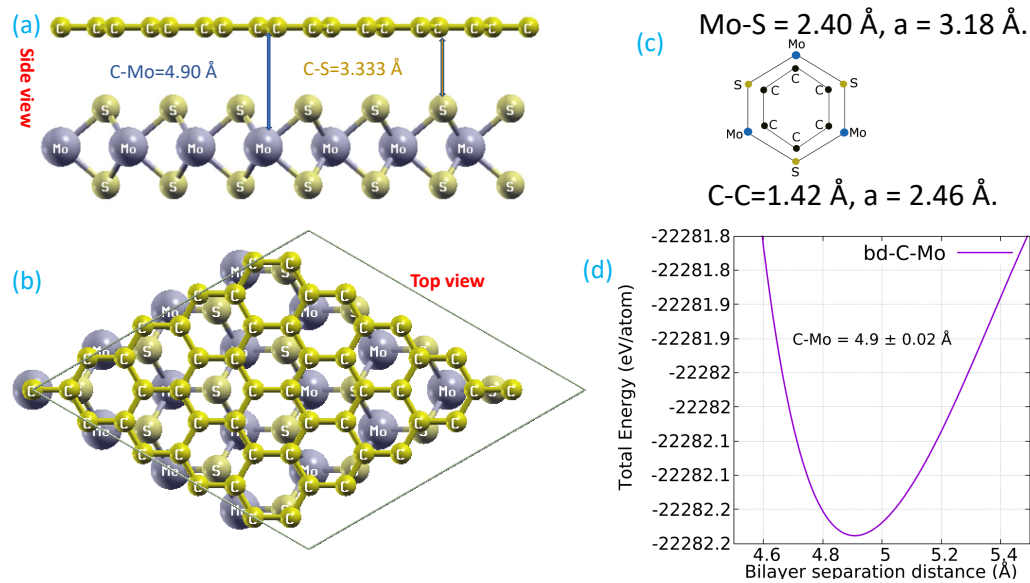


Figure 5.9: Non relaxed crystal structure of graphene/MoS<sub>2</sub> [5:4] bilayer heterostructure. (a) Side view (blue lines indicate the distance between the carbon to molybdenum, and carbon to top sulfur). (b) Top view. (c) Unit cells of graphene and MoS<sub>2</sub> monolayers lattice mismatch. (d) Bilayer separation distance between the graphene (5 × 5) and MoS<sub>2</sub> (4 × 4) layers, with the lattice parameter of MoS<sub>2</sub>. All the calculations have been done by using LDA-PW-PAW pseudopotentials and basic reference was taken MoS<sub>2</sub> (4×4) unit cell.

In graphene/MoS<sub>2</sub> bilayer heterostructures [5:4], graphene and MoS<sub>2</sub> monolayers weakly interact through long range vdW interactions. The experimentally reported interlayer distance between graphene and MoS<sub>2</sub> nano sheets is  $3.40 \pm 0.1$  Å [171]. However, many first principles studies inconsistently predicted interlayer distance (C-S) values ranging from 3.1 Å to 4.3 Å [43,56,75,85,102,189,193].

#### 5.4.1.2 Relaxed structure

To find out the most stable configuration of the graphene/MoS<sub>2</sub> [5:4] bilayer heterostructure, we relaxed the heterostructure using several starting positions of the graphene layer relative to the MoS<sub>2</sub> layer. The optimized lattice parameters of the 5:4 bilayer with the smallest lattice mismatch are  $a = b = 12.423$  Å see Fig. 5.10. The atomic positions and lattice parameters have changed, the MoS<sub>2</sub> sheet is being compressed by 2.35 % and the graphene sheet is stretched by 0.97 % from the optimized cell (lattice) parameters. Optimized average interlayer distances are: C-Mo distance 4.932 Å, C-S distance 3.287 Å and S-S



Figure 5.10: Simplified sketch of the lattice parameters of hexagonal super lattice of graphene/MoS<sub>2</sub> [5:4] bilayer heterostructure, comparison to MoS<sub>2</sub> and graphene supercells alone. In our work the basic reference (without relaxation) was taken to be MoS<sub>2</sub> (4×4) unit cell.

distance 3.288 Å. The bond lengths of Mo-S and C-C are changed which is in good agreement with the experimentally reported [171].

We analyzed structural optimization of graphene/MoS<sub>2</sub> [5:4] bilayer heterostructures along the  $z$ -direction see Fig. 5.11. Without optimization of carbon layer, position occupied along the  $c$ -axis at 4.9 Å, after optimization the atoms are moving up and down it seems to look like a cosine wave see Fig. 5.11-(a). The carbon layer atoms are moving along the  $c$ -axis the maximum is 4.9615 Å and the minimum is 4.8765 Å see Fig. 5.11-(a). The same phenomenon happened to the MoS<sub>2</sub> layer, without optimization the Mo atoms are at rest position at 0.0 Å along the  $c$ -axis, after optimization the Mo atoms are moving along the  $c$ -axis the maximum is 0.0012 Å and the minimum is -0.0025 Å see Fig. 5.11-(d). Without optimization the top S atoms are at rest position at 1.5667 Å along the  $c$ -axis, after optimization the top S atoms are moving along the  $c$ -axis the maximum is 1.6302 Å and the minimum is 1.623 Å see Fig. 5.11-(b). Without optimization the bottom S atoms stay at -1.5667 Å along the  $c$ -axis, after optimization top bottom S atoms are moving along the  $c$ -axis the maximum is -1.6557 Å and the minimum is -1.6689 Å see Fig. 5.11-(e). We took the reference of MoS<sub>2</sub> (4×4) unit cell values then constructed a 5:4 structure without optimization. After atomic positions and  $a_{cell}$  (lattice parameter) optimization, graphene layer has stretched and the MoS<sub>2</sub> layer has compressed see Fig. 5.10. We checked displacement of atoms in the  $xy$ -plane, they are very small  $\approx 10^{-4} a$  ( $a = 12.72$  Å). This small amount of atomic displacement does not affect the electronic properties of the vdW heterostructures of graphene/MoS<sub>2</sub> [5:4].

## 5.4.2 Electronic band structure

### 5.4.2.1 Relaxation effect

A comparison of the electronic band structure of graphene/MoS<sub>2</sub> [5:4] bilayer heterostructures with relaxation and without relaxation are shown in Fig. 5.12.

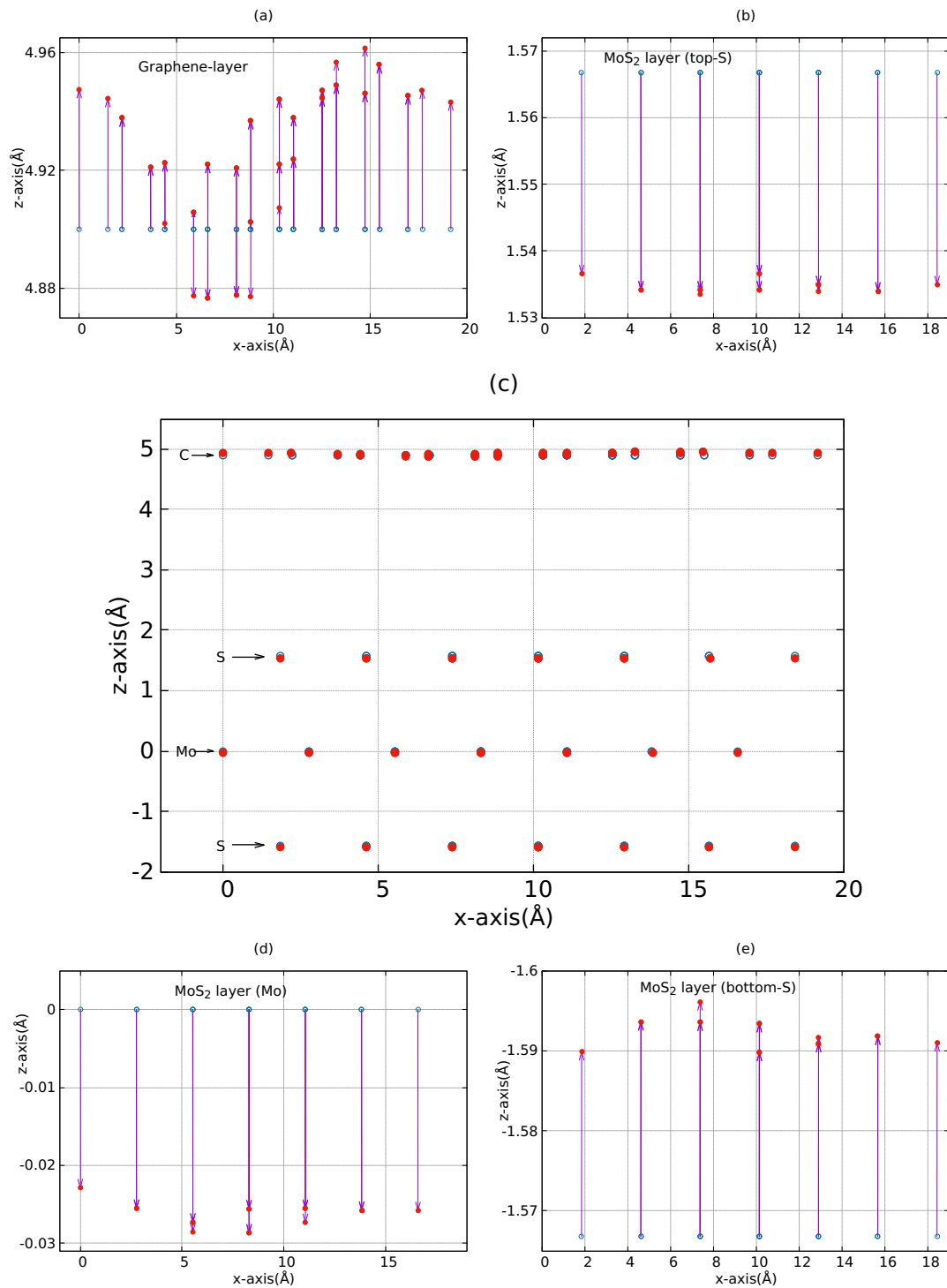


Figure 5.11: Variation of atomic positions along the  $z$ -direction in the unit cell of graphene/MoS<sub>2</sub> [5:4] heterostructure without (empty blue circles) and with (full red circles) relaxation: (a) Graphene layer (b) MoS<sub>2</sub> layer-sulfur (top) (c) graphene/MoS<sub>2</sub> [5:4] heterostructure position of atoms in the unit cell, (d) MoS<sub>2</sub> layer-molybdenum, (e) MoS<sub>2</sub> layer-sulfur (bottom).

After relaxation of the graphene/MoS<sub>2</sub> [5:4] bilayer heterostructure, the atomic positions and lattice parameters are changed with the effect that graphene and

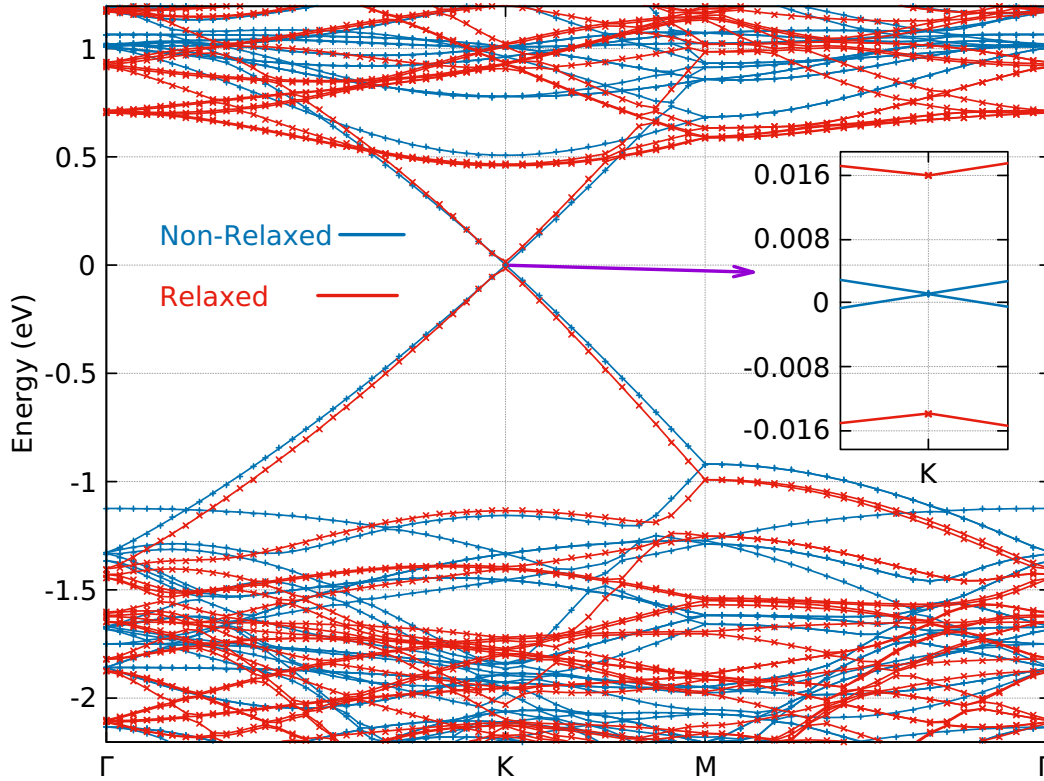


Figure 5.12: Comparison of electronic band structure of the graphene/MoS<sub>2</sub> [5:4] bilayer heterostructure with relaxation (red lines), without relaxation (blue lines). Zoom of the bands around the Dirac point (inset). The points are calculated results and lines are guide for the eyes. All the calculations have been done by using GGA-PAW pseudopotentials (PBE) including vdW. For the comparison of electronic bands, we shifted the Dirac cone to zero energy level and fermi level located near to the Dirac cone.

MoS<sub>2</sub> layers are either compressed or stretched as shown in Fig. 5.11 and Fig. 5.10. The 5:4 band structure has a bandgap at the Dirac point ( $K$ -point in the Brillouin zone) due to the optimized atomic positions, lattice parameters and also an effect on the MoS<sub>2</sub> layer. At the  $\Gamma$ -point in the Brillouin zone the minimum of the conduction band bands towards Fermi level and maximum of the valence band bands away from the Fermi level because of optimized atomic positions, and lattice parameters see Fig. 5.12.

After the relaxation of atomic positions and lattice parameters the 5:4 structure has an internal stress and the strain. Maybe this also a reason why we obtained a bandgap ( $\approx 31.32$  meV) at the Dirac point ( $K$ -point) see Fig. 5.12. Indeed, For the calculation of electronic and optical properties of the system, structural and lattice optimization plays a crucial role.

The linear dispersion of the Dirac cone lies within the bandgap of the MoS<sub>2</sub> monolayer in the 5:4 bilayer heterostructure. The weak vdW interaction between graphene and MoS<sub>2</sub> monolayers yields a small, but significant bandgap at the Dirac point. Fig. 5.12 shows that the bandgap in 5:4 bilayer is  $\approx 31.32$  meV. In 5:4 bilayer heterostructure, MoS<sub>2</sub> monolayer preserves its direct bandgap semi-conducting nature at the  $K$ -point of the Brillouin zone (the bandgap of the MoS<sub>2</sub> monolayer changes from 1.8 to 1.70 eV), which is in good agreement with the reported values in the literature [45, 176, 195]. Since the graphene/MoS<sub>2</sub> [5:4] bilayer heterostructure maintains the direct bandgap nature of the MoS<sub>2</sub> monolayer at the  $K$ -point, it can be concluded that the aforementioned transition in the 4:3 bilayer is primarily triggered by the strain effects arising due to the large lattice mismatch [196].

No charge transfer between the graphene and MoS<sub>2</sub> layers can be observed in Fig. 5.12, which is the case of minimal strain. This finding is consistent with the experimental observations by Diaz et al [31], who performed angle resolved photo emission spectroscopic (ARPES) measurements to probe the electronic structure of graphene/MoS<sub>2</sub> bilayer heterostructures. They observed that the Dirac cone of graphene remains intact and no significant charge transfer occurs between the graphene and MoS<sub>2</sub> layers.

In order to study the effect of direct interlayer coupling between the two layers, we compare the bands of the relaxed graphene/MoS<sub>2</sub> [5:4] bilayer heterostructure with bands of graphene alone with relaxed positions of the relaxed graphene/MoS<sub>2</sub> [5:4] bilayer heterostructure and the MoS<sub>2</sub> layer alone with the positions of relaxed graphene/MoS<sub>2</sub> [5:4] bilayer heterostructure see Fig. 5.13. The direct effect of interlayer coupling found at  $\Gamma$ -point and at the Dirac point ( $K$ -point) is very small. Indeed the electronic bands of graphene/MoS<sub>2</sub> [5:4] bilayer heterostructure are similar to the sum of the electronic bands of graphene alone and the electronic bands of MoS<sub>2</sub> alone [energy shifts because of atomic positions and lattice parameter values see section 5.4.1.2]. Therefore our calculations show that hopping terms of the Hamiltonian have no direct effect on the electronic band structure, but the relaxation of atomic positions and lattice parameters of the heterostructure modify significantly in the electronic band structure. The relaxation effect on the graphene/MoS<sub>2</sub> [5:4] bilayer heterostructure has not been discussed in previous works [43, 56, 75, 85, 102, 189, 193].

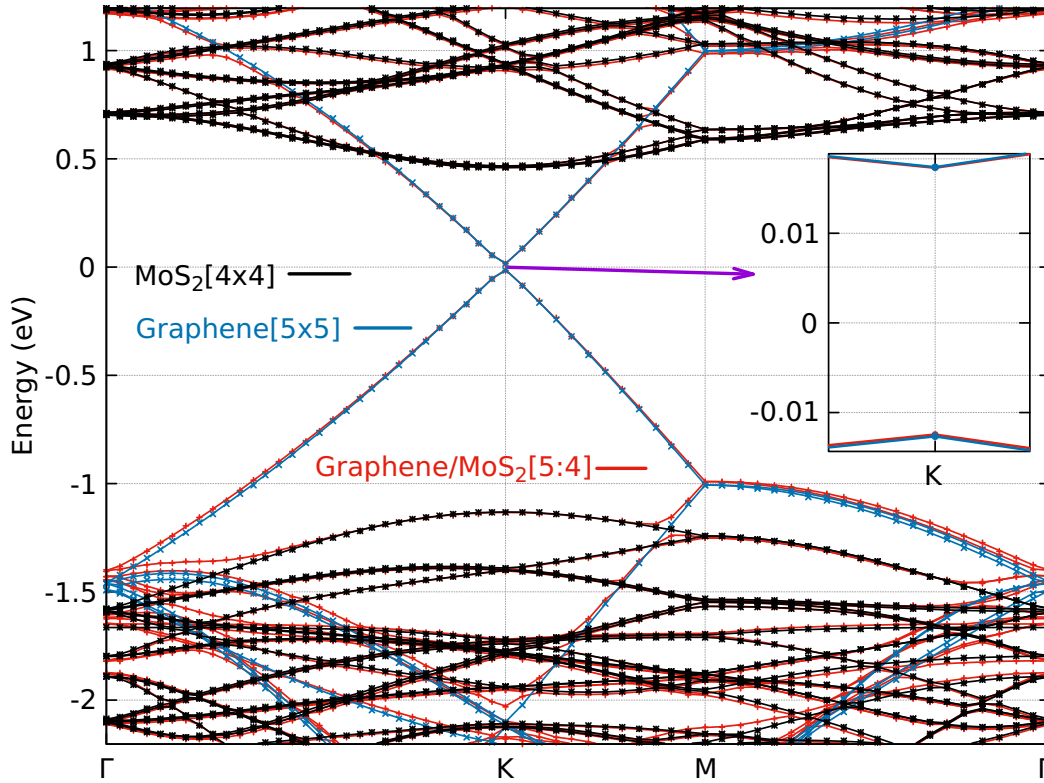


Figure 5.13: Electronic band structure of relaxed graphene/MoS<sub>2</sub> [5:4] bilayer heterostructure. Comparison between the electronic bands of relaxed graphene/MoS<sub>2</sub> [5:4] bilayer heterostructure, electronic bands of graphene layer alone and with the carbon atomic positions of the relaxed graphene/MoS<sub>2</sub> [5:4] bilayer heterostructure, electronic bands of MoS<sub>2</sub> layer alone and with the atomic positions of the relaxed graphene/MoS<sub>2</sub> [5:4] bilayer heterostructure. Zoom of the bands around the Dirac point (inset). The points are calculated results and lines are guide for the eyes. All the calculations have been done by using GGA-PAW pseudopotentials (PBE) including vdW.

#### 5.4.2.2 Spin orbit coupling effect

The effect of the spin orbit coupling (SOC) of the graphene/MoS<sub>2</sub> [5:4] bilayer heterostructure is not strong around the Dirac point see Fig. 5.14. The MoS<sub>2</sub> monolayer has a strong SOC effect at valence band ( $K$ -point) and band splitting around the  $K$  is  $\approx 148$  meV, which is in good agreement with previous theoretical works [47, 95, 186]. The band splitting of conduction band at the Dirac point ( $K$ ) is very small. The graphene/MoS<sub>2</sub> [5:4] bilayer heterostructure with and without SOC energy bandgap difference at the Dirac point is 2.02 meV.

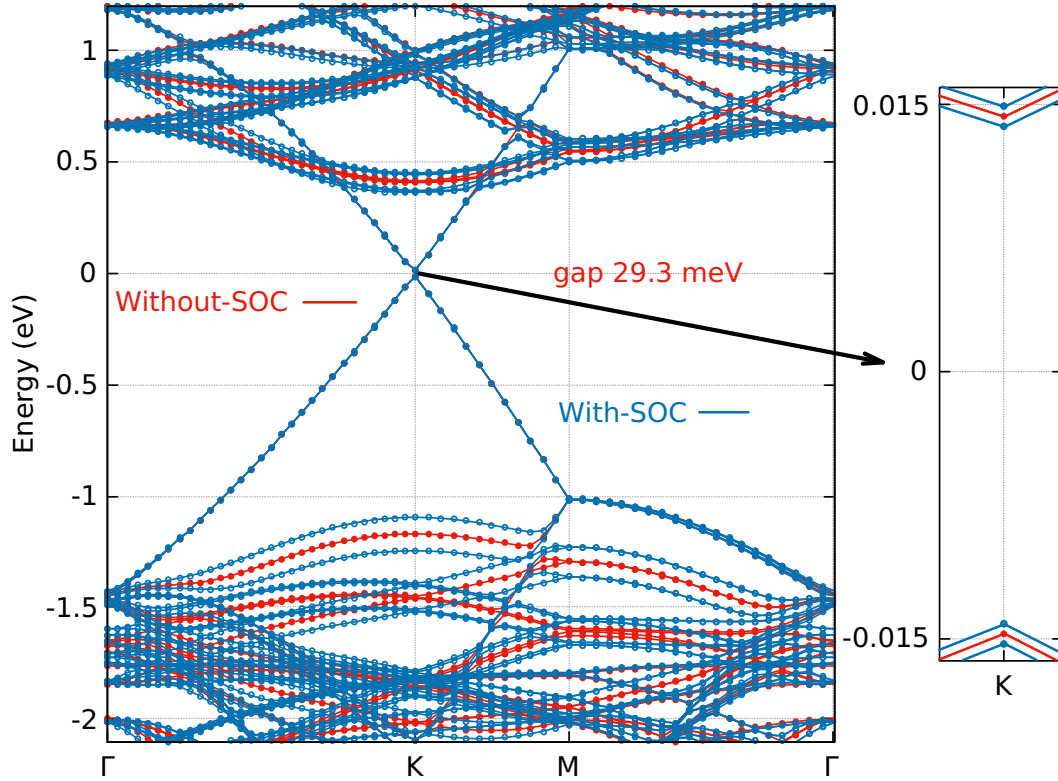


Figure 5.14: Electronic band structure of the graphene/MoS<sub>2</sub> [5:4] bilayer heterostructure with (blue lines) and without (red lines) spin orbit coupling along high symmetry lines. Zoom of the bands around the Dirac point (right). The points are calculated results and lines are guide for the eyes. After SOC bandgap at the Dirac point is reduced by 2.02 meV. All the calculations have been done by using GGA-PAW pseudopotentials (PBE) including vdW.

## 5.5 Graphene/MoS<sub>2</sub> heterostructure [9:7]

### 5.5.1 Atomic structure

#### 5.5.1.1 Non relaxed structure

The crystal structure of the graphene/MoS<sub>2</sub> [9:7] bilayer heterostructure is shown in Fig. 5.15 (a) side view, Fig. 5.15 (b) top view. We already shown (see sections 5.3.1 and 5.4.1) the lattice mismatch between the different structures. Further to minimize the lattice mismatch, one can vertically stack two commensurate super cells of graphene and monolayer MoS<sub>2</sub>. We take the reference of MoS<sub>2</sub> (7×7) lattice parameters to construct the graphene/MoS<sub>2</sub> [9:7] bilayer heterostructures by 9×9 unit cells of the graphene and 7×7 unit cells of the MoS<sub>2</sub> see Fig. 5.15. The induced lattice mismatch is smaller than 1 % ( $\approx 0.53$  %).

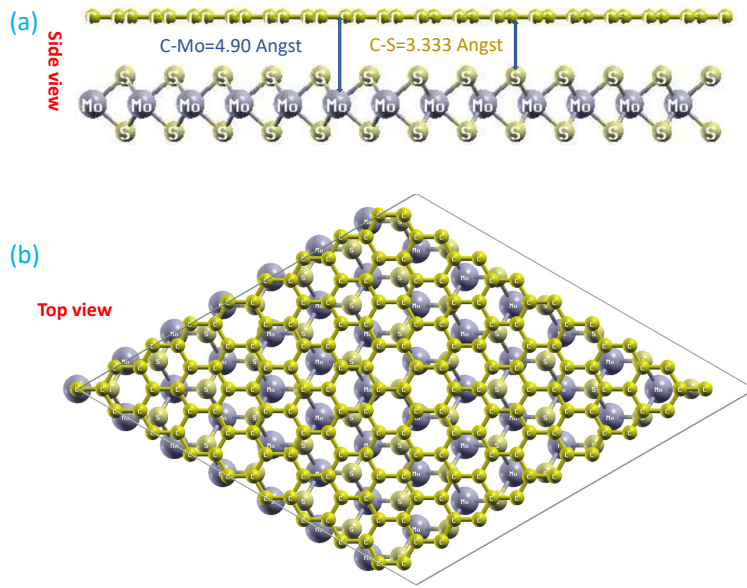


Figure 5.15: Non relaxed crystal structure of graphene/MoS<sub>2</sub> [9:7] bilayer heterostructure different views (a) Side view (blue lines indicate the distance between the carbon to molybdenum, and carbon to top sulfur). (b) Top view. All the calculations have been done by using LDA-PW-PAW pseudopotentials and basic reference has taken MoS<sub>2</sub> (7×7) unit cell.

In graphene/MoS<sub>2</sub> [9:7] bilayer heterostructures, graphene and MoS<sub>2</sub> monolayers weakly interact through long range vdW interactions. The experimentally reported interlayer distance between graphene and MoS<sub>2</sub> nano sheets is  $3.40 \pm 0.1$  Å [171]. We found that the interlayer distance ranges are approximately equal even though supercell structures are different like 4:3, 5:4 and 9:7. However, many first principles studies inconsistently predicted inter layer distance values ranging from 3.1 Å to 4.3 Å [43, 56, 75, 85, 102, 189, 193].

### 5.5.1.2 Relaxed structure

To find out the most stable configuration of the graphene/MoS<sub>2</sub> [9:7] bilayer heterostructure, we relaxed the heterostructure using several starting positions of the graphene layer relative to the MoS<sub>2</sub> layer. The optimized lattice parameters of the 9:7 bilayer with less lattice mismatch are  $a = b = 22.14$  Å see Fig. 5.16. The atomic positions and the lattice parameters are changed, in the case of MoS<sub>2</sub> the sheet is being compressed by 0.51 % (the 4:3 structure MoS<sub>2</sub> sheet is being stretched by 2.45 % and the 5:4 structure MoS<sub>2</sub> sheet is being compressed by 2.35 %) and the graphene sheet is almost neither stretched nor compressed (the 4:3 structure graphene sheet is being compressed by 0.5 % and the 5:4 structure graphene sheet is being stretched by 0.97 %) from the optimized cell (lattice) parameters see Fig. 5.16. Optimized average interlayer distances are: C-Mo

distance 4.981 Å, C-S distance 3.361 Å and S-S distance 3.239 Å.



Figure 5.16: Simplified sketch of the lattice parameters of hexagonal super lattice of graphene/MoS<sub>2</sub> [9:7] bilayer heterostructure, comparison to MoS<sub>2</sub> and graphene supercells alone. In our work the basic reference (without relaxation) has been taken as the MoS<sub>2</sub> (7×7) unit cell.

We analyzed structural optimization of the graphene/MoS<sub>2</sub> [9:7] bilayer heterostructure along the  $z$ -direction see Fig. 5.17. Carbon layer without optimization, position occupied along the  $c$ -axis at 4.9 Å after optimization the atoms are moving up and down it seems to look like a cosine wave see Fig. 5.17-(a). The carbon layer atoms are moving along the  $c$ -axis, maximum is 5.0210 Å and minimum is 4.9415 Å see Fig. 5.17-(a). The same phenomenon happened to the MoS<sub>2</sub> layer, without optimization the Mo atoms are at rest position at 0.0 Å along the  $c$ -axis. After optimization the Mo atoms are moving along the  $c$ -axis maximum is 0.0136 Å and minimum is 0.0029 Å see Fig. 5.17-(d). Without optimization the top S atoms are at rest position at 1.5667 Å along the  $c$ -axis, after optimization the top S atoms are moving along the  $c$ -axis maximum is 1.6324 Å and minimum is 1.6253 Å see Fig. 5.17-(b). Without optimization the bottom S atoms stay at -1.5667 Å along the  $c$ -axis, after optimization the top S atoms are moving along the  $c$ -axis maximum is -1.6047 Å and minimum is -1.6159 Å see Fig. 5.17-(e). We took the reference of MoS<sub>2</sub> (7×7) unit cell value then construct a 9:7 structure. After structural and lattice parameters optimization, graphene layer has neither stretched nor compressed and MoS<sub>2</sub> layer has compressed see Fig. 5.16. Comparison of structural behavior of different supercell geometries of graphene/MoS<sub>2</sub> bilayer heterostructure see table 5.1.

We also analyzed the structural optimization of the graphene/MoS<sub>2</sub> [9:7] bilayer heterostructure in the  $xy$ -plane see Fig. 5.18. We observed very small atomic displacements in the  $xy$ -plane and it shows an hexagonal symmetry pattern. We rescaled both  $x$  and  $y$  axis for the visualization purpose. The multiplication factor of  $x$  and  $y$  axis is 400.

## 5.5.2 Electronic band structure

### 5.5.2.1 Relaxation effect

A comparison of electronic band structure of graphene/MoS<sub>2</sub> [9:7] bilayer heterostructure with and without relaxation is shown in Fig. 5.19. After relaxation,

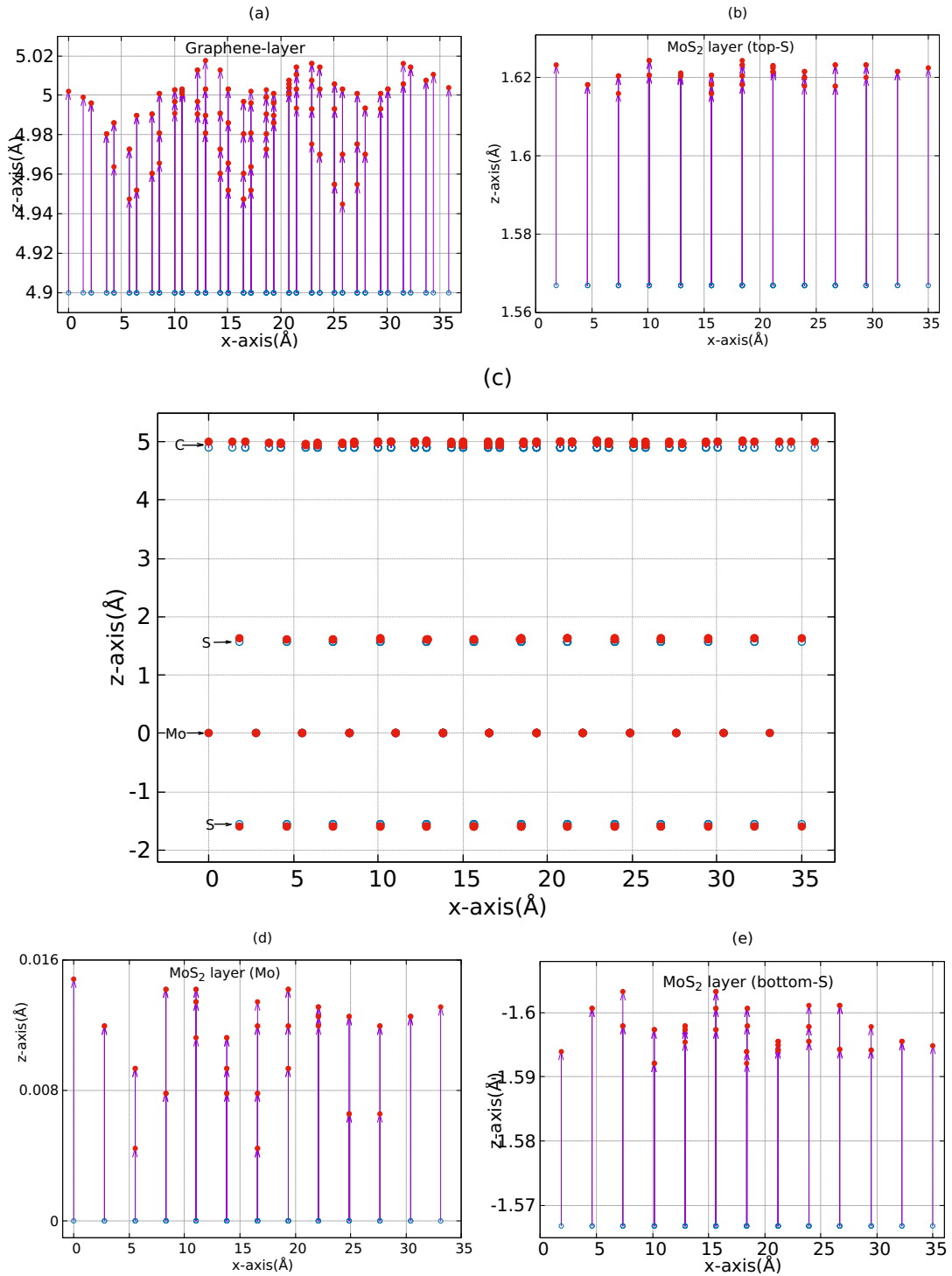


Figure 5.17: Variation of atoms in the unit cell of graphene/MoS<sub>2</sub> [9:7] bi-layer heterostructure along the  $z$ -direction without (empty blue circles) and with (full red circles) relaxation: (a) Graphene layer (b) MoS<sub>2</sub> layer-sulfur (top) (c) graphene/MoS<sub>2</sub> [9:7] heterostructure position of atoms in the unit cell (d) MoS<sub>2</sub> layer-molybdenum (e) MoS<sub>2</sub> layer-sulfur (bottom).

the atomic positions and lattice parameters are changed with the effect that graphene and MoS<sub>2</sub> layers are either compressed or stretched. But due to the

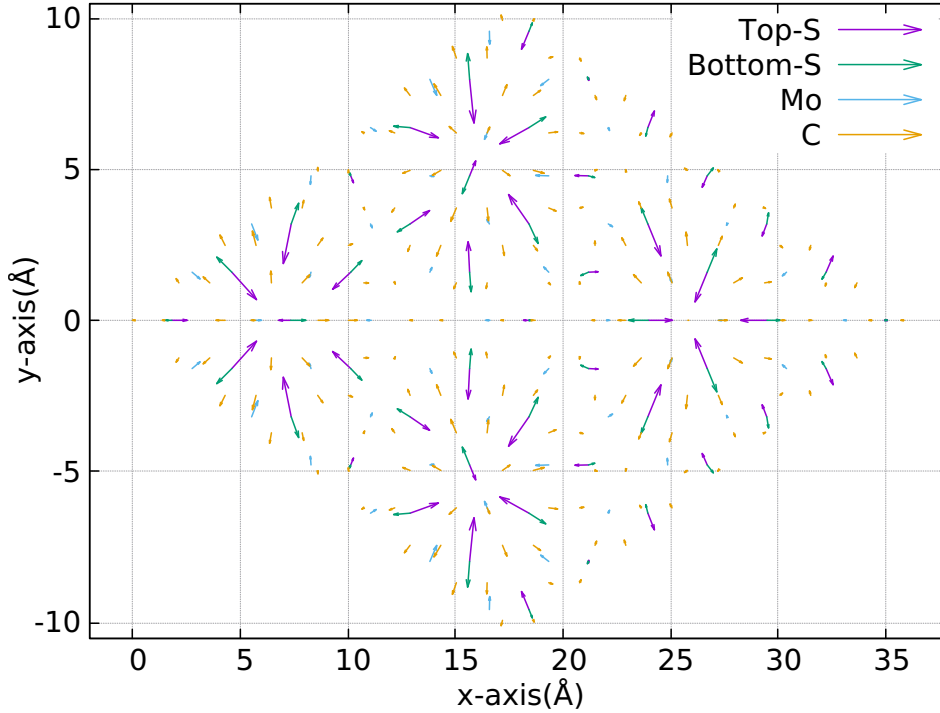


Figure 5.18: Variation of atomic positions in the unit cell of the graphene/MoS<sub>2</sub> [9:7] bilayer heterostructure along the  $xy$ -direction: The arrows show the displacement of atoms from non-relaxed positions to relaxed positions, with scaling factor of 400.

small mismatch between the layers, the graphene layer has neither stretched nor compressed [Fig. 5.17 and Fig. 5.16]. The 9:7 band structure has a bandgap at the Dirac point ( $\Gamma$ -point in the Brillouin zone because of the graphene supercell  $9 \times 9$  is multiple of 3) due to the optimized atomic positions, lattice parameters and also an effect of the MoS<sub>2</sub> layer. At  $K$ -point in the Brillouin zone minimum of the conduction band bends towards Fermi level (Dirac point) and maximum of the valence band bends towards Fermi level (Dirac point) because of optimized atomic positions. Lattice parameters and also bilayer (interlayer) distance effects are shown in Fig. 5.19.

The linear dispersion of the Dirac cone lies within the bandgap of the MoS<sub>2</sub> monolayer in the 9:7 bilayer heterostructure. The weak vdW interaction between graphene and MoS<sub>2</sub> monolayers yields a small, but significant, bandgap at the Dirac point see Fig. 5.19 and the Dirac point shifted from  $K$ -point to  $\Gamma$ -point for the individual layer of graphene see in appendix 3. The graphene/MoS<sub>2</sub> [9:7] bilayer heterostructure have a bandgap around the Dirac point ( $K$ ) is  $\approx 2.01$  meV see Fig. 5.19. In 9:7 bilayer heterostructure, the MoS<sub>2</sub> monolayer changes its indirect bandgap semiconducting nature at the maximum of the valence band at the  $K$ -point to the minimum of the conduction band at in-between  $K$  and  $\Gamma$ -points of Brillouin zone (the bandgap of MoS<sub>2</sub> monolayer changes from 1.8

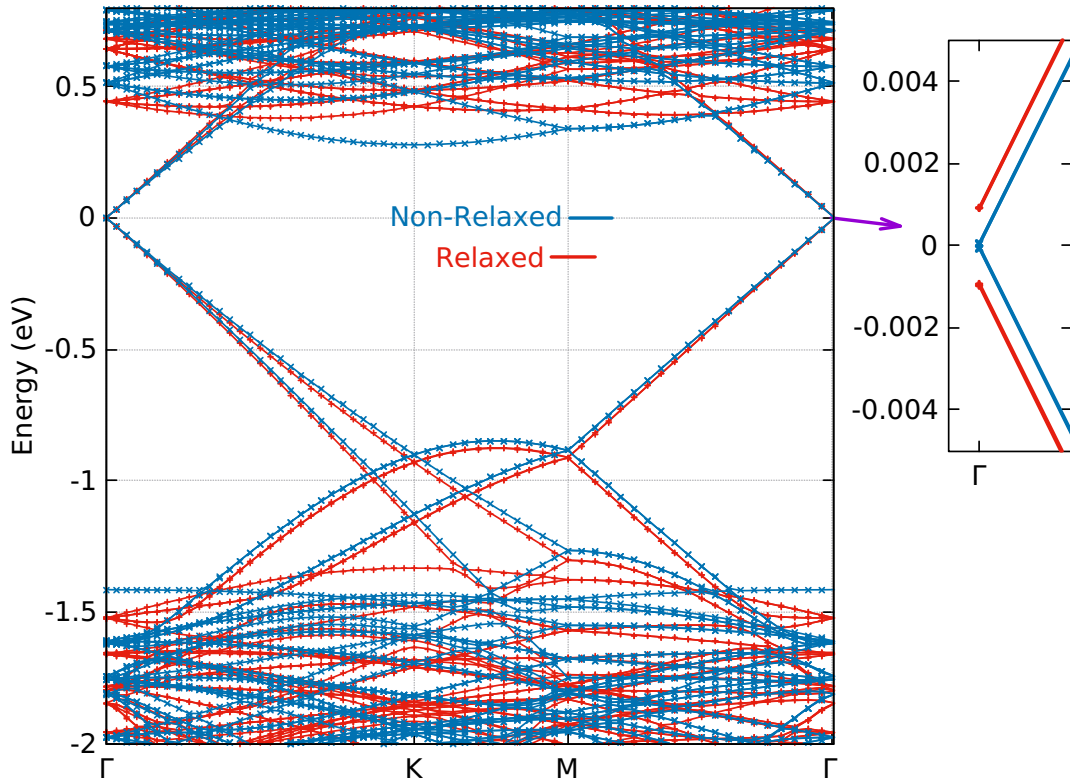


Figure 5.19: Comparison of electronic band structure of graphene/MoS<sub>2</sub> [9:7] bilayer heterostructure with relaxation (red lines), without relaxation (blue lines). Zoom of the bands around the Dirac point (right). The points are calculated results and lines are guide for the eyes. All the calculations have been done by using GGA-PAW pseudopotentials (PBE) including vdW.

to 1.6 eV). Since the graphene/MoS<sub>2</sub> [9:7] bilayer heterostructure maintains the indirect bandgap nature of MoS<sub>2</sub> monolayer at the *K*-point (because of the very small lattice mismatch), it can be concluded that the aforementioned transition in the 4:3 bilayer is primarily triggered by the strain effects arising due to the large lattice mismatch [196].

No such charge transfer between the graphene and MoS<sub>2</sub> layers can be observed see Fig. 5.19, which is very minimally strained. This finding is consistent with the experimental observations by Diaz et al [31], who performed angle resolved photo emission spectroscopic (ARPES) measurements to probe the electronic structure of the graphene/MoS<sub>2</sub> heterostructure. They observed that the Dirac cone of graphene remains intact and no significant charge transfer occurs between the graphene and MoS<sub>2</sub> layers.

In order to study the effect of direct interlayer coupling between the two layers, we compare the bands of the relaxed graphene/MoS<sub>2</sub> [9:7] bilayer het-

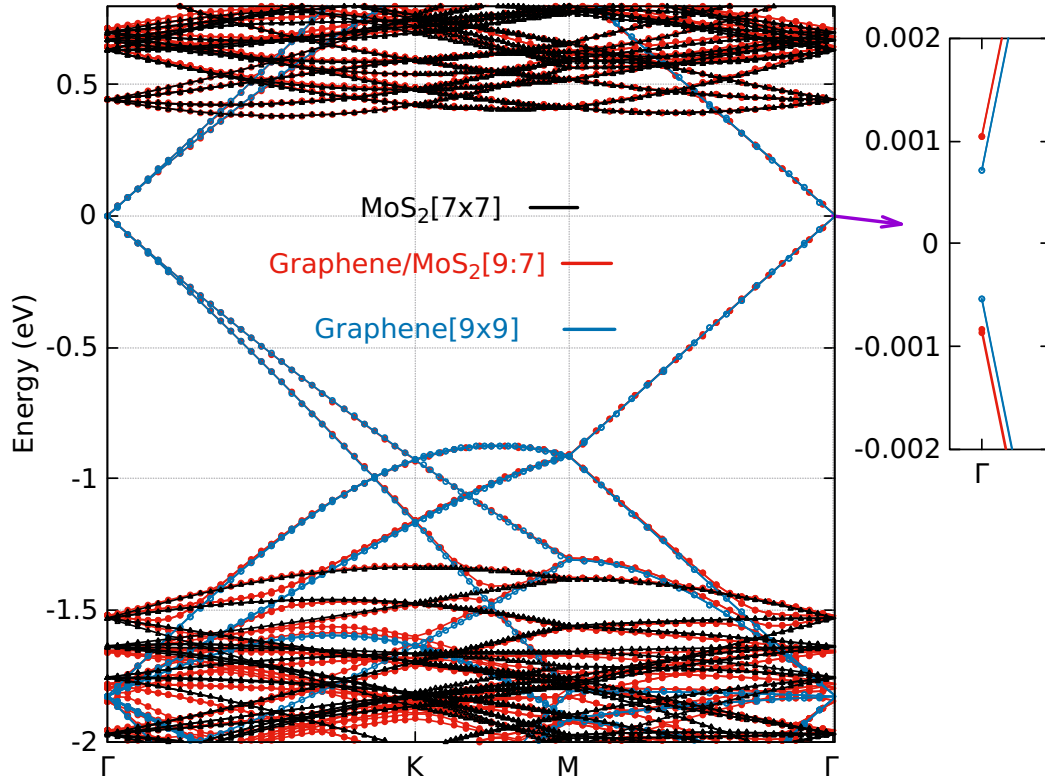


Figure 5.20: Electronic band structure of a relaxed graphene/MoS<sub>2</sub> [9:7] bilayer heterostructure. Comparison between the electronic bands of relaxed graphene/MoS<sub>2</sub> [9:7] bilayer heterostructure, electronic bands of a graphene layer alone with the carbon atomic positions of the relaxed graphene/MoS<sub>2</sub> [9:7] bilayer heterostructure, electronic bands of MoS<sub>2</sub> layer alone with the atomic positions of the relaxed graphene/MoS<sub>2</sub> [9:7] bilayer heterostructure. Zoom of the bands around the Dirac point (right). The points are calculated results and lines are guide for the eyes. All the calculations have been done by using GGA-PAW pseudopotentials (PBE) including vdW.

erostucture with bands of graphene alone with the relaxed position of relaxed graphene/MoS<sub>2</sub> [9:7] bilayer heterostructure and a MoS<sub>2</sub> layer alone with the positions of the relaxed graphene/MoS<sub>2</sub> [9:7] bilayer heterostructure see Fig. 5.20. Direct effect of interlayer coupling found at  $\Gamma$ -point and at the Dirac point ( $K$ -point) is very small. Indeed the electronic bands of graphene/MoS<sub>2</sub> [9:7] bilayer heterostructure are very similar to the sum of the electronic bands of graphene alone and the electronic bands of MoS<sub>2</sub> alone [energy shifts because of atomic positions and lattice parameter values see section 5.5.1.2]. Therefore our calculations show that hopping terms of the Hamiltonian has no direct effect on the electronic band structure, but the relaxation of atomic positions and lattice parameters of the heterostructure modify significantly the electronic band structure. We proposed a TB-model for the graphene/MoS<sub>2</sub> [5:4] and graphene/MoS<sub>2</sub>

[9:7] bilayer heterostructures to check interlayer effect on graphene/MoS<sub>2</sub> bilayer heterostructure see appendix C.3.

### 5.5.2.2 Spin orbit coupling effect

The effect of the spin orbit coupling (SOC) of graphene/MoS<sub>2</sub> [9:7] bilayer heterostructure is not strong around the Dirac point see Fig. 5.21. The MoS<sub>2</sub> monolayer has a strong SOC effect at valence band ( $K$ -point) and band splitting is  $\approx 148$  meV which is a good agreement with first principle calculations [47, 95, 186]. The conduction band at the Dirac point band splitting is very small. The graphene/MoS<sub>2</sub> [9:7] bilayer heterostructure with and without SOC energy bandgap difference at the Dirac point ( $\Gamma$ -point) is 0.77 meV.

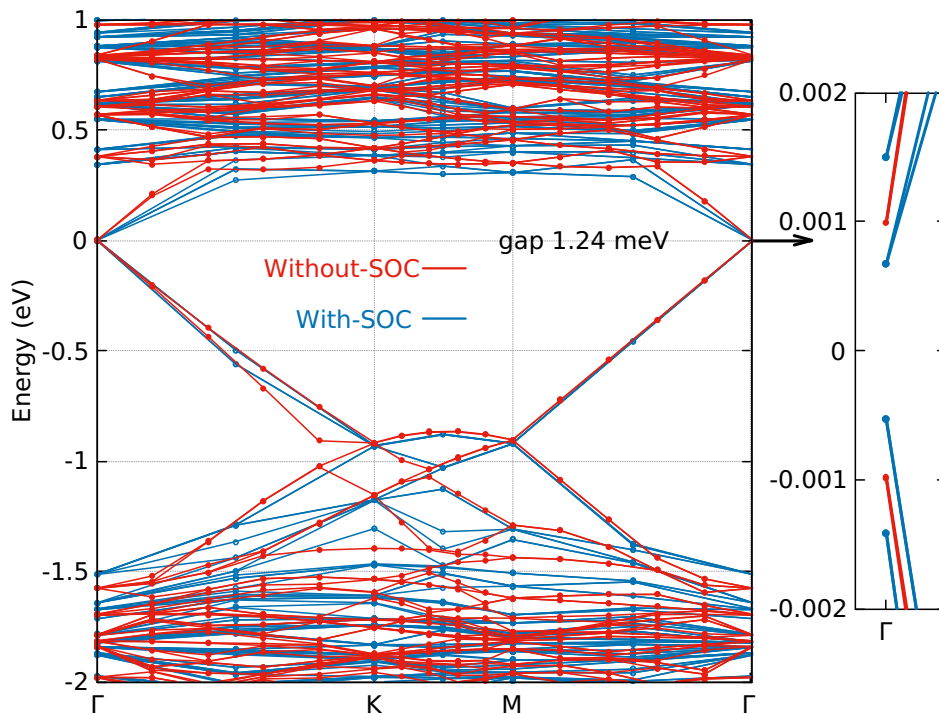


Figure 5.21: Electronic band structure of graphene/MoS<sub>2</sub> [9:7] bilayer heterostructure with (blue lines) and without (red lines) spin orbit coupling along high symmetry lines. The fine structure of the low energy bands at the Fermi level, around the Dirac point ( $\Gamma$ -point)(right). The points are calculated results and lines are guide for the eyes. After SOC bandgap at the Dirac point is reduced by 0.77 meV. All the calculations have been done by using GGA-PAW pseudopotentials (PBE) including vdW.

Graphene/MoS <sub>2</sub> (4:3, 5:4 and 9:7) bilayer heterostructure-structural properties			
Properties	4:3 structure	5:4 structure	9:7 structure
WOP	$a = b = 9.540 \text{ \AA}$ .	$a = b = 12.720 \text{ \AA}$ .	$a = b = 22.260 \text{ \AA}$ .
WP	$a = b = 9.784 \text{ \AA}$ .	$a = b = 12.423 \text{ \AA}$ .	$a = b = 22.138 \text{ \AA}$ .
Position of atoms			
Graphene layer [WOP]	4.900 $\text{\AA}$ .	4.900 $\text{\AA}$ .	4.900 $\text{\AA}$ .
Graphene layer [WP]	Maxi 4.914 $\text{\AA}$ & Min 4.887 $\text{\AA}$ .	Maxi 4.9615 $\text{\AA}$ & Min 4.8765 $\text{\AA}$ .	Maxi 5.021 $\text{\AA}$ & Min 4.9415 $\text{\AA}$ .
MoS <sub>2</sub> layer (Top-S)[WOP]	1.5667 $\text{\AA}$ .	1.5667 $\text{\AA}$ .	1.56694 $\text{\AA}$ .
MoS <sub>2</sub> layer (Top-S) [WP]	Maxi 1.5352 $\text{\AA}$ & Min 1.5335 $\text{\AA}$ .	Maxi 1.6303 $\text{\AA}$ & Min 1.6238 $\text{\AA}$ .	Maxi 1.6324 $\text{\AA}$ & Min 1.6253 $\text{\AA}$ .
MoS <sub>2</sub> layer (Mo) [WOP]	0.00 $\text{\AA}$ .	0.00 $\text{\AA}$ .	0.00 $\text{\AA}$ .
MoS <sub>2</sub> layer (Mo) [WP]	Maxi 0.0012 $\text{\AA}$ & Min -0.0026 $\text{\AA}$ .	Maxi 0.0012 $\text{\AA}$ & Min -0.0025 $\text{\AA}$ .	Maxi 0.01365 $\text{\AA}$ & Min 0.00291 $\text{\AA}$ .
MoS <sub>2</sub> layer (Bottom-S) [WOP]	-1.5667 $\text{\AA}$ .	-1.56694 $\text{\AA}$ .	-1.56694 $\text{\AA}$ .
MoS <sub>2</sub> layer (Bottom-S)[WP]	Maxi -1.5381 $\text{\AA}$ & Min -1.5387 $\text{\AA}$ .	Maxi -1.6557 $\text{\AA}$ & Min -1.6689 $\text{\AA}$ .	Maxi -1.6047 $\text{\AA}$ & Min -1.6159 $\text{\AA}$ .
Comparison-1	Lattice mismatch $\approx 3.33\%$ .	Lattice mismatch $\approx 2.52\%$ .	Lattice mismatch $\approx 0.53\%$ .
Comparison-2	MoS <sub>2</sub> is stretched ( $\approx 2.45\%$ ) Graphene is compressed ( $\approx 0.6\%$ ).	MoS <sub>2</sub> is compressed ( $\approx 2.35\%$ ) Graphene is stretched ( $\approx 0.97\%$ ).	MoS <sub>2</sub> is compressed ( $\approx 0.851\%$ ) Graphene is neither compressed nor stretched.
Comparison-3	Bandgap at the Dirac point (without SOC) $\approx 20.6$ meV. With and without SOC bandgap difference $\approx 1.86$ meV.	Bandgap at the Dirac point (without SOC) $\approx 31.3$ meV. With and without SOC bandgap difference $\approx 2.02$ meV.	Bandgap at the Dirac point (without SOC) $\approx 1.89$ meV. With and without SOC bandgap difference $\approx 0.77$ meV.

Table 5.1: Simplified comparison of the DFT optimized lattice parameters and atomic positions of different supercell geometries of graphene/MoS<sub>2</sub> bilayer. WP (with optimization) and WOP (without optimization).

## 5.6 Graphene/WSe<sub>2</sub> heterostructure [4:3]

### 5.6.1 Atomic structure

#### 5.6.1.1 Non relaxed structure

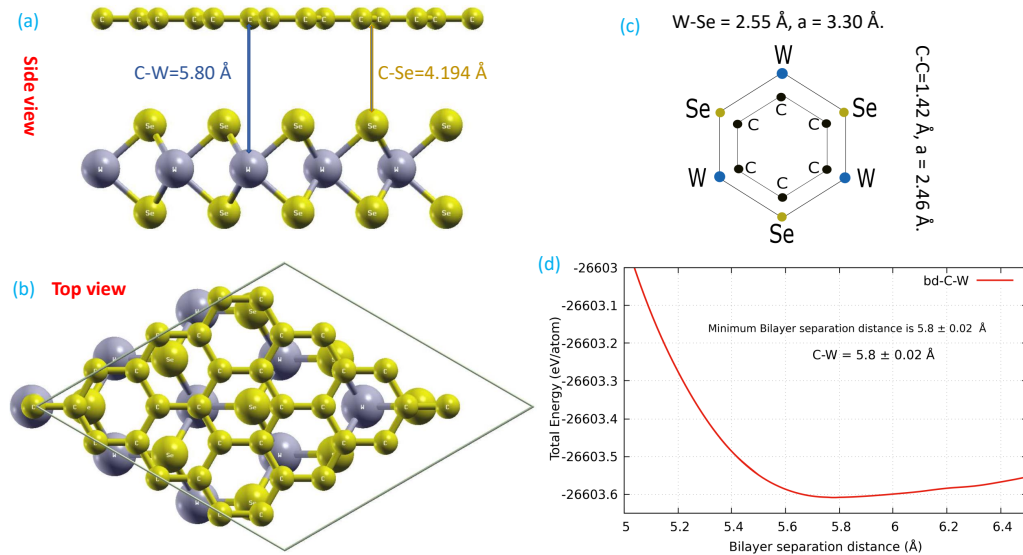


Figure 5.22: Non relaxed crystal structure of the graphene/WSe<sub>2</sub> [4:3] bilayer heterostructure. (a) Side view (blue lines indicate the distance between the carbon to tungsten, and carbon to top selenium). (b) Top view. (c) Unit cells of graphene and WSe<sub>2</sub> monolayers lattice mismatching. (d) Bilayer separation distance between the graphene (4×4) and WSe<sub>2</sub> (3×3) layers, with the a cell of MoS<sub>2</sub>. All the calculations have been done by using LDA-PAW pseudopotentials and basic reference was taken WSe<sub>2</sub> (3×3) unit cell.

The crystal structure of the graphene/WSe<sub>2</sub> bilayer heterostructure is shown in Fig. 5.22(a) side view, Fig. 5.22(b) top view. Unit cells and lattice parameters of graphene and WSe<sub>2</sub> monolayers are shown in Fig. 5.22(c) and bilayer separation distance between graphene and WSe<sub>2</sub> layers are shown in Fig. 5.22(d). The large lattice mismatch between the graphene and WSe<sub>2</sub> monolayers ( $\approx 25.45\%$ ) makes the *ab initio* modeling of graphene/WSe<sub>2</sub> bilayer heterostructure computationally demanding. In order to minimize the lattice mismatch, one can vertically stack two commensurate supercells of graphene and WSe<sub>2</sub> monolayers. We fixed the lattice constant of WSe<sub>2</sub> and construct the heterostructures by using 4×4 unit cells of graphene and 3×3 unit cells of WSe<sub>2</sub> are shown in Fig. 5.22. With this commensurate structure, the graphene/WSe<sub>2</sub> [4:3] bilayer heterostructure has an induced lattice mismatch smaller than 1% ( $\approx 0.606\%$ ). We have done

bilayer separation distance calculations by using LDA-PAW pseudopotentials. The obtained bilayer separation distances are: C-W between the two layers is 5.8 Å and C-Se distance is 4.15 Å in good agreement with previous theoretical studies [204].

### 5.6.1.2 Relaxed structure

To find out the most stable configuration of the graphene/WSe<sub>2</sub> [4:3] bilayer heterostructure, we relaxed the heterostructure using several starting positions of the graphene layer relative to the WSe<sub>2</sub> layer. The optimized lattice parameters of the graphene/WSe<sub>2</sub> [4:3] bilayer heterostructure with small lattice mismatch  $a = b = 9.912$  Å is shown in Fig. 5.23. The atomic positions and the lattice parameters are changed because of the WSe<sub>2</sub> sheet is being stretched by 0.12 % and the graphene sheet is also stretched by 0.72 % is shown in Fig. 5.23. Thus unlike for graphene/MoS<sub>2</sub> bilayer (see previous sections) both layers are stretched in graphene/WSe<sub>2</sub> [4:3] bilayer. Optimized average interlayer distances are: C-W distance 5.803 Å, C-Se distance 4.194 Å and Se-Se distance 3.373 Å. The bond lengths of W-Se and C-C are changed which is in good agreement with the previous works [89,204].

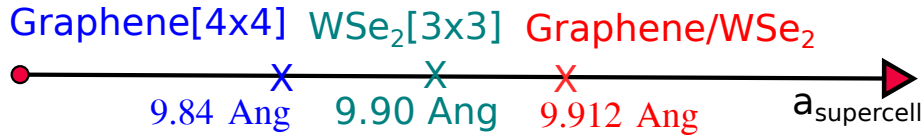


Figure 5.23: Simplified sketch of the lattice parameters of a hexagonal super lattice of graphene/WSe<sub>2</sub> [4:3] bilayer heterostructure, comparison to WSe<sub>2</sub> and graphene supercells alone. In our work the basic reference was taken to be the WSe<sub>2</sub> (3×3) unit cell.

We analyzed structural optimization of the graphene/WSe<sub>2</sub> [4:3] bilayer heterostructure along the  $z$ -direction is shown Fig. 5.24. The carbon layer without optimization, position occupied along the  $c$ -axis at 5.80 Å, after optimization the atoms are moving up and down it seems look like a cosine wave is shown Fig. 5.24-(a). The carbon layer atoms are moving along the  $c$ -axis. Maximum is 5.8053 Å and minimum is 5.8027 Å see Fig. 5.24-(a). The same phenomenon happened to the WSe<sub>2</sub> layer, without optimization W atoms are at rest position at 0.00 Å along the  $c$ -axis, after optimization the W atoms are moving along the  $c$ -axis. Maximum is -0.0040 Å and minimum is -0.0044 Å see Fig. 5.24-(d). Without optimization the top Se atoms are at rest position at 1.6437 Å along the  $c$ -axis, after optimization the top Se atoms are moving along the  $c$ -axis.

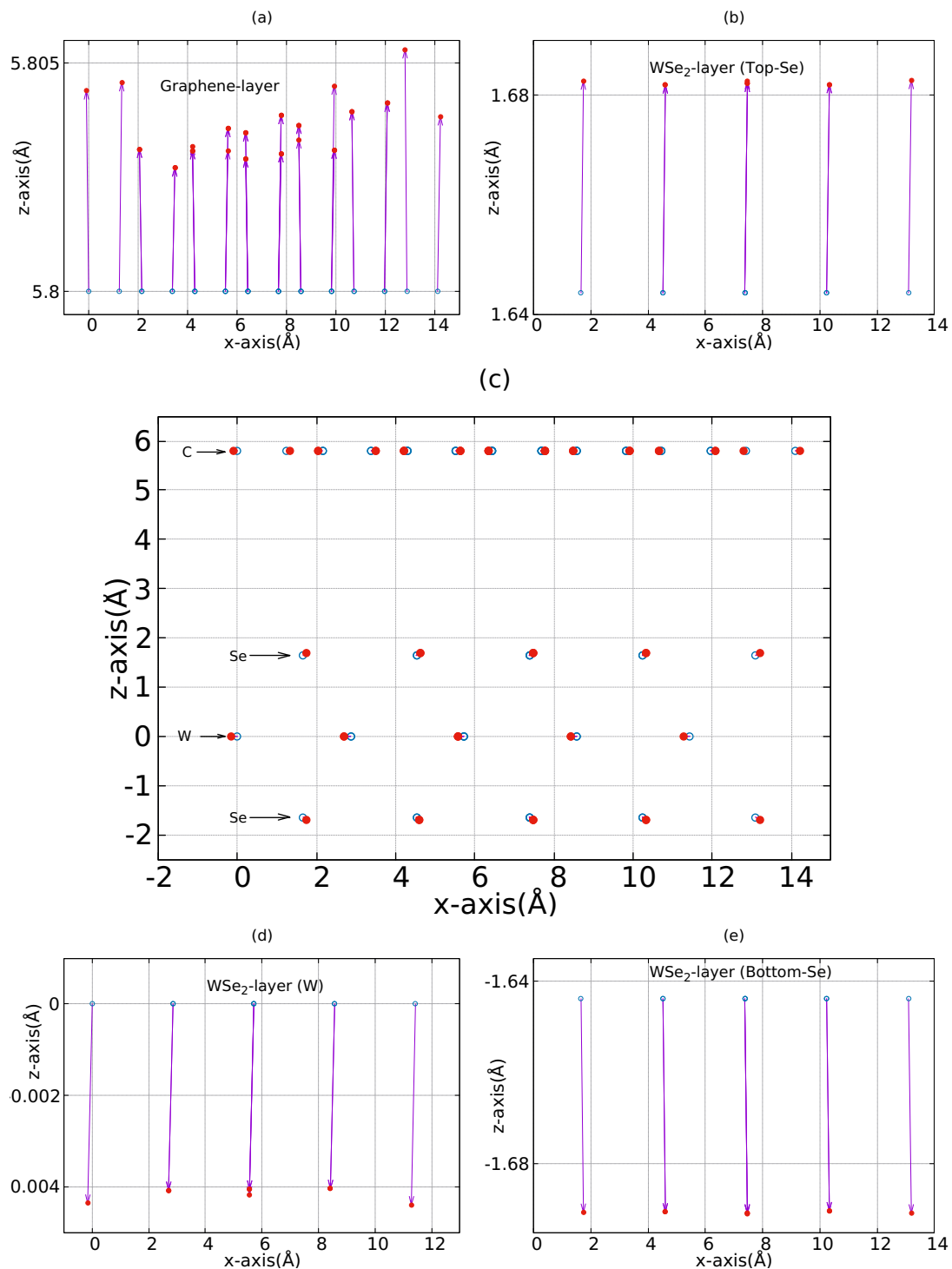


Figure 5.24: Variation of atomic positions along the  $z$ -direction in the unit cell of graphene/WSe<sub>2</sub> [4:3] bilayer heterostructure without (empty blue circles) and with (full red circles) relaxation: (a) Graphene layer (b) WSe<sub>2</sub> layer-selenium (top) (c) graphene/WSe<sub>2</sub> [4:3] heterostructure positions in the unit cell (d) WSe<sub>2</sub> layer-tungsten (e) WSe<sub>2</sub> layer-selenium (bottom). Basic reference was taken to be the WSe<sub>2</sub>(3×3) unit cell.

Maximum is 1.6826 Å and minimum is 1.6818 Å see Fig. 5.24-(b). Without optimization the bottom Se atoms stay at -1.6437 Å along the  $c$ -axis, after optimization the bottom Se atoms are moving along the  $c$ -axis. Maximum is -1.6903 Å and minimum is -1.6909 Å see Fig. 5.24-(e). We took the reference of WSe<sub>2</sub> (3×3) unit cell value then constructed a graphene/WSe<sub>2</sub> [4:3] structure. After atomic positions and lattice parameter optimization, the graphene layer has stretched a bit and the WSe<sub>2</sub> layer has very little stretched as shown in Fig. 5.23.

We also analyzed structural optimization of the graphene/WSe<sub>2</sub> [4:3] bilayer heterostructure along the  $xy$ -direction, obtained very small atomic displacements along the  $xy$ -direction and atomic displacement followed by a hexagonal symmetry pattern.

## 5.6.2 Electronic band structure

### 5.6.2.1 Relaxation effect

The linear dispersion of the Dirac cone lies within the bandgap of the WSe<sub>2</sub> monolayer in the 4:3 bilayer heterostructure. The weak vdW interaction between graphene and WSe<sub>2</sub> monolayers yields a small, but significant, bandgap at the Dirac point ( $K$ -point). Fig. 5.25 shows that the bandgap in 4:3 bilayer is  $\approx$  12.58 meV. In the 4:3 bilayer heterostructure, the WSe<sub>2</sub> monolayer preserves a semiconducting nature and it is direct bandgap at the  $K$ -point of Brillouin zone (the bandgap of the WSe<sub>2</sub> monolayer is 1.556 eV). The graphene/WSe<sub>2</sub> [4:3] bilayer heterostructure maintains the direct bandgap nature of WSe<sub>2</sub> monolayer but the symmetry point changed from  $K$ -point to  $\Gamma$ -point, as expected because of WSe<sub>2</sub> cell is 3×3.

No charge transfer between the graphene and WSe<sub>2</sub> layers can be observed in Fig. 5.25, which is a minimal strain. But this is a contrast to the graphene/MoS<sub>2</sub> [4:3] bilayer heterostructure.

In order to study the effect of direct interlayer coupling between the two layers, we compare the bands of relaxed graphene/WSe<sub>2</sub> [4:3] bilayer heterostructure with bands of graphene alone with relaxed position of relaxed graphene/WSe<sub>2</sub> [4:3] bilayer heterostructure and WSe<sub>2</sub> layer alone with the positions of relaxed graphene/WSe<sub>2</sub> [4:3] bilayer heterostructure see Fig. 5.25. A direct effect of interlayer coupling found at the Dirac point ( $K$ -point) and at  $\Gamma$ -point is very small. Indeed the electronic bands of graphene/WSe<sub>2</sub> [4:3] bilayer heterostructure is similar to the sum of the electronic bands of graphene alone and the electronic bands of WSe<sub>2</sub> alone [energy shift of Dirac cone due to interlayer dis-

tance see section 5.25, atomic positions and lattice parameter values see section 5.6.1.2]. Therefore our calculations show that hopping terms of the Hamiltonian have no direct effect on the electronic band structure, but the relaxation of atomic positions and lattice parameters of the heterostructure modify significantly the electronic band structure.

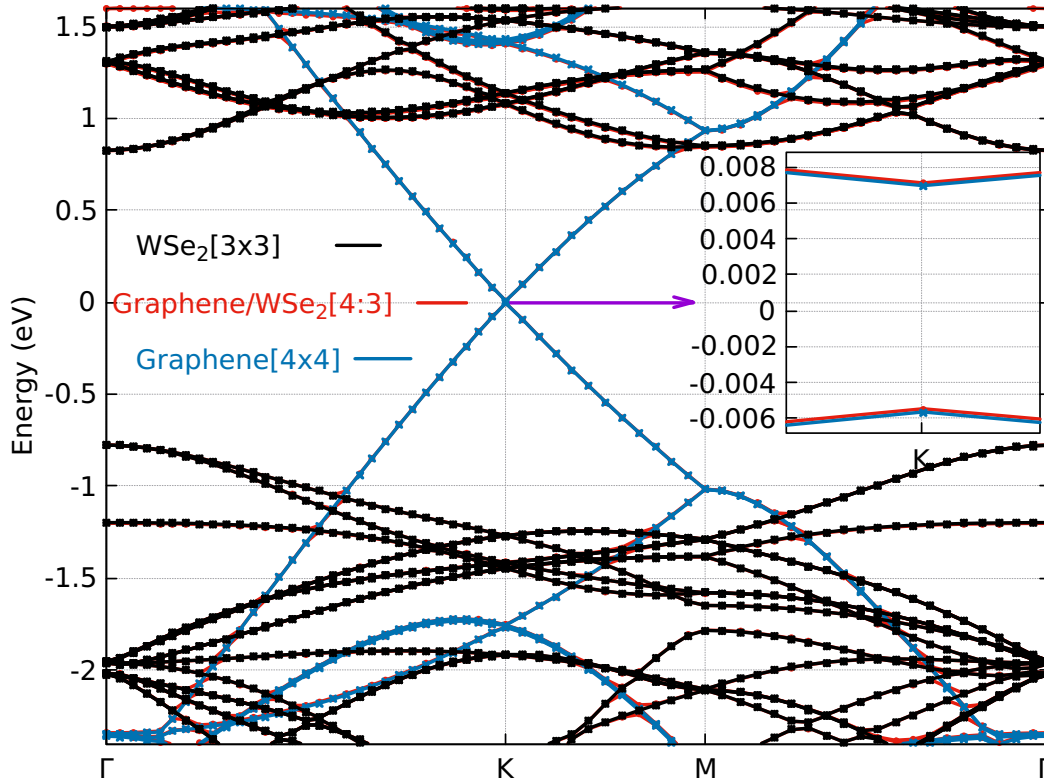


Figure 5.25: Electronic band structure of relaxed graphene/WSe<sub>2</sub> [4:3] bilayer heterostructure. Comparison between the electronic bands of relaxed graphene/WSe<sub>2</sub> [4:3] bilayer heterostructure, electronic bands of graphene layer alone with the carbon atomic positions of the relaxed graphene/WSe<sub>2</sub> [4:3] bilayer heterostructure, electronic bands of WSe<sub>2</sub> layer alone with the atomic positions of the relaxed graphene/WSe<sub>2</sub> [4:3] bilayer heterostructure. Zoom of the bands around the Dirac point (inset). The points are calculated results and lines are guide for the eyes. All the calculations have been done by using GGA-PAW pseudopotentials (PBE) including vdW.

### 5.6.2.2 Spin orbit coupling effect

The effect of the spin orbit coupling (SOC) on the graphene/WSe<sub>2</sub> [4:3] bilayer heterostructure is not strong around the Dirac point see Fig. 5.26. The WSe<sub>2</sub> monolayer has a strong SOC effect at valence band (*K*-point) and spin splitting

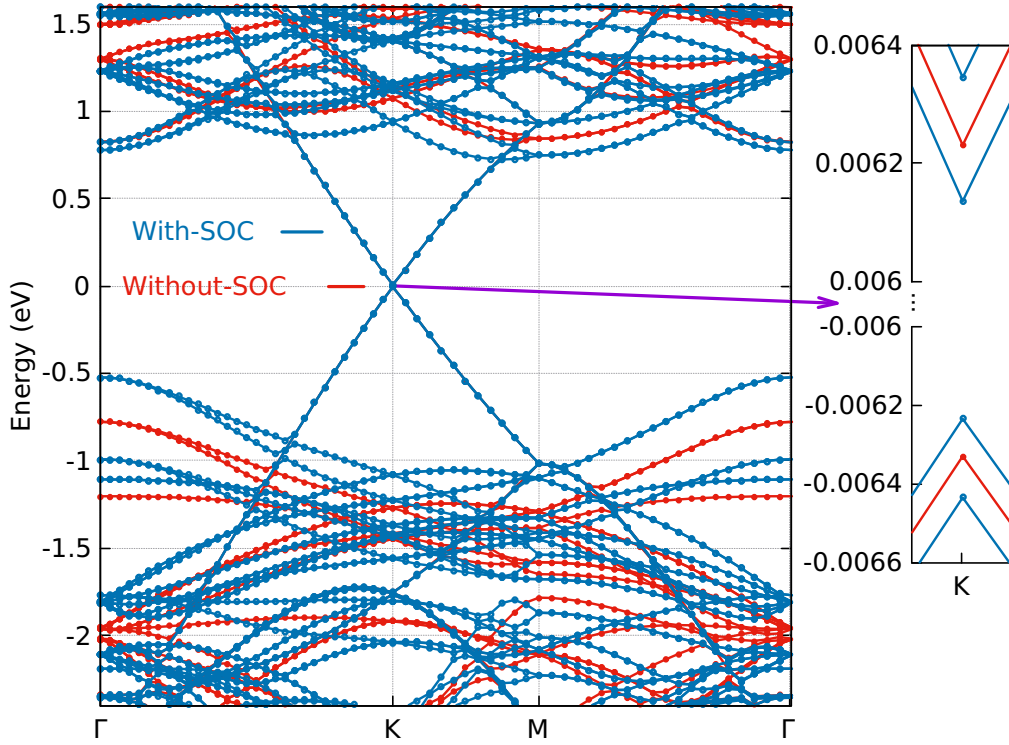


Figure 5.26: Electronic band structure of graphene/WSe<sub>2</sub> [4:3] bilayer heterostructure with (blue lines) and without (red lines) spin orbit coupling along high symmetry lines. The fine structure of the low energy bands at the Fermi level, around the Dirac point (right). The points are calculated results and lines are guide for the eyes. After SOC bandgap at Dirac point reduced by 0.07 meV. All the calculations have been done by using GGA-PAW pseudopotentials (PBE) including vdW.

is  $\approx 0.48$  eV. The conduction band spin splitting at the Dirac point is very small. The graphene/WSe<sub>2</sub> [4:3] bilayer heterostructure with and without SOC exhibits an energy bandgap difference at the Dirac point of 0.07 meV.

### 5.6.2.3 Structural imperfection effects

In this section, we present briefly some first results on static defects in graphene/WSe<sub>2</sub> [4:3] bilayer heterostructure. Four types of intrinsic defects were considered see Fig. 5.27:

- One C vacancy (removal of one carbon atom) in the graphene/WSe<sub>2</sub> supercell denoted by graphene/WSe<sub>2</sub>-V<sub>C</sub>.
- One W vacancy (removal of one tungsten atom) in the graphene/WSe<sub>2</sub> supercell denoted by graphene/WSe<sub>2</sub>-V<sub>W</sub>.

- Two Se vacancies (removal of two selenium atoms) in the graphene/WSe<sub>2</sub> supercell denoted by graphene/WSe<sub>2</sub>-V<sub>di-Se</sub>.
- Substitution of Fe in W-vacancy (substituting iron atom in place of tungsten atom) in the graphene/WSe<sub>2</sub> supercell denoted by graphene/WSe<sub>2</sub>-SV<sub>Fe</sub>.

We performed optimized (lattice parameter and atomic position optimization) calculations by DFT for each structure. We found interlayer distance between the graphene and WSe<sub>2</sub> layers with all types of vacancies  $\approx 4.194 \pm 0.1$  Å which is good agreement with previous theoretical works [204].

With defects of the graphene/WSe<sub>2</sub>-V<sub>C</sub>, graphene/WSe<sub>2</sub>-V<sub>W</sub>, graphene/WSe<sub>2</sub>-V<sub>di-Se</sub>, and graphene/WSe<sub>2</sub>-SV<sub>Fe</sub> (see Fig. 5.27). A common feature of the graphene/WSe<sub>2</sub> (see Fig. 5.26) and graphene/WSe<sub>2</sub>-V<sub>di-Se</sub> (see Fig. 5.27-(c)) systems is that the electronic structures of both the semiconducting layer and the graphene layer are well preserved upon binding. In Fig. 5.27-(a) we created a vacancy by removal of C atom on the graphene layer, due to the C-vacancy metallic behavior disappears at highest symmetry point K, and it shows the indirect bandgap semiconductor with a small gap. In Fig. 5.27-(b) we created a vacancy by removal of W atom on the WSe<sub>2</sub> layer, due to the W-vacancy several impurity states are formed close to the valence band edge, and some of them cross the Fermi level, suggesting metallic behavior. In Fig. 5.27-(c) we created a vacancy by removal of two Se atoms on the WSe<sub>2</sub> layer, two bands are appeared below the conduction band. In Fig. 5.27-(d) create vacancy by substituting the Fe atom in place of W on WSe<sub>2</sub> layer, this behavior is similar to that of electronic band structure of graphene/MoS<sub>2</sub>[4:3] bilayer heterostructure.

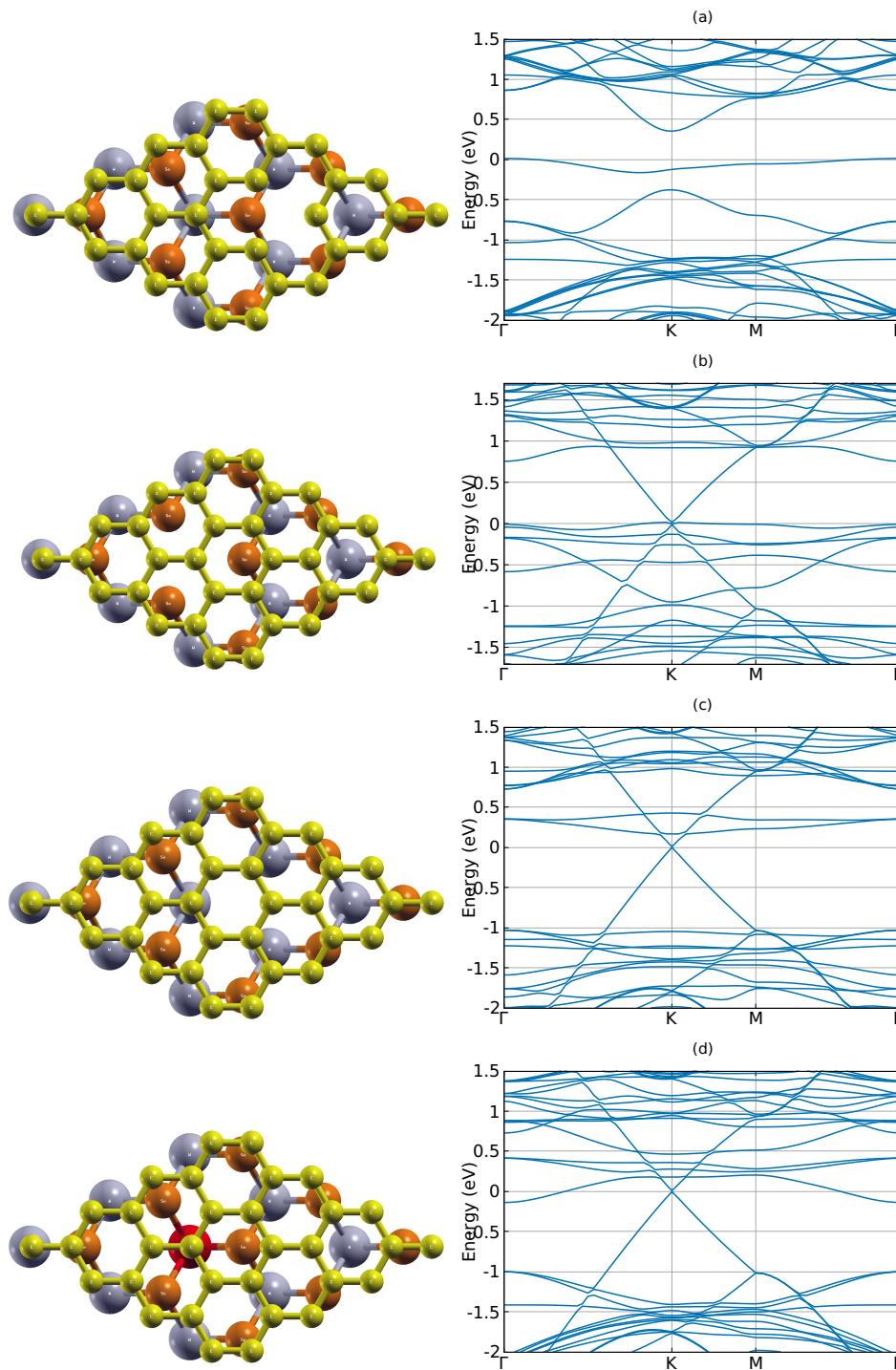


Figure 5.27: Atomic structure (left) and electronic band structure (right) of graphene/WSe<sub>2</sub> [4:3] bilayer heterostructure with point and substitutional defects (a) graphene/WSe<sub>2</sub>-V<sub>C</sub> (removal of one carbon atom in the graphene layer), (b) graphene/WSe<sub>2</sub>-V<sub>W</sub> (removal of one tungsten atom in the WSe<sub>2</sub> layer), (c) graphene/WSe<sub>2</sub>-V<sub>di-Se</sub> (removal of two selenium atoms (top and bottom) in WSe<sub>2</sub> layer), (d) graphene/WSe<sub>2</sub>-SV<sub>Fe</sub> (substituting iron (in place of tungsten) atom in the WSe<sub>2</sub> layer). All the calculations have been done by using GGA-PAW pseudopotentials (PBE) including vdW. All the calculations have been done with optimization and Without SOC.

## 5.7 Conclusion

In this chapter we have studied the properties of a new family of substrates for graphene. We focused on two different TMDs (MoS<sub>2</sub> and WSe<sub>2</sub>), but we expect the results should be similar to the other TMDs. A theoretical study of structural and electronic properties of graphene/MoS<sub>2</sub> and graphene/WSe<sub>2</sub> bilayer vdW heterostructures was performed using the ABINIT software program. For reducing the lattice mismatch between the layers we studied different configurations of graphene/MoS<sub>2</sub> [4:3 ( $\approx 3.33\%$ ), 5:4 ( $\approx 2.52\%$ ), and 9:7 ( $\approx 0.53\%$ )] and graphene/WSe<sub>2</sub> [4:3 ( $\approx 0.606\%$ )] bilayer vdW heterostructures.

We discovered that the strong lattice mismatch of graphene/MoS<sub>2</sub>[4:3] and graphene/MoS<sub>2</sub>[5:4] model structures, which has no experimental evidence, modifies strongly the band structures, and may induce an artificial charge transfer. These structures are thus not realistic to recover experimental results. Therefore, we investigated the graphene/MoS<sub>2</sub>[9:7] configuration, which has the least lattice mismatch and seems more realistic. Indeed, the resulting band structure turns out to be closer to two isolated graphene and MoS<sub>2</sub> layers, and no charge transfer occurs.

We know that weak vdW interactions exist between the graphene based TMDs bilayer heterostructures and predict the interlayer spacing accurately in graphene/MoS<sub>2</sub> and graphene/WSe<sub>2</sub> vdW heterostructures. The predicted interlayer spacing of graphene/MoS<sub>2</sub> heterostructures are 3.367 Å, 3.287 Å, and 3.361 Å respectively, which is in good agreement with the experimental data ( $3.4 \pm 0.1$  Å) [171] and graphene/WSe<sub>2</sub> vdW heterostructure is 4.194 Å. The electronic band structure analysis of graphene/MoS<sub>2</sub> bilayers using ABINIT reveals that the Dirac point of graphene is shifted upwards above the Fermi level and is located near the conduction bands of the MoS<sub>2</sub> sheet, yielding a considerable charge transfer in the 4:3 bilayer, whereas the Dirac point lies in the bandgap region in the 5:4 bilayer indicating no charge transfer between the constituent layers. The final configuration 9:7 bilayer, the Dirac point (shifted to K to  $\Gamma$ ) lies in the bandgap region it is indicated no charge transfer between the constituent layers because of a small lattice mismatch. According to the electronic band structure analysis of graphene/WSe<sub>2</sub> bilayers, the Dirac point lies in the bandgap region in 4:3 bilayer indicating no charge transfer between the constituent layers because of a small lattice mismatch between the layers. We observed that the location of the Dirac point can be shifted by tuning the interlayer spacing between the graphene and MoS<sub>2</sub> layers, and it's likely that this will happen to graphene and WSe<sub>2</sub> as well.

The effect of the spin orbit coupling (SOC) on graphene/MoS<sub>2</sub> and graphene/WSe<sub>2</sub> bilayer heterostructures is not strong around the Dirac point whereas in the monolayer with a MoS<sub>2</sub> and WSe<sub>2</sub> at the valence band (K-point) large band splitting observed due to a strong SOC effect and graphene layer at the Dirac point band splitting remains very small. The energy bandgap difference between bilayers with and without SOC at the Dirac point is very small. We also found that the electronic band structure has changed after the relaxation of the atomic positions and lattice parameters because of the internal stress and strain. For the electronic and optical properties, lattice optimization, relaxation of atoms in the unit cell are thus needed.

By the creation of C-vacancy in the graphene/WSe<sub>2</sub> [4:3] bilayer heterostructure, metallic behavior disappears and it shows indirect bandgap semiconductor. W-vacancy, shows a metallic behavior. Substitutional impurity (W replaced by Fe) similar behavior of the graphene/MoS<sub>2</sub> [4:3] bilayer heterostructure.

## Chapter No. 6

---

### *Twisted bilayer of MoS<sub>2</sub>*

---

	Page
6.1 Atomic structure . . . . .	127
6.1.1 Non relaxed structure . . . . .	127
6.1.2 Structural relaxation . . . . .	127
6.2 DFT calculations (Large angles) . . . . .	130
6.2.1 Electronic band structure of different angles . . . . .	130
6.2.2 Electronic band structure of different angles with and with- out structural relaxation . . . . .	132
6.3 Tight-Binding (TB) calculations . . . . .	133
6.3.1 TB-model for MoS <sub>2</sub> monolayer . . . . .	133
6.3.2 TB model for twisted bilayer MoS <sub>2</sub> (tb-MoS <sub>2</sub> ) . . . . .	134
6.3.3 Moiré pattern of tb-MoS <sub>2</sub> . . . . .	137
6.3.4 Analysis of bands of tb-MoS <sub>2</sub> built from AA stacking . . . . .	139
6.3.5 Analysis of bands of tb-MoS <sub>2</sub> built from AB stacking . . . . .	141
6.3.6 Local density of states (LDOS) . . . . .	142
6.3.7 Confined state in the AA region of the moiré pattern . . . . .	145
6.3.7.1 Electronic band structure with SOC at $\theta = 3.15^\circ$ and $\theta = 1.61^\circ$ . . . . .	146
6.3.7.2 Eigenstates corresponding to flat bands ( $\theta = 1.61^\circ$ ) in tb-MoS <sub>2</sub> . . . . .	146
6.4 Conclusion . . . . .	149

---

This chapter is based on the paper *Physical Review B* 102, 081103(R)(2020) [222]. Apart from the journal, we have explained the relaxation effect on band structures, different stacking of moiré pattern of tb-MoS<sub>2</sub>, different tight-binding models, band analysis of AB-stacking, and spin orbit coupling effect on band structures.

In recent years, the broad family of Transition Metal Dichalcogenides (TMD) [42, 111, 225], which offers a wide variety of possible rotationally stacked bilayer systems, has also prompted numerous experimental [77, 78, 113, 163, 212, 220, 234, 243, 249] and theoretical [29, 30, 46, 122, 123, 125, 146, 162, 186, 207, 208, 228, 231, 232] studies to understand such confined moiré states in semiconductor materials. Many of these studies analyze the interlayer distances, the possible atomic relaxation, the transition from a direct band gap in the monolayer system to an indirect band gap in bilayer (bulk) systems, and more generally the effect of interlayer coupling in those twisted 2D systems with various rotation angles  $\theta$ . At small values of  $\theta$ , the emergence of flat bands has been established [146] from first principle density functional theory calculations in twisted bilayer MoS<sub>2</sub> (tb-MoS<sub>2</sub>), and observed in a 3° twisted bilayer WSe<sub>2</sub> sample by using tunneling spectroscopy [249]. Recently, it has been shown numerically [123] that Lithium interaction in tb-MoS<sub>2</sub> increases interlayer coupling and thus promotes flat bands around the gap. There is also experimental evidence that moiré patterns may give rise to confined states due to the mismatch of the lattice parameters in MoS<sub>2</sub>-WSe<sub>2</sub> hetero bilayers [163].

Most theoretical investigations of the electronic structure of bilayer MoS<sub>2</sub> are density functional theory (DFT) studies [21, 29, 39, 46, 71, 77, 78, 113, 122, 146, 186, 203, 207, 209, 212, 220, 243] with eventually a Wannier wave function analysis [46]. Those approaches provide interesting results, but they do not allow a systematic analysis of the electronic structure as a function of the rotation angle  $\theta$ , in particular for small angles, *i.e.*, very large moiré cells, for which DFT calculations are not feasible. Several Tight-Binding (TB) models, based on Slater-Koster (SK) parameters, have been proposed for monolayer MoS<sub>2</sub> [23, 179, 187, 194, 241] and multi-layer MoS<sub>2</sub> [23, 46, 194, 212]. Following these efforts, we propose here a Slater-Koster (KS) set of parameters that match correctly the DFT bands around the gap of tb-MoS<sub>2</sub> with rotation angles  $\theta > 7^\circ$ . This SK-TB model, with the same parameters, is then used for smaller angles, in order to describe the confined moiré states.

We thus show that, for  $\theta \lesssim 6^\circ$ , the valence band with the highest energy is separated from the other valence states by a minigap of a few meV. In addition,

the width of this band decreases as  $\theta$  decreases so that the average velocity of these electronic states reaches 0 for  $\theta \lesssim 2^\circ$  such that flat bands emerge at these angles. This is reminiscent of the vanishing of the velocity at certain “magic” rotation angles in bilayer graphene [11, 117, 202, 213, 214] except that in the case of bilayer MoS<sub>2</sub> it arises for an interval of angles. Other minigaps and flat bands are also found in the conduction band. The confined states that are closest to the gap are localized in the AA stacking regions of the moiré pattern, like in twisted bilayer graphene.

## 6.1 Atomic structure

The commensurate structure of tb-MoS<sub>2</sub> can be defined in the same manner that is common for twisted bilayer graphene (see for instance Refs. [20, 136]). Here we use the same notation as in Refs. [213, 214]. A commensurate tb-MoS<sub>2</sub> with rotation angle  $\theta$  is defined by two integers  $n$  and  $m$ , such that

$$\cos \theta = \frac{n^2 + 4nm + m^2}{2(n^2 + nm + m^2)}, \quad (6.1)$$

and its lattice vectors are  $\vec{t} = n\vec{a}_1 + m\vec{a}_2$  and  $\vec{t}' = -m\vec{a}_1 + (n + m)\vec{a}_2$ , where  $\vec{a}_1$  ( $a\sqrt{3}/2, -a/2, 0$ ) and  $\vec{a}_2$  ( $a\sqrt{3}/2, a/2, 0$ ) are the lattice vectors of monolayer 2H-MoS<sub>2</sub>, with the lattice distance  $a = 0.318$  nm. A unit cell of tb-MoS<sub>2</sub> contains  $N = 6(n^2 + nm + m^2)$  atoms.

### 6.1.1 Non relaxed structure

The crystal structure of tb-MoS<sub>2</sub> for large angle ( $\theta = 13.17^\circ$ ) is shown in Fig. 6.1. Non relaxed structure of tb-MoS<sub>2</sub> unit cell containing 114 atoms see in equation 6.1  $n = 2$  and  $m = 3$ . The unit cell  $(\vec{a}_1, \vec{a}_2)$  of monolayer 2H-MoS<sub>2</sub> contains 3 atoms: Mo at  $(0, 0, 0)$ , S  $(0, a/\sqrt{3}, 0.49115a)$  and S  $(0, a/\sqrt{3}, -0.49115a)$  [79, 179].

### 6.1.2 Structural relaxation

To find out the most stable configuration of the tb-MoS<sub>2</sub>, we relaxed the structure using starting positions obtained from the equation 6.1. The optimized position of the atoms in the unit cell are allowed to vary but the unit cell was unchanged like same as of MoS<sub>2</sub> mono and bilayer ( $a = 0.318$  nm) [Unit cell was fixed].

Relaxation of atomic positions along the  $xz$ -direction in the unit cell of tb-MoS<sub>2</sub> with different configurations shown in Fig. 6.2 leads to a small variation of

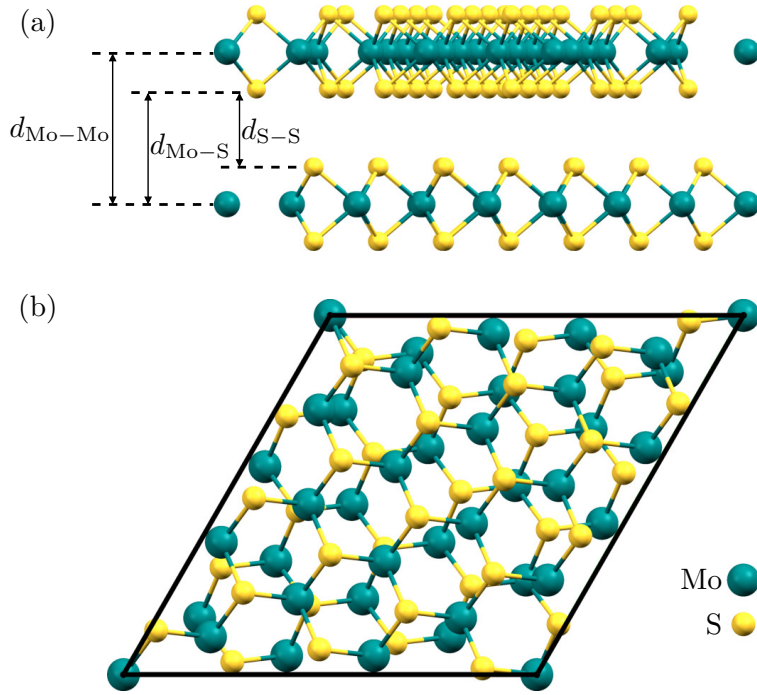


Figure 6.1: Atomic structure of bilayer MoS<sub>2</sub> at a twist angle  $\theta = 13.17^\circ$  ( $n = 2$  and  $m = 3$ ). (a) side view. (b) top view.

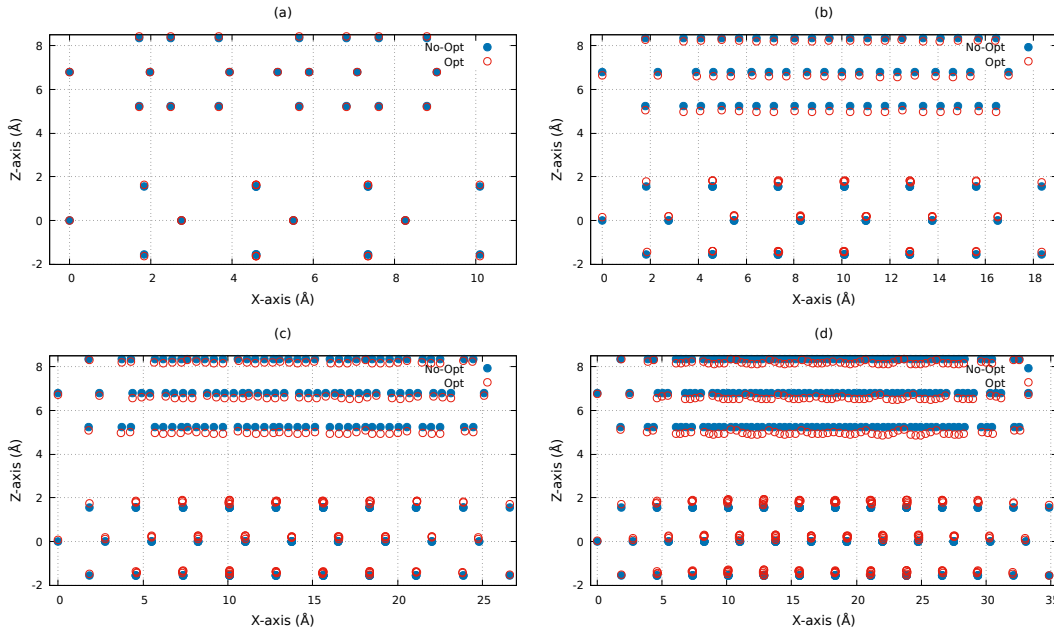


Figure 6.2: Variation of atomic positions along the  $xz$ -direction of tb-MoS<sub>2</sub> with (full blue circles) and without (empty red circles) relaxation of tb-MoS<sub>2</sub> different angles: (a) (1, 2)  $\theta = 21.79^\circ$ , (b) (2, 3)  $\theta = 13.17^\circ$ , (c) (3, 4)  $\theta = 9.43^\circ$ , and (d) (4, 5)  $\theta = 7.34^\circ$ .

atomic positions as well as interlayer distance see in Fig. 6.3 and table 6.1, this small variation nevertheless shows a large effect on the electronic band structure

Variation of atomic positions with relaxation in the unitcell of tb-MoS <sub>2</sub> .					
Angle (θ)	Atom type	Non relaxed (Average) (Å)	Relaxed		
			Minimum (Å)	Maximum (Å)	Average (Å)
<b>Top layer of tb-MoS<sub>2</sub></b>					
21.79°	S (Top)	8.3618	8.41184	8.41195	8.41189
	Mo	6.7999	6.79879	6.79909	6.79894
	S (Bottom)	5.2381	5.18333	5.18537	5.18435
13.17°	S (Top)	8.3618	8.19550	8.25118	8.22334
	Mo	6.7999	6.58041	6.63037	6.60539
	S (Bottom)	5.2381	4.96599	5.03606	5.10010
9.43°	S (Top)	8.3618	8.14464	8.30346	8.22405
	Mo	6.7999	6.55465	6.67651	6.61558
	S (Bottom)	5.2381	4.91389	5.08365	4.99877
7.34°	S (Top)	8.3618	8.10150	8.35520	8.22835
	Mo	6.7999	6.48560	6.72367	6.60463
	S (Bottom)	5.2381	4.89072	5.12878	5.00975
<b>Bottom layer of tb-MoS<sub>2</sub></b>					
21.79°	S (Top)	1.5618	1.61462	1.61666	1.61564
	Mo	0.0000	0.00088	0.00119	0.00103
	S (Bottom)	-1.5618	-1.61202	-1.61189	-1.61195
13.17°	S (Top)	1.5618	1.76400	1.83407	1.79903
	Mo	0.0000	0.16965	0.21961	0.19463
	S (Bottom)	-1.5618	-1.45133	-1.39587	-1.42376
9.43°	S (Top)	1.5618	1.71611	1.88519	1.80065
	Mo	0.0000	0.12309	0.27165	0.19737
	S (Bottom)	-1.5618	-1.50358	-1.34407	-1.42382
7.34°	S (Top)	1.5618	1.67073	1.92879	
	Mo	0.0000	0.07585	0.31392	0.19488
	S (Bottom)	-1.5618	-1.55466	-1.30269	-1.42867

Figure 6.3: Variation of atomic positions along the  $xz$ -direction of tb-MoS<sub>2</sub> with relaxation of tb-MoS<sub>2</sub> different angles: (a) (1, 2)  $\theta = 21.79^\circ$ , (b) (2, 3)  $\theta = 13.17^\circ$ , (c) (3, 4)  $\theta = 9.43^\circ$ , and (d) (4, 5)  $\theta = 7.34^\circ$ .

of tb-MoS<sub>2</sub>, it has explained in next section.

## 6.2 DFT calculations (Large angles)

Density functional theory (DFT) calculations based on first principle calculations were carried out with the ABINIT code, using the local density approximation (LDA) exchange-correlation functional and the Perdew-Burke-Ernzerhof (PBE) parameterized generalized gradient approximation (GGA) exchange-correlation functional. We considered fourteen valence electrons of Mo ( $4s^2, 4p^6, 4d^5, 5s^1$ ), six valence electrons of S ( $3s^2, 3p^4$ ) in the PAW pseudopotential. The Brillouin zone was sampled by a  $K$ -point mesh of  $0.8 \text{ nm}^{-1}$  separation in reciprocal space within the Monkhorst-Pack scheme [253], and the kinetic energy cutoff was chosen to be 544.22 eV. A vacuum region of 2 nm was inserted between the MoS<sub>2</sub> bilayers to avoid spurious interactions between periodic images.

### 6.2.1 Electronic band structure of different angles

For all of the DFT electronic band structure calculations done by LDA-PAW pseudopotentials to minimize the computational expense, we tested different pseudopotentials LDA-PAW and GGA-PAW +vdW obtained similar result, as shown in the appendix D.1.

Table 6.1: Calculated interlayer distance and supercell size of twisted bilayer MoS<sub>2</sub> with and without relaxation in different configurations.

Configuration	Super cell size	Interlayer distance- without relaxation (Å)	Interlayer distance-with relaxation (Å)
AA	2	6.790	6.790
21.79°	14	6.790	6.607
13.17°	38	6.790	6.608
9.43°	74	6.790	6.690
7.34°	122	6.790	6.586
5.08°	254	6.790	6.614

Figure 6.4 shows DFT bands of tb-MoS<sub>2</sub> along symmetric lines of the first Brillouin zone (see inset of the Fig. 6.4) for four values of the rotation angle  $\theta$ . Note that the size of the Brillouin zones depends on the size of a unit cell of the moiré pattern such that the scale of the horizontal axis varies with  $\theta$ . These bands should be compared with the monolayer bands plotted in the same first Brillouin zone as follows. On the one hand, some bands are not affected by the value of  $\theta$  see in appendix Fig. 10. The parabolic bands that emanates for the point  $S_0$  are not affected by  $\theta$ . Therefore, we always set the energy of  $S_0$  to zero. Similarly, for the angles shown in Fig. 6.4, the curvature of the parabola at the

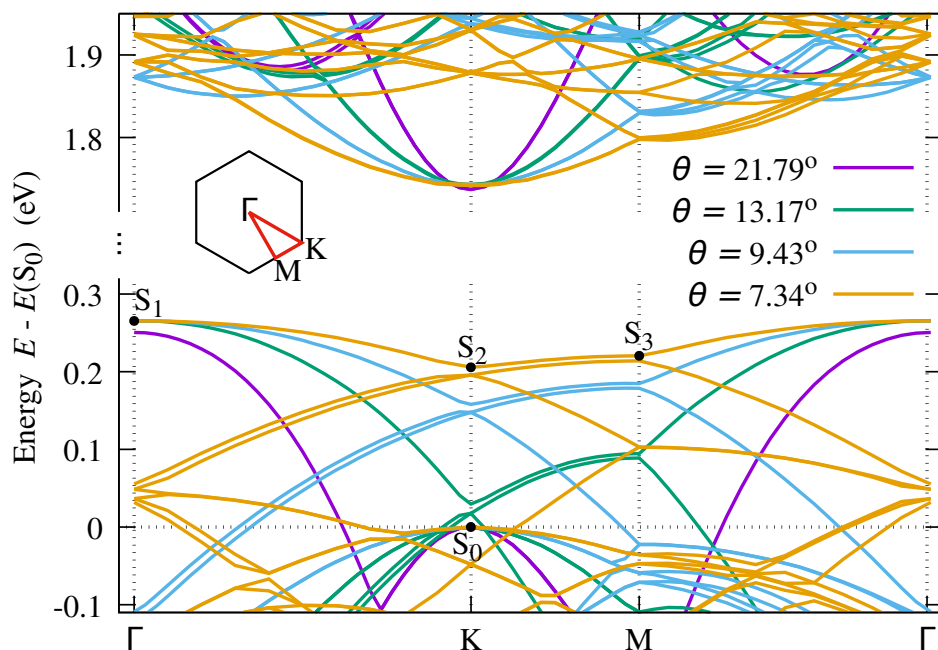


Figure 6.4: DFT conduction band (top) and valence band (bottom) in tb-MoS<sub>2</sub>: (1, 2)  $\theta = 21.79^\circ$ , (2, 3)  $\theta = 13.17^\circ$ , (3, 4)  $\theta = 9.43^\circ$  and (4, 5)  $\theta = 7.34^\circ$ . For every rotation angle, the origin of energy is fixed at the energy of the state  $S_0$  (see bottom). The first Brillouin zone is sketched in the insert, all the calculations have done by using LDA-PAW pseudopotentials.

lowest conduction band energy at  $K$  is not affected by  $\theta$ . On the other hand, many bands are modified with respect to the monolayer case. Like for simple stacking bilayers (AA, AB, AB', ...) [39, 71, 209], the highest valence energy at  $\Gamma$ ,  $E(S_1)$ , increases with respect to the monolayer such that the gap becomes indirect. However, for sufficiently large angles,  $E(S_1)$  does not vary significantly with  $\theta$ . In particular for the angles presented in Fig. 6.4, the curvature of the parabola at  $S_1$  is not affected by  $\theta$  and remains close to that of the monolayer.

Finally, considering the valence band, the most spectacular effect of decreasing  $\theta$  is the increase of the energies of some bands, thus gradually filling the gap. This is, for instance, clearly seen in Fig. 6.4 when considering the energy variation of the states  $S_2$  and  $S_3$  when  $\theta$  decreases. Similarly, some energies of certain conduction bands decrease as  $\theta$  decreases. Such a  $\theta$  dependence of bands has already been observed for some values of the rotation angle in previous DFT calculations [146]. In order to analyze it systematically, it is necessary to perform calculation for smaller angles which is difficult using DFT calculations. This is the reason why we have developed a TB model that can be used for every value

of  $\theta$ .

### 6.2.2 Electronic band structure of different angles with and without structural relaxation

As we explained in the structural relaxation of different angles, the position of atoms are moved until reach the minimum energy, but the unit cell ( $a = 0.318$  nm) remains the same before and after relaxation. Comparison of electronic band structure of tb-MoS<sub>2</sub> with and without relaxation of different angles (1,2)  $\theta = 21.79^\circ$  see in Fig. 6.5 and (2,3)  $\theta = 13.17^\circ$  tb-MoS<sub>2</sub> see in Fig. 6.6. After the relaxation bilayer separation distance between the layers have changed as shown in table 6.1 compare to the simple AA-stacking of MoS<sub>2</sub> bilayer, interlayer distance is decreasing because of internal stress or strain between the layers and atoms. This small variation of interlayer distance and atomic positions of the atoms in the unit cell of tb-MoS<sub>2</sub> band structure at the conduction band symmetry points  $\Gamma$  to  $K$  moves towards the valence band ( $\Gamma$ -point) and also modifies the bandgap as shown in Fig . 6.5 and Fig. 6.6.

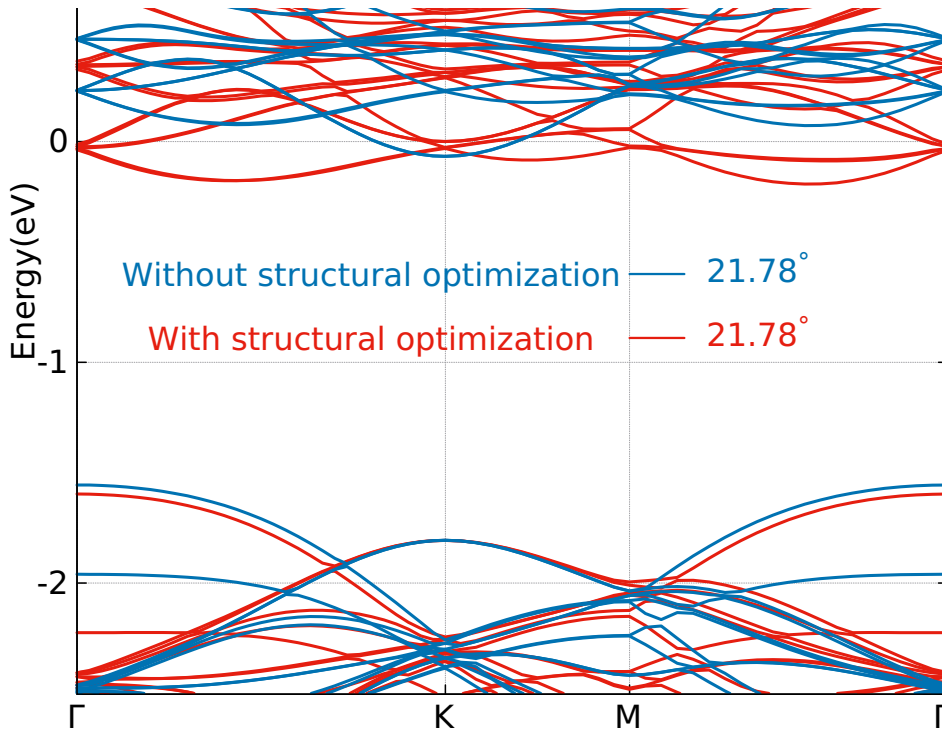


Figure 6.5: DFT bands around the gap in (1,2)  $\theta = 21.79^\circ$  tb-MoS<sub>2</sub> (built from AA stacking): Comparison between computation with and without structural relaxation. All the calculations have done by using LDA-PAW pseudopotentials.

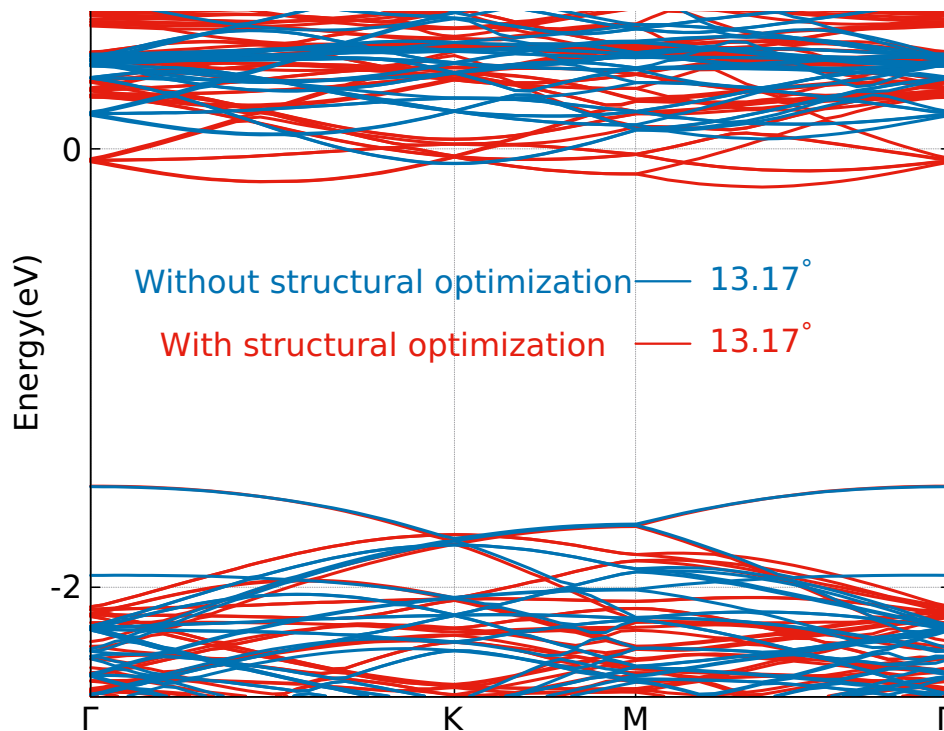


Figure 6.6: DFT bands around the gap in  $(2, 3)$   $\theta = 13.17^\circ$  tb-MoS<sub>2</sub> (built from AA stacking): Comparison between computation with and without structural relaxation.

## 6.3 Tight-Binding (TB) calculations

### 6.3.1 TB-model for MoS<sub>2</sub> monolayer

Our TB model for monolayer MoS<sub>2</sub> results from adapted onsite and hopping parameters of model proposed in Ref. [179] to our DFT result for monolayers as shown in Fig. 6.7. This TB-model is a recent update of the TB-model presented in chapter-4 (4.2.2), to account more correctly on the fact that there is two different  $S$ - $S$  first neighbor distances (see Table 6.3).

As in chapter-4, each unit cell of the monolayer contains 11 orbitals: 5d Mo orbitals ( $d_0 = 4d_{z^2}$ ,  $d_1 = 4d_{xz}$ ,  $4d_{yz}$ ,  $d_2 = 4d_{x^2-y^2}$ ,  $4d_{xy}$  of 1 Mo atom) and 6p S orbitals ( $3p_x$ ,  $3p_y$  and  $3p_z$  of 2 S atoms). Since the precise model may differ for valence and conduction states [179], we have decided to focus on reproducing the valence band accurately. The  $pS - pS$ ,  $dMo - dMo$  and  $dMo - pS$  hopping terms are calculated using a Slater-Koster formula with the parameters  $V_{pp\sigma}$ ,  $V_{pp\pi}$ ,  $V_{dd\sigma}$ ,  $V_{dd\pi}$ ,  $V_{dd\delta}$ ,  $V_{dp\sigma}$ ,  $V_{dp\pi}$ . For the monolayer, only first neighbor S-S, Mo-Mo and S-Mo hopping terms are taken into account. On-site energy values, number of neighbors taken into account, and values of Slater-Koster parameters are listed table 6.2.

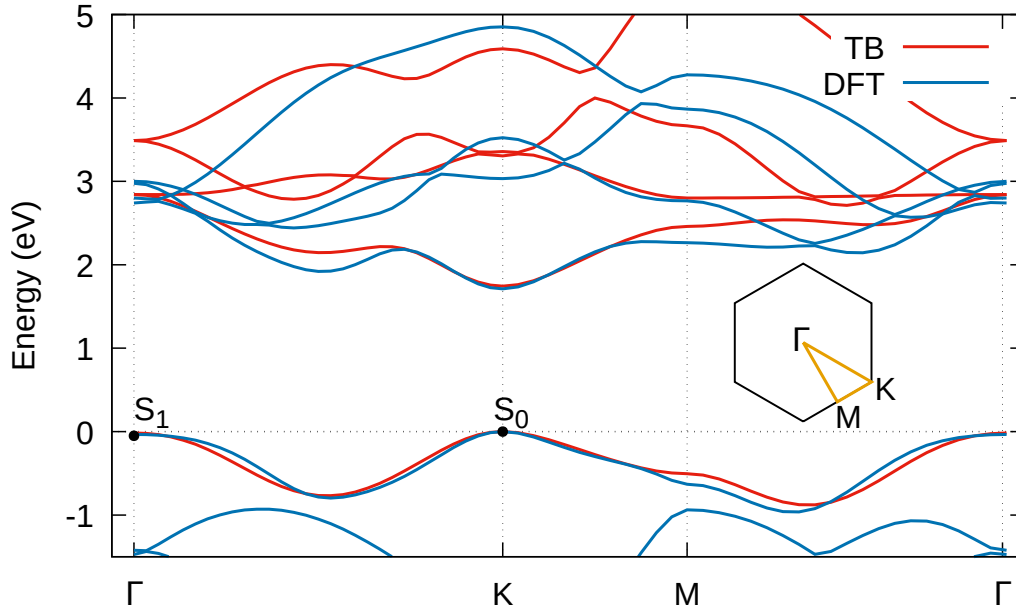


Figure 6.7: DFT and TB bands in monolayer MoS<sub>2</sub>. The origin of the energy is chosen at the maximum energy of the valence band, *i.e.*, at the energy of the states labeled  $S_0$ ,  $E(S_0) = 0$ . Since  $E(S_1) < E(S_0)$  the gap is direct at K. The first Brillouin zone is sketched in the insert.

Note that our TB model has been adapted to simulate not only the DFT monolayer bands, but also the DFT bands of twisted bilayers (mainly valence bands). Lattice vectors and lattice parameters are defined in section 6.1.

### 6.3.2 TB model for twisted bilayer MoS<sub>2</sub> (tb-MoS<sub>2</sub>)

In a second step, we consider the coupling between two layers of MoS<sub>2</sub>. Most previous studies [23, 46, 186, 241] include only  $pS - pS$  interlayer coupling terms, but  $dMo - pS$  and  $dMo - dMo$  terms may also be important because we do not limit the interlayer coupling to first neighbor hopping. Therefore, we include  $pS - pS$ ,  $dMo - pS$ , and  $dMo - dMo$  interlayer terms in our Slater-Koster scheme as shown in table 6.3. It turns out that the latter two are indeed important to reproduce the DFT valence band correctly. An exponential decay with interatomic distance [46] and a cutoff function [135] are applied to these interlayer terms, like in twisted bilayer graphene [214] for the explanation of cut-off distance see in appendix D.2. Figure 6.8 shows the comparison between DFT and TB bands for tb-MoS<sub>2</sub> with  $\theta = 21.79^\circ$  and  $9.43^\circ$ . The agreement is excellent for the highest energy valence bands and qualitatively correct for the conduction bands.

The atomic structure of commensurate twisted bilayer MoS<sub>2</sub> (tb-MoS<sub>2</sub>) have

Table 6.2: Tight-binding (TB) Slater-Koster parameters for monolayer MoS<sub>2</sub>, and pair of neighbors for which the hopping term is non zero. Lattice parameter of monolayer MoS<sub>2</sub>  $a = 0.318$  nm.

Atom	Orbitals	On-site energy (eV)
Mo	$d_0 = 4d_{z^2}$	$E_0^0 = 0.1356$
	$d_1 = 4d_{xz}, 4d_{yz}$	$E_1^0 = -0.4204$
	$d_2 = 4d_{x^2-y^2}, 4d_{xy}$	$E_2^0 = 0.0149$
S	$3p_x, 3p_y$	$E_{x,y}^0 = -38.71$
	$3p_z$	$E_z^0 = -29.45$

Atom	Neighbor	Number	Inter-atomic distance (nm)	Slater-Koster parameters (eV)
Mo	Mo	3	0.318	$V_{dd\sigma} = -0.9035$ $V_{dd\pi} = 0.7027$ $V_{dd\delta} = 0.0897$
	S	6	0.241	$V_{dp\sigma} = -7.193$ $V_{dp\pi} = 3.267$
S	S	1	0.312	$V_{pp\sigma} = 8.079$ $V_{pp\pi} = -2.678$
		6	0.318	$V_{pp\sigma} = 7.336$ $V_{pp\pi} = -2.432$

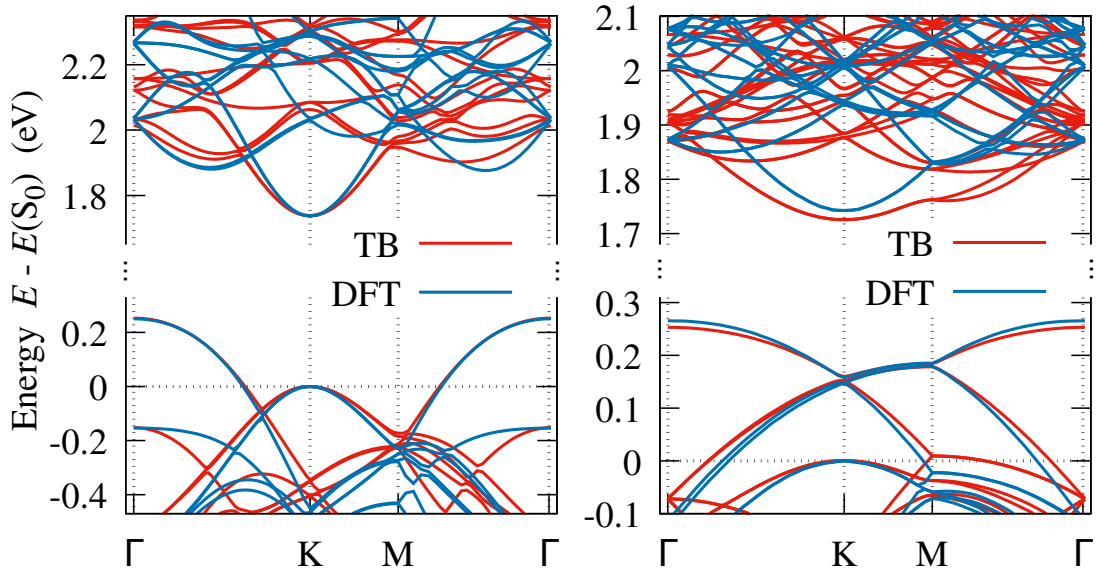


Figure 6.8: TB and DFT bands around the gap in tb-MoS<sub>2</sub>: (left) (1,2)  $\theta = 21.79^\circ$  and (right) (3,4)  $\theta = 9.43^\circ$ .

been used in the present work are listed table 6.4.

Table 6.3: TB Slater-Koster parameters for interlayer hopping terms in tb-MoS<sub>2</sub>.  $d^0$  is the interlayer distance; for the definition of  $d_{\text{Mo-Mo}}$ ,  $d_{\text{Mo-Mo}}$ , and  $d_{\text{Mo-S}}$ , see Fig. 6.1.

Atom	Neighbor	$d^0$ (nm)	$q$	Slater-Koster parameters (eV)
Mo	Mo	0.6800	11.6496	$V_{dd\sigma}^0 = -0.1416$ $V_{dd\pi}^0 = -0.4254$ $V_{dd\delta}^0 = -0.1237$
	S	0.5238	8.9738	$V_{dp\sigma}^0 = -1.4793$ $V_{dp\pi}^0 = 0.52431$
S	S	0.3676	6.2981	$V_{pp\sigma}^0 = 6.2782$ $V_{pp\pi}^0 = -8.9733$

Table 6.4:  $(n, m)$  twisted bilayer MoS<sub>2</sub> (tb-MoS<sub>2</sub>) structures that have been used in the present work.  $\theta$  is the rotation angle between the two layers and  $N$  the number of atoms in a cell.

$(n, m)$	$\theta$ [deg.]	$N$
(1,2)	21.787	42
(2,3)	13.174	114
(3,4)	9.430	222
(4,5)	7.341	366
(5,6)	6.009	546
(6,7)	5.086	762
(7,8)	4.408	1014
(10,11)	3.150	1986
(15,16)	2.134	4326
(16,17)	2.004	4902
(18,19)	1.788	6162
(19,20)	1.696	6846
(20,21)	1.614	7566
(22,23)	1.470	9114
(25,26)	1.297	11706
(27,28)	1.203	13614
(30,31)	1.085	16746
(33,34)	0.987	20202
(36,37)	0.906	23982

### 6.3.3 Moiré pattern of tb-MoS<sub>2</sub>

**Moiré pattern from AA:** We were constructed, a different type tb-MoS<sub>2</sub> moiré cells that can be built from AA-stacking, as the atoms of a monolayer unit cell are not equivalent by symmetry. For simplicity, we consider only moiré patterns constructed as follows. Starting from an AA stacked bilayer (where Mo atoms of a layer lie above the Mo atoms of the other layer, and S atoms of a layer lie above the S atoms of the other layer), the layer 2 is rotated with respect to the layer 1 by the angle  $\theta$  around a rotation axis going through two Mo atoms as shown in Fig. 6.9.

- AA stacking regions are regions where Mo atoms of a layer lie above a Mo atom of the other layer, and S atoms of a layer lie above an S atom of the other layer.
- AB' stacking regions are regions where Mo atoms of layer 1 lie above an S atom of layer 2, and S atoms of layer 1 (Mo atoms of layer 2) do not lie above an atom of layer 2 (layer 1).
- BA' stacking regions are regions where S atoms of layer 1 atoms lie above a Mo atom of layer 2, and Mo atoms of layer 1 (S atoms layer 2) do not lie above an atom of layer 2 (layer 1).

**Moiré pattern from AB:** Figure 6.10 shows a top view of the atomic structure of (6, 7) tb-MoS<sub>2</sub> built from AB stacking. Here one can identify several specific types of stacking regions: Starting from an AB stacked bilayer (where Mo atoms of layer 1 lie above a Mo atom of layer 2, and S atoms of each layer do not lie above an atom of the other layer), layer 2 is rotated with respect to layer 1 by the angle  $\theta$  around an axis containing two Mo atoms.

- AA' stacking regions are regions where Mo atoms (S atoms) of one layer lie above an S atom (Mo atom) of the other layer.
- AB stacking regions are regions where Mo atoms of layer 1 lie above a Mo atom of layer 2, and S atoms of each layer do not lie above an atom of the other layer.
- BA stacking regions are regions where S atoms of layer 1 lie above an S atom of layer 2, and Mo atoms each layer do not lie above an atom of the other layer.

In Fig. 6.10, AB stacking regions are located at the corners of the moiré cell. AA' and BA stacking regions are located at 1/3 and 2/3 of its long diagonal, respectively.

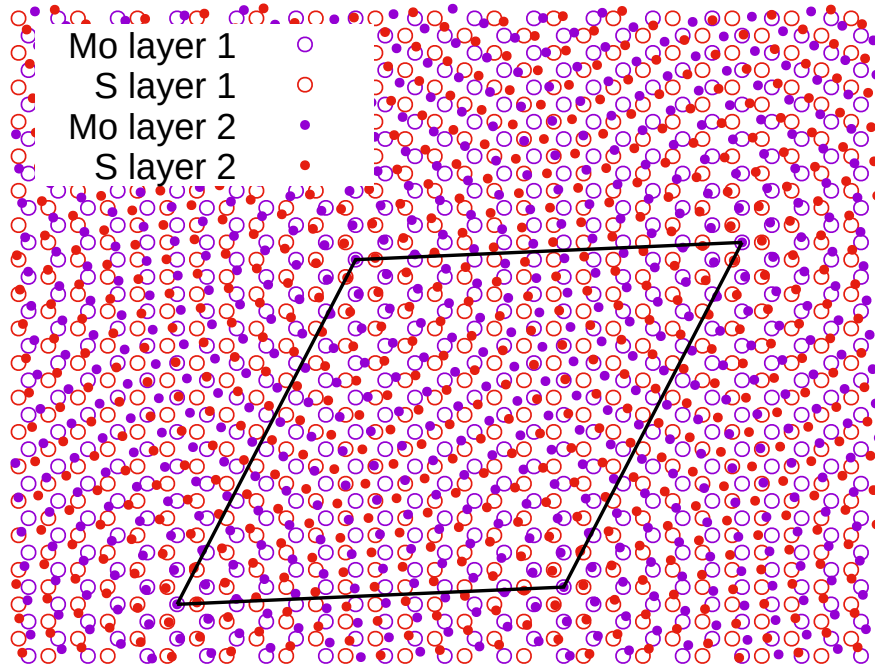


Figure 6.9: Atomic structure of (6,7) tb-MoS<sub>2</sub> built from AA stacked bilayers. Black lines show the unit cell. AA stacking regions are at the corners of this cell, BA' and AB' stacking regions are at 1/3 and 2/3 of its longest diagonal, respectively.

We have checked that the qualitative results presented below are also found in tb-MoS<sub>2</sub> built from an AB stacked bilayer before rotation. The interlayer distance between layers containing Mo atoms is fixed to  $d_{\text{Mo-Mo}} = 0.68$  nm which is the DFT-optimized interlayer distance for AA stacked bilayer MoS<sub>2</sub>. The atomic relaxation probably has an important effect on the electronic structure in tb-MoS<sub>2</sub> see in sections 6.1.2 and 6.2.2 [125, 146], like in twisted bilayer graphene [148]. However in this work, our aim is to provide a simple tight-binding (TB) scheme using Slater-Koster parameters that can be used for tb-MoS<sub>2</sub> at all angles in order to analyze qualitatively the electronic states that are confined by the moiré pattern. Indeed, as was the case for twisted bilayer graphene, the study of the non-relaxed structure should make it possible to identify generic properties that will persist with relaxation. Therefore, our numerical results should be qualitatively relevant even if they may not be quantitatively accurate.

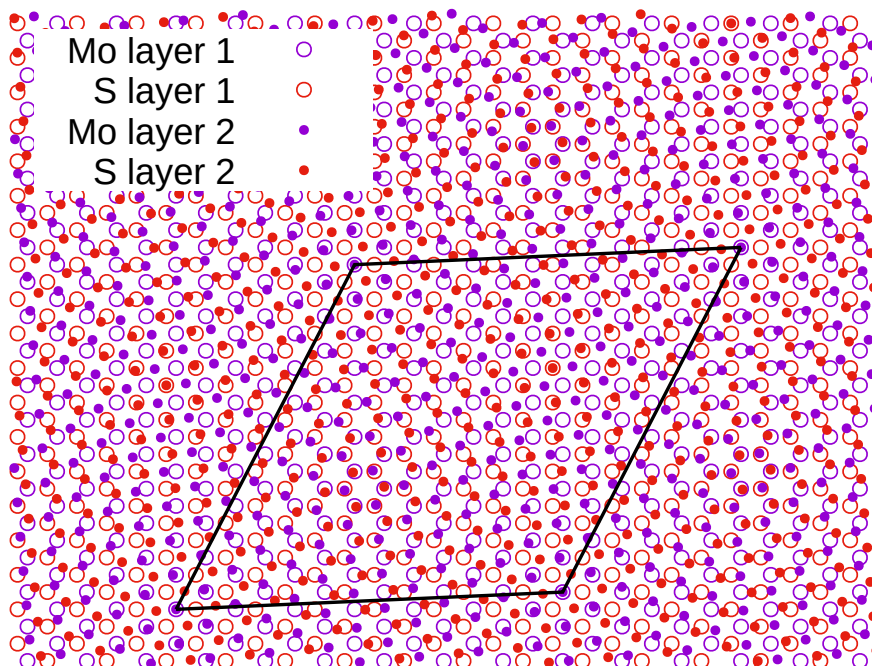


Figure 6.10: Atomic structure of (6,7) tb-MoS<sub>2</sub> built from AB stacked bilayers. Black lines show the unit cell. AB stacking regions are at the corners of this cell, AA' and BA stacking regions are at 1/3 and 2/3 of the longest diagonal, respectively.

### 6.3.4 Analysis of bands of tb-MoS<sub>2</sub> built from AA stacking

Now, we analyze the evolution of the bands around the main gap with  $\theta$ . Figure 6.11 shows this evolution for the top of the valence bands with a focus on the states labeled S<sub>1</sub>, S<sub>2</sub>, S<sub>3</sub>, and S<sub>4</sub>. Both DFT and TB results show that the energies  $E(S_2)$  and  $E(S_3)$  vary almost linearly with  $\theta^2$  (Fig. 6.11(b)), which is a strong indication that this phenomenon is a direct consequence of the moiré structure. Indeed, in the MoS<sub>2</sub> monolayer, the states around the gap are close to the  $\Gamma$  and K points in reciprocal space, with a parabolic dispersion. In the twisted bilayer, the points  $\Gamma_1$  and  $\Gamma_2$  of the 2 monolayers (layer 1 and layer 2) coincide, while K<sub>1</sub> and K<sub>2</sub> are separated by a small distance K<sub>1</sub>K<sub>2</sub> proportional to the angle  $\theta$  for small  $\theta$ . As the monolayer band dispersion is parabolic, the energy of the crossing of the bands of the two layers varies with  $\theta^2$ , and so do the changes in energy induced by the moiré pattern. Similarly, many studies have shown that the changes of energy due to the moiré pattern in twisted graphene bilayer varies linearly with  $\theta$  because the low-energy bands of a graphene monolayer are linear in  $\|\vec{K} - \vec{k}\|$  (see, e.g., Ref. [17]).

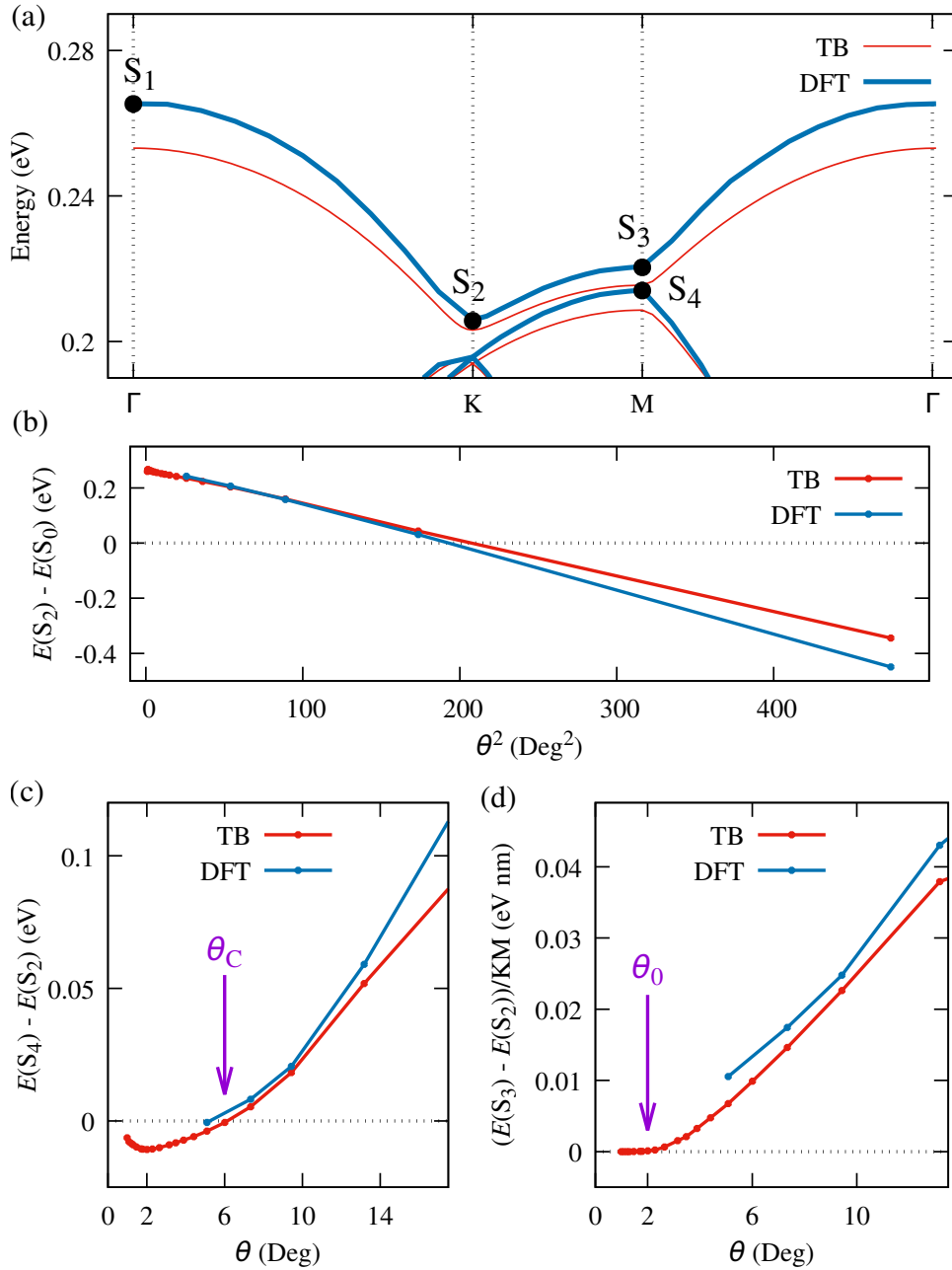


Figure 6.11: Dependence of valence bands on rotation angle  $\theta$ : (a) Valence band dispersion of (4,5) tb-MoS<sub>2</sub>,  $\theta = 7.34^\circ$ . (b) Energy  $E(S_2)$  of the state  $S_2$  (see panel (a)) versus  $\theta^2$ . (c) Energy difference between the states  $S_4$  and  $S_2$ ,  $\Delta E_{24} = E(S_4) - E(S_2)$ , versus  $\theta$ . A negative value of  $\Delta E_{24}$  means that a gap  $|\Delta E_{24}|$  exists between the band below the gap and the other valence bands. (d) Average slope of  $E(\vec{k})$  of the band between states  $S_2$  and  $S_3$ . For every rotation angle, the origin of energy is fixed at the energy  $E(S_0)$  of the state  $S_0$  (see Figs. 6.4).

Furthermore, our TB computations show that the highest energy valence band

is isolated from the remainder of the valence bands by a minigap for sufficiently small values of  $\theta$  (see in Fig. 6.15). This is illustrated by Fig. 6.11(c), showing that  $E(S_4) - E(S_2) < 0$ , *i.e.*, the presence of a minigap, for  $\theta < \theta_C \approx 6^\circ$ . This isolated band is not degenerate, thus it corresponds to one state per moiré cell. Figure 6.15 shows that such isolated bands are also present among the conduction bands with different values of  $\theta_C$ . Finally, for the smallest angles, several isolated bands appear both among the valence and conduction bands.

We also consider the average slope of the highest valence band between the points K and M, *i.e.*, between the states S<sub>2</sub> and S<sub>3</sub> (Fig. 6.11(a)). This quantity is proportional to the average Boltzmann velocity (intra-band velocity). As shown in Fig. 6.11(d), this velocity tends towards zero for small angles,  $\theta = \theta_0 \approx 2^\circ$ . This demonstrates an electronic confinement corresponding to a “flat band”, like it has been found for twisted bilayer graphene and twisted bilayer MoS<sub>2</sub> for specific angles, so-called magic angles [11, 117, 202, 213, 214, 247]. However, in tb-MoS<sub>2</sub>, this velocity vanishes not only for discrete values of  $\theta$ , but flat bands emerge for a continuous range of  $\theta$ ,  $\theta \lesssim \theta_0$ . We worked different TB-models, that one also shows qualitatively same behavior but quantitatively different behavior, for the tight-binding parameters and band analysis see in appendix D.3.

### 6.3.5 Analysis of bands of tb-MoS<sub>2</sub> built from AB stacking

Above section, we showed only results for tb-MoS<sub>2</sub> built from AA stacking. However, other types of moiré patterns exist in this system as well; in particular, one can start from AB stacking. Figure 6.12 presents a comparison of the  $\theta$ -dependence of the band structure between tb-MoS<sub>2</sub> between bilayers built from AA stacking and from AB stacking. The results are qualitatively very similar, which shows that the main results of our study do not depend on the type of moiré pattern. The main quantitative differences with respect to the results discussed in the main text are the values of  $\theta_C$  and  $\theta_0$ :  $\theta_C \approx 6^\circ$  versus  $\theta_C \approx 4.5^\circ$  for tb-MoS<sub>2</sub> built from AA and AB stacking, respectively;  $\theta_0 \approx 2^\circ$  versus  $\theta_0 \approx 1.8^\circ$  for tb-MoS<sub>2</sub> built from AA and AB stacking, respectively.

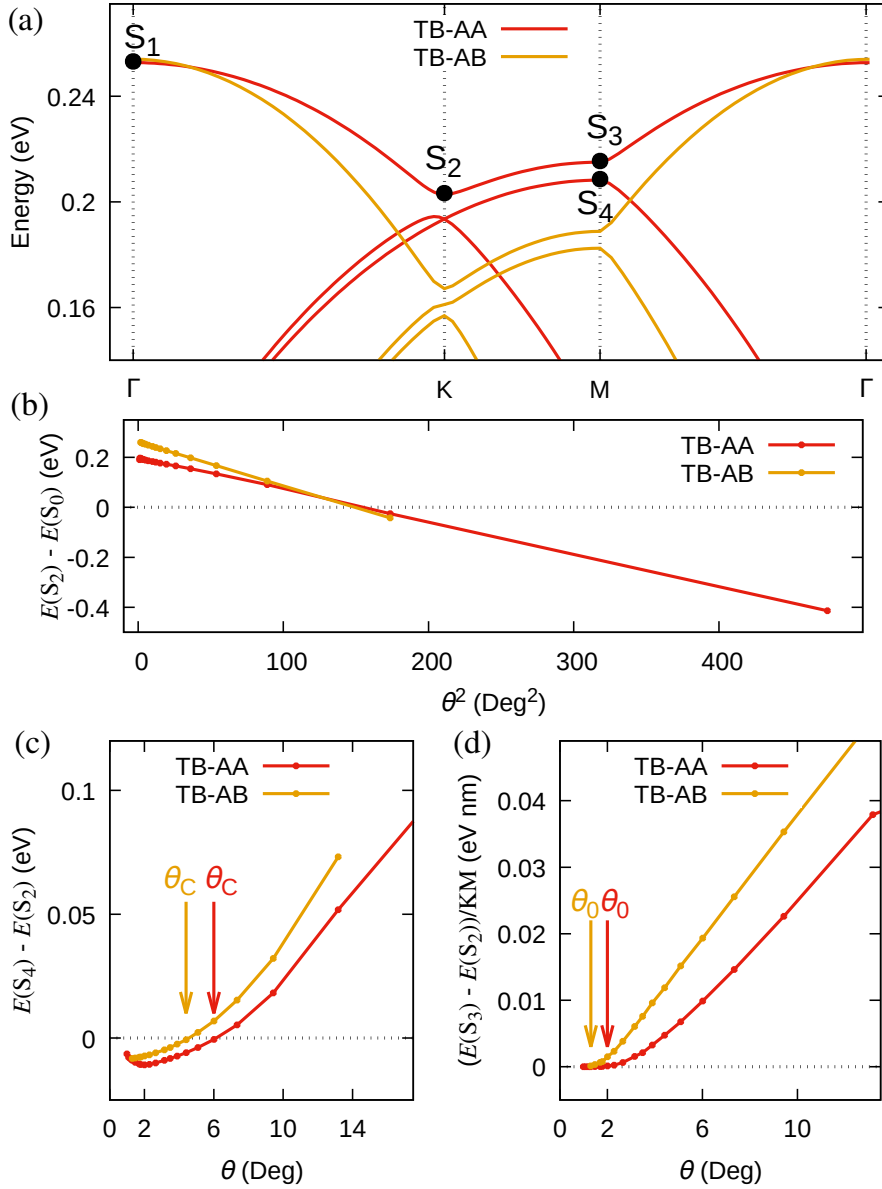


Figure 6.12: Dependence of valence bands on rotation angle  $\theta$ : Comparison between tb-MoS<sub>2</sub> built from AA stacking and tb-MoS<sub>2</sub> built from AB stacking. The TB-AA curves coincide with those of Fig. 6.11. (a) valence-band dispersion of (4,5) tb-MoS<sub>2</sub>,  $\theta = 7.34^\circ$ . (b) Energy  $E(S_2)$  of state  $S_2$  (see panel (a)) versus  $\theta^2$ . (c) Energy difference between states  $S_4$  and  $S_2$ ,  $\Delta E_{24} = E(S_4) - E(S_2)$ , versus  $\theta$ . A negative  $\Delta E_{24}$  value means that a gap  $|\Delta E_{24}|$  exists between the band below the gap and the other valence bands. (d) Average slope of  $E(\vec{k})$  of the band between states  $S_2$  and  $S_3$ . For every rotation angle, the origin of energy is fixed at the energy  $E(S_0)$  of the state  $S_0$  (see Fig. 6.4).

### 6.3.6 Local density of states (LDOS)

The TB density of states (DOS) is calculated employing a Gaussian broadening with a standard deviation  $\sigma = 2$  meV. For the  $k$ -integration we use a grid with

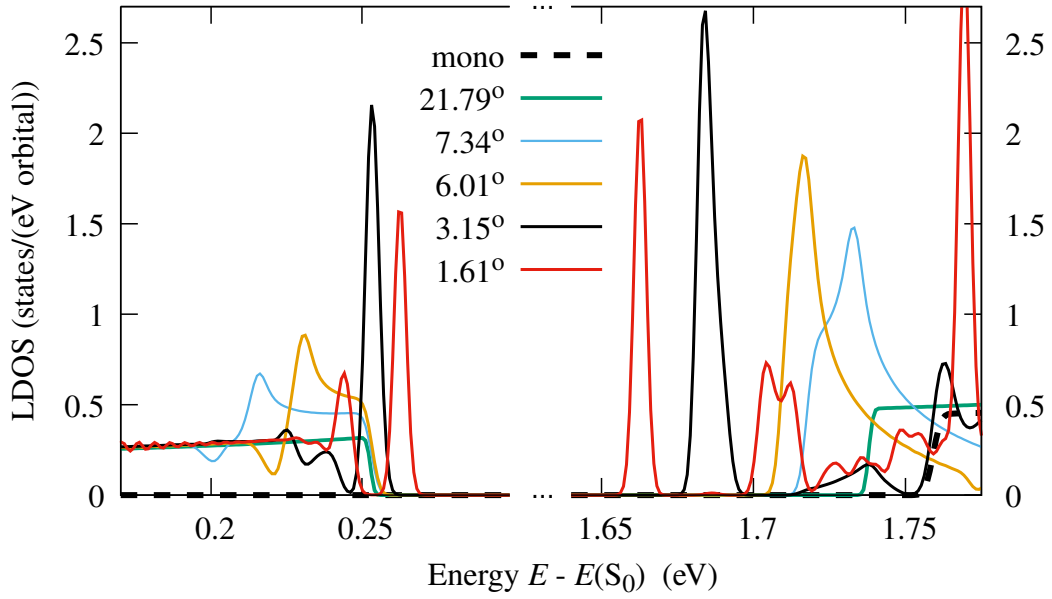


Figure 6.13: TB local density of states (LDOS) of the  $4d_{z^2}$  Mo orbital at the center of the AA stacking region for different rotation angles of tb-MoS<sub>2</sub>. The LDOS is calculated employing a Gaussian broadening with a standard deviation  $\sigma = 2$  meV.

$Nk_x \times Nk_y$  points in the reciprocal unit cell, with  $Nk_x = Nk_y$  large enough to obtain a DOS that is independent of these parameters. Due to this broadening, the minigaps found in the band structure are not always seen clearly in the DOS.

Figure 6.13 shows the LDOS for the  $d_0 = d_{z^2}$  orbital of an Mo atom at the center of the AA stacking region for several rotation angles  $\theta$ . Figure 6.14 (top panel) shows the local density of states (LDOS) of the  $d_0 = d_{z^2}$  Mo orbital for the selected rotation angle  $\theta = 5.09^\circ$ , but for Mo atoms located at different stacking regions of the moiré pattern (Fig. 6.9). Confined states (“flat bands”) lead to sharp peaks in the LDOS (Fig. 6.13). These states have  $d_{z^2}$  Mo character (Fig. 6.14 (bottom panel)), and a very small weight for the other  $d$  Mo orbitals. The flat bands are mainly located in the AA stacking region (Fig. 6.14 (top panel)). Figure 6.17 shows that the lowest-energy flat bands in the conduction and valence bands correspond to Mo atoms that are located at the center of the AA stacking regions, and that the next flat band in the conduction and valence bands corresponds to states located in a ring in the AA stacking regions.

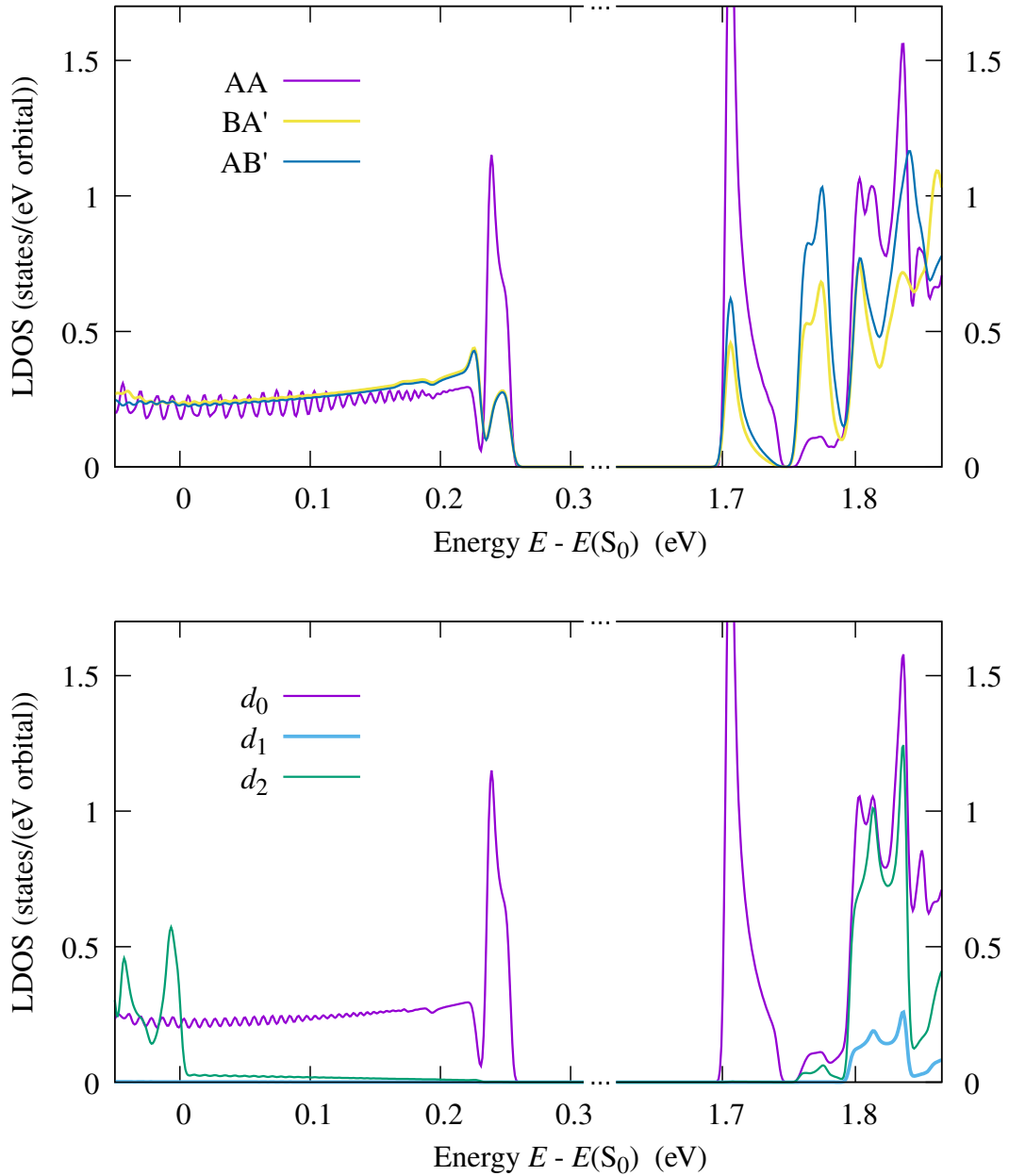


Figure 6.14: TB local density of states (LDOS) of the Mo orbital around the main gap in (6,7)  $\theta = 5.09^\circ$  tb-MoS<sub>2</sub> (built from AA stacking, see Fig. 6.9): (Top panel) LDOS of the  $d_0 = d_{z^2}$  Mo orbital at the center of AA, BA', and AB' stacking regions. (Bottom panel) LDOS of  $d_0$ ,  $d_1 = 4d_{xz}$ ,  $4d_{yz}$  and  $d_2 = 4d_{x^2-y^2}$ ,  $4d_{xy}$  Mo orbitals at the center of the AA stacking region. The LDOS is calculated employing a Gaussian broadening with the standard deviation  $\sigma = 2$  meV.

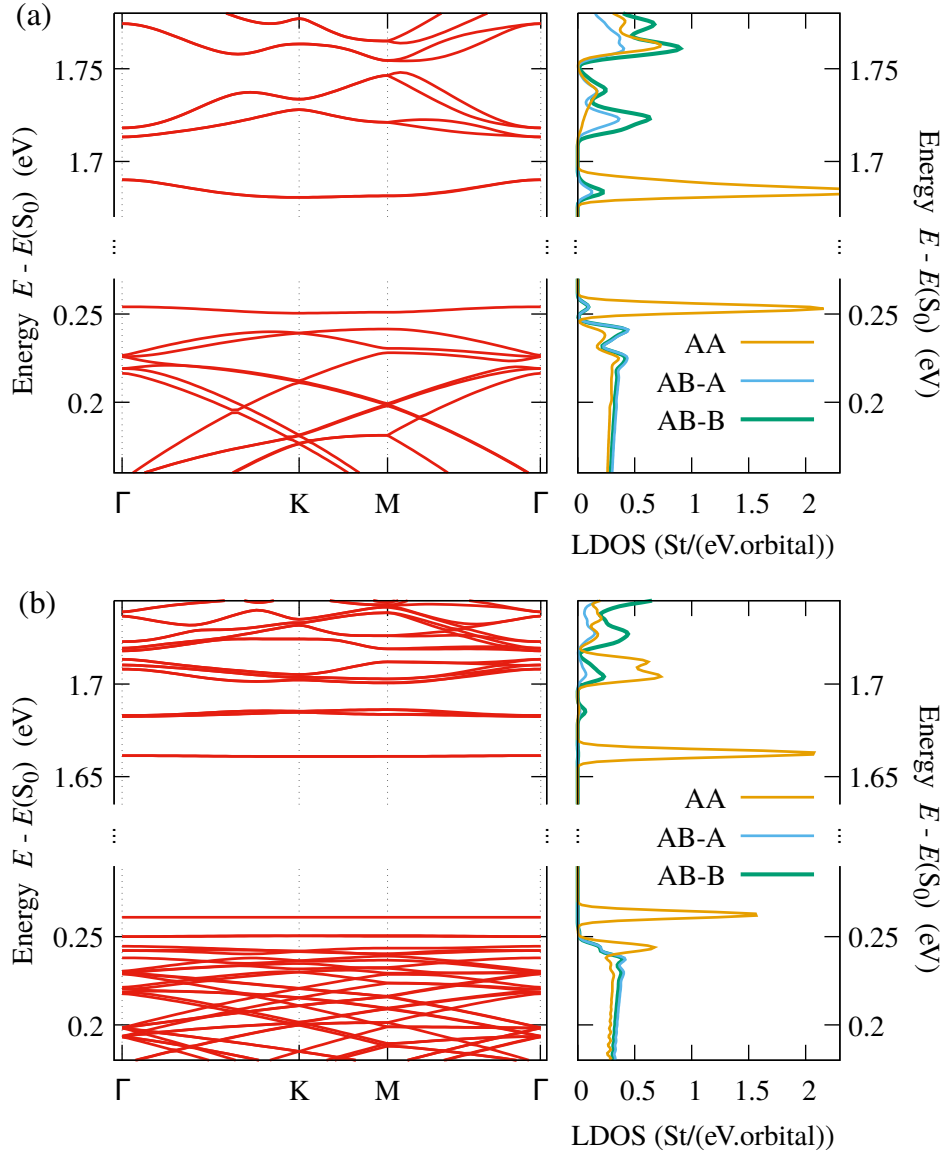


Figure 6.15: TB band dispersion and local density of states (LDOS) of  $d_0 = d_{z^2}$  Mo atoms at the center of the AA stacking region and the center of the AB region: (a) for (10, 11) tb-MoS<sub>2</sub>  $\theta = 3.15^\circ$ , and (b) for (20, 21) tb-MoS<sub>2</sub>  $\theta = 1.61^\circ$ . In a moiré cell, two symmetrically equivalent AB stacking regions are located at  $1/3$  and  $2/3$  of the longest diagonal of the cell (see Fig. 6.9)). Each AB stacking region contains two types of Mo atoms: (AB-A) Mo atom of a layer lying above an S atom of the other layer, (AB-B) Mo atom of a layer not lying above an atom of the other layer.

### 6.3.7 Confined state in the AA region of the moiré pattern

Like for the monolayer, the electronic states of tb-MoS<sub>2</sub> closest to the gap have mainly  $4d_{z^2}$  Mo character. This is still true for small angles, we explained in

previous section see 6.3.6 , but states of the isolated bands are mainly localized in the AA stacking region. Consequently, the local density of states (LDOS) for  $4d_{z^2}$  Mo at the center of AA region contains sharp peaks around the gap (Fig. 6.15). Note that in the LDOS (Fig. 6.15), the minigap discussed in the previous paragraph is not seen clearly because of the numerical Gaussian broadening used to calculate the LDOS. The sharp peaks closest to the main gap are found neither in the LDOS of the other  $4d$  Mo orbitals, nor in the LDOS of the Mo atoms that are not located in the AA stacking regions. Thus, the flat band states are confined in AA stacking regions, like in twisted bilayer graphene for small rotation angles [11,118,149,213,214]. The lowest energy flat bands (closest to the gap in the valence and conduction bands) are localized at the center of the AA regions, as is also reflected by a strong enhancement of the local density of states in the corresponding regions (Fig. 6.15), whereas the next flat bands are localized in a ring in the AA regions rather than at their center (see Fig. 6.17).

### 6.3.7.1 Electronic band structure with SOC at $\theta = 3.15^\circ$ and $\theta = 1.61^\circ$

The electronic band structure of twisted bilayer MoS<sub>2</sub> with SOC of (10,11) tb-MoS<sub>2</sub>  $\theta = 3.15^\circ$  and (20,21) tb-MoS<sub>2</sub>  $\theta = 1.61^\circ$  is shown in Fig. 6.16. As we explained in the monolayer case (see in Chapter-6 section 4.2.1.2) large spin splitting at valence band  $\approx 148$  meV. Similarly, we investigated the effect of SOC on electronic band structure of tb-MoS<sub>2</sub>, where the mirror symmetry broken by the rotation angle. Because of broken inversion symmetry, spin degeneracies are lifted along the highest symmetry path ( $\Gamma$ -K-M- $\Gamma$ ) in the Brillouin zone, but the time reversal invariant points  $\Gamma$  and M remain spin degenerate (for the time reversal symmetry see appendix A.2). Here, the splitting is opposite to the monolayer case, the effect of SOC more significant at the conduction band of the tb-MoS<sub>2</sub> [242]. The band splitting at the minimum of the conduction band is  $\approx 4.53$  meV.

### 6.3.7.2 Eigenstates corresponding to flat bands ( $\theta = 1.61^\circ$ ) in tb-MoS<sub>2</sub>

Analysis of the band dispersion (Fig. 6.15) shows that the first isolated flat band below the main gap (valence band) is non-degenerate and thus contains one state per moiré cell. By contrast, the two first isolated flat bands above the gap (conduction bands) are two-fold quasi degenerate. The weight of the eigenstates corresponding to these flat bands is mainly concentrated on  $d_0 = d_{z^2}$  Mo orbitals (more than 98% and 95%, respectively) located at the center of AA stacking regions. This is shown in Fig. 6.17(b,c) for eigenstates at the points  $\Gamma$ ,

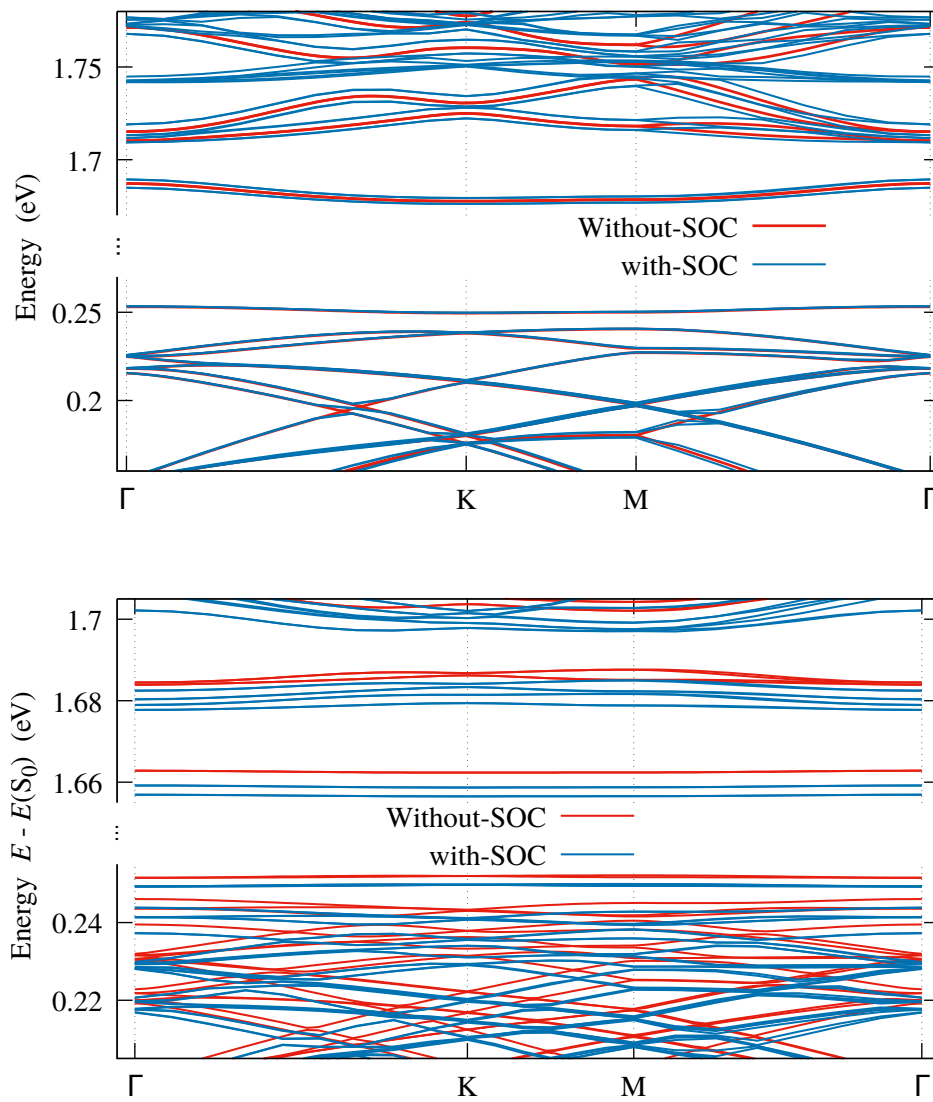


Figure 6.16: TB electronic band structure with and without SOC: (Top) for (10, 11) tb-MoS<sub>2</sub>  $\theta = 3.15^\circ$ , and (Bottom) for (20, 21) tb-MoS<sub>2</sub>  $\theta = 1.61^\circ$ .

K, and M of the flat band above and below the main gap, respectively.

For small enough angles, the next isolated flat bands (Fig. 6.15(b)) are four-fold quasi degenerate in the conduction band and two-fold quasi degenerate in the valence band. The weight of the eigenstates, corresponding to these flat bands at the points  $\Gamma$ , K, and M, is mainly located in a ring in AA stacking regions (Fig. 6.17(a,d)). Analysis of eigenstates corresponding to flat bands at  $\theta = 3.15^\circ$  see in appendix D.4.

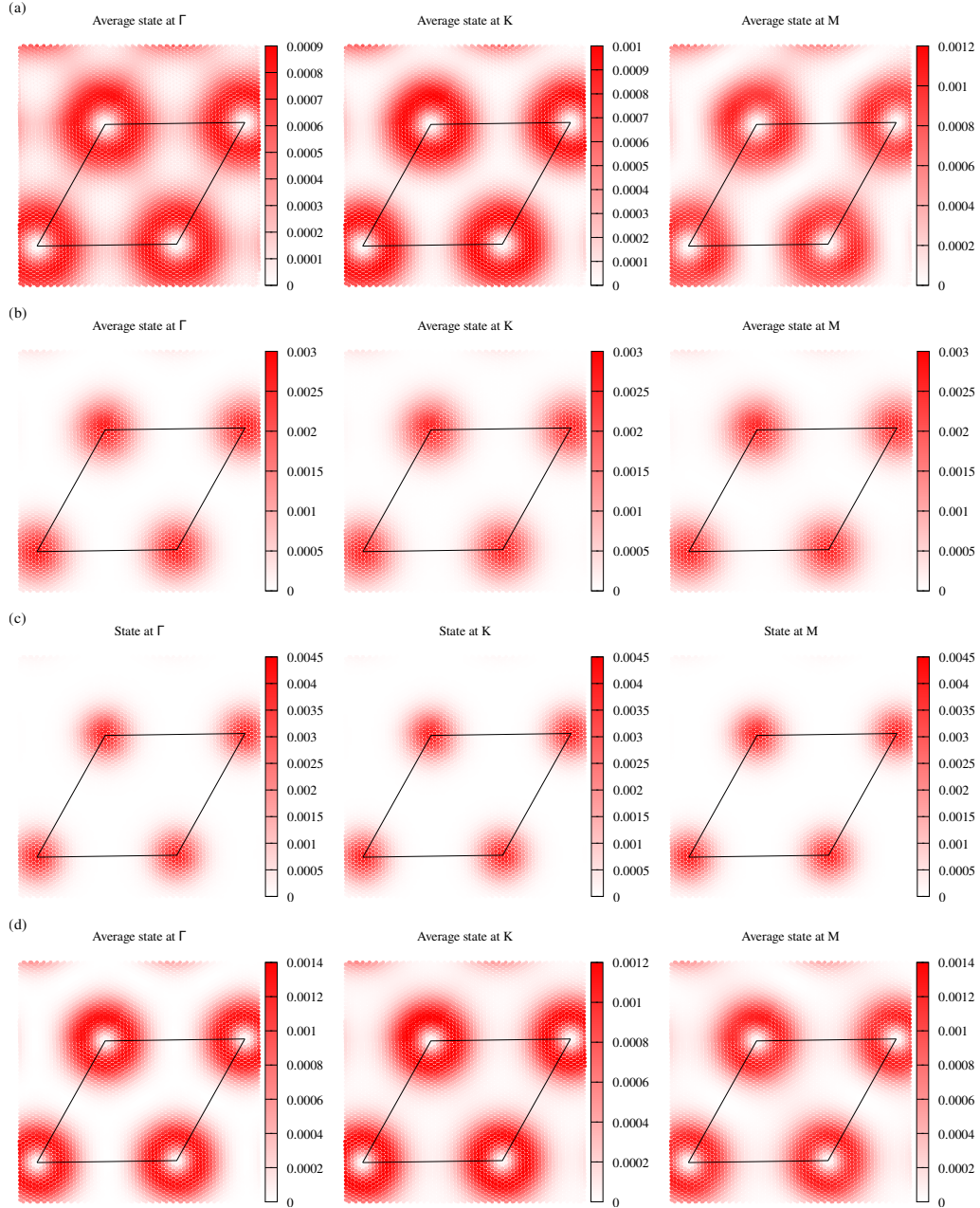


Figure 6.17: Average weight of the eigenstates at  $\Gamma$ ,  $K$ , and  $M$ , of the flat band around the gap in real space in  $(20, 21)$   $tb$ -MoS<sub>2</sub> (built from AA stacking, see Fig. 6.9) with a rotation angle  $\theta = 1.61^\circ$ , Conduction band: (a) Average of the four-fold quasi-degenerate band at energy  $E \simeq 1.686 \pm 0.002$  eV and (b) average of the two-fold quasi-degenerate band at energy  $E \simeq 1.6626 \pm 0.0002$  eV. Valence band: (c) non-degenerate bands at energy  $E \simeq 0.26249 \pm 0.00001$  eV, and (d) average of the two-fold quasi-degenerate band at energy  $E \simeq 0.2518 \pm 0.0003$  eV. The corresponding bands are shown in Fig. 6.15(b). The color scale shows the weight of the eigenstate on each  $d_0 = 4d_{z^2}$  orbital of the Mo atoms. The sum of these weights is more than 98% and 95% of each state for the valence and conduction band, respectively. Black lines show the unit cell containing 2522 Mo atoms. AA stacking regions are at the corners of this cell.

## 6.4 Conclusion

We have revisited the tight-binding description of twisted MoS<sub>2</sub> bilayers starting from DFT computations. Particular attention was paid to interlayer Slater-Koster parameters and we confirmed that not only the closest  $pS-pS$  interlayer coupling terms, but also  $dMo-pS$  and  $dMo-dMo$  coupling needs to be taken into account for an accurate description. We then used this tight-binding model to investigate the band structure of MoS<sub>2</sub> bilayers at smaller rotation angles  $\theta$  where the moiré unit cell becomes too large for DFT computations. We found that isolated bands appear in the valence and conduction bands close to the gap for  $\theta \lesssim 5-6^\circ$ . For even smaller angles  $\theta \lesssim 2^\circ$ , the average velocity vanishes. The emergence of the corresponding flat bands is reflected by sharp peaks in the density of states. This phenomenon is accompanied by a localization of the wave function mainly in AA stacking regions. Depending on the flat band, this real-space confinement can occur at the center of AA region and also in a ring around the center of the AA region.

In the present discussion, we have focused on rotated MoS<sub>2</sub> bilayers that are constructed from AA stacking, but we have checked that qualitatively the same behavior is found when one starts from AB stacking instead.

The vanishing velocity and related emergence of flat bands identifies weakly doped MoS<sub>2</sub> bilayers as good candidates for the observation of strong correlation effects. Beyond first theoretical efforts in this direction [232], we offer our DFT-based tight-binding model as a solid starting point for more detailed studies of correlation effects in twisted MoS<sub>2</sub> bilayers.



*Chapter No. 7*

---

*Summary*

---

This PhD thesis work focused on the electronic properties of monolayers of Transition Metal Dichalcogenides (TMDs), graphene/TMD bilayers, and twisted bilayers of TMDs. In order to study such complex structures, we have combined density functional theory (DFT) approaches and simplified tight-binding (TB) models.

We have first studied theoretically electronic and transport properties of TMDs. We focused on different TMDs of imperfections in the crystal structure, such as point defects that can strongly modify the transport properties of these materials. Here, we analyze the effect of point defects on the density of states, conductivity, microscopic conductivity, carrier concentration, and mobility of single layers of semiconducting TMDs with the form  $\text{MX}_2$  ( $\text{M} = \text{Mo}, \text{W}$  and  $\text{X} = \text{S}, \text{Se}, \text{Te}$ ). The electronic structure is considered within an eleven-band model, which accounts for the relevant combination of  $d$  orbitals of the metal  $\text{M}$  and  $p$  orbitals of the chalcogen  $\text{X}$ . We use the recursion method (Lanczos method) and Kubo-Greenwood formula for the numerical calculation of the conductivity in the TMDs with different distributions of disorder. Our results show that  $\text{M}$  or  $\text{X}$  defects create midgap states that localize charge carriers around the defects and modify the transport properties of the material.

Secondly, we analyzed a new family of graphene based transition metal dichalcogenide (TMDs) heterostructures including van der Waals interactions. We checked two different TMDs ( $\text{MoS}_2$  and  $\text{WSe}_2$ ), but results should be similar to the other TMDs. A study of first principle calculations (DFT) including vdW interactions and modeling of 2D graphene/ $\text{MoS}_2$ , and graphene/ $\text{WSe}_2$  bilayer vdW heterostructures was conducted by ABINIT software program. We checked different supercell configurations of the bilayer system to minimize the lattice mismatch between the layers: graphene/ $\text{MoS}_2$  [4:3 ( $\approx 3.33\%$ ), 5:4 ( $\approx 2.52\%$ ), and 9:7 ( $\approx 0.53\%$ )] and graphene/ $\text{WSe}_2$  [4:3 ( $\approx 0.606\%$ )].

We predicted accurate interlayer spacing between the graphene and  $\text{MoS}_2$  layers in the graphene/ $\text{MoS}_2$  bilayer heterostructure and the graphene and  $\text{WSe}_2$  layers in the graphene/ $\text{WSe}_2$  heterostructure. The predicted interlayer spacing of the three different configurations of graphene/ $\text{MoS}_2$  heterostructures are 3.367 Å, 3.287 Å, and 3.361 Å respectively, which is in good agreement with the experimental data ( $3.4 \pm 0.1$  Å) [171] and interlayer spacing between the layers of graphene/ $\text{WSe}_2$  heterostructure is 4.194 Å. We analyze the electronic band structure of graphene/ $\text{MoS}_2$  bilayer heterostructures using the ABINIT software program and find that the Dirac point of graphene is shifted upwards above the Fermi level and is located near the conduction bands of the  $\text{MoS}_2$  layer, yielding a considerable charge transfer in the 4:3 bilayer, whereas the Dirac point lies

in the bandgap region in the 5:4 bilayer indicating no charge transfer between the constituent layers and final configuration, the Dirac point (shifted from  $K$  to  $\Gamma$ ) lies in the bandgap region in the 9:7 bilayer indicating no charge transfer between the constituent layers because of the smaller lattice mismatch and minimal strain. The 9:7 system has minimized the lattice mismatch between the layers. We also analyzed the electronic band structure of the graphene/WSe<sub>2</sub> [4:3] bilayer heterostructure. The Dirac point lies in the bandgap region in the 4:3 bilayer indicating no charge transfer between the constituent layers because of the smaller lattice mismatch between the layers. We observed that the location of the Dirac point can be shifted by tuning the interlayer spacing between the graphene and MoS<sub>2</sub> layers, and it might happen to graphene and WSe<sub>2</sub>.

The effect of the spin orbit coupling (SOC) on graphene/MoS<sub>2</sub> and graphene/WSe<sub>2</sub> bilayer heterostructures is not strong around the Dirac point whereas in the monolayer with a MoS<sub>2</sub> and WSe<sub>2</sub> at the valence band (K-point) large band splitting (MoS<sub>2</sub>  $\approx$  148 meV and WSe<sub>2</sub>  $\approx$  475 meV) observed due to a strong SOC effect and the graphene layer at the Dirac point band splitting remains very small. For vdW bilayer heterostructures with and without SOC the energy bandgap difference at the Dirac point is very small. We also found that the electronic band structure has changed after the relaxation of the atomic positions and lattice parameters because of the internal stress and strain due to lattice mismatch between the graphene and TMDs layers. From our calculations, we strongly recommend to calculate the electronic and optical properties of vdW bilayer heterostructures, lattice optimization, relaxation of atoms in an unit cell with a small lattice mismatch.

The next step we will studied point defects, such as vacancies or substitution of atoms in order to calculate the electronic properties of these heterostructures. Some preliminary results (C-vacancy in the graphene/WSe<sub>2</sub> [4:3] bilayer, M replaced by Fe in graphene/WSe<sub>2</sub> [4:3] bilayer) are in progress.

Furthermore, we have revisited the tight-binding description of monolayers of TMDs as well as twisted MoS<sub>2</sub> bilayers starting from DFT computations. Particular attention was paid to interlayer Slater-Koster parameters and we confirmed that not only the closest  $pS - pS$  interlayer coupling terms, but also  $dMo - pS$  and  $dMo - dMo$  coupling needs to be taken into account for an accurate description. We then used this tight-binding model to investigate the band structure of MoS<sub>2</sub> bilayers at smaller rotation angles  $\theta$  where the moiré unit cell becomes too large for DFT computations. We found that isolated bands appear in the valence and conduction bands close to the gap for  $\theta \lesssim 5 - 6^\circ$ . For even smaller angles  $\theta \lesssim 2^\circ$ , the average velocity vanishes. The emergence of the corresponding flat bands is reflected by sharp peaks in the density of states. This

phenomenon is accompanied by a localization of the wave function mainly in AA stacking regions. Depending on the flat band, this real-space confinement can occur at the center of AA region and also in a ring around the center of the AA region.

In this last part, we have focused on rotated MoS<sub>2</sub> bilayers that are constructed from AA stacking, but we have checked that qualitatively the same behavior is found when one starts from AB stacking instead. The vanishing velocity and related emergence of flat bands identifies weakly doped MoS<sub>2</sub> bilayers as good candidates for the observation of strong correlation effects. Beyond first theoretical efforts in this direction [232], we offer our DFT-based tight-binding model as a solid starting point for more detailed studies of correlation effects in twisted MoS<sub>2</sub> bilayers. We have started to look into magnetic instabilities in the tb-MoS<sub>2</sub> at small angles and the first preliminary results show, as expected, a very strong reduction of the electronic interaction energy beyond which a magnetic state appears.

#### **Outlook:**

In Chapter-4, we proposed a tight-binding model for various TMDs and calculated transport properties of defected systems (point defect). A natural continuation would be to calculate the transport properties with effect of spin orbit coupling and substitutional atoms.

In Chapter-5, to study graphene/MoS<sub>2</sub> heterostructure, we consider the superlattice structure [9:7], characterised by a small lattice mismatch, which is more realistic with respect to ones used in previous studies ([4:3] and [5:4] structures). Now it would be interesting to study a twisted graphene/MoS<sub>2</sub> [9:7] bilayer and analyze the electronic properties as a function of twist angle. One could also investigate heterostructures band folding and compare the experimental result.

In chapter-6, we looked at the electronic confinement and weights of the low energy electronic states at the smallest angles using the tight-binding model of twisted bilayer MoS<sub>2</sub>. We will investigate the electronic properties effect of spin orbit coupling with small rotation angles, the relaxation effect and study the magnetic properties at smallest angles by using mean field theory.

---

## *Appendices*

---

	<b>Page</b>
<b>A</b> Spin Orbit Coupling (SOC) . . . . .	156
<b>A.1</b> Spin Orbit Coupling (SOC) of d-orbitals . . . . .	156
<b>A.2</b> Time Reversal Symmetry and Spatial Inversion Symmetry	156
<b>B</b> Transport properties of $\text{MX}_2$ . . . . .	158
<b>B.1</b> Conductivity and inelastic scattering length vs scattering time . . . . .	158
<b>B.2</b> Elastic mean free path . . . . .	158
<b>C</b> Graphene/ $\text{MoS}_2$ bilayer heterostructures DFT+TB calculations .	162
<b>C.1</b> Individual layers of graphene/ $\text{MoS}_2$ heterostructures of different configurations 4:3 and 9:7 . . . . .	162
<b>C.2</b> Electronic band structure of graphene/ $\text{MoS}_2$ [4:3] heterostruc- ture with and without relaxation . . . . .	164
<b>C.3</b> TB-model for graphene/ $\text{MoS}_2$ (5:4 and 9:7) . . . . .	165
<b>D</b> Electronic properties of tb- $\text{MoS}_2$ . . . . .	168
<b>D.1</b> Electronic band structure of different pseudopotentials . .	168
<b>D.2</b> Cut off distance of tb- $\text{MoS}_2$ . . . . .	169
<b>D.3</b> TB-model (alternative) for twisted bilayer $\text{MoS}_2$ . . . . .	170
<b>D.4</b> Eigenstates corresponding to flat bands ( $\theta = 3.15^\circ$ ) in tb- $\text{MoS}_2$ . . . . .	173

---

## A Spin Orbit Coupling (SOC)

The main text we explained the SOC Hamiltonian of p-orbital (see section 2.4.2), this appendix, we present the SOC Hamiltonian of the  $d$ -orbital (see section A.1). The calculation of electronic band structure of the TMDs including SOC, we used  $d$ -orbital of transition metal, the time reversal symmetry and spatial inversion symmetry see section A.2.

### A.1 Spin Orbit Coupling (SOC) of d-orbitals

For the simplicity  $d$ -orbitals can be represented as  $|d_{1\pm}\rangle = |d_{xy\pm}\rangle$ ,  $|d_{2\pm}\rangle = |d_{yz\pm}\rangle$ ,  $|d_{3\pm}\rangle = |d_{zx\pm}\rangle$ ,  $|d_{4\pm}\rangle = |d_{(x^2-y^2)\pm}\rangle$ , and  $|d_{5\pm}\rangle = |d_{(3z^2-r^2)\pm}\rangle$ . where  $+$  = spin up ( $\uparrow$ ) and  $-$  = spin down ( $\downarrow$ ) [87] see table 1.

	$ d_1^\uparrow\rangle$	$ d_2^\uparrow\rangle$	$ d_3^\uparrow\rangle$	$ d_4^\uparrow\rangle$	$ d_5^\uparrow\rangle$	$ d_1^\downarrow\rangle$	$ d_2^\downarrow\rangle$	$ d_3^\downarrow\rangle$	$ d_4^\downarrow\rangle$	$ d_5^\downarrow\rangle$
$ d_1^\uparrow\rangle$	0	0	0	$i\lambda$	0	0	$\frac{\lambda}{2}$	$-i\frac{\lambda}{2}$	0	0
$ d_2^\uparrow\rangle$	0	0	$i\frac{\lambda}{2}$	0	0	$-\frac{\lambda}{2}$	0	0	$-i\frac{\lambda}{2}$	$-i\frac{\sqrt{3}\lambda}{2}$
$ d_3^\uparrow\rangle$	0	$-i\frac{\lambda}{2}$	0	0	0	$i\frac{\lambda}{2}$	0	0	$-\frac{\lambda}{2}$	$+\frac{\sqrt{3}\lambda}{2}$
$ d_4^\uparrow\rangle$	$-i\lambda$	0	0	0	0	0	$i\frac{\lambda}{2}$	$\frac{\lambda}{2}$	0	0
$ d_5^\uparrow\rangle$	0	0	0	0	0	0	$i\frac{\sqrt{3}\lambda}{2}$	$-\frac{\sqrt{3}\lambda}{2}$	0	0
$ d_1^\downarrow\rangle$	0	$-\frac{\lambda}{2}$	$-i\frac{\lambda}{2}$	0	0	0	0	0	$-i\lambda$	0
$ d_2^\downarrow\rangle$	$\frac{\lambda}{2}$	0	0	$-i\frac{\lambda}{2}$	$-i\frac{\sqrt{3}\lambda}{2}$	0	0	$-i\frac{\lambda}{2}$	0	0
$ d_3^\downarrow\rangle$	$i\frac{\lambda}{2}$	0	0	$\frac{\lambda}{2}$	$-\frac{\sqrt{3}\lambda}{2}$	0	$i\frac{\lambda}{2}$	0	0	0
$ d_4^\downarrow\rangle$	0	$i\frac{\lambda}{2}$	$-\frac{\lambda}{2}$	0	0	$i\lambda$	0	0	0	0
$ d_5^\downarrow\rangle$	0	$i\frac{\sqrt{3}\lambda}{2}$	$\frac{\sqrt{3}\lambda}{2}$	0	0	0	0	0	0	0

Table 1: Spin orbit coupling Hamiltonian parameters in the basis set of atomic orbital ( $d$ ).

### A.2 Time Reversal Symmetry and Spatial Inversion Symmetry

Time reversal symmetry preserves the Kramer's degeneracy, which states that a wave function  $\psi$  only differs from its complex conjugate  $\psi^*$  by a reversal of wave vector and electron spin. The condition for time reversal symmetry in the Brillouin zone reads

$$E(\vec{k}, \uparrow) = E(-\vec{k}, \downarrow). \quad (1)$$

Equation 1 says that the energy of a state with wave vector  $\vec{k}$  and spin-up at a point in Brillouin zone is the same as the state with wave vector  $-\vec{k}$  and spin-down at the same point. On the other hand, if the crystal lattice has spatial inversion

---

symmetry (the crystal lattice does not change under the operation  $\vec{r} \rightarrow -\vec{r}$ ), the energy of the bands will satisfy

$$E(\vec{k}, \uparrow) = E(-\vec{k}, \uparrow) \quad \text{and} \quad E(\vec{k}, \downarrow) = E(-\vec{k}, \downarrow) \quad (2)$$

if the crystal has both time reversal and spatial inversion symmetry, the band structure of the crystal would satisfy both equation 1 and equation 2:

$$E(\vec{k}, \uparrow) = E(\vec{k}, \downarrow). \quad (3)$$

The energy level splitting will not only depend on SOC but also on the symmetries present in the solids. In other words, the energy bands will stay spin degenerate when there is any crystal symmetry even if the spin orbital interaction is considered.

## B Transport properties of $\text{MX}_2$

The chapter-4, we explained the conductivity and inelastic scattering length of different TMDs in small concentration of vacancies (1 %), here we present large concentration of vacancies (3 % and 10 %) to study the conductivity and inelastic scattering length of different TMDs see B.1. Elastic mean free path results see B.2.

### B.1 Conductivity and inelastic scattering length vs scattering time

Figures 1 and 2 show the variation of the conductivity  $\sigma$  and inelastic mean free path  $L_i$  versus  $\tau_i$  for different energies corresponding to the valence band to conduction band region in large vacancy concentration 3 and 10 % in a supercell respectively. The first case (i) conduction band region:  $\text{MoS}_2$  ( $E = 1.90$  eV),  $\text{MoSe}_2$  ( $E = 1.88$  eV),  $\text{MoTe}_2$  ( $E = 1.36$  eV),  $\text{WSe}_2$  ( $E = 2.10$  eV), and  $\text{WTe}_2$  ( $E = 1.62$  eV) see Figs. 1 and 2. The large values of  $\tau_i$ , the conductivity  $\sigma$  is almost constant as expected in a diffusive regime. This regime corresponds to energies for which the DOS is weakly affected by scatterers. We have checked that  $\sigma$  with different concentration of vacancies ( $c$ ),  $\sigma$  is almost independent on  $c$  which is expected by the Boltzmann theory of transport. Second case (ii) bandgap region:  $\text{MoS}_2$  ( $E = 0.80$  eV),  $\text{MoSe}_2$  ( $E = 0.66$  eV),  $\text{MoTe}_2$  ( $E = 0.56$  eV),  $\text{WSe}_2$  ( $E = 0.60$  eV), and  $\text{WTe}_2$  ( $E = 0.72$  eV) see Figs. 1 and 2. The transport is determined by diffusion of midgap states which are localized states. Therefore, the localization regime is reached at small  $\tau_i$ . Third case (iii) valence band region:  $\text{MoS}_2$  ( $E = -0.60$  eV),  $\text{MoSe}_2$  ( $E = -0.64$  eV),  $\text{MoTe}_2$  ( $E = -0.32$  eV),  $\text{WSe}_2$  ( $E = -0.56$  eV), and  $\text{WTe}_2$  ( $E = -0.58$  eV) in Figs. 1 and 2 the behavior similar to the first case. The first and third cases, for  $\tau_i$  closed to the elastic scattering time  $\tau_e$ , there is a diffusive behavior where the  $\sigma(\tau_i)$  reaches a maximum,  $\sigma_M$ ; for larger values of  $\tau_i$ ,  $\tau_i \gg \tau_e$ ,  $\sigma(\tau_i)$  decreases progressively as expected in the localization regime due to Anderson localization in 2D [104,142].

### B.2 Elastic mean free path

In our calculations  $\tau_i$  and then  $L_i$  are considered as adjustable parameters. Roughly speaking, when  $L_i \ll L_e$  ( $\tau_i \ll \tau_e$ ) the inelastic disorder dominates; it should correspond to very high temperatures (ballistic regime). When  $L_i \simeq L_e$  ( $\tau_i \simeq \tau_e$ ), the conductivity is equal to microscopic conductivity, which should correspond to the high temperature case, typically room temperature (diffusive regime). If  $L_i \gg L_e$  ( $\tau_i \gg \tau_e$ ), quantum localization will dominates transport

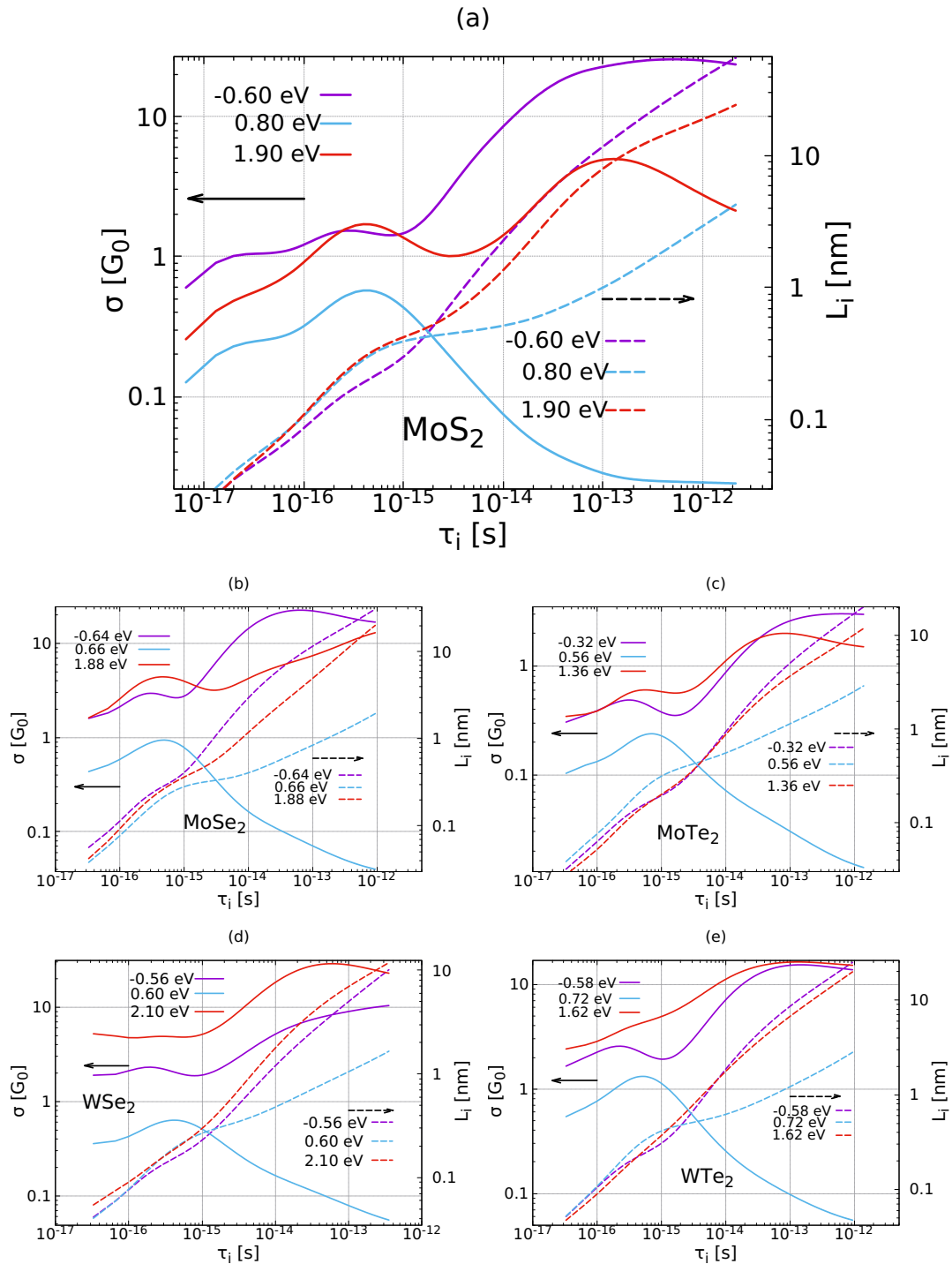


Figure 1: Conductivity  $\sigma$  (solid line) and inelastic scattering length  $L_i$  (dashed line) in MX<sub>2</sub> versus inelastic scattering time  $\tau_i$  for defect concentration  $c = 3\%$  of point defects (creating a vacancy by removal of atoms  $M = \text{Mo}, \text{W}$  or  $X = \text{S}, \text{Se}, \text{Te}$  randomly). For three energy values: Valence band (blue), inside midgap states region (magenta) and conduction band (red). (a) MoS<sub>2</sub>, (b) MoSe<sub>2</sub>, (c) MoTe<sub>2</sub>, (d) WSe<sub>2</sub>, and (e) WTe<sub>2</sub>. Where,  $G_0 = 2e^2/h$ .

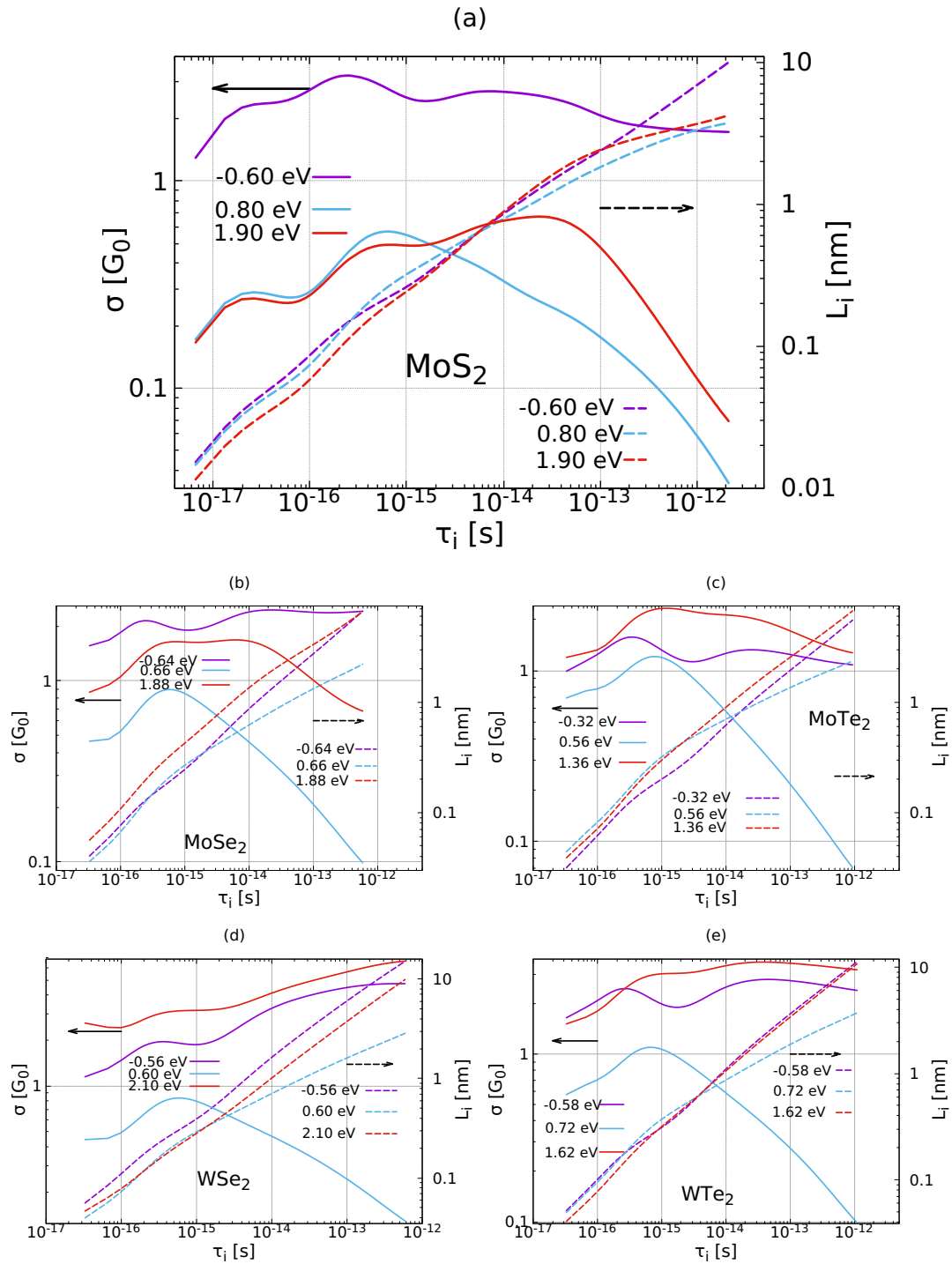


Figure 2: Conductivity  $\sigma$  (solid line) and inelastic scattering length  $L_i$  (dashed line) in MX<sub>2</sub> versus inelastic scattering time  $\tau_i$  for defect concentration  $c = 10\%$  of point defects (creating a vacancy by removal of atoms  $M = \text{Mo, W}$  or  $X = \text{S, Se, Te}$  randomly). For three energy values: Valence band (blue), inside midgap states region (magenta) and conduction band (red). (a) MoS<sub>2</sub>, (b) MoSe<sub>2</sub>, (c) MoTe<sub>2</sub>, (d) WSe<sub>2</sub>, and (e) WTe<sub>2</sub>. Where,  $G_0 = 2e^2/h$ .

properties (localization regime); this is the low temperature limit (see section 4.5.1).

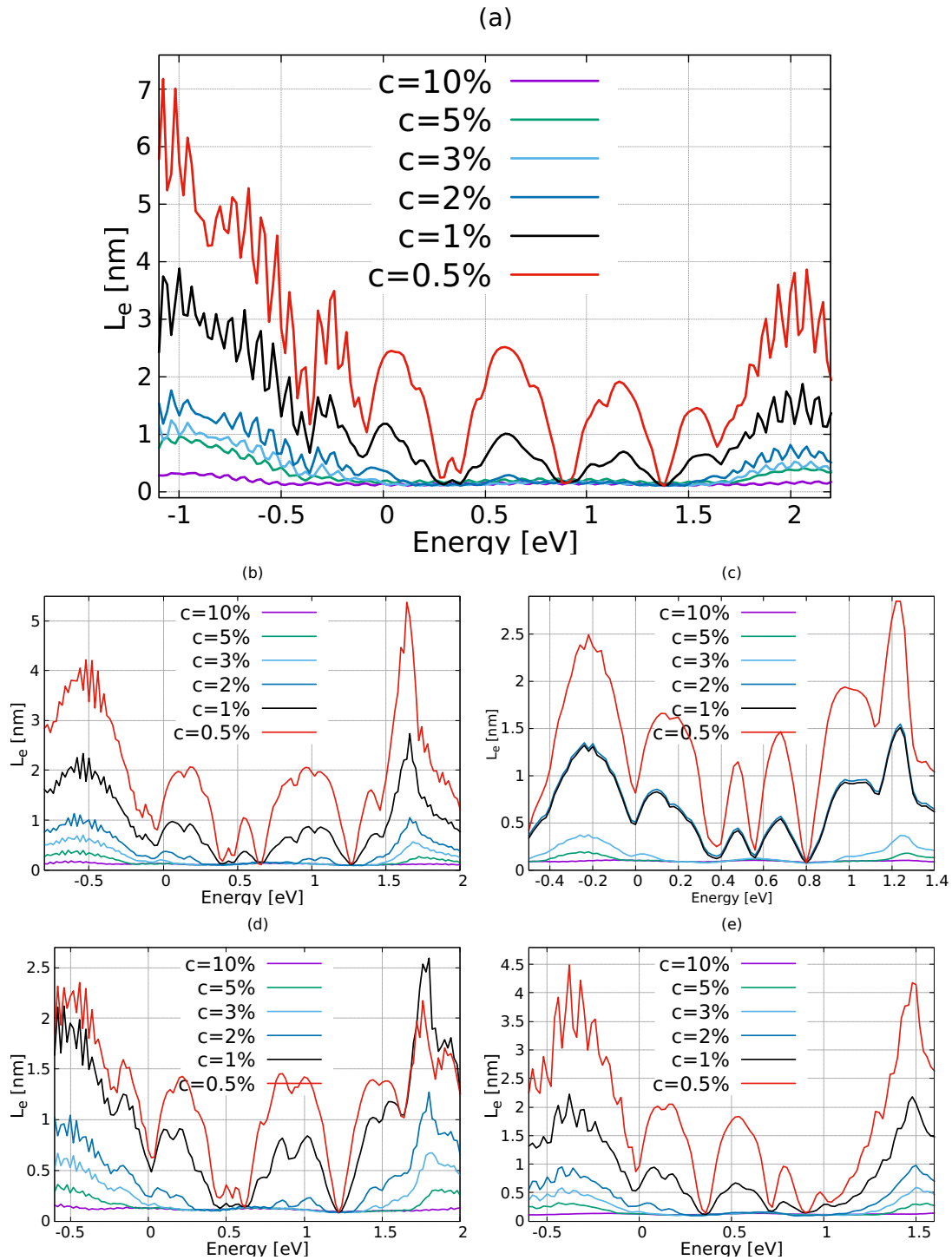


Figure 3: Elastic mean free path  $L_e(E)$  versus energy  $E$  in  $MX_2$  for different concentration ( $c = 0.5\%$ ,  $1\%$ ,  $2\%$ ,  $3\%$ ,  $5\%$ , and  $10\%$ ) of point defects (creating a vacancy by removal of atoms  $M = Mo, W$  or  $X = S, Se, Te$  randomly). (a)  $MoS_2$ , (b)  $MoSe_2$ , (c)  $MoTe_2$ , (d)  $WSe_2$ , and (e)  $WTe_2$ .

## C Graphene/MoS<sub>2</sub> bilayer heterostructures DFT+TB calculations

We have calculated, the electronic band structure of graphene/MoS<sub>2</sub> bilayer heterostructure of individual layers (graphene and MoS<sub>2</sub>) supercell structures see C.1. We analyze the electronic band structure of graphene/MoS<sub>2</sub> [4:3] bilayer heterostructure with and without optimization of atomic positions and lattice parameters see C.2. Finally, We proposed a tight-binding model for the graphene/MoS<sub>2</sub> bilayer heterostructure see C.3.

### C.1 Individual layers of graphene/MoS<sub>2</sub> heterostructures of different configurations 4:3 and 9:7

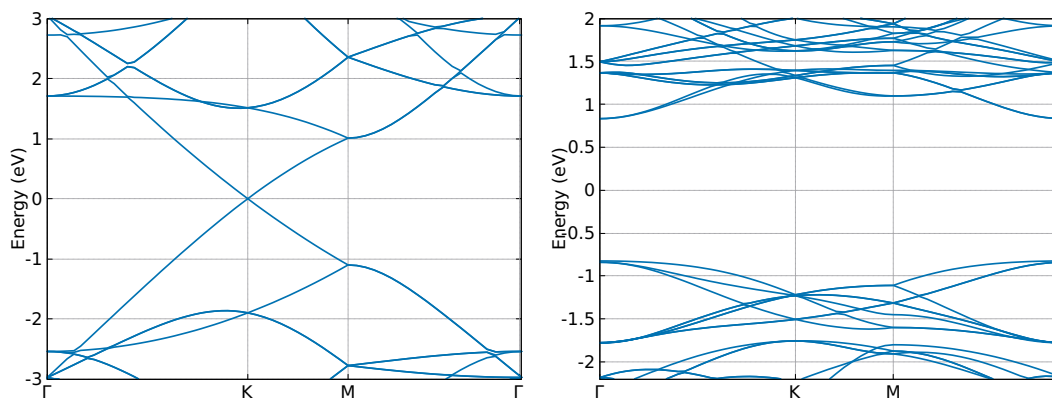


Figure 4: Electronic band structure of supercells of graphene (4×4) [Left] and MoS<sub>2</sub> (3×3) [Right] with optimized atomic positions and lattice parameters of graphene/MoS<sub>2</sub> [4:3] bilayer heterostructures. All the calculations have been done using LDA-PW-PAW pseudopotentials.

The electronic band structure of individual layers of supercell geometries of graphene (4×4) and MoS<sub>2</sub> (3×3) of graphene/MoS<sub>2</sub> [4:3] bilayer heterostructure see Fig. 4. We taken the graphene/MoS<sub>2</sub> [4:3] bilayer heterostructures without relaxation, and we separated graphene and MoS<sub>2</sub> layers with same atomic positions and lattice parameters of graphene/MoS<sub>2</sub> [4:3] heterostructure. We found that, the MoS<sub>2</sub> (3×3)[right] has a direct bandgap at the  $\Gamma$ -point, it move from  $K$ -point to  $\Gamma$  point in the Brillouin zone. The simple case MoS<sub>2</sub> (1×1) shows that the direct bandgap at the  $K$  point in the Brillouin zone. This comparison thus shows that the importance of the change of lattice parameters due to the mismatch imposed by the choice of a 4:3 supercell.

The electronic band structure of individual layers of supercell geometries of the

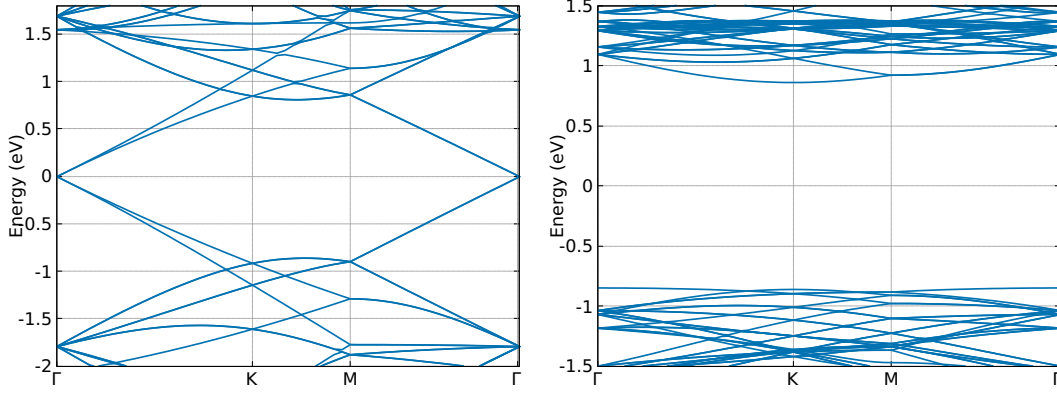


Figure 5: Electronic band structure of supercells of graphene ( $9 \times 9$ ) [Left] and  $\text{MoS}_2$  ( $7 \times 7$ ) [Right] with optimized atomic positions and lattice parameters of graphene/ $\text{MoS}_2$  [9:7] bilayer heterostructures. All the calculations have been done using LDA-PW-PAW pseudopotentials.

graphene ( $9 \times 9$ ) and  $\text{MoS}_2$  ( $7 \times 7$ ) of graphene/ $\text{MoS}_2$  [9:7] bilayer heterostructure see Fig. 5. The graphene/ $\text{MoS}_2$  [9:7] bilayer heterostructure without relaxation, we separated the graphene and  $\text{MoS}_2$  layers with same atomic positions and lattice parameters of graphene/ $\text{MoS}_2$  [9:7] heterostructure. We found that, the graphene ( $9 \times 9$ )[left] has a direct bandgap at the  $\Gamma$ -point, it move from  $K$ -point to  $\Gamma$  point in the Brillouin zone. The simple case graphene ( $1 \times 1$ ) shows that direct band gap at the  $K$  point in the Brillouin zone.

### Why direct band gap changes from $K$ to $\Gamma$ in the supercell $n \times n$ with $n$ a multiple of 3:

The reciprocal lattice vectors of a simple unit cell ( $1 \times 1$ ) are  $\vec{b}_1$  and  $\vec{b}_2$  in the Brillouin zone. The calculation of symmetry points in the Brillouin zone is  $K = \frac{1}{3}\vec{b}_1 + \frac{2}{3}\vec{b}_2$  (highest symmetry point  $K$  in the Brillouin zone). Let us take  $\vec{B}_1$ , and  $\vec{B}_2$  are reciprocal lattice vectors of a large unit cell ( $n \times n$ ) in the Brillouin zone.

Large unit cell reciprocal lattice vectors can be represented interms of the small unit cell reciprocal lattice vectors, so  $\vec{B}_1 = \frac{1}{n}\vec{b}_1$ , and  $\vec{B}_2 = \frac{1}{n}\vec{b}_2$ .

When  $K$  is at  $\Gamma$ , its possible to find out  $p$  &  $q$ , where  $p, q \in \mathbb{Z}$ , such as

$$K + p\vec{B}_1 + q\vec{B}_2 = 0 \iff \left(\frac{1}{3} + \frac{p}{n}\right)\vec{B}_1 + \left(\frac{2}{3} + \frac{q}{n}\right)\vec{B}_2 = 0 \quad (4)$$

$$\Rightarrow \left(\frac{n+3p}{3n}\right)\vec{B}_1 + \left(\frac{2n+3q}{3}\right)\vec{B}_2 = 0 \quad (5)$$

Therefore  $n = -3p, \frac{3q}{2}$ , this is possible only, where  $n$  is multiple of 3.

## C.2 Electronic band structure of graphene/MoS<sub>2</sub> [4:3] heterostructure with and without relaxation

We analyze the electronic band structure of graphene/MoS<sub>2</sub> [4:3] bilayer heterostructure with and without optimization of atomic positions and lattice parameters.

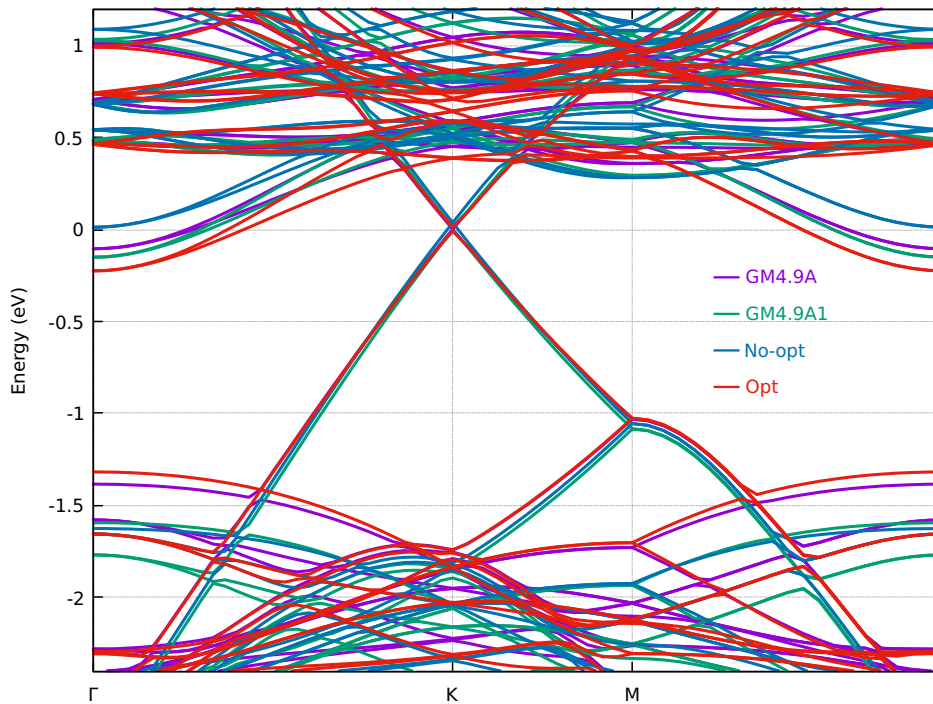


Figure 6: Comparison of electronic band structure of graphene/MoS<sub>2</sub> [4:3] bilayer heterostructure with relaxation (red lines), without relaxation (cyan lines). Atomic positions are not relaxed and lattice parameters are relaxed (blue lines), and atomic positions are relaxed and lattice parameters are not relaxed (green lines). All the calculations have been done by using GGA-PAW pseudopotentials (PBE) including vdW.

The electronic band structure of the graphene/MoS<sub>2</sub> [4:3] heterostructure with and without relaxation (lattice constant) is shown in Fig. 6. red color indicates optimization of atomic positions as well as lattice parameters, cyan color indicates the without optimization of atomic positions as well as lattice parameters (i.e. lattice parameters of isolated MoS<sub>2</sub> layer), green color indicates optimization of atomic positions and without optimization of lattice parameters, and blue color indicates without optimization of atomic positions and with optimization of lattice parameters.

### C.3 TB-model for graphene/MoS<sub>2</sub> (5:4 and 9:7)

We proposed a tight-binding model for the graphene/MoS<sub>2</sub> bilayer heterostructure.

In this TB-model, we choose pairs up to next nearest neighbors  $\langle ij \rangle$  in MoS<sub>2</sub> with a 11-band model basis. The MoS<sub>2</sub> monolayer have a five  $d$ -orbitals of Mo and six  $p$ -orbitals of two S see section 4.2.2, so that Hamiltonian of MoS<sub>2</sub> can be written as:

$$H_M = \sum_{i,\sigma,\nu} \varepsilon_{\nu,\sigma} C_{i\nu\sigma}^\dagger C_{i\nu\sigma} + \sum_{\langle ij \rangle, \sigma, \nu\mu} t_{i\nu,j\mu} C_{i\nu\sigma}^\dagger C_{j\mu\sigma} + h.c., \quad (6)$$

where  $C_{i\nu\sigma}^\dagger$  label the  $\nu$ -orbital site  $i$  of the Mo-lattice with spin  $\sigma$ . The first term considers the on-site energy of atom  $i$  and orbital  $\nu$ . The second term describes hopping between the Mo  $d$ -orbitals (d-d) to nearest and next nearest neighbors (similarly S  $p$ -orbitals (p-p) and also Mo  $d$ -orbitals - S  $p$ -orbitals (d-p). Strong MoS<sub>2</sub> spin orbit coupling is considered from the atomic SOC contribution. Parameters are given Table 2 .

For the model of graphene (Table 2), we adopt the usual single-orbital representation for the triangular lattice with a two-atom basis that couples only nearest neighbors  $\langle ij \rangle$ ,

$$H_G = \sum_{i,\sigma} \varepsilon_{i,\sigma} C_{i\sigma}^\dagger C_{i\sigma} + \sum_{\langle ij \rangle, \sigma} t_{i,j} C_{i\sigma}^\dagger C_{j\sigma} + h.c., \quad (7)$$

where  $\varepsilon$  of the first term describes the on-site energy, and the second term considers hopping to the nearest neighbors with coupling strength  $t_{i,j}$ .

For the inter-layer hopping, we include on the C-S coupling terms with a exponential decay versus the interatomic distance as in twisted bilayers (chap 6 and appendix D.2).

In the construction of a reliable TB model for graphene based heterostructures, we are guided by first principles DFT calculations that will provide the reference on which to calibrate the TB model. Our tight-binding model electronic band structure shows good agreement with the DFT electronic band structure see Fig. 7 and Fig. 8.

Table 2: Tight-binding (TB) Slater-Koster parameters for the graphene/MoS<sub>2</sub> bilayer heterostructure, and pair of neighbors for which the hopping term is non zero. The lattice parameter of the graphene/MoS<sub>2</sub>[5:4] are  $a = 1.276$  nm and graphene/MoS<sub>2</sub>[9:7]  $a = 2.214$  nm.

Atom	Orbitals	On-site energy (eV)
Mo	$d_0 = 4d_{z^2}$	$E_0^0 = 0.0644$
	$d_1 = 4d_{xz}, 4d_{yz}$	$E_1^0 = -0.4916$
	$d_2 = 4d_{x^2-y^2}, 4d_{xy}$	$E_2^0 = -0.0563$
S	$3p_x, 3p_y$	$E_{x,y}^0 = -38.7786$
	$3p_z$	$E_z^0 = -29.5254$
C	$2p_z$	$E_z^0 = 1.269$

Atom	Neighbor	Number	Inter-atomic distance (nm)	Slater-Koster parameters (eV)
Mo	Mo	3	0.318	$V_{dd\sigma} = -0.9035$ $V_{dd\pi} = 0.7027$ $V_{dd\delta} = 0.0897$
	S	6	0.241	$V_{dp\sigma} = -7.1933$ $V_{dp\pi} = 3.2674$
S	S	1	0.312	$V_{pp\sigma} = 8.0790$ $V_{pp\pi} = -2.6784$
		6	0.318	$V_{pp\sigma} = 7.336$ $V_{pp\pi} = -2.432$
C	C	3	0.142	$V_{pp\pi} = -2.8$

Table 3: TB Slater-Koster parameters for interlayer hopping terms in graphene/MoS<sub>2</sub>.  $d^0$  is the interlayer distance; for the definition of  $d_{C-S}$ . The  $q$  and  $d^0$  are parameters for the exponential decay (see appendix D.2)

Atom	Neighbor	$d^0$ (nm)	$q$	Slater-Koster parameters (eV)
C	S	0.342	6.4516	$V_{pp\sigma}^0 = 1.925$ $V_{pp\pi}^0 = -3.055$

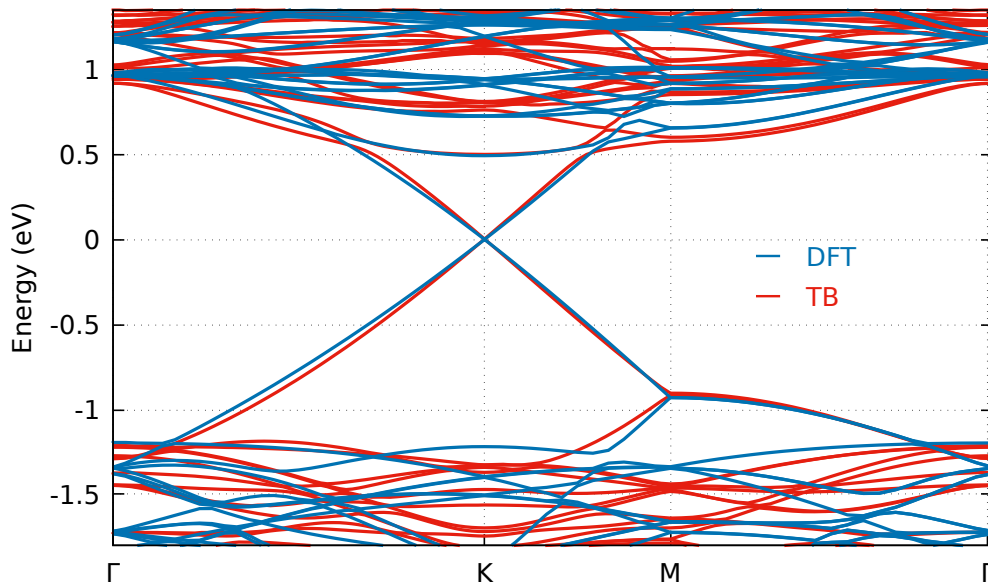


Figure 7: DFT and TB electronic band structure of graphene/MoS<sub>2</sub> [5:4] bilayer heterostructure without relaxation.

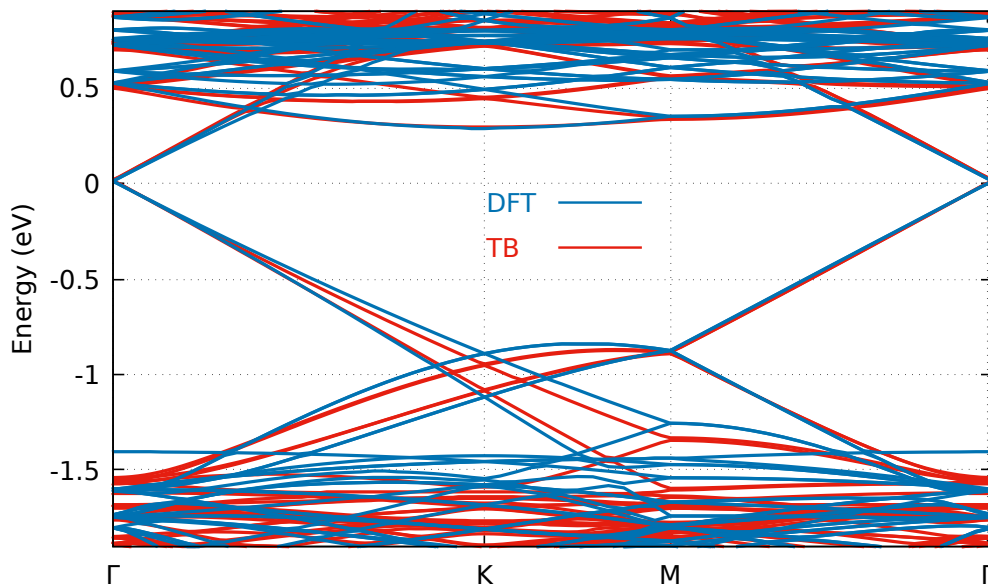


Figure 8: DFT and TB electronic band structure of graphene/MoS<sub>2</sub> [9:7] bilayer heterostructure without relaxation.

## D Electronic properties of tb-MoS<sub>2</sub>

We investigate the effect of different pseudopotentials (LDA-PAW and GGA-PAW + Van der Waals) on electronic band structure of MoS<sub>2</sub> monolayer see D.1. We gave a detailed formalism for the calculation of cut off radius in the twisted bilayer MoS<sub>2</sub> see D.2. We proposed a alternative Tight-binding (TB) Slater-Koster parameters for monolayer MoS<sub>2</sub> and twisted bilayer MoS<sub>2</sub>, to compare the electrical properties of tb-MoS<sub>2</sub> with alternative TB-model see D.3. All the explanations and calculations found in our paper [222].

### D.1 Electronic band structure of different pseudopotentials

This appendix we investigate the effect of different pseudopotentials (LDA-PAW and GGA-PAW + Van der Waals) on electronic band structure of MoS<sub>2</sub> monolayer. The LDA-PAW and GGA-PAW + Van der Waals exchange-correlation functionals yield very similar results (see Fig. 9).

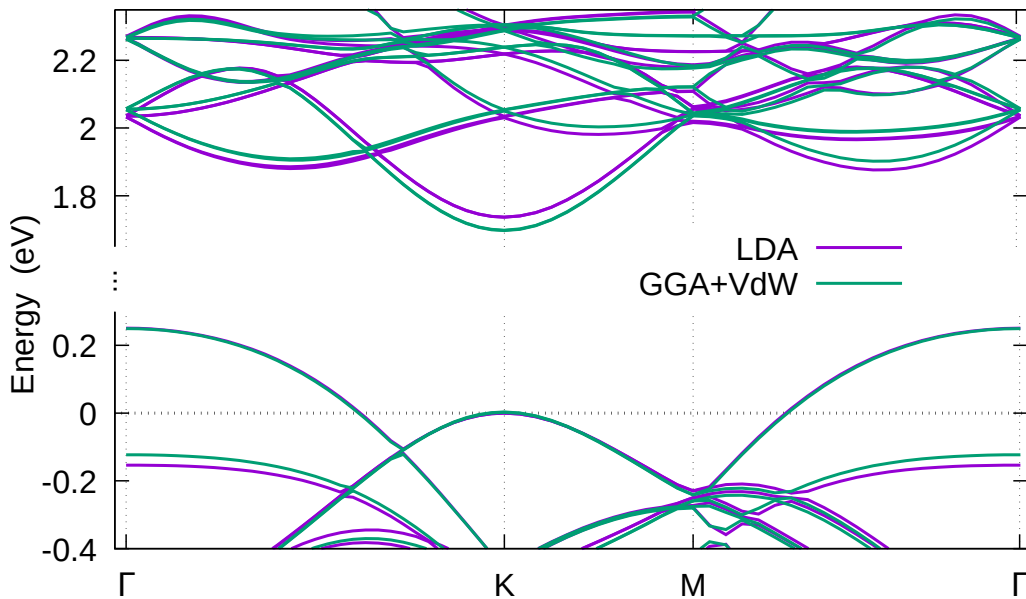


Figure 9: DFT bands around the gap in  $(1, 2)$   $\theta = 21.79^\circ$  tb-MoS<sub>2</sub> (built from AA stacking): Comparison between LDA-PAW and the GGA-PAW + Van der Waals exchange-correlation functional.

So all the results presented in the main text are based on LDA calculations, which require less computation time for large systems.

In Fig. 10, we compare the bands around the gap of  $\theta = 21.79^\circ$   $(1, 2)$  and  $\theta = 13.17^\circ$   $(2, 3)$  tb-MoS<sub>2</sub> with the monolayer case. For the purpose of comparison,

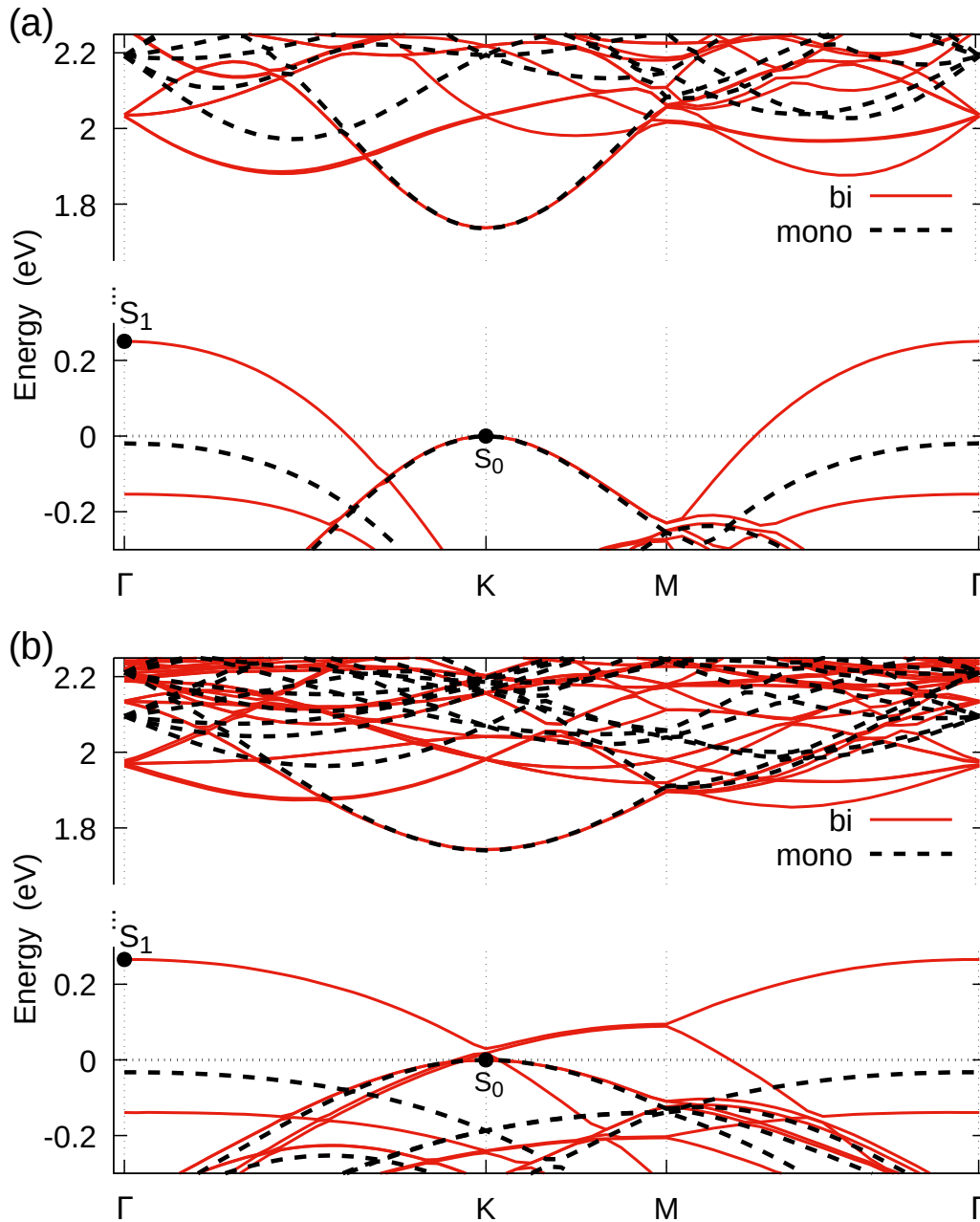


Figure 10: DFT bands around the gap in  $tb\text{-MoS}_2$  (built from AA stacking): (a) (1,2)  $\theta = 21.79^\circ$ , (b) (2,3)  $\theta = 13.17^\circ$ . (red color) bilayer, (black color) monolayer represented in the bilayer unit cell.

the monolayer unit cell has been mapped to the bilayer one. Some of the bands do not change with different angles of rotation of  $tb\text{-MoS}_2$ .

## D.2 Cut off distance of $tb\text{-MoS}_2$

This appendix we gave a formalism for the calculation of cut off radius in the twisted bilayer  $\text{MoS}_2$ . In twisted bilayer TMDs [46, 222] and twisted bilayer

graphene [213, 214], each interlayer Slater-Koster parameter  $V_i$  is assumed to decrease exponentially as a function of the distance  $d$  between orbitals:

$$V_i(d) = V_i^0 \exp\left(-q_i \frac{d - d_0}{d_0}\right) F_c(d), \quad (8)$$

where the  $V_i^0$  is S-S  $V_{pp\sigma}^0$ , S-S  $V_{pp\pi}^0$ , Mo-Mo  $V_{dd\sigma}^0$ , Mo-Mo  $V_{dd\pi}^0$ , Mo-Mo  $V_{dd\delta}^0$ , Mo-S  $V_{dp\sigma}^0$ , Mo-S  $V_{dp\pi}^0$ , respectively;  $d_i^0$  is the corresponding interlayer distance  $d_{\text{Mo-Mo}}$ ,  $d_{\text{Mo-Mo}}$ , and  $d_{\text{Mo-S}}$ , respectively (see Fig. 6.1). The coefficients  $q_i$  are fixed, like in twisted bilayer graphene [214], to have a reduction by a factor 10 between first neighbor hopping and second neighbor hopping terms,

$$q_i = \frac{\sqrt{3} \ln(10) d_i^0}{(\sqrt{3} - 1) a}. \quad (9)$$

Numerical values of  $V_i^0$ ,  $d_i^0$  and  $q_i$  are listed table 5. In equation (8) a smooth cutoff function [135] is used,

$$F_c(d) = \left(1 + \exp\left(\frac{d - r_c}{l_c}\right)\right)^{-1}, \quad (10)$$

with  $r_c$  the cutoff distance and  $l_c = 0.0265$  nm [135]. For  $r \ll r_c$ ,  $F_c(r) \simeq 1$ ; and for  $r \gg r_c$ ,  $F_c(r) \simeq 0$ . All results presented in the main text are calculated with  $r_c = 2.5a = 0.795$  nm.

### D.3 TB-model (alternative) for twisted bilayer MoS<sub>2</sub>

We have analyzed the evolution of the bands around the main gap with  $\theta$ . Figure 11 shows this evolution for the top of the valence bands with a focus on the states labeled S<sub>1</sub>, S<sub>2</sub>, S<sub>3</sub>, and S<sub>4</sub>. Both DFT and with alternative TB -method results show that the energies  $E(\text{S}_2)$  and  $E(\text{S}_3)$  vary almost linearly with  $\theta^2$  (Fig. 11(b)), which is a strong indication that this phenomenon is a direct consequence of the moiré structure. Furthermore, our TB computations show that the highest energy valence band is isolated from the remainder of the valence bands by a minigap for sufficiently small values of  $\theta$ . This is illustrated by Fig. 11(c), showing that  $E(\text{S}_4) - E(\text{S}_2) < 0$ , *i.e.*, the presence of a minigap, for  $\theta < \theta_C \approx 2^\circ$  (main TB-model  $\theta < \theta_C \approx 6^\circ$ ).

We also consider the average slope of the highest valence band between the points K and M, *i.e.*, between the states S<sub>2</sub> and S<sub>3</sub> (Fig. 11(a)). This quantity is proportional to the average Boltzmann velocity (intra-band velocity). As shown in Fig. 11(d), this velocity tends towards zero for small angles,  $\theta = \theta_0 \approx 2^\circ$ . This demonstrates an electronic confinement corresponding to a “flat band”, like it

Table 4: Alternative Tight-binding (TB) Slater-Koster parameters for monolayer MoS<sub>2</sub>, and pairs of neighbors for which the hopping term is non zero. The lattice parameter of monolayer MoS<sub>2</sub> is  $a = 0.318$  nm.

Atom	Orbitals		On-site energy (eV)	
Mo	$d_0 = 4d_{z^2}$		$E_0^0 = -1.0437$	
	$d_1 = 4d_{xz}, 4d_{yz}$		$E_1^0 = -2.499$	
	$d_2 = 4d_{x^2-y^2}, 4d_{xy}$		$E_2^0 = -1.4808$	
S	$3p_x, 3p_y$		$E_{x,y}^0 = -3.3868$	
	$3p_z$		$E_z^0 = -7.4352$	

Atom	Neighbor	Number	Inter-atomic distance (nm)	Slater-Koster parameters (eV)
Mo	Mo	3	0.318	$V_{dd\sigma} = -0.8477$ $V_{dd\pi} = 0.2372$ $V_{dd\delta} = 0.2136$
	S	6	0.241	$V_{dp\sigma} = 3.7132$ $V_{dp\pi} = -1.2064$
S	S	1	0.312	$V_{pp\sigma} = 1.323$ $V_{pp\pi} = -0.637$
		6	0.318	$V_{pp\sigma} = 1.336$ $V_{pp\pi} = -0.432$

Table 5: TB Slater-Koster parameters for interlayer hopping terms in tb-MoS<sub>2</sub>.  $d^0$  is the interlayer distance; for the definition of  $d_{\text{Mo-Mo}}$ ,  $d_{\text{S-S}}$ , and  $d_{\text{Mo-S}}$ .

Atom	Neighbor	$d^0$ (nm)	$q$	Slater-Koster parameters (eV)
Mo	Mo	0.6800	11.6496	$V_{dd\sigma}^0 = -0.0395$ $V_{dd\pi}^0 = -0.2482$ $V_{dd\delta}^0 = -0.0505$
	S	0.5238	8.9738	$V_{dp\sigma}^0 = -0.1992$ $V_{dp\pi}^0 = 0.$
S	S	0.3676	6.2981	$V_{pp\sigma}^0 = 0.2894$ $V_{pp\pi}^0 = -0.0742$

has been found for twisted bilayer graphene for specific angles, so-called magic angles [11, 117, 202, 213, 214]. However, in tb-MoS<sub>2</sub>, this velocity vanishes not only for discrete values of  $\theta$ , but flat bands emerge for a continuous range of  $\theta$ ,  $\theta \lesssim \theta_0$ .

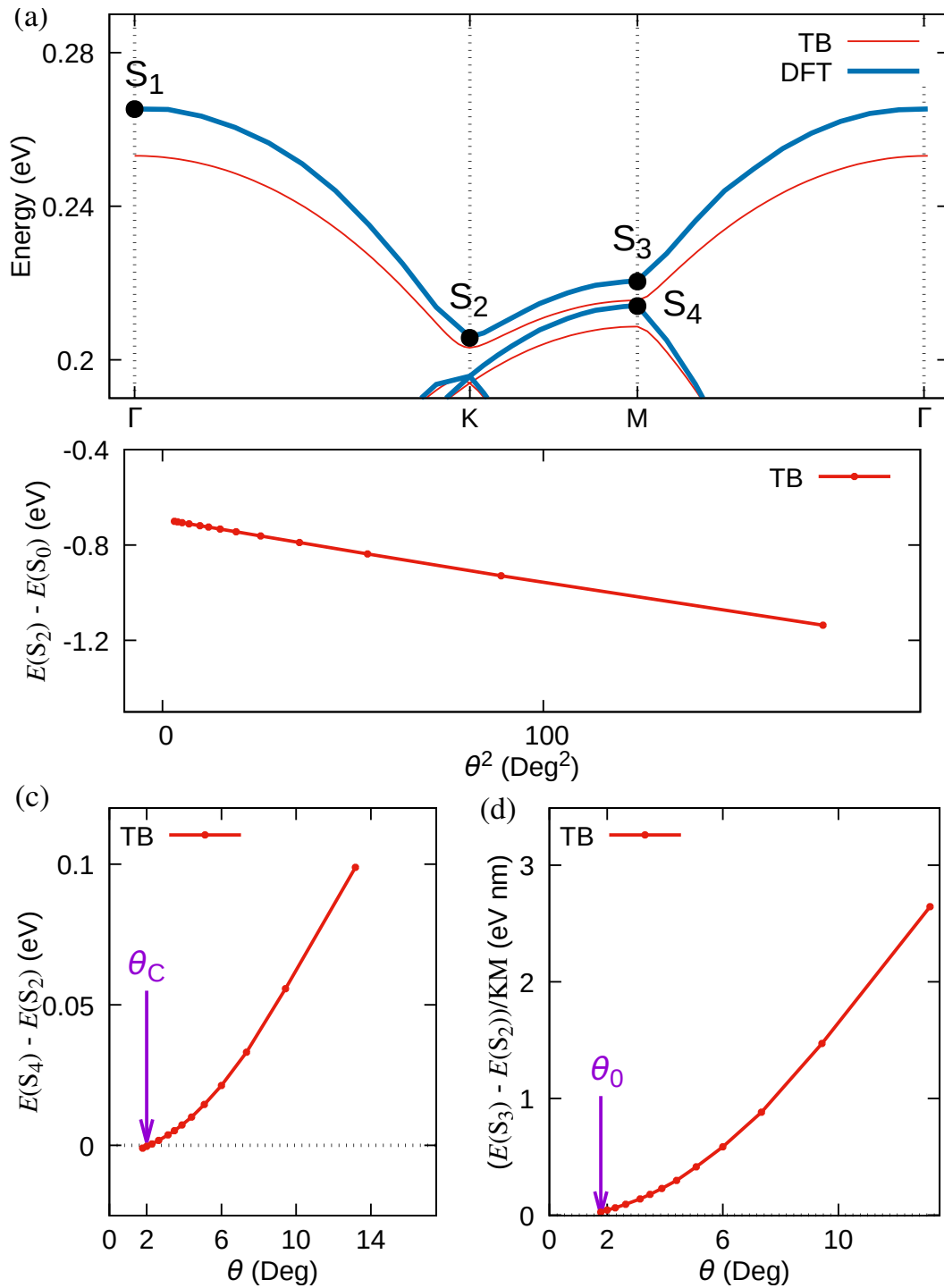


Figure 11: Dependence of valence bands on rotation angle  $\theta$ : (a) Valence band dispersion of (4,5) tb-MoS<sub>2</sub>,  $\theta = 7.34^\circ$ . (b) Energy  $E(S_2)$  of the state  $S_2$  (see panel (a)) versus  $\theta^2$ . (c) Energy difference between the states  $S_4$  and  $S_2$ ,  $\Delta E_{24} = E(S_4) - E(S_2)$ , versus  $\theta$ . A negative value of  $\Delta E_{24}$  means that a gap  $|\Delta E_{24}|$  exists between the band below the gap and the other valence bands. (d) Average slope of  $E(\vec{k})$  of the band between states  $S_2$  and  $S_3$ .

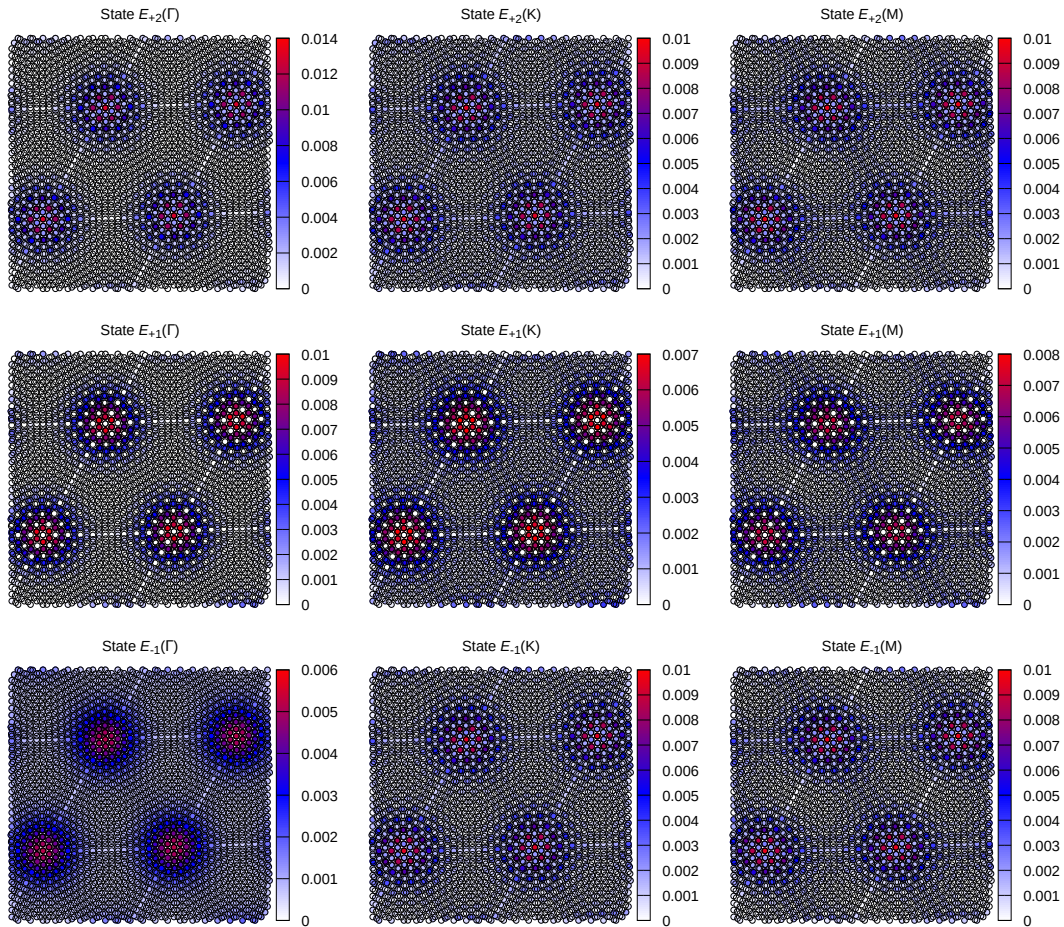


Figure 12: Weight of the eigenstates at  $\Gamma$ , K, and M, of the non-degenerate flat band below the gap (valence band), in real space, in (10, 11) tb-MoS<sub>2</sub> (built from AA) with a rotation angle  $\theta = 3.15^\circ$ . The color palette is the weight of the eigenstate on each orbital  $d_0 = 4d_{z^2}$  Mo. The sum of these weights is more than 98% of each state.

#### D.4 Eigenstates corresponding to flat bands ( $\theta = 3.15^\circ$ ) in tb-MoS<sub>2</sub>

We analyzed the band dispersion of large angle  $\theta = 3.15^\circ$  (Fig. 12) shows that the first isolated flat bands below the main gap (valence band) is non-degenerate and thus contains one state per moiré cell. By contrast, the two first isolated flat bands above the gap (conduction band) are two-fold quasi degenerate. The weight of eigenstates of these flat bands is mainly on  $d_0 = d_{z^2}$  Mo orbitals (more than 98%) located in AA stacking regions. This is shown in Fig. 12 for eigenstates at the points  $\Gamma$ , K, and M of the flat band below the main gap.

---

## *Bibliography*

---

- [1] Mahmoud M. Asmar Abdulrhman M. Alsharari and Sergio E. Ulloa. Mass inversion in graphene by proximity to dichalcogenide monolayer. *Physical Review B*, 94(24):241106, 2016.
- [2] G Allan. A linear prediction of the recursion coefficients. *Journal of Physics C: Solid State Physics*, 17(22):3945–3955, aug 1984.
- [3] Hideo Aoki and Mildred S Dresselhaus. *Physics of graphene*. Springer Science & Business Media, 2013.
- [4] Walter Edwin Arnoldi. The principle of minimized iterations in the solution of the matrix eigenvalue problem. *Quarterly of applied mathematics*, 9(1):17–29, 1951.
- [5] Phaedon Avouris, Tony F Heinz, and Tony Low. *2D Materials*. Cambridge University Press, 2017.
- [6] Ahmet Avsar, Jun You Tan, T Taychatanapat, J Balakrishnan, GWK Koon, Y Yeo, J Lahiri, A Carvalho, AS Rodin, ECT O’Farrell, et al. Spin–orbit proximity effect in graphene. *Nature communications*, 5(1):1–6, 2014.
- [7] Sivacarendran Balendhran, Sumeet Walia, Hussein Nili, Sharath Sriram, and Madhu Bhaskaran. Elemental analogues of graphene: silicene, germanene, stanene, and phosphorene. *Small*, 11(6):640–652, 2015.
- [8] Claire Berger, Zhimin Song, Tianbo Li, Xuebin Li, Asmerom Y Ogbazghi, Rui Feng, Zhenting Dai, Alexei N Marchenkov, Edward H Conrad, Phillip N First, et al. Ultrathin epitaxial graphite: 2D electron gas properties and a route toward graphene-based nanoelectronics. *The Journal of Physical Chemistry B*, 108(52):19912–19916, 2004.

- [9] Simone Bertolazzi, Daria Krasnozhan, and Andras Kis. Nonvolatile memory cells based on MoS<sub>2</sub>/graphene heterostructures. *ACS nano*, 7(4):3246–3252, 2013.
- [10] Swastibrata Bhattacharyya, Tribhuwan Pandey, and Abhishek K Singh. Effect of strain on electronic and thermoelectric properties of few layers to bulk MoS<sub>2</sub>. *Nanotechnology*, 25(46):465701, 2014.
- [11] Rafi Bistritzer and Allan H. MacDonald. Moiré bands in twisted double-layer graphene. *Proceedings of the National Academy of Sciences*, 108(30):12233–12237, 2011.
- [12] Felix Bloch. Über die Quantenmechanik der Elektronen in Kristallgittern. *Zeitschrift für Physik*, 52(7-8):555–600, 1929.
- [13] Th Böker, R Severin, A Müller, C Janowitz, R Manzke, D Voß, P Krüger, A Mazur, and J Pollmann. Band structure of MoS<sub>2</sub>, MoSe<sub>2</sub>, and  $\alpha$ -MoTe<sub>2</sub>: Angle-resolved photoelectron spectroscopy and ab initio calculations. *Physical Review B*, 64(23):235305, 2001.
- [14] K.I. Bolotin, K.J. Sikes, Z. Jiang, M. Klima, G. Fudenberg, J. Hone, P. Kim, and H.L. Stormer. Ultrahigh electron mobility in suspended graphene. *Solid State Communications*, 146(9):351 – 355, 2008.
- [15] Max Born and J Robert Oppenheimer. On the quantum theory of molecules. 1927.
- [16] SK Bose, K Winer, and OK Andersen. Electronic properties of a realistic model of amorphous silicon. *Physical Review B*, 37(11):6262, 1988.
- [17] I. Brihuega, P. Mallet, H. González-Herrero, G. Trambly de Laissardière, M. M. Ugeda, L. Magaud, J. M. Gómez-Rodríguez, F. Ynduráin, and J.-Y. Veullen. Unraveling the intrinsic and robust nature of van Hove singularities in twisted bilayer graphene by scanning tunneling microscopy and theoretical analysis. *Physical Review Letters*, 109(5):196802, 2012.
- [18] Liam Britnell, RM Ribeiro, A Eckmann, R Jalil, BD Belle, A Mishchenko, Y-J Kim, RV Gorbachev, T Georgiou, SV Morozov, et al. Strong light-matter interactions in heterostructures of atomically thin films. *Science*, 340(6138):1311–1314, 2013.
- [19] Sheneve Z Butler, Shawna M Hollen, Linyou Cao, Yi Cui, Jay A Gupta, Humberto R Gutiérrez, Tony F Heinz, Seung Sae Hong, Jiaying Huang, Ariel F Ismach, et al. Progress, challenges, and opportunities in two-dimensional materials beyond graphene. *ACS nano*, 7(4):2898–2926, 2013.

- [20] J. M. Campanera, G. Savini, I. Suarez-Martinez, and M. I. Heggie. Density functional calculations on the intricacies of moiré patterns on graphite. *Physical Review B*, 75:235449, Jun 2007.
- [21] Boxiao Cao and Tianshu Li. Interlayer electronic coupling in arbitrarily stacked MoS<sub>2</sub> bilayers controlled by interlayer S-S interaction. *The Journal of Physical Chemistry C*, 119(2):1247–1252, Jan 2015.
- [22] Yuan Cao, Valla Fatemi, Shiang Fang, Kenji Watanabe, Takashi Taniguchi, Efthimios Kaxiras, and Pablo Jarillo-Herrero. Unconventional superconductivity in magic-angle graphene superlattices. *Nature*, 556(7699):43–50, 2018.
- [23] E. Cappelluti, R. Roldán, J. A. Silva-Guillén, P. Ordejón, and F. Guinea. Tight-binding model and direct-gap/indirect-gap transition in single-layer and multilayer MoS<sub>2</sub>. *Physical Review B*, 88:075409, Aug 2013.
- [24] Ana Carpio, Luis L Bonilla, Fernando de Juan, and María A H Vozmediano. Dislocations in graphene. *New Journal of Physics*, 10(5):053021, May 2008.
- [25] David M Ceperley and Berni J Alder. Ground state of the electron gas by a stochastic method. *Physical Review Letters*, 45(7):566, 1980.
- [26] Rui Cheng, Shan Jiang, Yu Chen, Yuan Liu, Nathan Weiss, Hung-Chieh Cheng, Hao Wu, Yu Huang, and Xiangfeng Duan. Few-layer molybdenum disulfide transistors and circuits for high-speed flexible electronics. *Nature communications*, 5(1):1–9, 2014.
- [27] Byungjin Cho, Jongwon Yoon, Sung Kwan Lim, Ah Ra Kim, Dong-Ho Kim, Sung-Gyu Park, Jung-Dae Kwon, Young-Joo Lee, Kyu-Hwan Lee, Byoung Hun Lee, et al. Chemical sensing of 2D graphene/MoS<sub>2</sub> heterostructure device. *ACS applied materials & interfaces*, 7(30):16775–16780, 2015.
- [28] Min Sup Choi, Gwan-Hyoung Lee, Young-Jun Yu, Dae-Yeong Lee, Seung Hwan Lee, Philip Kim, James Hone, and Won Jong Yoo. Controlled charge trapping by molybdenum disulphide and graphene in ultrathin heterostructured memory devices. *Nature communications*, 4(1):1–7, 2013.
- [29] Gabriel C. Constantinescu and Nicholas D. M. Hine. Energy landscape and band-structure tuning in realistic MoS<sub>2</sub>/MoSe<sub>2</sub> heterostructures. *Physical Review B*, 91:195416, May 2015.

- [30] Felice Conte, Domenico Ninno, and Giovanni Cantele. Electronic properties and interlayer coupling of twisted MoS<sub>2</sub>/NbSe<sub>2</sub> heterobilayers. *Physical Review B*, 99:155429, Apr 2019.
- [31] Horacio Coy Diaz, José Avila, Chaoyu Chen, Rafik Addou, Maria C Asensio, and Matthias Batzill. Direct observation of interlayer hybridization and Dirac relativistic carriers in graphene/MoS<sub>2</sub> van der Waals heterostructures. *Nano Letters*, 15(2):1135–1140, 2015.
- [32] Alessandro Cresti, Giuseppe Grosso, and Giuseppe Pastori Parravicini. Analytic and numeric Green’s functions for a two-dimensional electron gas in an orthogonal magnetic field. *Annals of Physics*, 321(5):1075–1091, 2006.
- [33] Benjamin Crowell. *The Modern Revolution in Physics*, volume 6. Light and Matter, 2000.
- [34] Juan Carlos Cuevas. Introduction to density functional theory. *Universität Karlsruhe, Germany*, 2010.
- [35] F Cyrot-Lackmann and JP Gaspard. On the electronic structure of an impurity band: a cumulant approach. *Journal of Physics C: Solid State Physics*, 7(10):1829, 1974.
- [36] C. Davisson and L. H. Germer. Diffraction of electrons by a crystal of nickel. *Physical Review*, 30:705–740, Dec 1927.
- [37] Guy Trambly de Laissardière and Didier Mayou. Conductivity of graphene with resonant and nonresonant adsorbates. *Physical Review Letters*, 111(14):146601, 2013.
- [38] Guy Trambly de Laissardière and Didier Mayou. Anomalous electronic transport in quasicrystals and related complex metallic alloys. *Comptes Rendus Physique*, 15(1):70–81, 2014.
- [39] L. Debbichi, O. Eriksson, and S. Lebègue. Electronic structure of two-dimensional transition metal dichalcogenide bilayers from *ab initio* theory. *Physical Review B*, 89:205311, May 2014.
- [40] Budi Eka Dharma, Ahmad Syahroni, and Muhammad Aziz Majidi. Effects of spin-orbit coupling on the electronic and excitonic structures of monolayer WS<sub>2</sub>. In *Functional Properties of Modern Materials II*, volume 966 of *Materials Science Forum*, pages 48–53. Trans Tech Publications Ltd, 10 2019.

- [41] Sudipta Dubey, Simone Lisi, Goutham Nayak, Felix Herzig, Van-Dung Nguyen, Toai Le Quang, Vladimir Cherkez, César González, Yannick J Dappe, Kenji Watanabe, et al. Weakly trapped, charged, and free excitons in single-layer MoS<sub>2</sub> in the presence of defects, strain, and charged impurities. *ACS nano*, 11(11):11206–11216, 2017.
- [42] Dinh Loc Duong, Seok Joon Yun, and Young Hee Lee. van der waals layered materials: Opportunities and challenges. *ACS Nano*, 11(12):11803–11830, 2017.
- [43] Abbas Ebnonnasir, Badri Narayanan, Suneel Kodambaka, and Cristian V Ciobanu. Tunable MoS<sub>2</sub> bandgap in MoS<sub>2</sub>-graphene heterostructures. *Applied Physics Letters*, 105(3):031603, 2014.
- [44] Robert M Elder, Mahesh R Neupane, and Tanya L Chantawansri. Stacking order dependent mechanical properties of graphene/MoS<sub>2</sub> bilayer and trilayer heterostructures. *Applied Physics Letters*, 107(7):073101, 2015.
- [45] C Espejo, T Rangel, AH Romero, Xavier Gonze, and G-M Rignanese. Band structure tunability in MoS<sub>2</sub> under interlayer compression: A DFT and GW study. *Physical Review B*, 87(24):245114, 2013.
- [46] Shiang Fang, Rodrick Kuate Defo, Sharmila N. Shirodkar, Simon Lieu, Georgios A. Tritsarlis, and Efthimios Kaxiras. Ab initio tight-binding Hamiltonian for transition metal dichalcogenides. *Physical Review B*, 92:205108, Nov 2015.
- [47] Yago Ferreira and Alberto Cortijo. Large conduction band and Fermi velocity spin splitting due to Coulomb interactions in single-layer MoS<sub>2</sub>. *Physical Review B*, 90(19):195426, 2014.
- [48] Mike Finnis. *Interatomic forces in condensed matter*, volume 1. OUP Oxford, 2003.
- [49] Gianluca Fiori, Francesco Bonaccorso, Giuseppe Iannaccone, Tomás Palacios, Daniel Neumaier, Alan Seabaugh, Sanjay K Banerjee, and Luigi Colombo. Electronics based on two-dimensional materials. *Nature nanotechnology*, 9(10):768, 2014.
- [50] Charlotte Froese Fischer. Hartree-Fock method for atoms. A numerical approach. 1977.
- [51] R Fivaz and EJPR Mooser. Mobility of charge carriers in semiconducting layer structures. *Physical Review*, 163(3):743, 1967.

- [52] WMC Foulkes. Tight-Binding Models and Coulomb Interactions for s, p, and d Electrons. 2016.
- [53] Sai Manoj Gali, Anton Pershin, Aurélien Lherbier, Jean-Christophe Charlier, and David Beljonne. Electronic and Transport Properties in Defective MoS<sub>2</sub>: Impact of Sulfur Vacancies. *The Journal of Physical Chemistry C*, 124(28):15076–15084, 2020.
- [54] Andre K Geim and Irina V Grigorieva. Van der Waals heterostructures. *Nature*, 499(7459):419–425, 2013.
- [55] M. Gmitra, S. Konschuh, C. Ertler, C. Ambrosch-Draxl, and J. Fabian. Band-structure topologies of graphene: Spin-orbit coupling effects from first principles. *Physical Review B*, 80:235431, Dec 2009.
- [56] Martin Gmitra and Jaroslav Fabian. Graphene on transition-metal dichalcogenides: A platform for proximity spin-orbit physics and optospintronics. *Physical Review B*, 92(15):155403, 2015.
- [57] Martin Gmitra, Denis Kochan, Petra Högl, and Jaroslav Fabian. Trivial and inverted Dirac bands and the emergence of quantum spin Hall states in graphene on transition-metal dichalcogenides. *Physical Review B*, 93(15):155104, 2016.
- [58] X. Gonze, B. Amadon, P.-M. Anglade, J.-M. Beuken, F. Bottin, P. Boulanger, F. Bruneval, D. Caliste, R. Caracas, M. Côté, T. Deutsch, L. Genovese, Ph. Ghosez, M. Giantomassi, S. Goedecker, D. R. Hamann, P. Hermet, F. Jollet, G. Jomard, S. Leroux, M. Mancini, S. Mazevet, M. J. T. Oliveira, G. Onida, Y. Pouillon, T. Rangel, G.-M. Rignanese, D. Sangalli, R. Shaltaf, M. Torrent, M. J. Verstraete, G. Zerah, and J. W. Zwanziger. ABINIT: first-principles approach to material and nanosystem properties. *Computer Physics Communications*, 180(12):2582–2615, 2009.
- [59] X. Gonze, J.-M. Beuken, R. Caracas, F. Detraux, M. Fuchs, G.-M. Rignanese, L. Sindic, M. Verstraete, G. Zerah, F. Jollet, M. Torrent, A. Roy, M. Mikami, Ph. Ghosez, J.-Y. Raty, and D.C. Allan. First-principles computation of material properties: the ABINIT software project. *Computational Materials Science*, 25(3):478–492, 2002.
- [60] X. Gonze, F. Jollet, F. Abreu Araujo, D. Adams, B. Amadon, T. Applencourt, C. Audouze, J.-M. Beuken, J. Bieder, A. Bokhanchuk, E. Bousquet, F. Bruneval, D. Caliste, M. Côté, F. Dahm, F. Da Pieve, M. Delaveau, M. Di Gennaro, B. Dorado, C. Espejo, G. Geneste, L. Genovese,

- A. Gerossier, M. Giantomassi, Y. Gillet, D. R. Hamann, L. He, G. Jomard, J. Laflamme Janssen, S. Le Roux, A. Levitt, A. Lherbier, F. Liu, I. Lukačević, A. Martin, C. Martins, M. J. T. Oliveira, S. Poncé, Y. Pouillon, T. Rangel, G.-M. Rignanese, A. H. Romero, B. Rousseau, O. Rubel, A. A. Shukri, M. Stankovski, M. Torrent, M. J. Van Setten, B. Van Troeye, M. J. Verstraete, D. Waroquiers, J. Wiktor, B. Xu, A. Zhou, and J. W. Zwanziger. Recent developments in the ABINIT software package. *Computer Physics Communications*, 205:106–131, 2016.
- [61] CM Goringe, DR Bowler, and E Hernandez. Tight-binding modelling of materials. *Reports on Progress in Physics*, 60(12):1447, 1997.
- [62] Stefan Grimme. Semiempirical GGA-type density functional constructed with a long-range dispersion correction. *Journal of computational chemistry*, 27(15):1787–1799, 2006.
- [63] Stefan Grimme, Jens Antony, Stephan Ehrlich, and Helge Krieg. A consistent and accurate ab initio parametrization of density functional dispersion correction (DFT-D) for the 94 elements H-Pu. *The Journal of Chemical Physics*, 132(15):154104, 2010.
- [64] Julia Gusakova, Xingli Wang, Li Lynn Shiau, Anna Krivosheeva, Victor Shaposhnikov, Victor Borisenko, Vasili Gusakov, and Beng Kang Tay. Electronic properties of bulk and monolayer TMDs: theoretical study within DFT framework (GVJ-2e method). *physica status solidi (a)*, 214(12):1700218, 2017.
- [65] Fred A Hamprecht, Aron J Cohen, David J Tozer, and Nicholas C Handy. Development and assessment of new exchange-correlation functionals. *The Journal of chemical physics*, 109(15):6264–6271, 1998.
- [66] J Harris and RO Jones. The surface energy of a bounded electron gas. *Journal of Physics F: Metal Physics*, 4(8):1170, 1974.
- [67] Ayako Hashimoto, Kazu Suenaga, Alexandre Gloter, Koki Urita, and Sumio Iijima. Direct evidence for atomic defects in graphene layers. *Nature*, 430(7002):870–873, 2004.
- [68] R Haydock, V Heine, and MJ Kelly. Electronic structure based on the local atomic environment for tight-binding bands. II. *Journal of Physics C: Solid State Physics*, 8(16):2591, 1975.
- [69] R Haydock, Volker Heine, and MJ Kelly. Electronic structure based on the local atomic environment for tight-binding bands. *Journal of Physics C: Solid State Physics*, 5(20):2845, 1972.

- [70] Roger Haydock. The recursive solution of the Schrödinger equation. *Computer Physics Communications*, 20(1):11–16, 1980.
- [71] Jiangan He, Kerstin Hummer, and Cesare Franchini. Stacking effects on the electronic and optical properties of bilayer transition metal dichalcogenides MoS<sub>2</sub>, MoSe<sub>2</sub>, WS<sub>2</sub>, and WSe<sub>2</sub>. *Physical Review B*, 89:075409, Feb 2014.
- [72] C.H. Hodges. Van Hove singularities and continued fraction coefficients. *Journal de Physique Lettres*, 38(9):187–189, 1977.
- [73] P. Hohenberg and W. Kohn. Inhomogeneous electron gas. *Physical Review*, 136:B864–B871, Nov 1964.
- [74] P.C. Hohenberg, Walter Kohn, and L.J. Sham. The beginnings and some thoughts on the future. In Per-Olov Löwdin, editor, *Density Functional Theory of Many-Fermion Systems*, volume 21 of *Advances in Quantum Chemistry*, pages 7 – 26. Academic Press, 1990.
- [75] Wei Hu and Jinlong Yang. First-principles study of two-dimensional van der Waals heterojunctions. *Computational Materials Science*, 112:518–526, 2016.
- [76] Zehua Hu, Zhangting Wu, Cheng Han, Jun He, Zhenhua Ni, and Wei Chen. Two-dimensional transition metal dichalcogenides: interface and defect engineering. *Chemical Society Reviews*, 47(9):3100–3128, 2018.
- [77] Shengxi Huang, Liangbo Liang, Xi Ling, Alexander A. Puretzky, David B. Geohegan, Bobby G. Sumpter, Jing Kong, Vincent Meunier, and Mildred S. Dresselhaus. Low-frequency interlayer Raman modes to probe interface of twisted bilayer MoS<sub>2</sub>. *Nano Letters*, 16(2):1435–1444, Feb 2016.
- [78] Shengxi Huang, Xi Ling, Liangbo Liang, Jing Kong, Humberto Terrones, Vincent Meunier, and Mildred S. Dresselhaus. Probing the interlayer coupling of Twisted Bilayer MoS<sub>2</sub> using photoluminescence spectroscopy. *Nano Letters*, 14(10):5500–5508, Oct 2014.
- [79] R. Huisman, R. de Jonge, C. Haas, and F. Jellinek. Trigonal-prismatic coordination in solid compounds of transition metals. *Journal of Solid State Chemistry*, 3(1):56–66, 1971.
- [80] Nengjie Huo, Yujue Yang, and Jingbo Li. Optoelectronics based on 2D TMDs and heterostructures. *Journal of Semiconductors*, 38(3):031002, 2017.

- [81] J. D. Jackson. Classical Electrodynamics, 3rd ed. *American Journal of Physics*, 67(9):841–842, 1999.
- [82] Deep Jariwala, Tobin J Marks, and Mark C Hersam. Mixed-dimensional van der Waals heterostructures. *Nature materials*, 16(2):170–181, 2017.
- [83] Deep Jariwala, Vinod K Sangwan, Lincoln J Lauhon, Tobin J Marks, and Mark C Hersam. Emerging device applications for semiconducting two-dimensional transition metal dichalcogenides. *ACS nano*, 8(2):1102–1120, 2014.
- [84] Jin-Wu Jiang. Graphene versus MoS<sub>2</sub>: A short review. *Frontiers of Physics*, 10(3):287–302, 2015.
- [85] Wencan Jin, Po-Chun Yeh, Nader Zaki, Daniel Chenet, Ghidewon Arefe, Yufeng Hao, Alessandro Sala, Tevfik Onur Menten, Jerry I Dadap, Andrea Locatelli, et al. Tuning the electronic structure of monolayer graphene/MoS<sub>2</sub> van der Waals heterostructures via interlayer twist. *Physical Review B*, 92(20):201409, 2015.
- [86] François Jollet, Marc Torrent, and Natalie Holzwarth. Generation of projector augmented-wave atomic data: A 71 element validated table in the xml format. *Computer Physics Communications*, 185(4):1246–1254, 2014.
- [87] MD Jones and RC Albers. Spin-orbit coupling in an f-electron tight-binding model: Electronic properties of Th, U, and Pu. *Physical Review B*, 79(4):045107, 2009.
- [88] R. O. Jones and O. Gunnarsson. The density functional formalism, its applications and prospects. *Rev. Mod. Phys.*, 61:689–746, Jul 1989.
- [89] Thaneshwor P Kaloni, Liangzhi Kou, Thomas Frauenheim, and U. Schwingenschlögl. Quantum spin Hall states in graphene interacting with WS<sub>2</sub> or WSe<sub>2</sub>. *Applied Physics Letters*, 105(23):233112, 2014.
- [90] Mikhail I Katsnelson. *Graphene: carbon in two dimensions*. Cambridge University press, 2012.
- [91] Andras Kis et al. Graphene is not alone. *Nat. Nanotechnol.*, 7:683, 2012.
- [92] Jorge Kohanoff. *Electronic structure calculations for solids and molecules: theory and computational methods*. Cambridge University Press, 2006.
- [93] W. Kohn and L. J. Sham. Self-consistent equations including exchange and correlation effects. *Physical Review*, 140:A1133–A1138, Nov 1965.

- [94] Anton Kokalj. XCrySDen-a new program for displaying crystalline structures and electron densities. *Journal of Molecular Graphics and Modelling*, 17(3):176–179, 1999.
- [95] Andor Kormányos, Viktor Zólyomi, Neil D Drummond, Péter Rakyta, Guido Burkard, and Vladimir I Fal’ko. Monolayer MoS<sub>2</sub>: Trigonal warping, the  $\Gamma$  valley, and spin-orbit coupling effects. *Physical Review B*, 88(4):045416, 2013.
- [96] Wei Ku, Helge Rosner, Warren E Pickett, and Richard T Scalettar. Insulating ferromagnetism in  $La_4Ba_2Cu_2O_{10}$ : An *Ab initio* Wannier Function Analysis. *Physical Review Letters*, 89(16):167204, 2002.
- [97] A Kumar and PK Ahluwalia. Electronic structure of transition metal dichalcogenides monolayers 1H-MX<sub>2</sub> (M= Mo, W; X= S, Se, Te) from ab-initio theory: new direct band gap semiconductors. *The European Physical Journal B*, 85(6):1–7, 2012.
- [98] JL Lado and J Fernández-Rossier. Landau levels in 2D materials using wannier hamiltonians obtained by first principles. *2D Materials*, 3(3):035023, 2016.
- [99] Cornelius Lanczos. *An iteration method for the solution of the eigenvalue problem of linear differential and integral operators*. United States Government. Press Office Los Angeles, CA, 1950.
- [100] LD Landau. Zur Theorie der Phasenumwandlungen II. *Phys. Z. Sowjetunion*, 11(545):26–35, 1937.
- [101] Stefano Larentis, John R Tolsma, Babak Fallahazad, David C Dillen, Kyoungwan Kim, Allan H MacDonald, and Emanuel Tutuc. Band offset and negative compressibility in graphene-MoS<sub>2</sub> heterostructures. *Nano Letters*, 14(4):2039–2045, 2014.
- [102] Nam B Le, Tran Doan Huan, and Lilia M Woods. Interlayer interactions in van der Waals heterostructures: electron and phonon properties. *ACS applied materials & interfaces*, 8(9):6286–6292, 2016.
- [103] Kyuho Lee, Éamonn D Murray, Lingzhu Kong, Bengt I Lundqvist, and David C Langreth. Higher-accuracy van der Waals density functional. *Physical Review B*, 82(8):081101, 2010.
- [104] Patrick A Lee and TV Ramakrishnan. Disordered electronic systems. *Reviews of Modern Physics*, 57(2):287, 1985.

- [105] Mel Levy. On the simple constrained-search reformulation of the Hohenberg–Kohn theorem to include degeneracies and more (1964–1979). *International Journal of Quantum Chemistry*, 110(15):3140–3144, 2010.
- [106] Aurélien Lherbier. *Étude des propriétés électroniques et des propriétés de transport de nanofils semiconducteurs et de plans de graphène*. PhD thesis, 2008.
- [107] Lu Hua Li and Ying Chen. Atomically thin boron nitride: Unique properties and applications. *Advanced Functional Materials*, 26(16):2594–2608, 2016.
- [108] Song-Lin Li, Kazuhito Tsukagoshi, Emanuele Orgiu, and Paolo Samorì. Charge transport and mobility engineering in two-dimensional transition metal chalcogenide semiconductors. *Chemical Society Reviews*, 45(1):118–151, 2016.
- [109] Wu Li, Jesús Carrete, and Natalio Mingo. Thermal conductivity and phonon linewidths of monolayer MoS<sub>2</sub> from first principles. *Applied Physics Letters*, 103(25):253103, 2013.
- [110] Gui-Bin Liu, Wen-Yu Shan, Yugui Yao, Wang Yao, and Di Xiao. Three-band tight-binding model for monolayers of group-VIB transition metal dichalcogenides. *Physical Review B*, 88:085433, Aug 2013.
- [111] Gui-Bin Liu, Di Xiao, Yugui Yao, Xiaodong Xu, and Wang Yao. Electronic structures and theoretical modelling of two-dimensional group-VIB transition metal dichalcogenides. *Chem. Soc. Rev.*, 44:2643–2663, 2015.
- [112] Han Liu and D Ye Peide. MoS<sub>2</sub> dual-gate MOSFET with atomic-layer-deposited Al<sub>2</sub>O<sub>3</sub> as Top-Gate Dielectric. *IEEE electron device letters*, 33(4):546–548, 2012.
- [113] Kaihui Liu, Liming Zhang, Ting Cao, Chenhao Jin, Diana Qiu, Qin Zhou, Alex Zettl, Peidong Yang, Steve G. Louie, and Feng Wang. Evolution of interlayer coupling in twisted molybdenum disulfide bilayers. *Nature Communications*, 5(1):4966, 2014.
- [114] Xiaoze Liu, Tal Galfsky, Zheng Sun, Fengnian Xia, Erh-chen Lin, Yi-Hsien Lee, Stéphane Kéna-Cohen, and Vinod M Menon. Strong light–matter coupling in two-dimensional atomic crystals. *Nature Photonics*, 9(1):30, 2015.

- [115] Yuan Liu, Nathan O. Weiss, Xidong Duan, Hung-Chieh Cheng, Yu Huang, and Xiangfeng Duan. Van der Waals heterostructures and devices. *Nature Reviews Materials*, 1(9):16042, Jul 2016.
- [116] Dieter J Lohrmann, Lorenzo Resca, Giuseppe Pastori Parravicini, and Ronald D Graft. Shallow and deep impurity levels in multivalley semiconductors: A Green-function study of a cubic model by the recursion method. *Physical Review B*, 40(12):8404, 1989.
- [117] J. M. B. Lopes dos Santos, N. M. R. Peres, and A. H. Castro Neto. Graphene bilayer with a twist: Electronic structure. *Physical Review Letters*, 99:256802, Dec 2007.
- [118] J. M. B. Lopes dos Santos, N. M. R. Peres, and A. H. Castro Neto. Continuum model of the twisted graphene bilayer. *Physical Review B*, 86:155449, Oct 2012.
- [119] Tony Low, Andrey Chaves, Joshua D Caldwell, Anshuman Kumar, Nicholas X Fang, Phaedon Avouris, Tony F Heinz, Francisco Guinea, Luis Martin-Moreno, and Frank Koppens. Polaritons in layered two-dimensional materials. *Nature materials*, 16(2):182–194, 2017.
- [120] Chih-Pin Lu, Guohong Li, K Watanabe, T Taniguchi, and Eva Y Andrei. MoS<sub>2</sub>: choice substrate for accessing and tuning the electronic properties of graphene. *Physical Review Letters*, 113(15):156804, 2014.
- [121] Junpeng Lu, Alexandra Carvalho, Xinhui Kim Chan, Hongwei Liu, Bo Liu, Eng Soon Tok, Kian Ping Loh, AH Castro Neto, and Chorng Haur Sow. Atomic healing of defects in transition metal dichalcogenides. *Nano Letters*, 15(5):3524–3532, 2015.
- [122] Ning Lu, Hongyan Guo, Zhiwen Zhuo, Lu Wang, Xiaojun Wu, and Xiao Cheng Zeng. Twisted MX<sub>2</sub>/MoS<sub>2</sub> heterobilayers: effect of van der Waals interaction on the electronic structure. *Nanoscale*, 9:19131–19138, 2017.
- [123] Zheyu Lu, Stephen Carr, Daniel T. Larson, and Efthimios Kaxiras. Lithium intercalation in MoS<sub>2</sub> bilayers and implications for moiré flat bands. *Physical Review B*, 102:125424, Sep 2020.
- [124] P. Lykos and G. W. Pratt. Discussion on the Hartree-Fock approximation. *Rev. Mod. Phys.*, 35:496–501, Jul 1963.

- [125] Indrajit Maity, Prabal K Maiti, HR Krishnamurthy, and Manish Jain. Reconstruction of moiré lattices in twisted transition metal dichalcogenide bilayers. *arXiv preprint arXiv:1912.08702*, 2019.
- [126] Kin Fai Mak, Keliang He, Jie Shan, and Tony F Heinz. Control of valley polarization in monolayer MoS<sub>2</sub> by optical helicity. *Nature nanotechnology*, 7(8):494–498, 2012.
- [127] Kin Fai Mak, Changgu Lee, James Hone, Jie Shan, and Tony F Heinz. Atomically thin MoS<sub>2</sub>: a new direct-gap semiconductor. *Physical Review Letters*, 105(13):136805, 2010.
- [128] Richard M Martin and Richard Milton Martin. *Electronic structure: basic theory and practical methods*. Cambridge University press, 2004.
- [129] Nicola Marzari and David Vanderbilt. Maximally localized generalized Wannier functions for composite energy bands. *Physical Review B*, 56(20):12847, 1997.
- [130] D Mayou. Calculation of the Conductivity in the Short-Mean-Free-Path Regime. *EPL (Europhysics Letters)*, 6(6):549, 1988.
- [131] D Mayou and SN Khanna. A real-space approach to electronic transport. *Journal de Physique I*, 5(9):1199–1211, 1995.
- [132] Didier Mayou. Generalized Drude formula for the optical conductivity of quasicrystals. *Physical Review Letters*, 85:1290–1293, Aug 2000.
- [133] Didier Mayou and Guy Trambly de Laissardière. Chapter 7 quantum transport in quasicrystals and complex metallic alloys. In Takeo Fujiwara and Yasushi Ishii, editors, *Quasicrystals*, volume 3 of *Handbook of Metal Physics*, pages 209 – 265. Elsevier, 2008.
- [134] Edward McCann and Mikito Koshino. The electronic properties of bilayer graphene. *Reports on Progress in Physics*, 76(5):056503, 2013.
- [135] Michael J. Mehl and Dimitrios A. Papaconstantopoulos. Applications of a tight-binding total-energy method for transition and noble metals: Elastic constants, vacancies, and surfaces of monatomic metals. *Physical Review B*, 54:4519–4530, Aug 1996.
- [136] E. J. Mele. Commensuration and interlayer coherence in twisted bilayer graphene. *Physical Review B*, 81:161405, Apr 2010.
- [137] E J Mele. Interlayer coupling in rotationally faulted multilayer graphenes. *Journal of Physics D: Applied Physics*, 45(15):154004, mar 2012.

- [138] Souheyr Meziane, Houda Feraoun, Tarik Ouahrani, and Claude Esling. Effects of Li and Na intercalation on electronic, bonding and thermoelectric transport properties of  $\text{MX}_2$  ( $\text{M}=\text{Ta}$ ;  $\text{X}=\text{S}$  or  $\text{Se}$ ) dichalcogenides – Ab initio investigation. *Journal of Alloys and Compounds*, 581:731 – 740, 2013.
- [139] Pere Miró, Martha Audiffred, and Thomas Heine. An atlas of two-dimensional materials. *Chemical Society Reviews*, 43(18):6537–6554, 2014.
- [140] Artem Mishchenko, JS Tu, Y Cao, RV Gorbachev, JR Wallbank, MT Greenaway, VE Morozov, SV Morozov, MJ Zhu, SL Wong, et al. Twist-controlled resonant tunnelling in graphene/boron nitride/graphene heterostructures. *Nature nanotechnology*, 9(10):808–813, 2014.
- [141] Ahmed Missaoui. *Etude des propriétés de transport quantique dans les systèmes bidimensionnels à base de Carbone : Graphène, semi-conducteurs organiques*. Theses, Faculté des Sciences Mathématiques, Physiques et Naturelles de Tunis, September 2017.
- [142] Ahmed Missaoui, Jouda Jemaa Khabthani, Nejm-Eddine Jaidane, Didier Mayou, and Guy Trambly de Laissardière. Numerical analysis of electronic conductivity in graphene with resonant adsorbates: comparison of monolayer and bernal bilayer. *The European Physical Journal B*, 90(4):1–9, 2017.
- [143] Pilkyung Moon and Mikito Koshino. Optical absorption in twisted bilayer graphene. *Physical Review B*, 87:205404, May 2013.
- [144] Arash A. Mostofi, Jonathan R. Yates, Giovanni Pizzi, Young-Su Lee, Ivo Souza, David Vanderbilt, and Nicola Marzari. An updated version of wannier90: A tool for obtaining maximally-localised Wannier functions. *Computer Physics Communications*, 185(8):2309 – 2310, 2014.
- [145] RS Mulliken. Electronic population analysis on LCAO-MO molecular wave functions. II. Overlap populations, bond orders, and covalent bond energies. *The Journal of Chemical Physics*, 23(10):1841–1846, 1955.
- [146] Mit H. Naik and Manish Jain. Ultraflatbands and shear solitons in Moiré patterns of twisted bilayer transition metal dichalcogenides. *Physical Review Letters*, 121:266401, Dec 2018.
- [147] Michio Naito and Shoji Tanaka. Electrical Transport Properties in  $2\text{H-NbS}_2$ ,  $-\text{NbSe}_2$ ,  $-\text{TaS}_2$  and  $-\text{TaSe}_2$ . *Journal of the Physical Society of Japan*, 51(1):219–227, 1982.

- [148] Nguyen N. T. Nam and Mikito Koshino. Lattice relaxation and energy band modulation in twisted bilayer graphene. *Physical Review B*, 96:075311, Aug 2017.
- [149] Omid Faizy Namarvar, Ahmed Missaoui, Laurence Magaud, Didier Mayou, and Guy Trambly de Laissardière. Electronic structure and quantum transport in twisted bilayer graphene with resonant scatterers. *Physical Review B*, 101:245407, Jun 2020.
- [150] Tahreem Nawz, Amna Safdar, Muzammil Hussain, Dae Sung Lee, and Muhammad Siyar. Graphene to advanced MoS<sub>2</sub>: a review of structure, synthesis, and optoelectronic device application. *Crystals*, 10(10):902, 2020.
- [151] AH Castro Neto, Francisco Guinea, Nuno MR Peres, Kostya S Novoselov, and Andre K Geim. The electronic properties of graphene. *Reviews of Modern Physics*, 81(1):109, 2009.
- [152] Janne Nevalaita and Pekka Koskinen. Atlas for the properties of elemental two-dimensional metals. *Physical Review B*, 97(3):035411, 2018.
- [153] Konstantin S Novoselov, VI Fal, L Colombo, PR Gellert, MG Schwab, K Kim, et al. A roadmap for graphene. *Nature*, 490(7419):192–200, 2012.
- [154] Konstantin S Novoselov and AK Geim. The rise of graphene. *Nature Materials*, 6(3):183–191, 2007.
- [155] Kostya S Novoselov, Andre K Geim, Sergei V Morozov, D Jiang, Y. Zhang, Sergey V Dubonos, Irina V Grigorieva, and Alexandr A Firsov. Electric field effect in atomically thin carbon films. *Science*, 306(5696):666–669, 2004.
- [156] Kostya S Novoselov, D Jiang, F Schedin, TJ Booth, VV Khotkevich, SV Morozov, and Andre K Geim. Two-dimensional atomic crystals. *Proceedings of the National Academy of Sciences*, 102(30):10451–10453, 2005.
- [157] K.S. Novoselov, A. Mishchenko, A. Carvalho, and A. H. Castro Neto. 2D materials and van der Waals heterostructures. *Science*, 353(6298), 2016.
- [158] Richard Olsen, Ralph van Gelderen, and C Morais Smith. Ferromagnetism in ABC-stacked trilayer graphene. *Physical Review B*, 87(11):115414, 2013.
- [159] Christopher Conway Paige. *The computation of eigenvalues and eigenvectors of very large sparse matrices*. PhD thesis, University of London, 1971.

- [160] GS Painter and FW Averill. Bonding in the first-row diatomic molecules within the local spin-density approximation. *Physical Review B*, 26(4):1781, 1982.
- [161] J. J. Palacios, J. Fernández-Rossier, and L. Brey. Vacancy-induced magnetism in graphene and graphene ribbons. *Physical Review B*, 77:195428, May 2008.
- [162] Haining Pan, Fengcheng Wu, and Sankar Das Sarma. Band topology, Hubbard model, Heisenberg model, and Dzyaloshinskii-Moriya interaction in twisted bilayer WSe<sub>2</sub>. *Physical Review Research*, 2:033087, Jul 2020.
- [163] Yi Pan, Stefan Fölsch, Yifan Nie, Dacen Waters, Yu-Chuan Lin, Bhakti Jariwala, Kehao Zhang, Kyeongjae Cho, Joshua A. Robinson, and Randall M. Feenstra. Quantum-confined electronic states arising from the Moiré pattern of MoS<sub>2</sub>-WSe<sub>2</sub> heterobilayers. *Nano Letters*, 18(3):1849–1855, 2018.
- [164] Tribhuwan Pandey, Avinash P Nayak, Jin Liu, Samuel T Moran, Joon-Seok Kim, Lain-Jong Li, Jung-Fu Lin, Deji Akinwande, and Abhishek K Singh. Pressure-induced charge transfer doping of monolayer graphene/MoS<sub>2</sub> heterostructure. *Small*, 12(30):4063–4069, 2016.
- [165] DA Papaconstantopoulos and MJ Mehl. The Slater-Koster tight-binding method: a computationally efficient and accurate approach. *Journal of Physics: Condensed Matter*, 15(10):R413, 2003.
- [166] B Partoens and FM Peeters. Normal and Dirac fermions in graphene multilayers: Tight-binding description of the electronic structure. *Physical Review B*, 75(19):193402, 2007.
- [167] RE Peierls. Bemerkungen über Umwandlungstemperaturen. *Helv. Phys. Acta*, 7(2):81, 1934.
- [168] John P Perdew, Kieron Burke, and Matthias Ernzerhof. Generalized gradient approximation made simple. *Physical Review Letters*, 77(18):3865, 1996.
- [169] John P Perdew and Alex Zunger. Self-interaction correction to density-functional approximations for many-electron systems. *Physical Review B*, 23(10):5048, 1981.
- [170] A. L. C. Pereira and P. A. Schulz. Additional levels between Landau bands due to vacancies in graphene: Towards defect engineering. *Physical Review B*, 78:125402, Sep 2008.

- [171] Debora Pierucci, Hugo Henck, Jose Avila, Adrian Balan, Carl H Naylor, Gilles Patriarche, Yannick J Dappe, Mathieu G Silly, Fausto Sirotti, AT Charlie Johnson, et al. Band alignment and minigaps in monolayer MoS<sub>2</sub>-graphene van der Waals heterostructures. *Nano Letters*, 16(7):4054–4061, 2016.
- [172] Giovanni Pizzi, Valerio Vitale, Ryotaro Arita, Stefan Blügel, Frank Freimuth, Guillaume Géranton, Marco Gibertini, Dominik Gresch, Charles Johnson, Takashi Koretsune, Julen Ibañez-Azpiroz, Hyungjun Lee, Jae-Mo Lihm, Daniel Marchand, Antimo Marrazzo, Yuriy Mokrousov, Jamal I Mustafa, Yoshiro Nohara, Yusuke Nomura, Lorenzo Paulatto, Samuel Poncé, Thomas Ponweiser, Junfeng Qiao, Florian Thöle, Stepan S Tsirkin, Małgorzata Wierzbowska, Nicola Marzari, David Vanderbilt, Ivo Souza, Arash A Mostofi, and Jonathan R Yates. Wannier90 as a community code: new features and applications. *Journal of Physics: Condensed Matter*, 32(16):165902, jan 2020.
- [173] NV Podberezskaya, SA Magarill, NV Pervukhina, and SV Borisov. Crystal chemistry of dichalcogenides of MX<sub>2</sub> composition. *Zhurnal Strukturnoj Khimii*, 42(4):783–817, 2001.
- [174] Bin Qiu, Xiuwen Zhao, Guichao Hu, Weiwei Yue, Junfeng Ren, and Xiaobo Yuan. Optical properties of Graphene/MoS<sub>2</sub> heterostructure: First principles calculations. *Nanomaterials*, 8(11):962, 2018.
- [175] Branimir Radisavljevic, Aleksandra Radenovic, Jacopo Brivio, Valentina Giacometti, and Andras Kis. Single-layer MoS<sub>2</sub> transistors. *Nature nanotechnology*, 6(3):147, 2011.
- [176] Ashwin Ramasubramaniam. Large excitonic effects in monolayers of molybdenum and tungsten dichalcogenides. *Physical Review B*, 86(11):115409, 2012.
- [177] Stephanie Reich, Janina Maultzsch, Christian Thomsen, and Pablo Ordejon. Tight-binding description of graphene. *Physical Review B*, 66(3):035412, 2002.
- [178] R M Ribeiro, Vitor M Pereira, N M R Peres, P R Briddon, and A H Castro Neto. Strained graphene: tight-binding and density functional calculations. *New Journal of Physics*, 11(11):115002, 2009.
- [179] E. Ridolfi, D. Le, T. S. Rahman, E. R. Mucciolo, and C. H. Lewenkopf. A tight-binding model for MoS<sub>2</sub> monolayers. *Journal of Physics: Condensed Matter*, 27(36):365501, aug 2015.

- [180] Stéphan Roche. *Contribution à l'étude théorique du transport électronique dans les quasicristaux*. PhD thesis, Grenoble 1, 1996.
- [181] Stephan Roche. Quantum transport by means of  $O(N)$  real-space methods. *Physical Review B*, 59(3):2284, 1999.
- [182] Stephan Roche, Nicolas Leconte, Frank Ortmann, Aurélien Lherbier, David Soriano, and Jean-Christophe Charlier. Quantum transport in disordered graphene: A theoretical perspective. *Solid State Communications*, 152(15):1404–1410, 2012.
- [183] Stephan Roche and Didier Mayou. Conductivity of quasiperiodic systems: A numerical study. *Physical Review Letters*, 79(13):2518, 1997.
- [184] Stephan Roche and Didier Mayou. Formalism for the computation of the RKKY interaction in aperiodic systems. *Physical Review B*, 60(1):322, 1999.
- [185] R. Roldán, M. P. López-Sancho, F. Guinea, E/ Cappelluti, J. A. Silva-Guillén, and P. Ordejón. Momentum dependence of spin-orbit interaction effects in single-layer and multi-layer transition metal dichalcogenides. *2D Materials*, 1(3):034003, nov 2014.
- [186] Rafael Roldán, Jose A. Silva-Guillén, M. Pilar López-Sancho, Francisco Guinea, Emmanuele Cappelluti, and Pablo Ordejón. Electronic properties of single-layer and multilayer transition metal dichalcogenides  $MX_2$  ( $M = \text{Mo}, \text{W}$  and  $X = \text{S}, \text{Se}$ ). *Annalen der Physik*, 526(9-10):347–357, 2014.
- [187] Habib Rostami, Ali G. Moghaddam, and Reza Asgari. Effective lattice Hamiltonian for monolayer  $\text{MoS}_2$ : Tailoring electronic structure with perpendicular electric and magnetic fields. *Physical Review B*, 88:085440, Aug 2013.
- [188] Kallol Roy, Medini Padmanabhan, Srijit Goswami, T Phanindra Sai, Gopalakrishnan Ramalingam, Srinivasan Raghavan, and Arindam Ghosh. Graphene- $\text{MoS}_2$  hybrid structures for multifunctional photoresponsive memory devices. *Nature nanotechnology*, 8(11):826–830, 2013.
- [189] B Sachs, L Britnell, TO Wehling, A Eckmann, R Jalil, BD Belle, AI Lichtenstein, MI Katsnelson, and KS Novoselov. Doping mechanisms in graphene- $\text{MoS}_2$  hybrids. *Applied Physics Letters*, 103(25):251607, 2013.
- [190] John R Schaibley, Hongyi Yu, Genevieve Clark, Pasqual Rivera, Jason S Ross, Kyle L Seyler, Wang Yao, and Xiaodong Xu. Valleytronics in 2D materials. *Nature Reviews Materials*, 1(11):1–15, 2016.

- [191] Frank Schwierz, Jörg Pezoldt, and Ralf Granzner. Two-dimensional materials and their prospects in transistor electronics. *Nanoscale*, 7(18):8261–8283, 2015.
- [192] Li Shao, Guangde Chen, Honggang Ye, Yelong Wu, Haibo Niu, and Youzhang Zhu. Electronic properties of MoS<sub>2</sub> sandwiched between graphene monolayers. *EPL (Europhysics Letters)*, 106(4):47003, 2014.
- [193] Xiji Shao, Kedong Wang, Rui Pang, and Xingqiang Shi. Lithium intercalation in Graphene/MoS<sub>2</sub> composites: first-principles insights. *The Journal of Physical Chemistry C*, 119(46):25860–25867, 2015.
- [194] Jose Ángel Silva-Guillén, Pablo San-Jose, and Rafael Roldán. Electronic Band Structure of Transition Metal Dichalcogenides from Ab Initio and Slater-Koster tight-binding model. *Applied Sciences*, 6(10):284, 2016.
- [195] Sobhit Singh, Abdulrhman M. Alsharari, Sergio E. Ulloa, and Aldo H. Romero. *Proximity-Induced Topological Transition and Strain-Induced Charge Transfer in Graphene/MoS<sub>2</sub> Bilayer Heterostructures*, chapter 1, pages 1–28. John Wiley & Sons, Ltd, 2019.
- [196] Sobhit Singh, Camilo Espejo, and Aldo H Romero. Structural, electronic, vibrational, and elastic properties of graphene/MoS<sub>2</sub> bilayer heterostructures. *Physical Review B*, 98(15):155309, 2018.
- [197] Sobhit Singh and Aldo H Romero. Giant tunable rashba spin splitting in a two-dimensional BiSb monolayer and in BiSb/AlN heterostructures. *Physical Review B*, 95(16):165444, 2017.
- [198] John C Slater and George F Koster. Simplified LCAO method for the periodic potential problem. *Physical Review*, 94(6):1498, 1954.
- [199] José M Soler, Emilio Artacho, Julian D Gale, Alberto García, Javier Junquera, Pablo Ordejón, and Daniel Sánchez-Portal. The SIESTA method for *ab initio* order-N materials simulation. *Journal of Physics: Condensed Matter*, 14(11):2745, 2002.
- [200] Ivo Souza, Nicola Marzari, and David Vanderbilt. Maximally localized Wannier functions for entangled energy bands. *Physical Review B*, 65(3):035109, 2001.
- [201] John M Stephan Gasiorowicz. *Quantum physics*. John Wiley and Sons Ltd, 1974.

- [202] E. Suárez Morell, J. D. Correa, P. Vargas, M. Pacheco, and Z. Barticevic. Flat bands in slightly twisted bilayer graphene: Tight-binding calculations. *Physical Review B*, 82:121407, Sep 2010.
- [203] Feng Sun, Ting Luo, Lin Li, Aijun Hong, Cailei Yuan, and Wei Zhang. Influence of different exchange-correlation potentials on twisted structures of bilayer  $\text{XS}_2$  ( $X = \text{Mo}, \text{Cr}$ ). *Computational Materials Science*, page 110205, 2020.
- [204] Minglei Sun, Jyh-Pin Chou, Jin Yu, and Wencheng Tang. Effects of structural imperfection on the electronic properties of graphene/ $\text{WSe}_2$  heterostructures. *Journal of Materials Chemistry C*, 5(39):10383–10390, 2017.
- [205] C. J. Tabert and E. J. Nicol. Optical conductivity of twisted bilayer graphene. *Physical Review B*, 87:121402, Mar 2013.
- [206] Chaoliang Tan, Xiehong Cao, Xue-Jun Wu, Qiyuan He, Jian Yang, Xiao Zhang, Junze Chen, Wei Zhao, Shikui Han, Gwang-Hyeon Nam, et al. Recent advances in ultrathin two-dimensional nanomaterials. *Chemical Reviews*, 117(9):6225–6331, 2017.
- [207] Yaohua Tan, Fan W. Chen, and Avik W. Ghosh. First principles study and empirical parametrization of twisted bilayer  $\text{MoS}_2$  based on band-unfolding. *Applied Physics Letters*, 109(10):101601, 2016.
- [208] Yanhao Tang, Lizhong Li, Tingxin Li, Yang Xu, Song Liu, Katayun Barmak, Kenji Watanabe, Takashi Taniguchi, Allan H. MacDonald, Jie Shan, and Kin Fai Mak. Simulation of Hubbard model physics in  $\text{WSe}_2/\text{WS}_2$  moiré superlattices. *Nature*, 579(7799):353–358, 2020.
- [209] Peng Tao, Huai-Hong Guo, Teng Yang, and Zhi-Dong Zhang. Stacking stability of  $\text{MoS}_2$  bilayer: An *ab initio* study. *Chinese Physics B*, 23(10):106801, oct 2014.
- [210] Tran Duy Thanh, Nguyen Dinh Chuong, Hoa Van Hien, Tolendra Kshetri, Nam Hoon Kim, Joong Hee Lee, et al. Recent advances in two-dimensional transition metal dichalcogenides-graphene heterostructured materials for electrochemical applications. *Progress in Materials Science*, 96:51–85, 2018.
- [211] Luis EF Foa Torres, Stephan Roche, and Jean-Christophe Charlier. *Introduction to graphene-based nanomaterials: from electronic structure to quantum transport*. Cambridge University Press, 2020.

- [212] Daniel J. Trainer, Aleksei V. Putilov, Cinzia Di Giorgio, Timo Saari, Baokai Wang, Mattheus Wolak, Ravini U. Chandrasena, Christopher Lane, Tay-Rong Chang, Horng-Tay Jeng, Hsin Lin, Florian Kronast, Alexander X. Gray, Xiaoxing Xi, Jouko Nieminen, Arun Bansil, and Maria Iavarone. Inter-layer coupling induced valence band edge shift in mono- to few-layer MoS<sub>2</sub>. *Scientific Reports*, 7(1):40559, 2017.
- [213] Guy Trambly de Laissardière, Didier Mayou, and Laurence Magaud. Localization of Dirac electrons in rotated graphene bilayers. *Nano Letters*, 10(3):804–808, 2010.
- [214] Guy Trambly de Laissardière, Didier Mayou, and Laurence Magaud. Numerical studies of confined states in rotated bilayers of graphene. *Physical Review B*, 86(7):125413, 2012.
- [215] Lloyd N Trefethen and David Bau III. *Numerical linear algebra*, volume 50. Siam, 1997.
- [216] François Triozon. *Diffusion quantique et conductivité dans les systèmes aperiodiques*. PhD thesis, Université Joseph-Fourier-Grenoble I, 2002.
- [217] François Triozon, Julien Vidal, Rémy Mosseri, and Didier Mayou. Quantum dynamics in two-and three-dimensional quasiperiodic tilings. *Physical Review B*, 65(22):220202, 2002.
- [218] Alexei M Tsvetlik. *Quantum field theory in condensed matter physics*. Cambridge University press, 2007.
- [219] Nicolas Ubrig, P Blake, Dirk Van Der Marel, and AB Kuzmenko. Infrared spectroscopy of hole-doped ABA-stacked trilayer graphene. *EPL (Europhysics Letters)*, 100(5):58003, 2012.
- [220] Arend M. van der Zande, Jens Kunstmann, Alexey Chernikov, Daniel A. Chenet, YuMeang You, XiaoXiao Zhang, Pinshane Y. Huang, Timothy C. Berkelbach, Lei Wang, Fan Zhang, Mark S. Hybertsen, David A. Muller, David R. Reichman, Tony F. Heinz, and James C. Hone. Tailoring the electronic structure in bilayer molybdenum disulfide via interlayer twist. *Nano Letters*, 14(7):3869–3875, Jul 2014.
- [221] Matěj Velický and Peter S Toth. From two-dimensional materials to their heterostructures: An electrochemist’s perspective. *Applied Materials Today*, 8:68–103, 2017.

- [222] Somepalli Venkateswarlu, Andreas Honecker, and Guy Trambly de Laisardière. Electronic localization in twisted bilayer MoS<sub>2</sub> with small rotation angle. *Physical Review B*, 102:081103, Aug 2020.
- [223] T Wakamura, NJ Wu, AD Chepelianskii, S Guéron, M Och, M Ferrier, T Taniguchi, K Watanabe, C Mattevi, and H Bouchiat. Spin-Orbit-Enhanced Robustness of Supercurrent in Graphene/WS<sub>2</sub> Josephson Junctions. *Physical Review Letters*, 125(26):266801, 2020.
- [224] Philip Richard Wallace. The band theory of graphite. *Physical Review*, 71(9):622, 1947.
- [225] Haotian Wang, Hongtao Yuan, Seung Sae Hong, Yanbin Li, and Yi Cui. Physical and chemical tuning of two-dimensional transition metal dichalcogenides. *Chemical Society Reviews*, 44(9):2664–2680, 2015.
- [226] Qing Hua Wang, Kourosch Kalantar-Zadeh, Andras Kis, Jonathan N Coleman, and Michael S Strano. Electronics and optoelectronics of two-dimensional transition metal dichalcogenides. *Nature nanotechnology*, 7(11):699, 2012.
- [227] Zhe Wang, Dong-Keun Ki, Hua Chen, Helmuth Berger, Allan H MacDonald, and Alberto F Morpurgo. Strong interface-induced spin-orbit interaction in graphene on WS<sub>2</sub>. *Nature communications*, 6:8339, 2015.
- [228] Zilu Wang, Qian Chen, and Jinlan Wang. Electronic structure of twisted bilayers of graphene/MoS<sub>2</sub> and MoS<sub>2</sub>/MoS<sub>2</sub>. *The Journal of Physical Chemistry C*, 119(9):4752–4758, 2015.
- [229] Gregory H Wannier. The structure of electronic excitation levels in insulating crystals. *Physical Review*, 52(3):191, 1937.
- [230] CR Woods, L Britnell, A Eckmann, RS Ma, JC Lu, HM Guo, X Lin, GL Yu, Y Cao, RV Gorbachev, et al. Commensurate–incommensurate transition in graphene on hexagonal boron nitride. *Nature Physics*, 10(6):451–456, 2014.
- [231] Jiafang Wu, Lijun Meng, Jun Yu, and Yizhi Li. A first-principles study of electronic properties of twisted MoTe<sub>2</sub>. *physica status solidi (b)*, 257(3):1900412, 2020.
- [232] Lede Xian, Martin Claassen, Dominik Kiese, Michael M Scherer, Simon Trebst, Dante M Kennes, and Angel Rubio. Realization of nearly dispersionless bands with strong orbital anisotropy from destructive interference in twisted bilayer MoS<sub>2</sub>. *arXiv preprint arXiv:2004.02964*, 2020.

- [233] Di Xiao, Gui-Bin Liu, Wanxiang Feng, Xiaodong Xu, and Wang Yao. Coupled spin and valley physics in monolayers of MoS<sub>2</sub> and other group-VI dichalcogenides. *Physical Review Letters*, 108(19):196802, 2012.
- [234] Po-Chun Yeh, Wencan Jin, Nader Zaki, Jens Kunstmann, Daniel Chenet, Ghidewon Arefe, Jerzy T. Sadowski, Jerry I. Dadap, Peter Sutter, James Hone, and Richard M. Osgood. Direct measurement of the tunable electronic structure of bilayer MoS<sub>2</sub> by interlayer twist. *Nano Letters*, 16(2):953–959, Feb 2016.
- [235] Erik R Ylvisaker and Warren E Pickett. First-principles study of the electronic and vibrational properties of LiNbO<sub>2</sub>. *Physical Review B*, 74(7):075104, 2006.
- [236] Thomas Young. I. The Bakerian Lecture. Experiments and calculations relative to physical optics. *Philosophical transactions of the Royal Society of London*, (94):1–16, 1804.
- [237] Woo Jong Yu, Zheng Li, Hailong Zhou, Yu Chen, Yang Wang, Yu Huang, and Xiangfeng Duan. Vertically stacked multi-heterostructures of layered materials for logic transistors and complementary inverters. *Nature materials*, 12(3):246–252, 2013.
- [238] Xiaoliang Yu, Jie Tang, Kazuya Terabe, Taizo Sasaki, Runsheng Gao, Yoshikazu Ito, Kensuke Nakura, Kazuko Asano, and Masa-aki Suzuki. Fabrication of graphene/MoS<sub>2</sub> alternately stacked structure for enhanced lithium storage. *Materials Chemistry and Physics*, 239:121987, 2020.
- [239] Shengjun Yuan, Rafael Roldán, Antti-Pekka Jauho, and M. I. Katsnelson. Electronic properties of disordered graphene antidot lattices. *Physical Review B*, 87:085430, Feb 2013.
- [240] Shengjun Yuan, Rafael Roldán, MI Katsnelson, and Francisco Guinea. Effect of point defects on the optical and transport properties of MoS<sub>2</sub> and WS<sub>2</sub>. *Physical Review B*, 90(4):041402, 2014.
- [241] Ferdows Zahid, Lei Liu, Yu Zhu, Jian Wang, and Hong Guo. A generic tight-binding model for monolayer, bilayer and bulk MoS<sub>2</sub>. *AIP Advances*, 3(5):052111, 2013.
- [242] Zhen Zhan, Yipei Zhang, Pengfei Lv, Hongxia Zhong, Guodong Yu, Francisco Guinea, José Ángel Silva-Guillén, and Shengjun Yuan. Tunability of multiple ultraflat bands and effect of spin-orbit coupling in twisted bilayer transition metal dichalcogenides. *Physical Review B*, 102(24):241106, 2020.

- [243] Chendong Zhang, Chih-Piao Chuu, Xibiao Ren, Ming-Yang Li, Lain-Jong Li, Chuanhong Jin, Mei-Yin Chou, and Chih-Kang Shih. Interlayer couplings, moiré patterns, and 2D electronic superlattices in MoS<sub>2</sub>/WSe<sub>2</sub> hetero-bilayers. *Science Advances*, 3(1):1601459, 2017.
- [244] Hua Zhang. Ultrathin two-dimensional nanomaterials. *ACS nano*, 9(10):9451–9469, 2015.
- [245] Hua Zhang. Introduction: 2D Materials Chemistry. *Chemical Reviews*, 118(13):6089–6090, 2018. PMID: 29991267.
- [246] Hua Zhang, Hui-Ming Cheng, and Peide Ye. 2D nanomaterials: beyond graphene and transition metal dichalcogenides. *Chemical Society Reviews*, 47(16):6009–6012, 2018.
- [247] Yipei Zhang, Zhen Zhan, Francisco Guinea, Jose Ángel Silva-Guillén, and Shengjun Yuan. Tuning band gaps in twisted bilayer MoS<sub>2</sub>. *Physical Review B*, 102:235418, Dec 2020.
- [248] Yuanbo Zhang, Yan-Wen Tan, Horst L Stormer, and Philip Kim. Experimental observation of the quantum Hall effect and Berry’s phase in graphene. *Nature*, 438(7065):201–204, 2005.
- [249] Zhiming Zhang, Yimeng Wang, Kenji Watanabe, Takashi Taniguchi, Keiji Ueno, Emanuel Tutuc, and Brian J. LeRoy. Flat bands in twisted bilayer transition metal dichalcogenides. *Nature Physics*, 16(11):1093–1096, Nov 2020.
- [250] Wenjuan Zhu, Tony Low, Yi Hsien Lee, Han Wang, Damon B. Farmer, Jing Kong, Fengnian Xia, and Phaeton Avouris. Electronic transport and device prospects of monolayer molybdenum disulphide grown by chemical vapour deposition. *Nature Communications*, 5, January 2014.
- [251] Yanwu Zhu, Shanthi Murali, Weiwei Cai, Xuesong Li, Ji Won Suk, Jeffrey R. Potts, and Rodney S. Ruoff. Graphene and Graphene Oxide: Synthesis, Properties, and Applications. *Advanced Materials*, 22(35):3906–3924, 2010.
- [252] John M Ziman. *Principles of the Theory of Solids*. Cambridge University press, 1972.
- [253] Aleš Zupan, Peter Blaha, Karlheinz Schwarz, and John P. Perdew. Pressure-induced phase transitions in solid Si, SiO<sub>2</sub>, and Fe: Performance of local-spin-density and generalized-gradient-approximation density functionals. *Physical Review B*, 58:11266–11272, Nov 1998.